Mechanical properties of aerospace composite parts made from stitched multilayer 3D carbon fibre preforms

Scott Jeffrey Audette

Thesis submitted to the
Faculty of Graduate and Postdoctoral Studies
In partial fulfillment of the requirements
For the M.A.Sc. degree in
Mechanical Engineering

Ottawa-Carleton Institute for Mechanical and Aerospace Engineering
Faculty of Engineering
University of Ottawa

©Scott Jeffrey Audette, Ottawa, Canada, 2014

Abstract

Producing composite parts using low-cost processes such as resin transfer moulding (RTM) has received much interest in the aerospace industry. RTM manufactured components require near net shape preforms which closely fit mould cavities. To reduce labour costs associated with composite production, automated preforming processes must be utilized. However, obtaining reproducible high quality preforms is required for manufacturing consistent high quality parts. Stitched multilayer 3D non crimp fabric preforms are well suited for automation and an investigation into quality and performance of components manufactured from these preforms is required.

This thesis provides an initial evaluation of quality and mechanical properties of components made from stitched multilayer 3D non crimp fabric preforms using RTM. Similar sized flat plates of varying fibre volume fractions were manufactured to evaluate flexural modulus and strength, short beam shear strength and drop weight impact resistance of the material. Also, integral reinforced panels (IRPs) featuring a reinforcing section joined to a flat plate of varying laminating sequences were manufactured to evaluate debonding strength between sections. Optical microscopy was performed on component samples to determine quality based on void content and was found to be within acceptable limits for production composites. Flexural moduli were found to be comparable with theoretical expected values, however flexural strength was limited by the presence of transverse stitches. Short beam shear strength results showed high consistency between specimens, however were lower than comparable values found in literature. Impact specimens showed consistency among specimens, with greater damage resistance than comparable values found in literature. Determining debonding strength proved difficult as different failure modes were observed between IRPs, however, initial baseline values were acquired.

Acknowledgements

I would like to express my most sincere gratitude to my supervisor Dr. François Robitaille for all off his help, guidance and support during my time spent working on this thesis. I am very thankful for his patience, encouragement and good humour, for which I could not have made it through this process without.

I would also like to thank the Mechanical Shop staff; John, James, Stan and Mike who helped with manufacturing moulds, parts and for providing assistance and advice making my research possible.

I would also like to thank Simon Hind, Richard Desnoyers and the NRC for allowing access to material testing equipment and assistance while testing.

I would also like to thank all of my colleagues for sharing information, resources and insight, especially Andrew Stewart and Aymen Sakka for their collaboration during the manufacturing stages of this work. Also, to all of the great people whom I shared CBY B08D with.

Finally, I would like to thank my family and friends for their constant support and for enabling me to pursue my academic goals. Most particularly, Genevieve Lafontaine for her love and support over the last few years, and my mother Sandy and father Eugene for their continuing motivation and support.

Contents

Abstract ii

Acknowledgements iii

Contents iv

List of Figures vi

List of Tables xi

Nomenclature xvii

1 Introduction 1
- 1.1 PMC Manufacturing . . . 2
  - 1.1.1 Resin Transfer Moulding . . . 3
  - 1.1.2 Preforming . . . 4
- 1.2 Thesis Overview & Objectives . . . 9

2 Literature Review 11
- 2.1 Mechanical Properties . . . 11
  - 2.1.1 Hooke's Law . . . 12
  - 2.1.2 Elastic behaviour of the Unidirectional Lamina . . . 14
    - 2.1.2.1 Material Properties of the Unidirectional Lamina . . . 16
    - 2.1.2.2 Stress-Strain Transformations . . . 18
  - 2.1.3 Classical Laminate Theory . . . 20
  - 2.1.4 Failure Mechanisms PMCs . . . 28
    - 2.1.4.1 Unidirectional PMCs . . . 29
    - 2.1.4.2 Multidirectional PMC Laminates . . . 31
  - 2.1.5 Effects of Preforming Structures on Mechanical Properties . . . 35
    - 2.1.5.1 Multidirectional PMC Laminates . . . 36
    - 2.1.5.2 Through-Thickness Reinforcements of Laminates . . . 36
  - 2.1.6 Impact Properties . . . 41

3 Experimental Setup and Procedures 45
- 3.1 Preform and PMC component Manufacturing . . . 45
  - 3.1.1 Preform Manufacturing . . . 46
    - 3.1.1.1 Layup . . . 48

3.1.1.2 Stitching . . . 52
3.1.1.3 Preform Compaction . . . 56
3.1.1.4 Preform Cutting . . . 58
3.1.2 PMC Manufacturing . . . 59
3.1.2.1 Flat Plate Mould . . . 60
3.1.2.2 Integral Reinforced Panel Mould . . . 62
3.1.2.3 Integral Reinforced Panel Preform Manufacturing . . . 66
3.1.2.4 Mould Preparation . . . 68
3.1.2.5 Resin Injection Apparatus . . . 71
3.1.2.6 Resin Injection Procedure . . . 76
3.2 Mechanical Testing . . . 81
3.2.1 Long Span Four-Point Bending Tests . . . 83
3.2.2 Short Span Three-Point Bending Tests . . . 90
3.2.3 Drop Weight Impact Tests . . . 95
3.2.4 Long Span Four-Point Bending Tests of Integral Reinforced Panel . 102
3.2.5 Optical Microscopy Imaging and Analysis . . . 106

4 Results and Analysis **109**
4.1 Quality Description and Analysis of PMC Components . . . 109
4.1.1 Flat Plates . . . 111
4.1.2 Integral Reinforced Panels . . . 117
4.2 Mechanical Testing of Flat Plates . . . 128
4.2.1 Long Span Four-Point Bending . . . 128
4.2.1.1 Specimen Set 1: $\mathsf{v}_{f,c} = 52\%$, Tested Along 0^{o} Reference Direction . . . 130
4.2.1.2 Specimen Set 2: $\mathsf{v}_{f,c} = 52\%$, Tested Along 90^{o} Reference Direction . . . 133
4.2.1.3 Specimen Set 3: $\mathsf{v}_{f,c} = 63.5\%$, Tested Along 0^{o} Reference Direction . . . 139
4.2.1.4 Specimen Set 4: $\mathsf{v}_{f,c} = 63.5\%$, Tested Along 90^{o} Reference Direction . . . 145
4.2.2 Short Span Three-Point Bending . . . 149
4.2.2.1 Specimen Set 5: $\mathsf{v}_{f,c} = 52\%$, Tested Along 0^{o} Reference Direction . . . 150
4.2.2.2 Specimen Set 6: $\mathsf{v}_{f,c} = 52\%$, Tested Along 90^{o} Reference Direction . . . 153
4.2.2.3 Specimen Set 7: $\mathsf{v}_{f,c} = 63.5\%$, Tested Along 0^{o} Reference Direction . . . 155
4.2.2.4 Specimen Set 8: $\mathsf{v}_{f,c} = 63.5\%$, Tested Along 90^{o} Reference Direction . . . 157
4.2.3 Drop Weight Impact . . . 158
4.3 Mechanical Testing of Integral Reinforced Panels . . . 164
4.3.1 Long Span Four-Point Bending . . . 164

5 Conclusion and Recommendations **171**

References **174**

Appendix A Load-Deflection Curves for Long Span Four-Point Bending of Flat Plates **180**

Appendix B Load vs. Deflection Curves for Short Span Three-Point Bending of Flat Plates **187**

Appendix C Load-Time Curves for Drop-Weight Impact Tests of Flat Plates **194**

Appendix D Load-Deflection curves for Drop-Weight Impact Tests of Flat Plates **196**

Appendix E Load-Deflection Curves for Long Span Four-Point Bending of IRPs **198**

List of Figures

Figure 1.1 RTM process steps [9] 4
Figure 1.2 Cost allocation of a RTM-manufactured part [10] 5
Figure 1.3 Stiffness of a unidirectional composite as a function of fibre orientation angle 6
Figure 1.4 Types of fabric structures [14] 7
Figure 1.5 3D woven reinforcement [15] 8
Figure 1.6 Various stitches used in multilayer textile preforms: lock stitch (left), chain stitch (middle), modified lock stitch (right) [18] . 9
Figure 1.7 Manufactured 3D carbon fibre epoxy integral reinforced panel component 10

Figure 2.1 Levels of composite observation and analysis [19] 12
Figure 2.2 General stress tensor at a point [19] 13
Figure 2.3 Principal coordinates of unidirectional lamina [19] 15
Figure 2.4 Stress components referred to loading axes (x, y) and material principal axes (1, 2) [19] 18
Figure 2.5 Laminate stacking sequence [24] 21
Figure 2.6 Laminate section before (left) and after (right) deformation [19] 22
Figure 2.7 Resultant forces N and moments M of k^{th} lamina [22] 23
Figure 2.8 Laminate thickness with coordinates of individual lamina [19] . 24
Figure 2.9 Mechanical behaviours associated with individual laminate stiffness matrix terms [22] 26

Figure 2.10 Variability in tensile strength of carbon fibres [26] 29
Figure 2.11 Microfailure modes from longitudinal tensile loading of unidirectional PMC [26] 30
Figure 2.12 Uniaxial strength of unidirectional E-glass/epoxy lamina as a function of orientation angle [19] 31
Figure 2.13 Tensile stress-strain schematic of a [0°/90°] cross-ply laminate tested along 0° direction [26] 32
Figure 2.14 Mode I, II and III delamination types [34] 33
Figure 2.15 Load-displacement curve (left) and compliance-crack size curve (right) from DCB test [26] 34
Figure 2.16 Mixed-mode fracture criterion for a toughened carbon/epoxy composite [36] 35
Figure 2.17 Comparison of in-plane and through-thickness tensile strengths of multiple PMC laminates [16] 36
Figure 2.18 Fibre distortion and resin-rich areas within a z-pinned laminate [50] 37
Figure 2.19 Flexural strength and modulus vs. z-pin content and diameter [50] 38
Figure 2.20 Illustration of ideal crack bridging by CNTs between laminate plies (left) and between crack (right) [52] 39
Figure 2.21 Normalized flexural modulus vs. stitch density from multiple studies [18] 40
Figure 2.22 Severe fibre misalignment in PMC component made from 3D woven preform [57] 41
Figure 2.23 Load vs. time comparison for 24 layer Carbon/Epoxy laminates under different impact energies [61] 43
Figure 2.24 Load vs. deflection curve from a 9.7 J impact of a $[0^\circ_2/45^\circ_2/90^\circ_2/-45]_s$ carbon/epoxy ($\mathsf{v}_f = 60\%$) [63] 44

Figure 3.1 Preform manufacturing - layup 46
Figure 3.2 300 mm x 300 mm Pinboard 49
Figure 3.3 Pin arrangement on 300 mm x 300 mm Pinboard 50
Figure 3.4 Clamping frame for 300 mm x 300 mm preform 51
Figure 3.5 Fibre press 51
Figure 3.6 Fibre lay-up 52
Figure 3.7 Modified Brother LX-3125 sewing machine 53
Figure 3.8 Cam and limit switch modification 54
Figure 3.9 Stitches in NCF carbon fibre preform - 9.5x magnification . . . 55
Figure 3.10 Fully stitched NCF carbon fibre preform 56
Figure 3.11 Aluminium compaction platens 57
Figure 3.12 Preform before (left) and after (right) compaction cycling . . . 58
Figure 3.13 Stitched NCF carbon fibre preform cutting setup 59
Figure 3.14 CAD drawing of female flat mould 60
Figure 3.15 CAD drawing of flat mould cover 61
Figure 3.16 Flat plate mould components 62

Figure 3.17 CAD drawing of integral reinforced panel 62
Figure 3.18 IRP mould pieces 63
Figure 3.19 CAD drawing of IRP lower mould piece 63
Figure 3.20 CAD drawing of IRP upper mould piece 64
Figure 3.21 CAD drawing of IRP inner mould piece 64
Figure 3.22 CAD drawing of IRP intermediate mould piece 65
Figure 3.23 IRP pre-stitching preform placement 67
Figure 3.24 IRP preform stitching 68
Figure 3.25 IRP preform before (left) and after (right) edge cutting 68
Figure 3.26 Chem Trend® CHEMLEASE 70-90 and accompanying mould cleaner 69
Figure 3.27 Flat plate female mould piece with preform and o-ring 70
Figure 3.28 IRP mould assembly 71
Figure 3.29 Tri-tex L-1911 resin used for injections 72
Figure 3.30 Experimental resin injection apparatus 73
Figure 3.31 Diagram of resin injection apparatus 74
Figure 3.32 Aluminium blocks used for stopping cylinder rotation 75
Figure 3.33 Vacuum pump gauge readout at steady state 78
Figure 3.34 Stainless steel resin pot and injection apparatus 79
Figure 3.35 Mould inlet tube from three way wye valve 79
Figure 3.36 Sealed moulds during oven cure cycle 80
Figure 3.37 Removal of inner mould piece using hydraulic ram, IRP3 . . . 81
Figure 3.38 320 mm square plate cutting plan 83
Figure 3.39 Four-point bending test setup [66] 84
Figure 3.40 Advanced video extensometer set-up 85
Figure 3.41 Four-point flexural test apparatus 86
Figure 3.42 Load-deflection curve from long span four-point bending test of specimen P1_LSB1 87
Figure 3.43 Stress-strain curve from long span four-point bending test of specimen P1_LSB1 88
Figure 3.44 Specimen P1_LSB1 post-test image 90
Figure 3.45 Short span three-point bending test setup [68] 91
Figure 3.46 Short span three-point bending test apparatus 92
Figure 3.47 Load-displacement curve from short span three-point bending test of specimen P1_SSB1 93
Figure 3.48 Possible short span three-point bending test failure modes[69] . 94
Figure 3.49 Specimen P1_SSB1 post test image 95
Figure 3.50 Instron 8200 series drop weight impact testing tower, NRC Ottawa 96
Figure 3.51 Drop head assembly 97
Figure 3.52 Support fixture with clamps 98
Figure 3.53 Load versus time curve from drop weight impact of specimen P1_IMP1 99
Figure 3.54 Dent depth measurement apparatus 100
Figure 3.55 Dent depth measurement diagram 101

Figure 3.56 Common external damage modes from out-of-plane drop weight impact testing [69] . . . 101
Figure 3.57 Top surface images of P1_IMP1 impact damage . . . 102
Figure 3.58 Bottom surface images of P1_IMP1 impact damage . . . 102
Figure 3.59 Cutting Pattern of Integral Reinforced Panel (dimensions in inches) . . . 103
Figure 3.60 IRP four-point bending test setup (dimensions in mm) . . . 104
Figure 3.61 Four-point flexural testing apparatus for IRP samples . . . 105
Figure 3.62 Specimen IRP1_LSB6 during test . . . 105
Figure 3.63 Clemex PE & Lite camera on optical microscope with sample . 107
Figure 3.64 Sample micrographs of IRP1 50x (left) and 400x (right) . . . 107
Figure 3.65 Area selected for microscopic fibre volume fraction analysis at 400x magnification, IRP3 . . . 108

Figure 4.1 Injection pressure profiles from PMC component manufacture 110
Figure 4.2 Fibre washing from resin flow, plate 4 . . . 112
Figure 4.3 Bottom-side of resin inlet, plate 4 . . . 112
Figure 4.4 Dry sports from resin starved areas, plate 6 . . . 113
Figure 4.5 Voids caused as a results of trapped air, plate 3 . . . 113
Figure 4.6 Voids near outer edge, plate 1 . . . 114
Figure 4.7 Void contained within single reinforcing layer at 400x magnification, plate 2 . . . 115
Figure 4.8 Stitch induced out of plane yarn waviness at 50x magnification, plate 3 . . . 116
Figure 4.9 Resin rich zone caused by stitch-loop at 50x magnification, plate 3117
Figure 4.10 Fibre misalignment, top surface IRP 1 . . . 118
Figure 4.11 Bottom surface, IRP 1 . . . 118
Figure 4.12 Dry spots from incomplete resin impregnation, IRP 3 bottom 119
Figure 4.13 Voids from trapped air, IRP 2 bottom . . . 119
Figure 4.14 End view of the inner mould pieces used for IRP 1 (left) compared to IRPs 2 and 3 (right) . . . 120
Figure 4.15 Inner mould shearing, IRP 1 . . . 120
Figure 4.16 Resin rich zone, IRP 2 . . . 121
Figure 4.17 Micrograph showing layer thickness measurements at 50x magnification, IRP 2 . . . 123
Figure 4.18 Through-thickness stitch at 50x magnification, IRP 2 . . . 124
Figure 4.19 Interlaminar gaps of curved section at 50x magnification, IRP 1 125
Figure 4.20 Knife-edge crack opening at 50x magnification, IRP 1 . . . 126
Figure 4.21 Voids of various shapes and sizes at 50x magnification, IRP 2 . 127
Figure 4.22 Compression-buckling failure on top surface during test (top) and after test (bottom), P2_LSB1 . . . 132
Figure 4.23 Resin-rich zone caused by stitch before test (top) and after test (bottom), P1_LSB1 . . . 133
Figure 4.24 Initial tension failure of bottom surface followed by interlaminar shear during test (top) and after test (bottom), P3_LSB4 . . . 136

Figure 4.25 Initial compression failure of top surface followed by interlaminar shear during test (top) and after test (bottom), P3_LSB5 . . . 137
Figure 4.26 Interlaminar shear cracks without stitch line (top), P2_LSB6 and with stitch line (bottom), P3_LSB5 . . . 138
Figure 4.27 Tensile flexural failure causing complete separation, P2_LSB4 (top) and P2_LSB5 (bottom) . . . 139
Figure 4.28 Combined failure mode: buckling followed by interlaminar shear, P5_LSB1 . . . 142
Figure 4.29 Premature interlaminar shear failure, P5_LSB3 . . . 143
Figure 4.30 Interlaminar shear failure of multiple layers under left (top) and right (bottom) loading noses, P6_LSB6 . . . 144
Figure 4.31 Interlaminar shear crack propagation halted at stitch-line, P5_LSB2 . . . 145
Figure 4.32 Dry spots from poor resin saturation, P4_LSB6 . . . 147
Figure 4.33 Buckling near dry fibre region during test (top) and after test (bottom), P4_LSB6 . . . 148
Figure 4.34 Buckling near left loading nose, P6_LSB5 . . . 149
Figure 4.35 Inelastic deformation with combined interlaminar cracks, P2_SSB2152
Figure 4.36 Failure of 90º layers at ±45º angle, P2_SSB3 . . . 153
Figure 4.37 Combined tensile and interlaminar shear short beam failure, P1_SSB6 . . . 155
Figure 4.38 ±45º cracks within 90º layers, P2_SSB6 . . . 155
Figure 4.39 Compressive cracks underneath loading nose and ILS failure towards right end, P5_SSB1 . . . 157
Figure 4.40 Load vs. time curves for impacted specimens P1_IMP and P5_IMP . . . 159
Figure 4.41 Load vs. Deflection curves for specimens P3_IMP (left) and P2_IMP (right) . . . 160
Figure 4.42 Material description and normalized impact data for AS4/3501-6 prepreg [64] . . . 162
Figure 4.43 Images of impact surface (left) and bottom surface (right), P2_IMP . . . 162
Figure 4.44 Impact surface crack length comparison of P2_IMP (left) and P6_IMP (right) . . . 163
Figure 4.45 Bottom surface crack comparison of P2_IMP (left) and P6_IMP (right) . . . 164
Figure 4.46 Interlaminar debonding cracks originating at thickness transition, IRP1_LSB2 . . . 168
Figure 4.47 Complete separation of curved section from flat section, IRP1_LSB4168
Figure 4.48 Interlaminar debonding cracks originating inside junction of curved and flat sections, IRP1_LSB6 . . . 168
Figure 4.49 Interlaminar cracking of left and right side flat sections outside of loading noses, IRP2_LSB1 . . . 169

Figure 4.50 Through-thickness and combined interlaminar cracks outside of loading nose, IRP2_LSB4 169
Figure 4.51 Interlaminar debonding crack between flat section and curved section and interlaminar cracks within outer flat section, IRP3_LSB1170

List of Tables

Table 1.1 Properties of common engineering materials 2

Table 3.1 Laminating sequences and fibre volume fractions, flat plates . . 47
Table 3.2 Laminating sequences and fibre volume fractions, IRPs 48
Table 3.3 Flexural test specimen failure identification codes [66] 90

Table 4.1 Resin Injection Information 110
Table 4.2 Measured thicknesses and adjusted fibre volume fraction of flat plates 115
Table 4.3 Measured thicknesses of individual IRP specimens 122
Table 4.4 Average overall thicknesses of IRPs 122
Table 4.5 Porosity of IRP samples 127
Table 4.6 Fibre volume fractions of IRPs 128
Table 4.7 Experimental flexural moduli compared with theoretical flexural moduli 130
Table 4.8 Flexural properties and failure codes for specimen set 1 131
Table 4.9 Statistical values from specimen set 1 flexural properties 131
Table 4.10 Flexural properties and failure codes for specimen set 2 134
Table 4.11 Statistical values from specimen set 2 flexural properties 135
Table 4.12 Flexural properties and failure codes for specimen set 3 141
Table 4.13 Statistical values from specimen set 3 flexural properties 141
Table 4.14 Flexural properties and failure codes for specimen set 4 146
Table 4.15 Statistical values from specimen set 4 flexural properties 146
Table 4.16 Short beam testing results 150
Table 4.17 Short beam shear strength values obtained from literature . . . 150
Table 4.18 Short span properties and failure modes of specimen set 5 . . . 151
Table 4.19 Statistical values from specimen set 5 short span properties . . 151
Table 4.20 Short span properties and failure modes of specimen set 6 . . . 154
Table 4.21 Statistical values from specimen set 6 short span properties . . 154
Table 4.22 Short span properties and failure modes of specimen set 7 . . . 156
Table 4.23 Statistical values from specimen set 7 short span properties . . 156
Table 4.24 Short span properties and failure modes of specimen set 8 . . . 158

Table 4.25 Statistical values from specimen set 8 short span properties . . 158
Table 4.26 Drop weight impact testing data ($m_{dh} = 6.14$ kg, $H = 0.432$ m) 161
Table 4.27 Normalized impact data 161
Table 4.28 Statistical data from drop weight impact testing 161
Table 4.29 Specimen and test data from long span four-point bending of IRPs 165
Table 4.30 Statistical data from long span four-point bending of IRPs . . 165
Table 4.31 Failure observations for long span four-point testing of IRPs . . 167

Nomenclature

A_{cyl}	Cross-sectional area of hydraulic cylinder	$[m^2]$
A_ij	Extensional stiffness matrix terms	$[Pa \cdot m]$
a_ij	Extensional compliance matrix terms of laminate	$[(Pa \cdot m)^{-1}]$
A_p	Projected area of compacted preform	$[m^2]$
A_y	Cross-sectional area of carbon fibre yarn	$[m^2]$
B_ij	Stiffness coupling matrix terms	$[Pa \cdot m^2]$
b_{ls}	Four point long span specimen width	$[mm]$
C	General stiffness tensor	$[Pa]$
C_E	Specified ratio of impact energy to specimen thickness	$[\frac{J}{mm}]$
C_{ij}	Stiffness matrix terms	$[Pa]$
D_{cyl}	Diameter of hydraulic cylinder	$[m]$
D_ij	Flexural stiffness matrix terms	$[Pa \cdot m^3]$
d_ij	Flexural compliance matrix terms of laminate	$[(Pa \cdot m^3)^{-1}]$
E	Impact energy	$[J]$
E_1	Young's Modulus in longitudinal direction of fibres	$[Pa]$
E_{1f}	Longitudinal Young's Modulus of fibres	$[Pa]$
E_{1f}	Longitudinal Young's Modulus of fibres	$[Pa]$
E_2	Young's Modulus in transverse direction of fibres	$[Pa]$
$\bar{E}_1$	Effective theoretical flexural modulus of specimen set 1	$[Pa]$
$\bar{E}_2$	Effective theoretical flexural modulus of specimen set 2	$[Pa]$
$\bar{E}_3$	Effective theoretical flexural modulus of specimen set 3	$[Pa]$

$\bar{E}_4$	Effective theoretical flexural modulus of specimen set 4	$[Pa]$
$\bar{E}_{fx}$	Effective laminate flexural modulus in x-direction	$[Pa]$
$\bar{E}_{yf}$	Effective laminate flexural modulus in y-direction	$[Pa]$
$\bar{E}_x$	Effective laminate Young's modulus in x-direction	$[Pa]$
$\bar{E}_y$	Effective laminate Young's modulus in y-direction	$[Pa]$
E_F	Flexural modulus of elasticity	$[MPa]$
E_m	Young's Modulus of Matrix	$[Pa]$
F	Applied force from loading nose	$[N]$
F_c	Impact test contact load	$[N]$
F_f	Four-point long span bending first failure force	$[N]$
F_{max}	Four-point long span bending peak force	$[N]$
F_p	Preform compaction force	$[N]$
g	Acceleration due to gravity	$[\frac{m}{s^2}]$
G_{12}	Shear modulus in 1-2 plane	$[Pa]$
G_{12f}	Shear modulus of fibres	$[Pa]$
$\bar{G}_{xy}$	Effective laminate shear modulus	$[Pa]$
G_m	Shear modulus of matrix	$[Pa]$
H	Impact drop height	$[m]$
h	Total thickness of laminate	$[m]$
h_{dent}	Depth of dent from out-of-plane drop weight impact event	$[mm]$
K	Impact test structure stiffness	$[Pa]$
t_c	Impact test contact time	$[s]$
l_{ga}	AVE gauge length output	$[mm]$
L_{ls}	Four point long span test support span	$[mm]$
m_c	Impact test total contactor mass	$[kg]$
m_{dh}	Mass of drop head	$[kg]$
m_f	Mass of fibre contained in PMC part	$[g]$

M_s	Resultant twisting moment per unit width in xy-plane	$[Pa \cdot m^2]$
M_x	Resultant bending moments per unit width along x	$[Pa \cdot m^2]$
M_y	Resultant bending moments per unit width along y	$[Pa \cdot m^2]$
N_a	Actual number of carbon fibre layers	
N_l	Number of carbon fibre layers	
N_s	Resultant shear forces per unit thickness in xy-plane	$[Pa \cdot m]$
N_x	Resultant normal forces per unit width in x	$[Pa \cdot m]$
N_y	Resultant normal forces per unit width in y	$[Pa \cdot m]$
P_p	Preform compaction pressure	$[Pa]$
q	Imposed resin flow rate	$[\frac{m^3}{s}]$
Q_{ij}	Reduced stiffness matrix components	$[Pa]$
S	General compliance tensor	$[\frac{1}{PA}]$
s_c	Instron crosshead speed	$[\frac{m}{s}]$
S_F	Flexural strength	$[Pa]$
S_{Ff}	First failure strength	$[Pa]$
b_{ss}	Short span bending specimen width	$[mm]$
S_{SB}	Short beam strength	$[Pa]$
s_y	Yarn spacing	$[m]$
t	PMC plate thickness	$[mm]$
t	Thickness of composite	$[m]$
τ_i	Shear stresses in stress tensor	$[Pa]$
v_{12}	Poisson's ratio when loaded in direction 1 with strain in direction 2	
v_{12f}	Major Poisson's ratio of fibres	
v_{21}	Poisson's ratio when loaded in direction 2 with strain in direction 1	
$\bar{v}_{xy}$	Effective laminate major Poisson's ratio	
$\bar{v}_{yx}$	Effective laminate minor Poisson's ratio	

v_f	Fibre volume fraction of PMC component	$[\%]$
$\mathsf{v}_{f,c}$	Calculated fibre volume fraction of composite	$[\%]$
$\mathsf{v}_{f,t}$	Target fibre volume fraction of composite	$[\%]$
v_i	Impact test initial contact velocity of drophead	$[\frac{m}{s}]$
υ_m	Poisson's ratio of matrix	
z	General coordinate variable in through thickness direction	$[m]$
δ_m	Midpoint deflection	$[mm]$
$\boldsymbol{\epsilon}$	General strain tensor	
ϵ_{AVE}	AVE strain output	
ϵ_F	Maximum flexural strain	
ϵ_x^o	Normal strain on reference plane in x-direction	
ϵ_y^o	Normal strain on reference plane in y-direction	
ϵ_x	Normal strain in x-direction	
ϵ_y	Normal strain in y-direction	
γ_j	Shear strains in strain tensor	
γ_s^o	Shear strain in reference xy plane	
γ_s	Shear strain in xy-plane	
κ_s	Laminate curvature coupling in xy-plane	$[\frac{1}{m}]$
κ_x	Laminate curvature along x-direction	$[\frac{1}{m}]$
κ_y	Laminate curvature along y-direction	$[\frac{1}{m}]$
ρ_f	Density of carbon fibre	$[\frac{g}{m^3}]$
ρ_s	Surface fibre density of single unidirectional layer	$[\frac{g}{m^2}]$
$\boldsymbol{\sigma}$	General stress tensor	$[Pa]$
σ_F	Maximum flexural stress	$[MPa]$
σ_{FU}	Longitudianl tensile strength of fibres	$[Pa]$
σ_{LCU}	Longitudinal compressive strength of unidirectional PMC	$[Pa]$
σ_{LU}	Longitudianl tensile strength of unidirectional PMC	$[Pa]$

$\sigma_M^{'}$	Tensile stress of matrix	$[Pa]$
σ_{MU}	Tensile strength of matrix	$[Pa]$
σ_{TU}	Transverse tensile strength of unidirectional PMC	$[Pa]$
σ_x	Normal stress in x-direction	$[Pa]$
σ_y	Normal stress in y-direction	$[Pa]$
θ	Angle of ply orientation from reference axis to principal fibre direction (axis 1)	$[^\circ]$
τ_s	Shear stress in xy-plane	$[Pa]$
ζ_1	Reinforcing efficiency factor for transverse loading	
ζ_2	Reinforcing efficiency factor for in-plane shear	

Chapter 1

Introduction

Composites are engineering materials made by combining two distinct materials, typically one acting as the reinforcement and the other as a surrounding matrix. The reinforcement of the composite generally imparts mechanical benefits such as high stiffness and strength, whereas the matrix provides a media to hold the reinforcing materials in place, transmit loads to the reinforcement and protect the reinforcement from the environment. Polymer matrix composites (PMCs) feature reinforcements with high specific stiffness and strength characteristics contained within a polymer-based matrix. This thesis focuses on PMCs featuring reinforcing carbon fibre yarns set within a thermoset epoxy resin matrix.

PMCs combine the low density of polymers with high tensile stiffness and strength fibres to achieve superior specific properties compared with other engineering materials. This allows PMCs to have high strength and stiffness while at the same time being lighter than other materials, like steel, aluminium and titanium alloys, as shown in Table 1.1. Therefore, many industries utilize PMCs in their products, most notably in aerospace, nautical and automotive applications. The use of composites in the aerospace industry is increasing, for example when Boeing's 777 first entered service in 1995 it contained only 12 % composites by weight [1, 2]; whereas in 2011, when Boeing's 787 Dreamliner entered service it contained 50 % composites by weight [2].

Table 1.1: Properties of common engineering materials

Materials	Tensile Modulus [GPa]	Ultimate Tensile Strength [MPa]	Density $[\frac{g}{cm^3}]$	Specific Tensile Modulus $[GPa \cdot \frac{cm^3}{g}]$	Specific Ultimate Tensile Strength $[MPa \cdot \frac{cm^3}{g}]$
1020 Alloy Steel (CD) [3]	207	420	7.9	26.2	53.2
6061-T6 Aluminium Alloy [3]	69	310	2.7	25.6	115
Ti-6Al-4V (HT) Titanium Alloy [3]	114	1172	4.4	25.9	266
Tenax-J Carbon Fibre [4]	239	4275	1.8	135.8	2375
Tri-Tex L-1911 Epoxy [5]	3	70	1.1	2.7	63.6

Theoretical calculations of mass, mechanical and other properties which are commonly used for describing PMCs are based on the fibre volume fraction, v_f. The v_f is defined as the fraction of the volume of the final PMC part that is occupied by the fibre reinforcement, mathematically expressed in Equation 1.1 :

$$\mathsf{v}_f = \frac{V_f}{V_p} = \frac{\frac{m_f}{\rho_f}}{V_p} \tag{1.1}$$

where V_f is the fibre volume in the part, V_p is the volume of the part, m_f is the mass of fibre within the part and ρ_f is the density of the fibres used in the part. The v_f in PMCs may vary from part to part, but to achieve high specific properties it is generally greater than 55 % with upper limits based on maximum packing densities for cylindrical fibres.

1.1 PMC Manufacturing

Performance characteristics of PMC components are highly dependant on the process used for their manufacture. There are two main groups of processes through which PMCs may be manufactured: manual or semi-manual layup using prepreg, and liquid composite moulding. Prepreg composites are made by individually layering thin sheets of carbon fibre reinforcements pre-impregnated with a partially cured resin. Once the desired orientation and number of layers is laid over the mould, the assembly is debulked, sealed,

vacuumed and placed inside an autoclave and heated under pressure to cure the resin. PMC parts made using prepreg are highly reproducible and high quality parts may be achieved. However, the disadvantages of manufacturing PMCs from prepreg are that the lay-up process is labour intensive and therefore expensive, requiring an autoclave which limits production rates and part size, and prepreg presents storage and shelf-life limitations from maintaining partial cure of the resin.

Another group of PMC manufacturing processes is termed liquid composite moulding, where thick dry fibre structures near to the final component shape, called preforms, are placed within a mould and injected with liquid polymers which are allowed to cure or harden within the mould. Two common liquid composite moulding processes that have found widespread use are resin transfer moulding (RTM) and vacuum assisted resin transfer moulding (VARTM). RTM consists in placing a preform inside a rigid mould and then pumping liquid resin into the mould cavity. The part is removed after cure. RTM is described further in the following section as this thesis work examines parts made using RTM. VARTM is generally similar to RTM, but the preform is placed atop a one-sided rigid mould with a flexible vacuum bag placed on top where resin is drawn into the mould via an imposed vacuum. VARTM is effective when making large composite parts such as boat hulls and wind turbine blades since there is no need for a matched metal mould and high pressures are not imparted on the resin; moulds can be made of less expensive materials such as wood or fibreglass reinforced plastics (FRPs). Liquid composite moulding is a cost-effective way of producing PMC parts as the materials are cheaper and autoclaves are not necessary [6, 7]. However, it is difficult to achieve consistent quality at levels required for the aerospace industry due to variability during preform manufacturing, and resin flow characteristics [8].

1.1.1 Resin Transfer Moulding

As previously stated, RTM requires that a fibre preform of correct dimensions be placed into a cavity formed by rigid mould halves; moulds for parts with complex geometry may feature more than 2 components. With the preform properly loaded inside a mould cavity, other components of the mould are brought together so that the resulting cavity

is filled by the preform, completely and precisely. Once the mould is properly closed, the components are fastened or otherwise assembled securely and sealed, ensuring the desired mould cavity geometry. The sealed mould is then injected with liquid resin under pressure through one or multiple injection points until the preform and cavity are completely filled. Injection may proceed under and imposed pressure difference or an imposed flow rate, and may be assisted by a vacuum applied at the outlets. Outlets and inlets may be opened or closed sequentially. Once the mould is filled and the preform is impregnated, inlets and outlets are sealed and the resin is allowed to cure, sometimes followed by a post-cure procedure, prior to demoulding. RTM is a commonly used process as it enables the production of PMC parts of high v_f with excellent surface finishes and dimensional tolerances [6]. With a proper selection of resin in terms of cure time, the process also can achieve high production rates compared with other composite manufacturing methods. The process is more amenable to automation, resin storage issues are limited, and the resin and reinforcements can be formulated and designed independently. However, the process is strongly dependent on the availability of a preform of high quality and consistency.

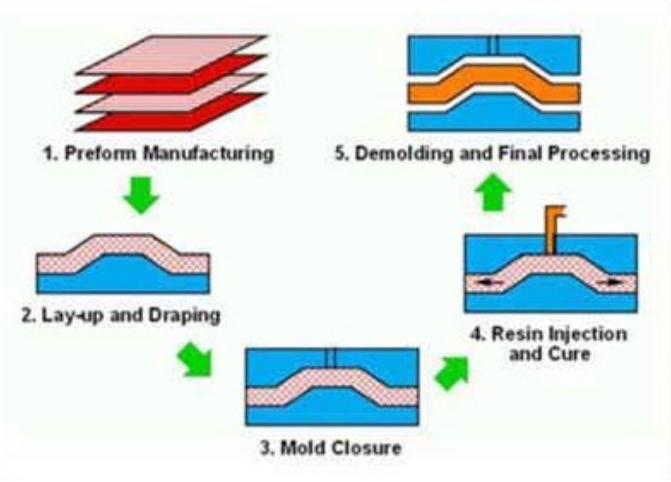


Figure 1.1: RTM process steps [9]

1.1.2 Preforming

Preforming is the process through which dry fibre structures are created, most often by stacking and stitching together layers of woven or non-woven reinforcement fabrics. The

quality and consistency of PMC parts is directly related to the quality of the preforms used for making them. The preform not only is the most important component of a PMC part; furthermore, preform configuration strongly influences processing, notably injection. Costs associated with preforming can reach up to 40 % of the overall cost of a PMC component, and up to 66 % of the total manufacturing cost [10]. Figure 1.2 shows a cost breakdown for a complex PMC part manufactured by RTM. Much of the cost when preforming is through the labour associated with lay-up, therefore there is much interest in automated preforming [7, 11, 12, 13]. As presented by Mills, a cost reduction of 60 % was modelled for a regional plane tail skin section using RTM and preform automation compared to an automated prepreg tape laying process with autoclave curing [7].

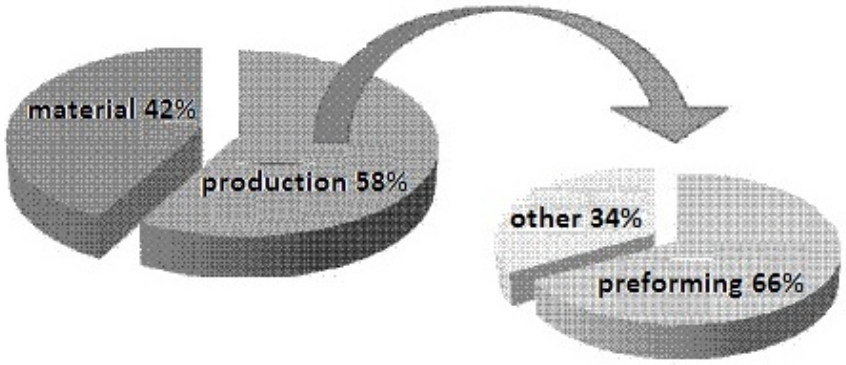


Figure 1.2: Cost allocation of a RTM-manufactured part [10]

Preforms of good quality consist of fibres aligned precisely according to specifications, featuring consistent v_f within all layers throughout the preform, and devoid of interfibre gaps or wrinkles larger than a set tolerance. Also, preform edges should be cut cleanly and precisely, free from fraying, and should match the size of the mould cavity accurately including the thickness required for reaching the target v_f in the part. Deficiencies related to improper yarn alignment and fluctuating v_f may lead to insufficient strength and stiffness, whereas other preform defects such as variable or large interyarn gaps, wrinkles and edge fraying may lead to poor wetting and micro/macro voids, and as a result decreased mechanical properties of the final PMC part. In RTM manufactured parts, increasing target v_f decreases the regions open to resin flow causing infusion to be slower or require higher resin pressures, pushing the limits of manufacturing equipment.

Fibre orientations are the direction along which layers of reinforcement are placed, imparting high strength and stiffness along those directions. There is a high sensitivity of strength and stiffness to fibre orientations in PMCs. Fibres oriented wrongly, or out of specifications and tolerances, lead to components with lower than expected mechanical properties. For the case of a commercial unidirectional prepreg, fibre misalignment leads to decreases in part stiffness, as shown in Figure 1.3. Also, as loading conditions cannot always be completely foreseen at the design stage, it is important to avoid purely unidirectional parts as even very small off-axis loads can cause failure. Therefore, PMC components are generally made of multiple layers with fibres orientated along diverse angles with respect to a reference axis. As preforms are fabricated, the general envelope of loading scenarios that may be imposed on the component is considered. This is to ensure that adequate reinforcement be oriented along required directions whilst maintaining the total amount of fibres, resin and part thickness to a practical minimum that will enable the realization of the PMC's potential in terms of specific stiffness and strength. The proportion of layers oriented in each direction should generally coincide with the magnitude of loads expected in that same direction, using the synergetic effects quantifiable through the classical laminate theory (CLT) as described later in this thesis.

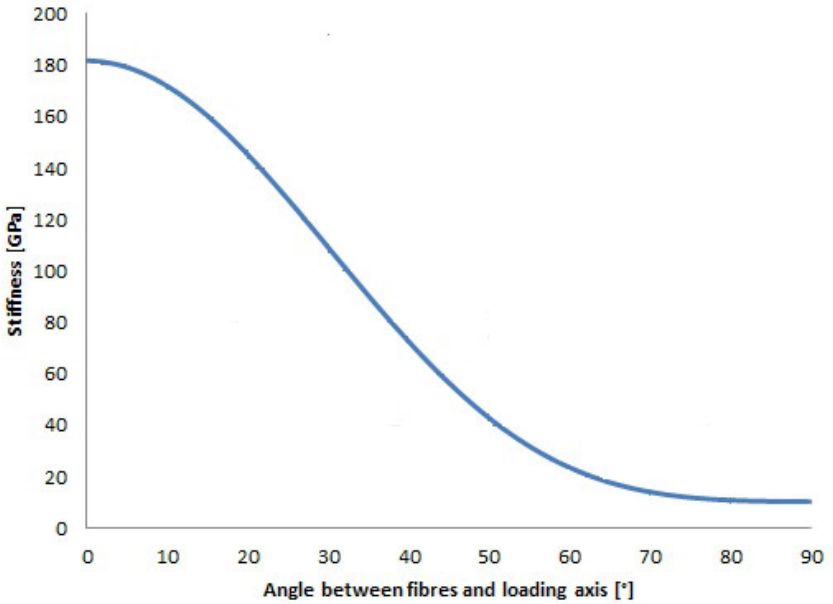


Figure 1.3: Stiffness of a unidirectional composite as a function of fibre orientation angle

Carbon fibre reinforcements traditionally come as rolled fabrics, from which tailored pieces are cut to size as required, draped and laid along required orientations, and superimposed, forming a multilayered preform within a mould of the target thickness. Performing this reinforcement layup within the mould generates mould down time, adding to labour and consistency issues. As a result, much interest is being devoted to generating thick, near net shape preforms in a stand-alone form. They can be made from assembled and stacked thin fabrics or single pieces of 3D fabrics which require no further assembly steps or trimming, and may be manufactured through largely automated processes. Thin fabrics used in preform assembly contain reinforcing yarns that are woven, braided, knit, tufted or non-woven, Figure 1.4. Woven and braided fabrics feature interlacing of reinforcing yarns, knitting and tufting feature interlooping of reinforcing yarns, and non-wovens feature neither interlacing or interlooping. Crimp is the term given to the out-of plane waviness of yarns caused by interlacing and interlooping, hence non-woven fabrics are also known as non-crimp fabrics (NCFs). Thick reinforcements may also be assembled from stacked layers of thin fabrics, and then knitted or stitched together to maintain integrity.

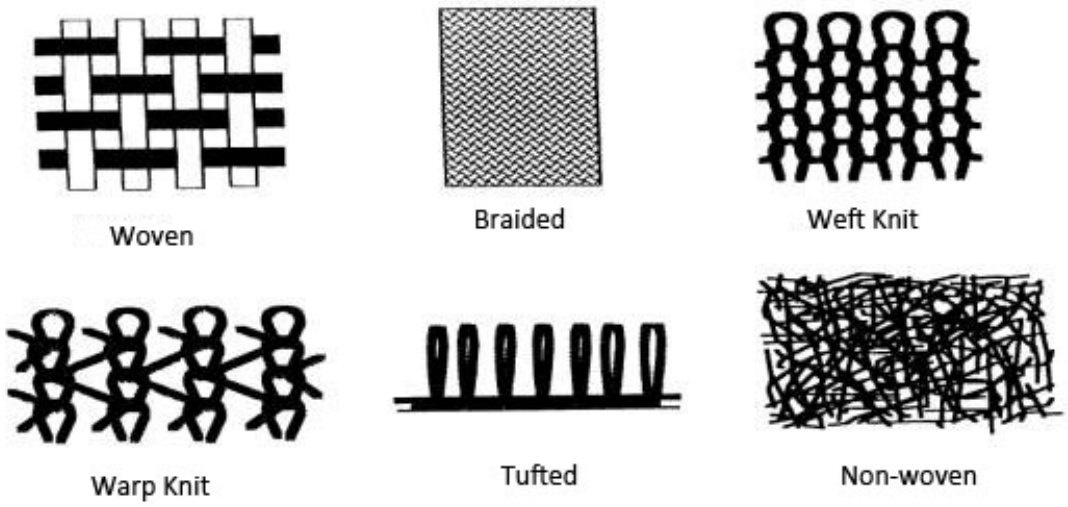


Figure 1.4: Types of fabric structures [14]

Thick carbon fibre fabrics may also be manufactured using techniques such as 3D

weaving, 3D braiding and 3D knitting. These techniques are similar to those above for thin fabrics, however they feature interlacing yarns in the direction of the thickness as well as in the horizontal plane, Figure 1.5. The major advantages of these techniques are their ability to control yarn and fibre orientations while full automation is possible; however, more complex manufacturing processes are required.

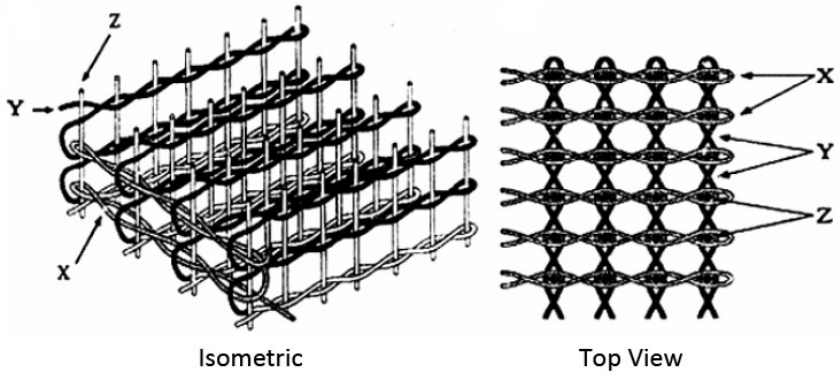


Figure 1.5: 3D woven reinforcement [15]

Preform integrity is critical for handling whilst maintaining yarn alignment and spacing. However, preforms may also be required to shear in-plane in order to follow mould curvatures without wrinkling; referred to as drapability. Therefore, using different fibre structures for preforms can alter the drapability of the preform. For example, preforms made using 3D braided or 3D knitted reinforcements are more drapable compared with preforms made from woven reinforcements [16, 17].

Preform integrity may also be increased by stitching assembled layers of fabric together. There are three main types of stitches that may be used for making multilayer preforms: the lock stitch, chain stitch and modified lock stitches, shown in Figure 1.6. The lock and chain stitches tend to cause greater distortions in load bearing fibres and yarns as their loops join within the thickness of the fabric, as opposed to the modified lock stitch where threads are looped on one side of the preform [18].

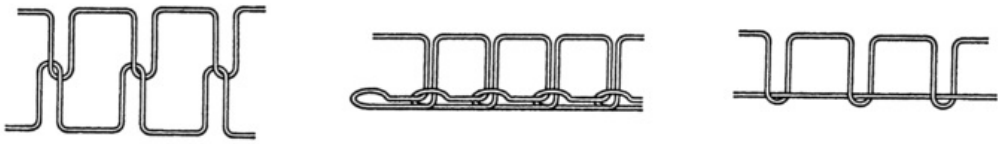


Figure 1.6: Various stitches used in multilayer textile preforms: lock stitch (left), chain stitch (middle), modified lock stitch (right) [18]

For this work, spools of carbon fibre yarn, or rovings, were used as reinforcement for stitched multilayer 3D NCF preforms. To form each reinforcement layer, parallel individual yarns were laid down side by side to the full width followed by successive layers at specific orientations governed by the desired laminating sequence. The assembly of layers was then stitched using a modified lock stitch. Preforms were finished by trimming the stitched assembled layers to the size of the mould cavity.

1.2 Thesis Overview & Objectives

The goal of 3D near net-shape preforms is to create consistent, repeatable composite components with reduced variability in strength, stiffness and toughness while quickening operations through automation and removing the burden of handling, cutting and laying pieces of fabrics. This thesis work is an initial attempt to evaluate the quality and mechanical behaviour of PMC components made using a specific preforming process. The process used for manufacturing preforms for this thesis reflects the same process for which automation techniques are being developed at the University of Ottawa.

Two types of PMC components were made from stitched multilayer 3D NCF preforms manufactured in house using RTM to establish a baseline level of PMC component quality. Two moulds were designed for manufacturing the carbon fibre epoxy parts; a 305 mm x 305 mm (12" x 12") flat plate and a 203 mm x 203 mm (8" x 8") integral reinforced panel (IRP) shown in Figure 1.7. Nominal part thicknesses of 4 mm were consistent in both components where six flat plates, 3 with a target v_f of 52 % and 3 with a target v_f of 63.5 %, and 3 IRPs with a target v_f of 52 % were manufactured. Flat plates allowed for standard mechanical evaluation of flexural stiffness and strength, short beam shear

strength and impact resistance. The IRPs were manufactured to demonstrate the capabilities of the preforming process used in components with greater geometric complexity. Furthermore, IRP specimens were tested to determine debonding strength of flat and reinforcing sections as requested by an industry partner. Due to confidentiality reasons, project documents pertaining to this may not be presented or discussed.



Figure 1.7: Manufactured 3D carbon fibre epoxy integral reinforced panel component

Important concepts and prior work relating to this thesis, such as methods of predicting mechanical properties of PMCs, and issues relating to RTM injection processes and to preforming are discussed in Chapter 2. The preforms, moulds and injection system used for manufacturing PMC components were all manufactured and developed in house and are discussed in Chapter 3. The final PMC parts were cut into specimens for measuring specific material properties through mechanical testing and for observing part quality using optical microscopy. Flexural modulus and strength were measured using long span four-point bending, short beam shear strength was measured using short span three-point testing, and impact resistance was measured using drop-weight impact testing. Debonding strength of the IRP specimens was measured using non-standard long span four-point bending. Properties measured from mechanical testing were tabulated and compared with theoretical expected values when applicable in Chapter 4. Research conclusions and recommendations for future work are presented in Chapter 5.

Chapter 2

Literature Review

2.1 Mechanical Properties

Mechanical properties are characteristics that may quantitatively determine a material's reaction when subjected to various loads. Often, the mechanics of materials use the assumption that most engineering materials, such as metals or polymers, are homogeneous and isotropic with mechanical properties independent of location and orientation within the bulk of the material. Since FRPs are comprised of straight encased fibres within a polymer matrix, they are microscopically inhomogeneous, and so predicting their mechanical properties is more complex. Many steps are required to build an analytical model for a composite. Figure 2.1 outlines these steps beginning with the micromechanics of fibre-matrix interactions to lamination theory and finally to more complex structures.

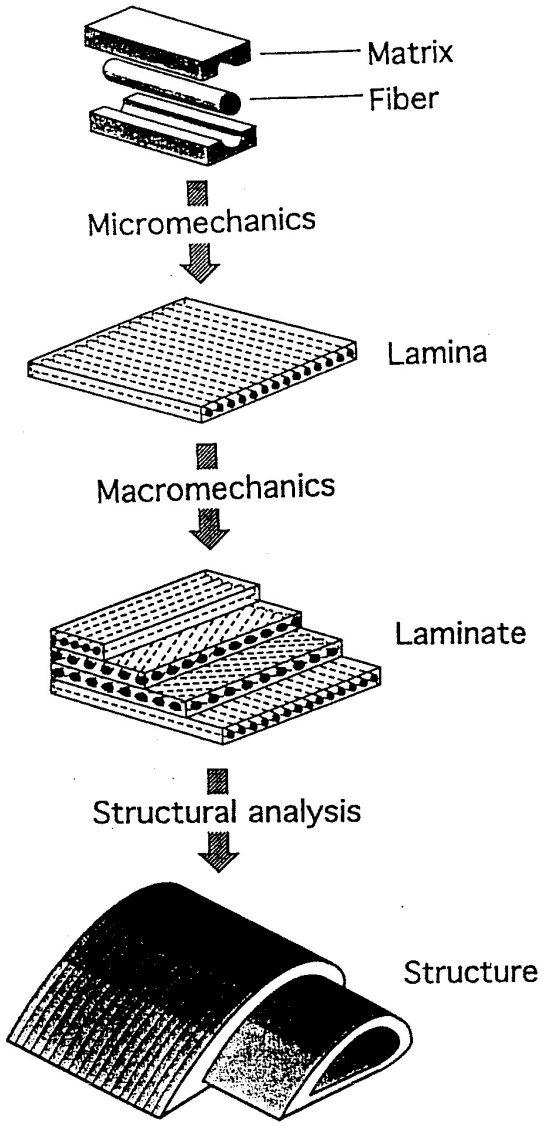


Figure 2.1: Levels of composite observation and analysis [19]

2.1.1 Hooke's Law

From the mechanics of materials, the behaviour of materials subjected to a state of stress can be described by Hooke's Law which provides a relationship between the stress tensor $\boldsymbol{\sigma}$ and the strain tensor $\boldsymbol{\epsilon}$. Hooke's Law may take the forms shown in Equations 2.1 in terms of stiffness, or 2.2 in terms of compliance:

$$\boldsymbol{\sigma} = C \cdot \boldsymbol{\epsilon} \tag{2.1}$$

$$\boldsymbol{\epsilon} = S \cdot \boldsymbol{\sigma} \tag{2.2}$$

where C is the general stiffness matrix and S the compliance matrix that link the strain tensor and the stress tensor. In a general 3D state, Figure 2.2where 1, 2 and 3 represent general Cartesian coordinates, the stress and strain tensors take the form:

$$\boldsymbol{\sigma} = [\sigma_{ij}] = \begin{bmatrix} \sigma_{11} & \sigma_{12} & \sigma_{13} \\ \sigma_{21} & \sigma_{22} & \sigma_{23} \\ \sigma_{31} & \sigma_{32} & \sigma_{33} \end{bmatrix} \qquad \boldsymbol{\epsilon} = [\epsilon_{kl}] = \begin{bmatrix} \epsilon_{11} & \epsilon_{12} & \epsilon_{13} \\ \epsilon_{21} & \epsilon_{22} & \epsilon_{23} \\ \epsilon_{31} & \epsilon_{32} & \epsilon_{33} \end{bmatrix} \tag{2.3}$$

where i and k represent the direction normal to a face and j and l represent the direction of the stress or strain as shown in Figure 2.2. Normal stresses are represented when $i = j$ and shear stresses are represented when $i \neq j$.

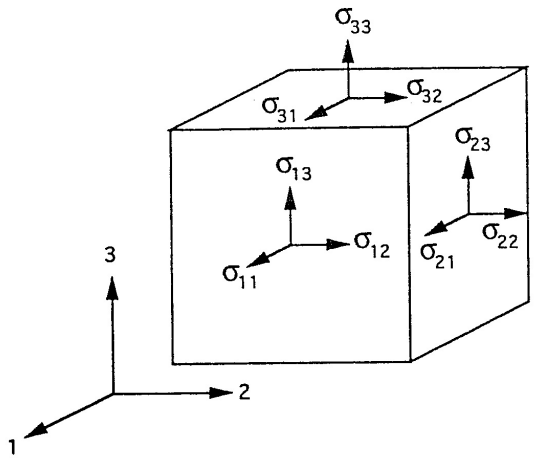


Figure 2.2: General stress tensor at a point [19]

The general stiffness matrix c is a 9 x 9 matrix which satisfies Equation 2.1. However, due to the symmetry of $\boldsymbol{\sigma}$ and $\boldsymbol{\epsilon}$, where, for example,$\sigma_{ij} = \sigma_{ji}$ and $\epsilon_{kl} = \epsilon_{lk}$ some matrix terms are not independent. Therefore the stress and strain tensors may be written as

columns and contracted:

$$\boldsymbol{\sigma} = \begin{bmatrix} \sigma_{11} \\ \sigma_{22} \\ \sigma_{33} \\ \sigma_{23} \\ \sigma_{13} \\ \sigma_{12} \end{bmatrix} = \begin{bmatrix} \sigma_1 \\ \sigma_2 \\ \sigma_3 \\ \tau_4 \\ \tau_5 \\ \tau_6 \end{bmatrix} \qquad \boldsymbol{\epsilon} = \begin{bmatrix} \epsilon_{11} \\ \epsilon_{22} \\ \epsilon_{33} \\ \epsilon_{23} \\ \epsilon_{13} \\ \epsilon_{12} \end{bmatrix} = \begin{bmatrix} \epsilon_1 \\ \epsilon_2 \\ \epsilon_3 \\ \gamma_4 \\ \gamma_5 \\ \gamma_6 \end{bmatrix} \tag{2.4}$$

where τ_i represents shear stress components and γ_j represent shear strain components. For a linear elastic anisotropic material, Hooke's law becomes:

$$\begin{bmatrix} \sigma_1 \\ \sigma_2 \\ \sigma_3 \\ \tau_4 \\ \tau_5 \\ \tau_6 \end{bmatrix} = \begin{bmatrix} C_{11} & C_{12} & C_{13} & C_{14} & C_{15} & C_{16} \\ C_{21} & C_{22} & C_{23} & C_{24} & C_{25} & C_{26} \\ C_{31} & C_{32} & C_{33} & C_{34} & C_{35} & C_{36} \\ C_{41} & C_{42} & C_{43} & C_{44} & C_{45} & C_{46} \\ C_{51} & C_{52} & C_{53} & C_{54} & C_{55} & C_{56} \\ C_{61} & C_{62} & C_{63} & C_{64} & C_{65} & C_{66} \end{bmatrix} \begin{bmatrix} \epsilon_1 \\ \epsilon_2 \\ \epsilon_3 \\ \gamma_4 \\ \gamma_5 \\ \gamma_6 \end{bmatrix} \tag{2.5}$$

where C_{ij} are stiffness matrix components.

2.1.2 Elastic behaviour of the Unidirectional Lamina

Considering a unidirectional reinforced lamina is useful in developing stress-strain relationships for composite materials. The principal directions of a lamina are shown in Figure 2.3 where the longitudinal fibre direction is 1, the in-plane transverse direction perpendicular to the fibres is 2 and the out-of-plane direction perpendicular to the fibres is 3.

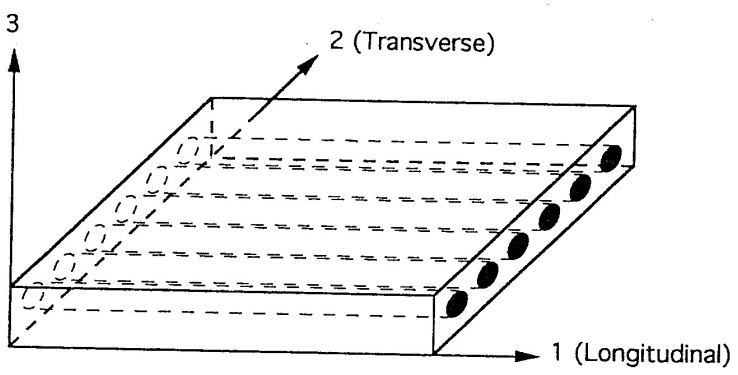


Figure 2.3: Principal coordinates of unidirectional lamina [19]

A unidirectional lamina can be considered an orthotropic material where three mutually perpendicular planes of symmetry exist. In this case, Equation 2.5 reduces to:

$$\begin{bmatrix} \sigma_1 \\ \sigma_2 \\ \sigma_3 \\ \tau_4 \\ \tau_5 \\ \tau_6 \end{bmatrix} = \begin{bmatrix} C_{11} & C_{12} & C_{13} & 0 & 0 & 0 \\ C_{21} & C_{22} & C_{23} & 0 & 0 & 0 \\ C_{31} & C_{32} & C_{33} & 0 & 0 & 0 \\ 0 & 0 & 0 & C_{44} & 0 & 0 \\ 0 & 0 & 0 & 0 & C_{55} & 0 \\ 0 & 0 & 0 & 0 & 0 & C_{66} \end{bmatrix} \begin{bmatrix} \epsilon_1 \\ \epsilon_2 \\ \epsilon_3 \\ \gamma_4 \\ \gamma_5 \\ \gamma_6 \end{bmatrix} \tag{2.6}$$

Then the fact that composite materials in most situations are used as thin laminates loaded in their plane is considered [19]. In such cases, composite lamina may be safely regarded as under a state of plane stress with all stress components involving the out-of-plane direction 3 being zero ($\sigma_3 = \tau_4 = \tau_5 = 0$). The stress-strain relationship along the principal axes in terms of stiffness becomes:

$$\begin{bmatrix} \sigma_1 \\ \sigma_2 \\ \tau_6 \end{bmatrix} = \begin{bmatrix} Q_{11} & Q_{12} & 0 \\ Q_{21} & Q_{22} & 0 \\ 0 & 0 & Q_{66} \end{bmatrix} \begin{bmatrix} \epsilon_1 \\ \epsilon_2 \\ \gamma_6 \end{bmatrix} \tag{2.7}$$

which may be contracted to

$$[\sigma]_{1,2} = [Q]_{1,2} [\epsilon]_{1,2}$$

where Q_{ij} are the reduced stiffness components with $Q_{ij} = C_{ij} - \frac{C_{i3} \cdot C_{j3}}{C_{33}}$ $(i, j = 1, 2, 6)$. In terms of engineering material constants,

$$\begin{aligned} Q_{11} &= \frac{E_1}{1 - v_{12} \cdot v_{21}} \\ Q_{22} &= \frac{E_2}{1 - v_{12} \cdot v_{21}} \\ Q_{12} &= \frac{v_{21} \cdot E_1}{1 - v_{12} \cdot v_{21}} \\ Q_{66} &= G_{12} \end{aligned} \tag{2.8}$$

where E_1 is Young's Modulus along the fibres, E_2 is Young's Modulus transverse to the fibres, G_{12} is the shear modulus in the 1 - 2 plane, v_{12} is major Poisson's ratio representing strain in direction 2 from loading in direction 1, and v_{21} is minor Poisson's ratio representing strain in direction 1 from loading in direction 2.

Predicting values for engineering constants requires a micromechanical approach considering the properties of each constituent material and interactions between them. While formulating equations it is assumed that perfect bonding occurs between fibres and matrix, fibres are sufficiently long to ignore critical length limitations, there are no voids or imperfections within the component, and all fibres remain perfectly aligned.

2.1.2.1 Material Properties of the Unidirectional Lamina

Halpin and Tsai [20] approximated the fibre dominated material properties E_1 and v_{12} as follows:

$$E_1 = E_{1f} \cdot \mathsf{v}_f + E_m \cdot (1 - \mathsf{v}_f) \tag{2.9}$$

$$v_{12} = v_{12,f} \cdot \mathsf{v}_f + v_m \cdot (1 - \mathsf{v}_f) \tag{2.10}$$

where E_{1f} is the longitudinal Young's modulus of the fibres, E_m is Young's modulus of the matrix, $v_{12,f}$ is the major Poisson's ratio of the fibres and v_m is the Poisson's ratio of the matrix. As for the matrix dominated properties E_2 and G_{12}, early approximate models based on mechanics of materials in Equations 2.11 and 2.12 tend to underestimate the properties [19]:

$$E_2 = \frac{E_{2f} \cdot E_m}{\mathsf{v}_f \cdot E_m + (1 - \mathsf{v}_f) \cdot E_{2f}} \tag{2.11}$$

$$G_{12} = \frac{G_{12f} \cdot G_m}{\mathsf{v}_f \cdot G_m + (1 - \mathsf{v}_f) \cdot G_{12f}} \tag{2.12}$$

where E_{2f} is the transverse Young's modulus of fibres, G_{12f} is the shear modulus of the fibres, and G_m is the shear modulus of the matrix. A more accurate semi-empirical model was developed by Halpin and Tsai for calculating both E_2 and G_{12} [21]:

$$E_2 = E_m \cdot \frac{1 + \zeta_1 \cdot \eta_1 \cdot \mathsf{v}_f}{1 - \eta_1 \cdot \mathsf{v}_f} \tag{2.13}$$

where

$$\eta_1 = \frac{E_{2f} - E_m}{E_{2f} + \zeta_1 \cdot E_m} \tag{2.14}$$

and ζ_1 is the reinforcing efficiency factor for transverse loading, where $\zeta_1 \backsimeq 2$ for circular fibres [21]. Similarly,

$$G_{12} = G_m \cdot \frac{1 + \zeta_2 \cdot \eta_2 \cdot \mathsf{v}_f}{1 - \eta_2 \cdot \mathsf{v}_f} \tag{2.15}$$

where

$$\eta_2 = \frac{G_{12f} - G_m}{G_{12f} + \zeta_2 \cdot G_m} \tag{2.16}$$

and ζ_2 is the reinforcing efficiency factor for in-plane shear, where $\zeta_2 \backsimeq 1$ [21]. There-

fore:

$$G_{12} = G_m \cdot \frac{(G_{12f} + G_m) + \mathsf{v}_f \cdot (G_{12f} - G_m)}{(G_{12f} + G_m) - \mathsf{v}_f \cdot (G_{12f} - G_m)} \tag{2.17}$$

where

$$G_{12f} = \frac{E_{2f}}{2(1 + v_f)} \text{and} \qquad G_m = \frac{E_m}{2(1 + v_m)} \tag{2.18}$$

The minor Poisson's ratio v_{21} is a function of the longitudinal and transverse Young's moduli:

$$v_{21} = v_{12} \cdot \frac{E_2}{E_1} \tag{2.19}$$

2.1.2.2 Stress-Strain Transformations

The lamina principal axes or on-axis directions 1 and 2 may not correspond to loading or reference axes x and y, or off-axis directions. Figure 2.4 shows that the on-axis directions 1 and 2 and off-axis directions x and y are related through angle θ. Angle θ is considered positive when moving counterclockwise from x to 1.

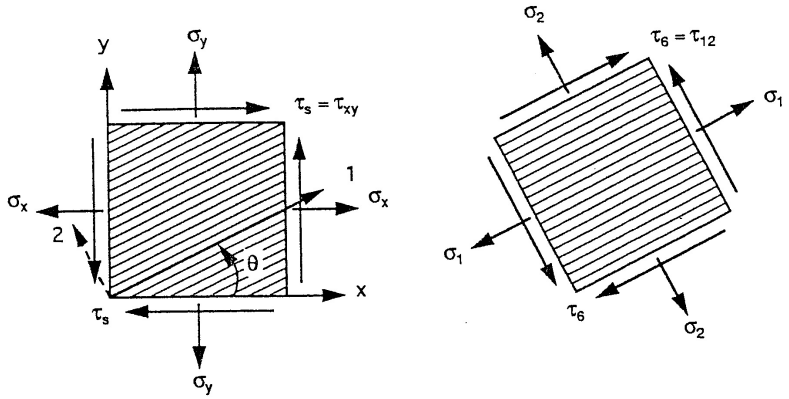


Figure 2.4: Stress components referred to loading axes (x, y) and material principal axes (1, 2) [19]

On-axis stresses and strains may be transformed into off-axis stresses and strains using the following transformation relations:

$$\begin{bmatrix} \sigma_x \\ \sigma_y \\ \tau_s \end{bmatrix} = [T]^{-1} \begin{bmatrix} \sigma_1 \\ \sigma_2 \\ \tau_6 \end{bmatrix} \qquad \text{and} \qquad \begin{bmatrix} \epsilon_x \\ \epsilon_y \\ \gamma_s \end{bmatrix} = [T]^{-1} \begin{bmatrix} \epsilon_1 \\ \epsilon_2 \\ \gamma_6 \end{bmatrix} \tag{2.20}$$

contracted to

$$[\sigma]_{x.y} = [T]^{-1} [\sigma]_{1,2} \qquad \text{and} \qquad [\epsilon]_{x,y} = [T]^{-1} [\epsilon]_{1,2} \tag{2.21}$$

where σ_x and σ_y are the normal stresses in the x and y directions respectively, τ_s is the shear stress within the xy plane, ϵ_x and ϵ_y are the normal strains in the x and y directions respectively, γ_s is the shear strain in the xy plane and $[T]$ is the transformation matrix:

$$[T] = \begin{bmatrix} \cos^2\theta & \sin^2\theta & 2\sin\theta\cos\theta \\ \sin^2\theta & \cos^2\theta & -2\sin\theta\cos\theta \\ -\sin\theta\cos\theta & \sin\theta\cos\theta & \cos^2\theta - \sin^2\theta \end{bmatrix} \tag{2.22}$$

and

$$[T]^{-1} = \begin{bmatrix} \cos^2\theta & \sin^2\theta & -2\sin\theta\cos\theta \\ \sin^2\theta & \cos^2\theta & 2\sin\theta\cos\theta \\ \sin\theta\cos\theta & -\sin\theta\cos\theta & \cos^2\theta - \sin^2\theta \end{bmatrix} \tag{2.23}$$

The off-axis stress-strain relationship for a unidirectional lamina can be written as:

$$\begin{bmatrix} \sigma_x \\ \sigma_y \\ \tau_s \end{bmatrix} = \begin{bmatrix} Q_{xx} & Q_{xy} & Q_{xs} \\ Q_{yx} & Q_{yy} & Q_{ys} \\ Q_{sx} & Q_{sy} & Q_{ss} \end{bmatrix} \begin{bmatrix} \epsilon_x \\ \epsilon_y \\ \gamma_s \end{bmatrix} \tag{2.24}$$

contracted to:

$$[\sigma]_{x,y} = [Q]_{x,y} [\epsilon]_{x,y}$$

Equations 2.7 and 2.20 are then applied to Equation 2.24 to transform the on-axis stiffness matrix $[Q]_{1,2}$ to any off-axis stiffness matrix $[Q]_{x,y}$. The off-axis stiffness matrix becomes:

$$[Q]_{x,y} = [T]^{-1} [Q]_{1,2} [T]^{-T} \tag{2.25}$$

The off-axis stiffnesses as functions of the on axis stiffnesses are therefore:

$$\begin{aligned}
Q_{xx} =& Q_{11}\cos^4\theta + 2(Q_{12} + 2Q_{66})\sin^2\theta\cos^2\theta + Q_{22}\sin^4\theta \\
Q_{yy} =& Q_{11}\sin^4\theta + 2(Q_{12} + 2Q_{66})\sin^2\theta\cos^2\theta + Q_{22}\cos^4\theta \\
Q_{xy} =& (Q_{11} + Q_{22} - 4Q_{66})\sin^2\theta\cos^2\theta + Q_{12}(\sin^4\theta + \cos^4\theta) \\
Q_{xs} = Q_{sx} =& (Q_{11} - Q_{12} - 2Q_{66})\sin\theta\cos^3\theta + (Q_{12} - Q_{22} + 2Q_{66})\sin^3\theta\cos\theta \\
Q_{ys} = Q_{sy} =& (Q_{11} - Q_{12} - 2Q_{66})\sin^3\theta\cos\theta + (Q_{12} - Q_{22} + 2Q_{66})\sin\theta\cos^3\theta \\
Q_{ss} =& (Q_{11} + Q_{22} - 2Q_{12} - 2Q_{66})\sin^2\theta\cos^2\theta + Q_{66}(\sin^4\theta + \cos^4\theta)
\end{aligned} \tag{2.26}$$

An off-axis compliance matrix may also be described similarly, where:

$$[S]_{x,y} = [T]^{T} [S]_{1,2} [T] \tag{2.27}$$

with

$$[\epsilon]_{x,y} = [S]_{x,y} [\sigma]_{x,y} \tag{2.28}$$

2.1.3 Classical Laminate Theory

The classical Laminate Theory (CLT) is used for predicting in-plane and flexural properties of composites made of distinct superimposed layers. A laminate is formed by stacking individual laminae made of unidirectional fibres to build thickness. Laminae are rotated about the vertical axis and stacked along different directions.

The stacking sequence is the designation of the complete laminate based on the orientations of the layers within the composite. The convention that is generally followed is that the sequence begins with the bottom-most lamina, progressing upward. For exam-

ple, the stacking sequence of $[0/+45/-45/90]_s$ represents a composite as shown on the right side of Figure 2.5, where the subscript "s" identifies a symmetrical sequence where the lower half of the stacking sequence is repeated in the upper half in reverse order.

The CLT is based on the Kirchoff-Love theory of thin plates where a midsurface plane may represent a three-dimensional plate in a two-dimensional form [22]. The assumptions and restrictions required for the CLT are that the laminae are perfectly bonded together without slipping, each lamina is linear elastic, orthotropic, and of uniform thickness, the strains and displacements are small, and the transverse shear stresses on the top and bottom surfaces are zero [23].

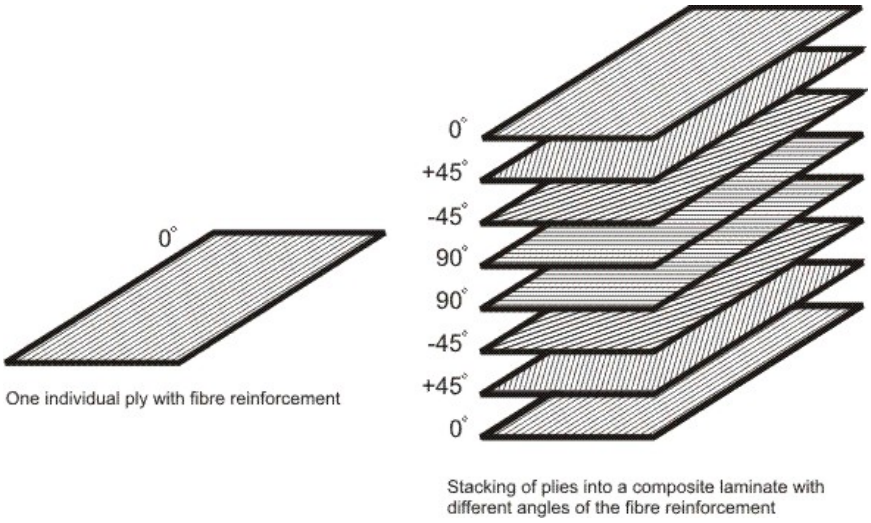


Figure 2.5: Laminate stacking sequence [24]

The CLT begins with strain-displacement relations described in Figure 2.6 where the resulting deformation of the plate is a combination of reference plane strain and laminate curvatures described mathematically in Equation 2.29.

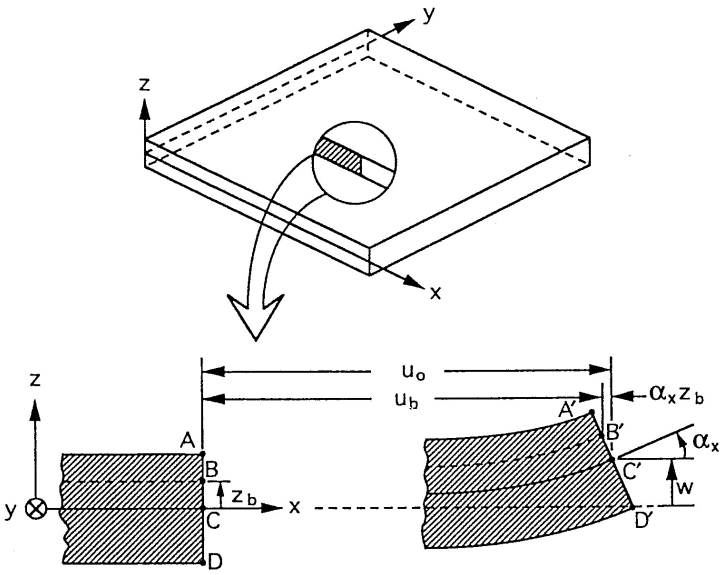


Figure 2.6: Laminate section before (left) and after (right) deformation [19]

$$\begin{bmatrix} \epsilon_x \\ \epsilon_y \\ \gamma_s \end{bmatrix} = \begin{bmatrix} \epsilon_x^o \\ \epsilon_y^o \\ \gamma_s^o \end{bmatrix} + z \begin{bmatrix} \kappa_x \\ \kappa_y \\ \kappa_s \end{bmatrix} \tag{2.29}$$

where ϵ_x^o , ϵ_y^o and γ_s^o are the strain components of the reference plane, κ_x, κ_y and κ_s are the curvatures of the laminate and z is the general coordinate variable through the thickness of the laminate. Considering any single layer k within the laminate, the stress-strain relation from Equation 2.24 now becomes:

$$\begin{bmatrix} \sigma_x \\ \sigma_y \\ \tau_s \end{bmatrix}_k = \begin{bmatrix} Q_{xx} & Q_{xy} & Q_{xs} \\ Q_{yx} & Q_{yy} & Q_{ys} \\ Q_{sx} & Q_{sy} & Q_{ss} \end{bmatrix}_k \begin{bmatrix} \epsilon_x^o \\ \epsilon_y^o \\ \gamma_s^o \end{bmatrix} + z \begin{bmatrix} Q_{xx} & Q_{xy} & Q_{xs} \\ Q_{yx} & Q_{yy} & Q_{ys} \\ Q_{sx} & Q_{sy} & Q_{ss} \end{bmatrix}_k \begin{bmatrix} \kappa_x \\ \kappa_y \\ \kappa_s \end{bmatrix} \tag{2.30}$$

contracted to

$$[\sigma]_{x,y}^k = [Q]_{x,y}^k [\epsilon^o]_{x,y} + z [Q]_{x,y}^k [\kappa]_{x,y}$$

Due to the continuity of the laminate, or to laminae being perfectly bonded, the strains throughout the laminate vary linearly through its thickness. However due to dif-

ferences in stiffness along different lamina orientations, stresses throughout its thickness do not vary linearly. Although there may be stress gradients within the layers, these are generally disregarded and average stresses in each layer are determined using Equation 2.30 [19]. The average stresses within a lamina can be replaced by resultant forces and moments as shown in Figure 2.7. The resultant forces and moments are integrated through the thickness of each ply and then combined to represent overall resultants of the full thickness laminate as shown in Equations 2.31 and 2.32.

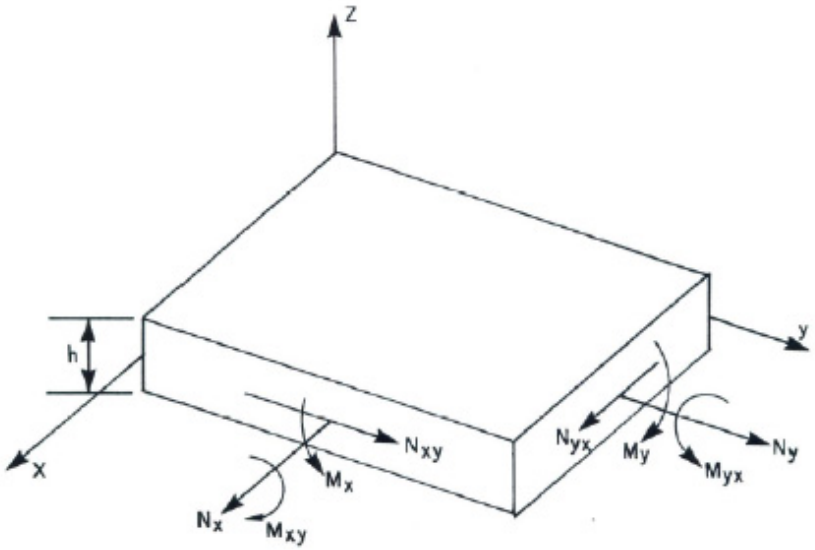


Figure 2.7: Resultant forces N and moments M of k^{th} lamina [22]

$$\begin{bmatrix} N_x \\ N_y \\ N_s \end{bmatrix} = \sum_{k=1}^{n} \int_{h_{k-1}}^{h_k} \begin{bmatrix} \sigma_x \\ \sigma_y \\ \tau_s \end{bmatrix}_k dz \tag{2.31}$$

$$\begin{bmatrix} M_x \\ M_y \\ M_s \end{bmatrix} = \sum_{k=1}^{n} \int_{h_{k-1}}^{h_k} \begin{bmatrix} \sigma_x \\ \sigma_y \\ \tau_s \end{bmatrix}_k z dz \tag{2.32}$$

where N_x and N_y are the resultant normal forces per unit width in x and y respectively, N_s is the resultant shear force per unit width, M_x and M_y are the resultant bending moments per unit width along x and y respectively, M_s is the twisting moment per unit

width, and h_k and h_{k-1} are the upper and lower z direction coordinates of the k^{th} lamina as shown in Figure 2.8.

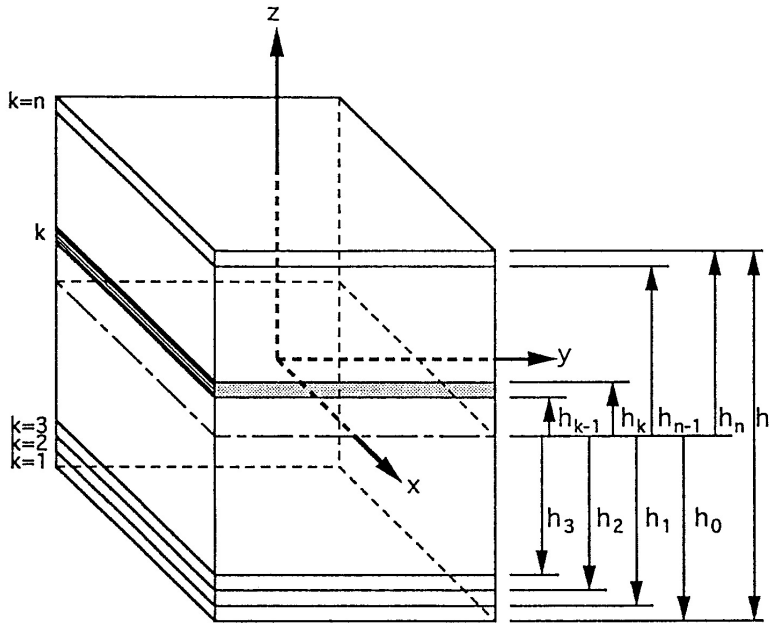


Figure 2.8: Laminate thickness with coordinates of individual lamina [19]

Substituting Equation 2.30 into Equations 2.31 and 2.32, the force-deformation and moment-deformation relations can be determined:

$$[N]_{x,y} = [A]_{x,y}\,[\epsilon^o]_{x,y} + [B]_{x,y}\,[\kappa]_{x,y} \tag{2.33}$$

and

$$[M]_{x,y} = [B]_{x,y}\,[\epsilon^o]_{x,y} + [D]_{x,y}\,[\kappa]_{x,y} \tag{2.34}$$

with

$$A_{ij} = \sum_{k=1}^{n} Q_{ij}^{k}(h_k - h_{k-1})$$

$$B_{ij} = \frac{1}{2}\sum_{k=1}^{n} Q_{ij}^{k}(h_k^2 - h_{k-1}^2) \tag{2.35}$$

$$D_{ij} = \frac{1}{3}\sum_{k=1}^{n} Q_{ij}^{k}(h_k^3 - h_{k-1}^3)$$

with i, j =x, y, s and $[A]_{x,y}$ is the extensional stiffness matrix which relates in-plane loads to in-plane strains, $[B]_{x,y}$ is the stiffness coupling matrix which relates in-plane loads to curvatures and moments to in-plane strains, and $[D]_{x,y}$ is the flexural stiffness matrix which relates bending moments to curvatures. Combining Equations 2.33, 2.34 and 2.35 gives the overall laminate stiffness matrix:

$$\left[\begin{array}{c} N_x \\ N_y \\ N_s \\ \hline M_x \\ M_y \\ M_s \end{array}\right] = \left[\begin{array}{ccc|ccc} A_{xx} & A_{xy} & A_{xs} & B_{xx} & B_{xy} & B_{xs} \\ A_{yx} & A_{yy} & A_{ys} & B_{yx} & B_{yy} & B_{ys} \\ A_{sx} & A_{sy} & A_{ss} & B_{sx} & B_{sy} & B_{ss} \\ \hline B_{xx} & B_{xy} & B_{xs} & D_{xx} & D_{xy} & D_{xs} \\ B_{yx} & B_{yy} & B_{ys} & D_{yx} & D_{yy} & D_{ys} \\ B_{sx} & B_{sy} & B_{ss} & D_{sx} & D_{sy} & D_{ss} \end{array}\right] \left[\begin{array}{c} \epsilon_x^o \\ \epsilon_y^o \\ \gamma_s^o \\ \hline \kappa_x \\ \kappa_y \\ \kappa_s \end{array}\right] \tag{2.36}$$

contracted to

$$\left[\begin{array}{c} N \\ \hline M \end{array}\right] = \left[\begin{array}{c|c} A & B \\ \hline B & D \end{array}\right] \left[\begin{array}{c} \epsilon^o \\ \hline \kappa \end{array}\right]$$

where sub-matrices $[A]_{x,y}$, $[B]_{x,y}$, and $[D]_{x,y}$ are symmetric with $A_{ij} = A_{ji}$, $B_{ij} = B_{ji}$ and $D_{ij} = D_{ji}$ for i, j =x, y, s. A visual representation of mechanical behaviours associated with some laminate stiffness matrix terms is shown in Figure 2.9. Generally, it is undesirable for the $[B]$ matrix to have non-zero elements as it leads to curvature or warping of the composite under in-plane loading. However, in some cases the extension-

curvature can be used as an interesting design feature such as, for example composite propeller blades whose angle of attack changes automatically with rotational speed [25].

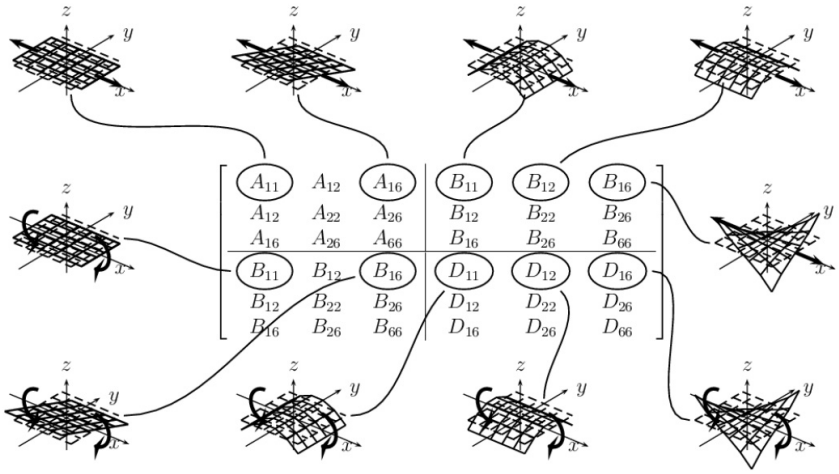


Figure 2.9: Mechanical behaviours associated with individual laminate stiffness matrix terms [22]

For the special case of a symmetric cross-ply laminate, a laminate made of only 0^o and 90^o lamina, $B_{ij} = 0$ and the load-deformation relations in terms of stiffness reduce to:

$$\begin{bmatrix} N_x \\ N_y \\ N_s \end{bmatrix} = \begin{bmatrix} A_{xx} & A_{xy} & 0 \\ A_{yx} & A_{yy} & 0 \\ 0 & 0 & A_{ss} \end{bmatrix} \begin{bmatrix} \epsilon_x^o \\ \epsilon_y^o \\ \gamma_s^o \end{bmatrix} \tag{2.37}$$

and

$$\begin{bmatrix} M_x \\ M_y \\ M_s \end{bmatrix} = \begin{bmatrix} D_{xx} & D_{xy} & 0 \\ D_{yx} & D_{yy} & 0 \\ 0 & 0 & D_{ss} \end{bmatrix} \begin{bmatrix} \kappa_x \\ \kappa_y \\ \kappa_s \end{bmatrix} \tag{2.38}$$

Equations for midplane strains and curvatures of a cross ply laminate, the load deformation relations in terms of compliances can be found by inverting individual matrices A and D [26]:

$$\begin{bmatrix} \epsilon_x^o \\ \epsilon_y^o \\ \gamma_s^o \end{bmatrix} = \left[A^{-1}\right] \begin{bmatrix} N_x \\ N_y \\ N_s \end{bmatrix} = \begin{bmatrix} a_{xx} & a_{xy} & a_{xs} \\ a_{yx} & a_{yy} & a_{ys} \\ a_{sx} & a_{sy} & a_{ss} \end{bmatrix} \begin{bmatrix} N_x \\ N_y \\ N_s \end{bmatrix} \tag{2.39}$$

and

$$\begin{bmatrix} \kappa_x \\ \kappa_y \\ \kappa_s \end{bmatrix} = \left[D^{-1}\right] \begin{bmatrix} M_x \\ M_y \\ M_s \end{bmatrix} = \begin{bmatrix} d_{xx} & d_{xy} & d_{xs} \\ d_{yx} & d_{yy} & d_{ys} \\ d_{sx} & d_{sy} & d_{ss} \end{bmatrix} \begin{bmatrix} M_x \\ M_y \\ M_s \end{bmatrix} \tag{2.40}$$

where a_{ij} and d_{ij} are the compliance terms of matrices $[A^{-1}]$ and $[D^{-1}]$. In-plane engineering properties of the laminate can be calculated from $[A]$ matrix, for comparison with other materials towards material selection, as follows:

$$\bar{E}_x = \frac{1}{h} \cdot \left[A_{xx} - \frac{A_{xy}^2}{A_{yy}}\right] \tag{2.41}$$

$$\bar{E}_y = \frac{1}{h} \cdot \left[A_{yy} - \frac{A_{xy}^2}{A_{xx}}\right] \tag{2.42}$$

$$\bar{v}_{xy} = \frac{A_{xy}}{A_{yy}} \tag{2.43}$$

$$\bar{v}_{yx} = \frac{A_{xy}}{A_{xx}} \tag{2.44}$$

$$\bar{G}_{xy} = \frac{A_{ss}}{h} \tag{2.45}$$

where $\bar{E}_x$ and $\bar{E}_y$ are the effective laminate Young's moduli in the x and y directions respectively, $\bar{v}_{xy}$ and $\bar{v}_{yx}$ are the effective laminate major and minor Poisson's ratios respectively, $\bar{G}_{xy}$ is the effective shear modulus of the laminate and h is the total thickness of the laminate.

Also, flexural engineering properties of the laminate can be found from the $[D^{-1}]$ matrix:

$$\bar{E}_{fx} = \frac{12}{h^3} \cdot \frac{1}{d_{xx}} \tag{2.46}$$

$$\bar{E}_{fy} = \frac{12}{h^3} \cdot \frac{1}{d_{yy}} \tag{2.47}$$

where $\bar{E}_{fx}$ and $\bar{E}_{fy}$ are the effective laminate flexural moduli in the x and y directions respectively.

2.1.4 Failure Mechanisms PMCs

Previously, the CLT considered the response of PMCs within their elastic domain. However, PMC behaviour beyond the elastic region leading to failure is very complex and depends on many factors. Failure can be a result of fibre failure, matrix failure, fibre-matrix interface failure or any combination of them. Reinforcing fibres generally control properties such as in-plane and flexural stiffness and strength, whereas the matrix and fibre-matrix interface control properties such as interlaminar strength and fracture toughness.

Fibres with high modulus and strength tend to experience low failure strains and high variability in tensile strength, as shown in Figure 2.10. However, reinforcing carbon fibre yarns contain thousands of individual fibres, therefore leading to progressive failure as many fibres maintain integrity after low stress failure of others has occurred. Matrix materials feature much lower tensile stiffness and strength, yet much higher strains to failure.

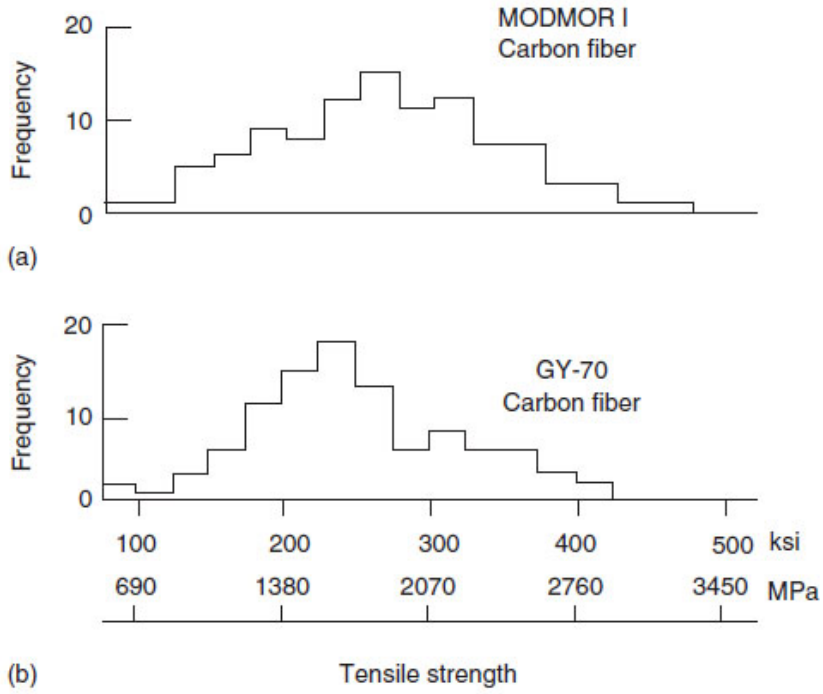


Figure 2.10: Variability in tensile strength of carbon fibres [26]

2.1.4.1 Unidirectional PMCs

Failure of unidirectional PMCs subjected to in-plane tensile loading depends highly on the angle between the load and fibres. For tensile loading parallel to the fibres, the tensile strength σ_{LU} may be estimated based on the law of mixtures [26]:

$$\sigma_{LU} = \sigma_{FU} \cdot \mathsf{v}_f + \sigma'_M \cdot (\mathsf{v}_f - 1) \tag{2.48}$$

where σ_{FU} is the longitudinal tensile strength of the fibres, and σ'_M the tensile stress of the matrix at the fibre failure strain since the fibres fail at a lower strain. The estimated tensile strength assumes linearity and that all fibres fail at the same strain, however, both assumptions limit its accuracy due to the non-linearity of typical matrix materials and variability in tensile strengths of fibres[26]. Unidirectional PMCs in longitudinal tension experience different microfailure modes depending on strain levels. Initially, fibre-matrix debonding occurs from interfacial shear stresses caused by the difference in fibre and matrix stiffness, followed by matrix cracking and eventually fibre pullout, Figure 2.11.

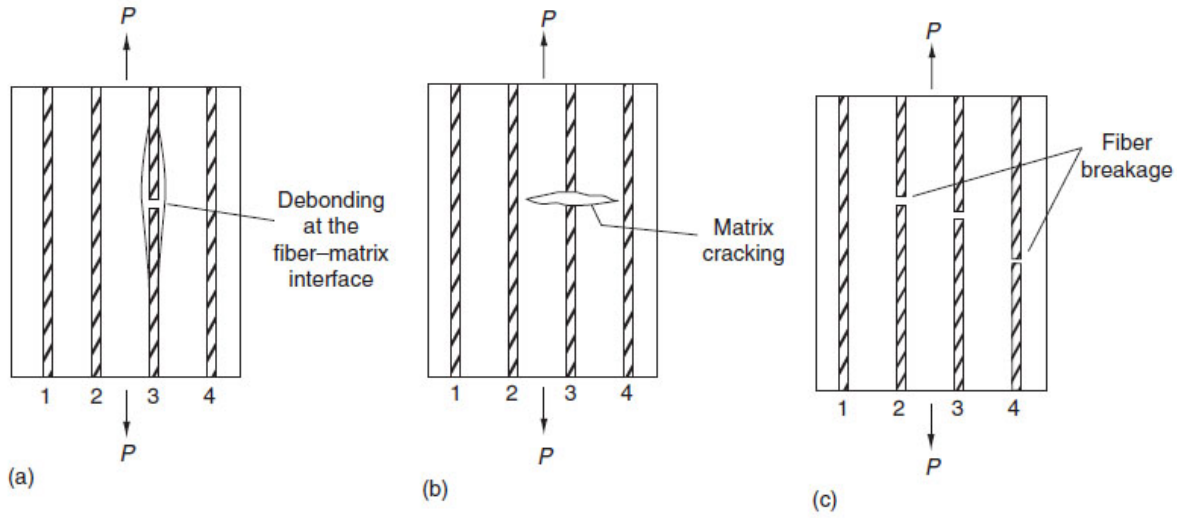


Figure 2.11: Microfailure modes from longitudinal tensile loading of unidirectional PMC [26]

The transverse tensile strength of a unidirectional PMC is much lower than the tensile strength of the matrix as the fibres act as hard inclusions, not load-bearing reinforcement. The stress in the matrix surrounding the fibres is amplified from stress concentrations created by the rigid fibres. It has been shown that the transverse tensile strength σ_{TU} decreases with an increase in both fibre stiffness and v_f and can be estimated from [27]:

$$\sigma_{TU} = \sigma_{MU} \cdot \frac{1 - \left(\frac{4 \cdot \mathsf{v}_f}{\pi}\right)^{\frac{1}{2}} \left[1 - \frac{E_m}{E_{2f}}\right]}{1 - \mathsf{v}_f \left[1 - \frac{E_m}{E_{2f}}\right]} \tag{2.49}$$

where σ_{MU} is the tensile strength of the matrix.

In longitudinal compression, the matrix of a unidirectional PMC provides lateral stability to the fibres and prevents buckling at low stresses. Estimating the compressive strength depends on the microbuckling mode, either extensional, where the transverse motion of fibres are opposite one another, or in shear, where transverse motion of fibres is parallel. It was found that for v_f greater than 20 %, PMCs exclusively experience shear buckling of fibres and the longitudinal compressive strength σ_{LCU} can be estimated using [28]:

$$\sigma_{LCU} = \frac{G_m}{1 - \mathsf{v}_f} \tag{2.50}$$

Transverse compressive loading of a unidirectional PMC causes matrix shear failures which initiate from matrix fibre debonding [26]. Also, the transverse compressive strength is considerable lower than longitudinal compressive strength and has been shown to be nearly independent of v_f [29]. Three regions on the in-plane strength as a function vs. orientation angle curve can be identified as fibre failure, shear failure and transverse tensile or compressive failure of a unidirectional PMC, Figure 2.12.

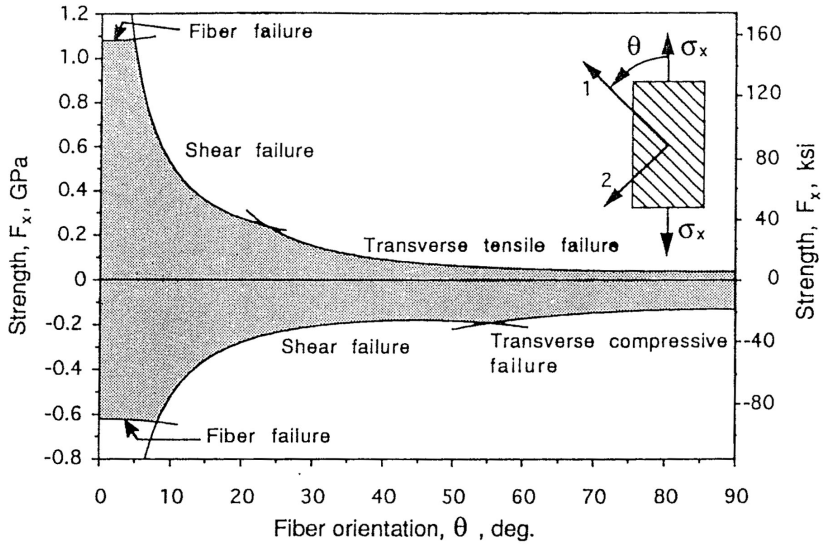


Figure 2.12: Uniaxial strength of unidirectional E-glass/epoxy lamina as a function of orientation angle [19]

2.1.4.2 Multidirectional PMC Laminates

Failure mechanisms of multidirectional PMC laminates are very complex. They experience failure as described above for unidirectional PMCs within each layer, but also experience failure from interactions of distinct layers. There are three main types of failure defined for PMC laminates: first ply or lamina failure (FPF), ultimate laminate failure or interlaminar failure [19]. The FPF criterion is a conservative approach that considers overall failure when failure of the first lamina occurs. Although the laminate may still function, failure is considered to have occurred as some PMCs may become

susceptible to environmental effects from moisture or have high notch sensitivity leading to failure soon after [26]. Ultimate laminate failure is considered when the maximum load limit is reached leading to complete PMC failure. Interlaminar failure is considered to have occurred when separation of adjacent laminae has occurred while the laminae themselves remain intact. Interlaminar failure is also referred to as delamination.

For the case of a cross-ply laminate in tension along its 0° reference direction, lamina with a 90° orientation fail first from fiber-matrix debonding, Figure 2.13. FPF dictates that failure of the laminate occurs where the knee occurs as the change in slope indicates failure of the 90° laminae.

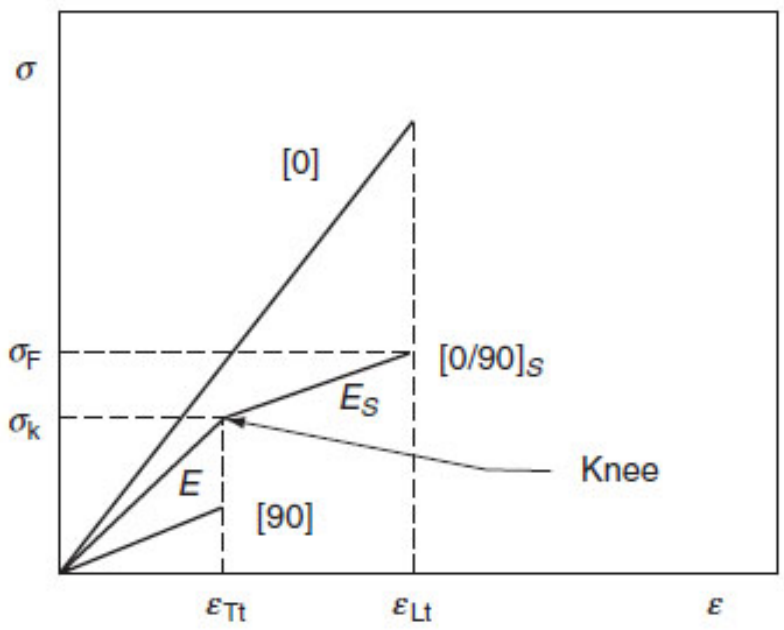


Figure 2.13: Tensile stress-strain schematic of a [0°/90°] cross-ply laminate tested along 0° direction [26]

Interlaminar delamination is one of the largest areas of concern in PMC laminates. Delamination limits flexural properties, reduces fatigue resistance, causes premature failure and increases a laminate's susceptibility to the environment [30, 31, 32, 33]. Normal tensile interlaminar stresses cause Mode I delamination, interlaminar shear stresses lead to both Mode II and Mode III delamination, Figure 2.14. The plane stress assumption required by the CLT was appropriate for sections far from any free edges where interlam-

inar stresses may be present. In tension, angle-ply composites can generate interlaminar shear stresses due to a shear coupling mismatch, whereas cross-ply laminates can generate interlaminar normal and shear stresses from the effects of a Poisson's ratio mismatch [19].

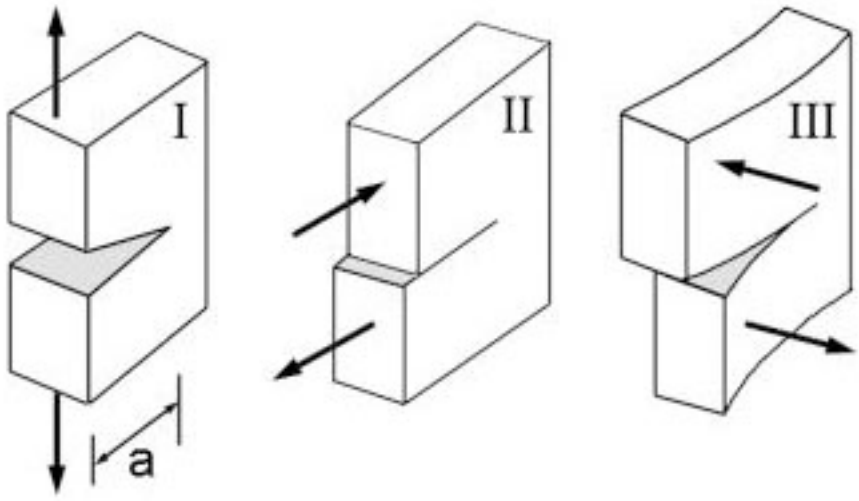


Figure 2.14: Mode I, II and III delamination types [34]

Mechanical testing is generally required to analyze interlaminar strength and toughness since modelling shear stresses is very complex. To measure Mode I interlaminar fracture toughness, the double cantilever beam (DCB) test or the edge delamination test are used. Both test methods induce interlaminar normal stresses in laminates containing an initial crack of known size. With the DCB test, hinged end tabs are attached to the upper and lower surfaces at the end of a laminate, Figure 2.15. The tabs are subjected to load cycles in tension normal to upper and lower surfaces in constant crack size intervals and crack growth is measured using x-ray or optical microscopy [33, 32, 35].

Mode II delamination can be analyzed using the 3 and 4 point end notch flexural (ENF) test. A laminate specimen with a initial crack is subjected to either 3 or 4 point bending, again loaded and reloaded based on set crack growth intervals. Fracture tough-

ness in Mode I G_{Ic} and Mode II G_{IIc} of the materials can be calculated from [26, 33]:

$$G_{Ic} \text{ or } G_{IIc} = \frac{P_c^2}{2w} \cdot \frac{dC}{da} \tag{2.51}$$

where P_c is the critical load and $\frac{dC}{da}$ is the compliance as a function of crack length at the onset of delamination propagation and w is the width of the specimen. Both test methods require $\frac{dC}{da}$, which is generated from the load unload cycles, where $C = \frac{\Delta\delta}{\Delta P}$ and δ is the crack displacement, shown in Figure 2.15 from the DCB test.

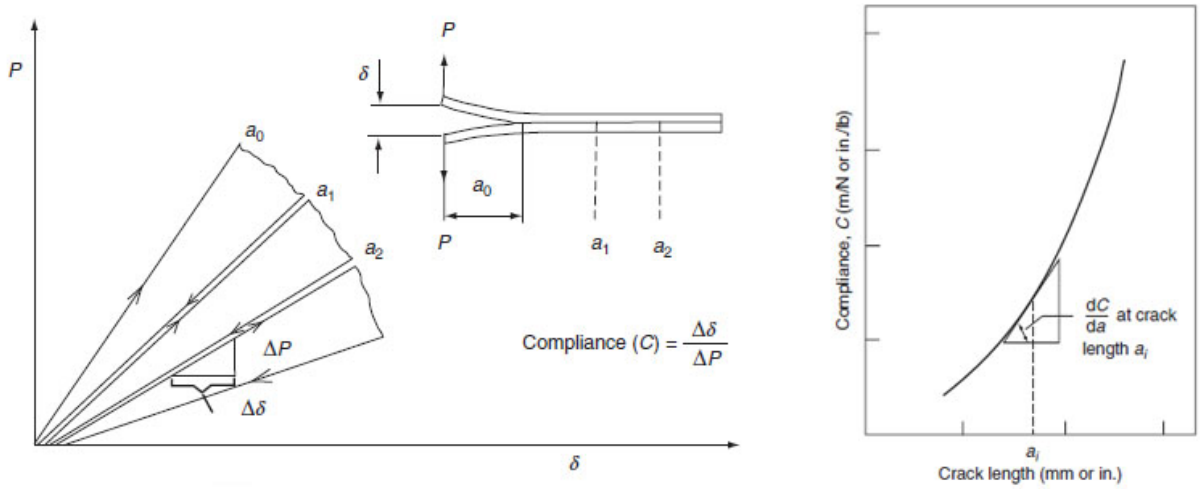


Figure 2.15: Load-displacement curve (left) and compliance-crack size curve (right) from DCB test [26]

Mode III delamination analysis has not been performed in great detail as if has been found difficult to isolate Mode III delamination [19]. However, there is great interest in testing mixed mode delamination, namely determining a fracture criterion that encompasses Modes I, II and III delamination [36]. However, only mixed mode interaction of Modes I and II have been modelled. Benzeggah and Kenane proposed that failure is expected when the total energy release rate G_T exceeds the mixed-mode fracture toughness, G_c:

$$G_c = G_{Ic} + (G_{IIc} - G_{Ic}) \cdot \left(\frac{G_{II}}{G_T}\right)^{\eta} \tag{2.52}$$

where $\frac{G_{II}}{G_T}$ is the mixed mode ratio, which ranges from 0 to 1 and is equal to 0 for Mode I DCB testing and 1 Mode II ENF testing, and η is an experimentally determined through a curve fitting process. An example of the curve fitting process in which tests

featuring exclusively Mode I, Mode II or mixed mode delamination are conducted, is shown in Figure 2.16.

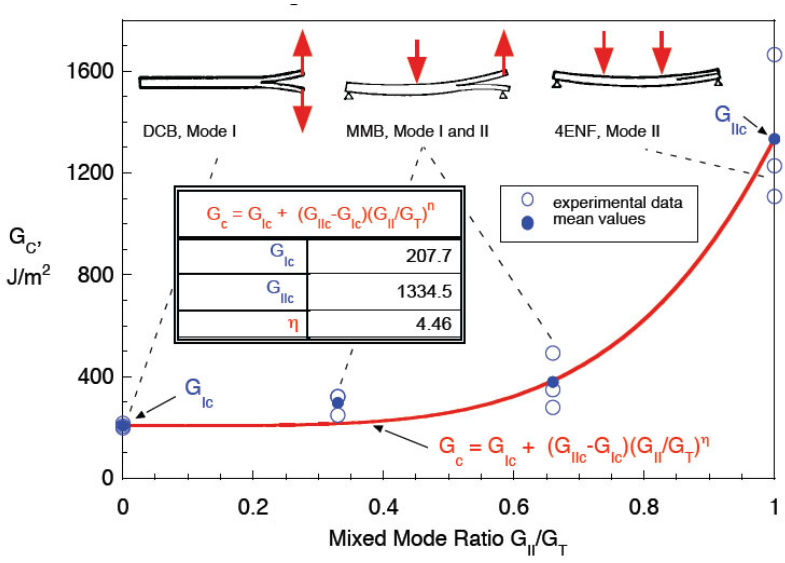


Figure 2.16: Mixed-mode fracture criterion for a toughened carbon/epoxy composite [36]

There are research areas focused on improving delamination resistance; the main topics involve matrix modification [33, 37], through thickness reinforcements [38, 39, 40], and 3D preform manufacturing [41, 42, 43].

2.1.5 Effects of Preforming Structures on Mechanical Properties

Unlike homogenous engineering materials, mechanical properties of two composites components made from the same constituent materials can differ by varying v_f, laminating sequence, fabric structure and manufacturing process used. Aerospace PMCs require in-plane, through thickness and flexural stiffness and strength, impact and fatigue resistance and toughness, among others. PMC component properties can be altered to suit requirements by changing the amount, composition, preforming technique and position of reinforcing fibres. Therefore, composite design requires balance between which mechanical properties are required for each component based on expected loading scenarios. Although the CLT may predict the behaviour of a laminated PMC, mechanical testing is necessary to accurately determine and predict behaviour of a specific composite.

2.1.5.1 Multidirectional PMC Laminates

Laminates, manufactured from prepreg or by LCM processes, contain stacked layers of thin reinforcements. Laminates feature excellent in-plane and flexural properties, such as tensile, compressive and flexural stiffness and strength [40], however they tend to show poor interlaminar and through thickness strength and toughness, Figure 2.17 [41, 44]. Therefore, traditional laminates are limited in their use when concentrated out-of-plane loads are present. Much interest has been focused on improving the interlaminar strength and toughness of PMC laminates [40, 45, 46, 47]. On the other hand, techniques which show improvements in interlaminar strength and toughness, tend to reduce in-plane stiffness and strength. Therefore, a balance must be achieved between maintaining in-plane properties and improving interlaminar shear strength and toughness.

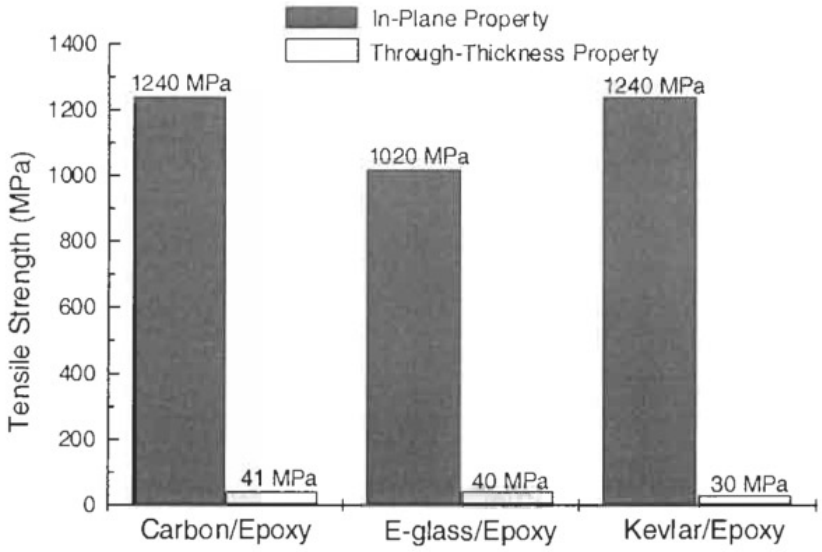


Figure 2.17: Comparison of in-plane and through-thickness tensile strengths of multiple PMC laminates [16]

2.1.5.2 Through-Thickness Reinforcements of Laminates

Through thickness reinforcements, such as z-pinning, carbon nanotubes (CNT), stitching and 3D fibre preforms are among the methods used to improve through-thickness properties and damage tolerance of laminate PMCs. These reinforcements are generally inserted through the assembled preforms in the out-of-plane direction. They have been shown to

improve interlaminar shear strength [48][49], in-plane shear [49] and interlaminar toughness [39]. However, in plane properties are affected by introduced out-of-plane crimping, in-plane distortion, breakage of fibres and formations of resin rich zones [50] caused by the insertion of such through thickness reinforcements. Figure 2.18 shows in-plane fibre distortion causing the formation of resin rich zones surrounding a z-pin.

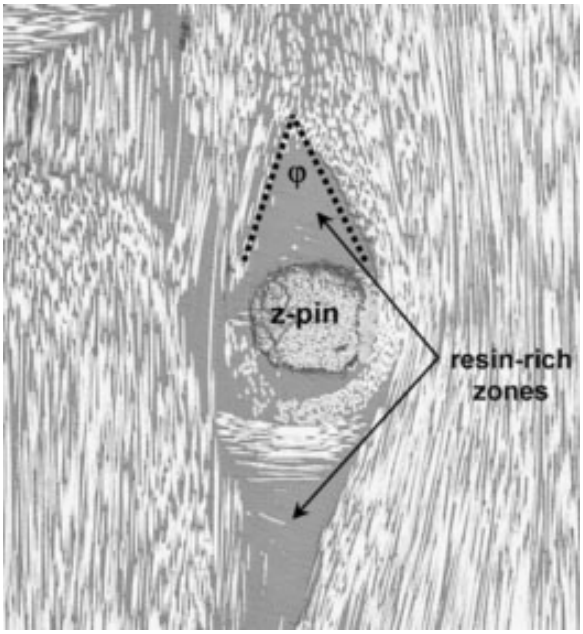


Figure 2.18: Fibre distortion and resin-rich areas within a z-pinned laminate [50]

Steeves et al. observed reductions of 27 % in tensile strength and 30 % in compressive strength with the addition of z-pins in carbon/epoxy composites[39]. Also, it was shown by Chang et al. that as z-pin content and diameter increased, flexural strength decreased significantly, however, flexural modulus was relatively unchanged , Figure 2.19 [50].

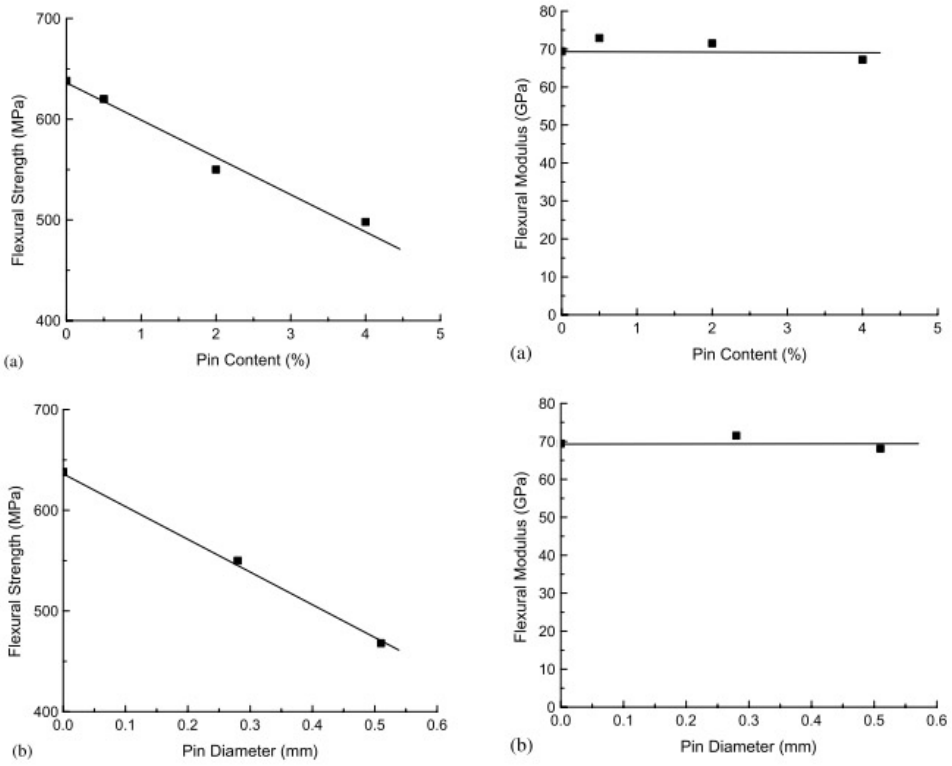


Figure 2.19: Flexural strength and modulus vs. z-pin content and diameter [50]

CNTs are similar to z-pins, however, they feature much smaller diameters which limit in-plane and flexural strength and stiffness reduction factors. CNTs are still quite new in their application in PMCs, however significant improvements in Modes I and II fracture toughness have been observed [51, 52]. CNTs improve fracture toughness mainly through crack bridging, which increases the surface area across cracks requiring more energy for crack growth, Figure 2.20. Garcia et al. showed an improvement of 154 % in Mode I fracture toughness and 214 % in Mode II fracture toughness from CNT placement between unidirectional layers of prepreg [52].

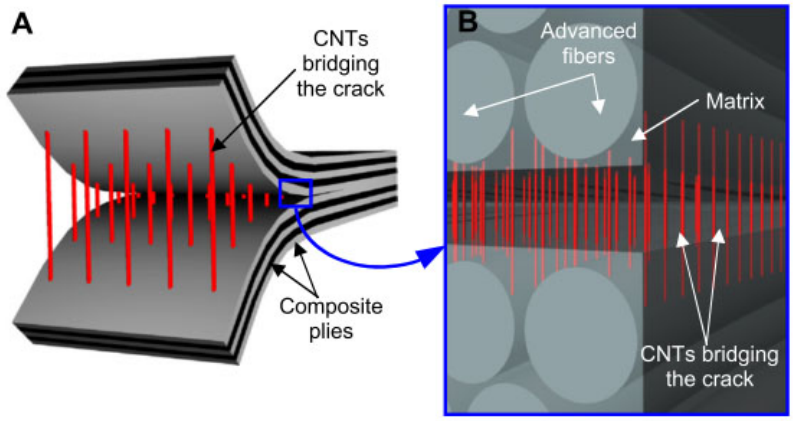


Figure 2.20: Illustration of ideal crack bridging by CNTs between laminate plies (left) and between crack (right) [52]

Stitching can be non-structural, as a method of consolidating layers and joining separate preforms, or structural, providing though thickness reinforcement. Compared with other preforming techniques, such as weaving and braiding, there is less influence on the in-plane properties [45]. In a comprehensive study by Mouritz and Cox, it was revealed that stitching generally reduces stiffness, strength and fatigue resistance not more than 10-20 % compared with an equivalent unstitched laminate [18]. However, factors such as stitch density, stitch tension and stitch thread material are highly variable and lead to conflicting reports on the effects on mechanical properties. For example, Figure 2.21 presents normalized flexural modulus vs. stitch density, in which modulus is normalized against the modulus of the unstitched laminate. Some data suggests a dramatic increase in flexural modulus with stitching, whereas others suggest a slight decline in flexural modulus. Tensile strength of the stitching yarn was also found to increase flexural stiffness in stitched laminate PMCs [53].

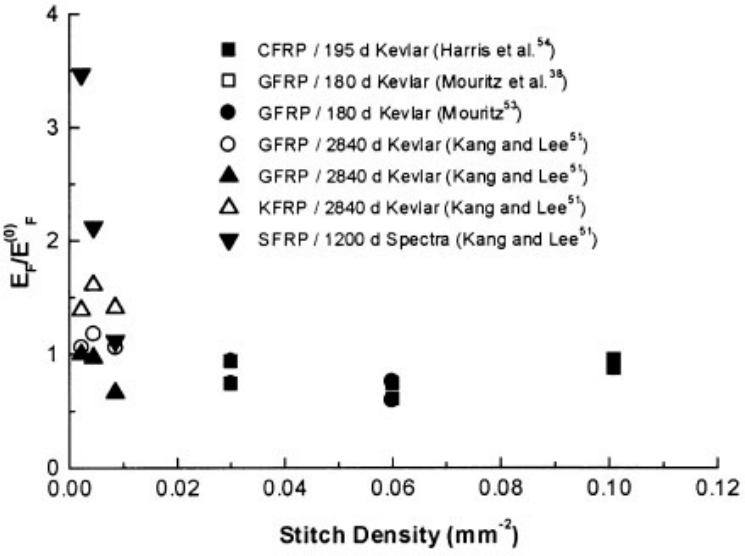


Figure 2.21: Normalized flexural modulus vs. stitch density from multiple studies [18]

Similar to z-pins, stitching causes fibre breakage, misalignment and fibre-free zones. However, it was shown that a very small amount of fibres are broken, below 0.5% [54, 55], therefore mechanical degradation is mainly the result of fibre misalignment. Fibre misalignment of up to 20° have been noted in glass fiber cross-ply laminates, with average misalignment around 10° [18]. In response to these defects, it was presented that stitching effects can be mitigated by using stitching yarns made from low-temperature or soluble thermoplastics which melt or dissolve leaving only formed reinforcement behind [48].

The other main area of through-thickness reinforcement is 3D fibre preforms. The development of 3D preform manufacturing is a cost-effective way to combat the issues prone to laminates, such as poor through-thickness mechanical properties and fracture toughness. Thick 3D fibre preforms are made from processes such as 3D weaving, 3D braiding, 3D knitting and 3D stitching. These processes are integrated forms of through thickness reinforcement. Fibre misalignment is still a major concern with 3D fibre preforms, however, with 3D weaving, 3D braiding and 3D knitting there is less likelihood of other issues such as fibre breakage and fibre-free zones.

There are many advantages of 3D fibre preforms compared to laminates, such as improved delamination resistance, interlaminar fracture toughness and impact tolerance while allowing for the manufacture of complex near-net shape preforms [17]. It has been

shown that stiffness values of 3D woven fabrics are comparable to 2D laminates, however tensile and compressive strength is lower from the severe misalignment of fibres during processing, as shown in Figure 2.22 [17, 56, 57]. The use of 3D fibre preforms is not widespread since mechanisms which control behaviour of preforms and PMC components made from 3D preforms are not fully understood [17, 58, 59, 46]. The limitations are due to the complexity of accurately modelling fibre structures and their interaction with the matrix. Also, if current accepted mechanical testing methods are used, measurement of properties may not be accurate as the standards assume material homogeneity and do not account for variability in properties [46].

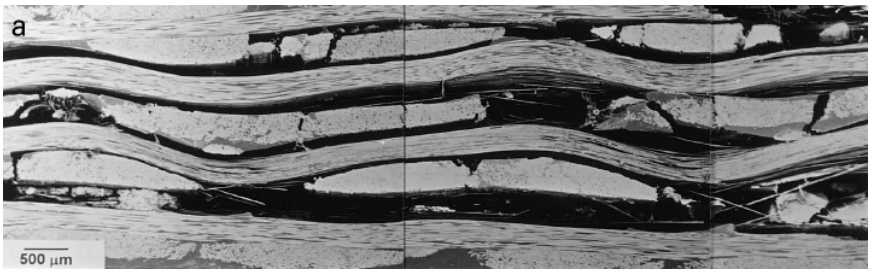


Figure 2.22: Severe fibre misalignment in PMC component made from 3D woven preform [57]

2.1.6 Impact Properties

Advanced composites are typically vulnerable to impact which leads to high maintenance and inspection costs [40, 60]. Laminates in particular, compared to composites made from thick 3D reinforcements are at higher risk [17]. Impact is classified as a concentrated load which is applied over a very short time. Dynamic material behaviour caused by impact loads is much different than that caused by static loading. Modelling and predicting impact toughness is very complicated as it deals with crack initiation and propagation, therefore mechanical testing is generally required to determine a PMCs impact behaviour. Drop-weight impact testing is one method used to measure impact properties of composites.

Typical impact zone event features crushing zone on top, shear cracks and delaminations of increasing length through the thickness and largest at the bottom [60]. A PMC plate can absorb energy through a variety of failure mechanisms such as impact

face indentation, a combination of local matrix crushing and fibre breakage, interlaminar delaminations and backside fibre peeling or splitting[61]. The stages at which these mechanisms occur can be determined from data obtained from drop-weight impact testing as described below.

The delamination threshold limit (DTL) is the impact load at which a composite plate experiences significant damage, indicated by a sudden drop in the measured load curve corresponding to a significant reduction in stiffness [61]. Figure 2.23 shows two load vs. time curves subjected to different impact energies. The specimen subjected to a higher impact energy experienced significant damage with an identifiable DTL present while the other specimen experienced a less damaging impact. The oscillations, more notably with the higher impact energy, near the peak load show progressive damage likely from delamination and crack formation.

The load vs time curve for a drop weight impact specimen within the elastic region without damage can be modelled accurately with [62]:

$$F_c = \mathrm{v}_i \sqrt{KM} \sin \sqrt{\frac{K}{m_c t_c}} \tag{2.53}$$

where F_c is the contact load, v_i is the initial velocity of the drop head, K is the stiffness of the structure, m_c is the total mass of the contactor and t_c is time. The load vs. time curve from the specimen tested at the lower impact energy of 4.61 J in Figure 2.23 takes the shape of a half sin curve as described in Equation 2.53.

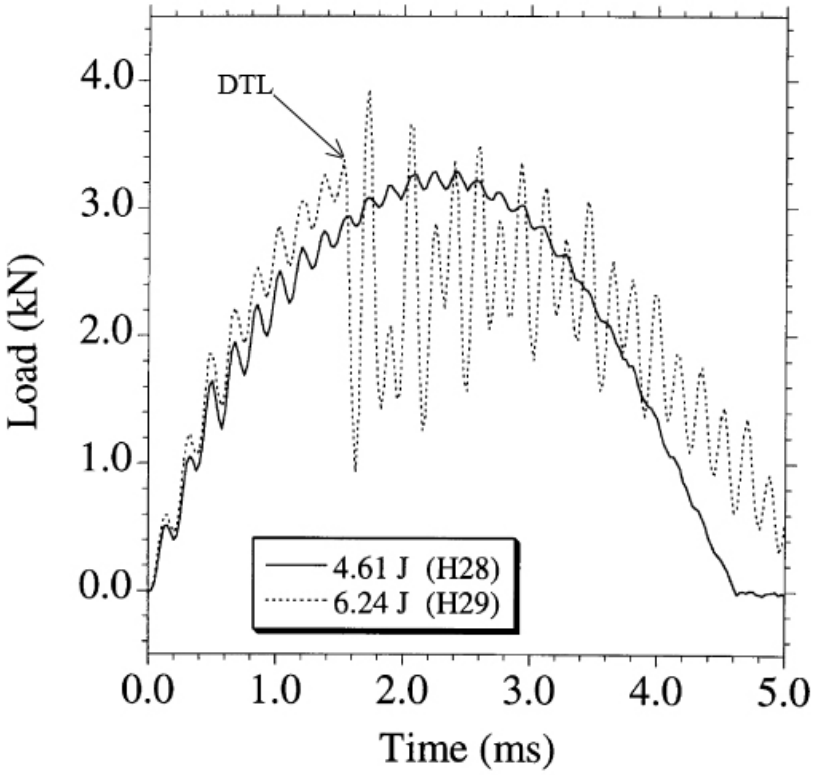


Figure 2.23: Load vs. time comparison for 24 layer Carbon/Epoxy laminates under different impact energies [61]

The energy absorbed by the composite can be determined from its load-deflection curve, Figure 2.24. The hysteresis loop in the curve accounts for the energy absorbed by the composite. Energy is only absorbed, meaning some form of failure or crack generation, by specimens whose load-deflection curves features a different load rejection curve than initial loading curve, as shown in Figure 2.24.

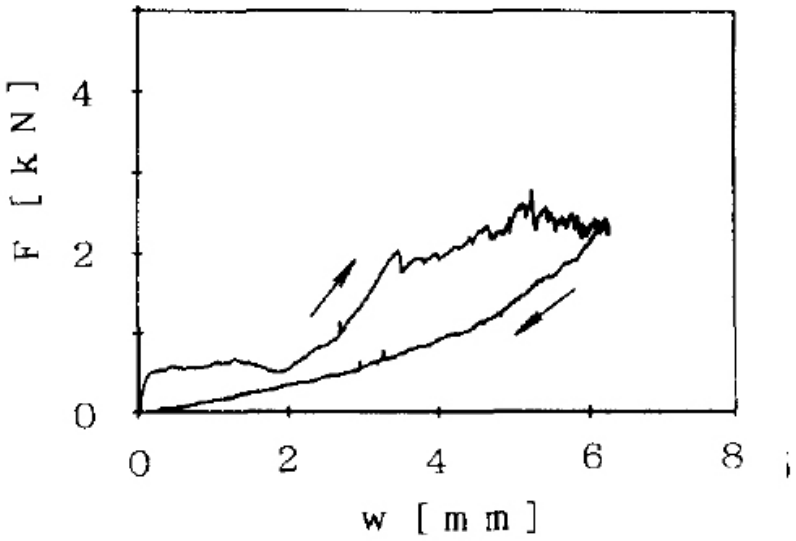


Figure 2.24: Load vs. deflection curve from a 9.7 J impact of a $[0_2^o/45_2^o/90_2^o/-45]_s$ carbon/epoxy ($\mathsf{v}_f = 60\%$) [63]

It was shown by Ujihashi that materials with higher absorbed impact energies are less resistant to damage and feature more damage [63], which can be explained by the energy required for cracks to initiate and propagate. Certain fibre structures that are thick or made from fabrics have greater impact toughness than thinner or random mat laminates [63, 64]. The effects of laminating sequences on impact toughness has also been studied, however, no differences were noted when angle-play and cross-ply laminates of similar numbers of layers [62]. PMCs with a thermoplastic matrix also feature a higher impact resistance than PMCs made from a thermoset matrix with equivalent reinforcements [63].

Chapter 3

Experimental Setup and Procedures

3.1 Preform and PMC component Manufacturing

The PMC components manufactured as part of this thesis work were made using the RTM process, from stitched NCF near net shape preforms made from carbon fibre yarns. The preform was placed within an aluminium mould and tightly sealed. Epoxy resin was injected into the mould, under an imposed flow rate to wet the preform. Mould inlets and outlets were sealed after the mould cavity was filled, and resin was allowed to cure. Each PMC component was then removed from the mould and excess material was trimmed at the edges to finish the component. The numbers of stacked layers of yarns within the various preforms manufactured in the context of this thesis were chosen based primarily on target fibre volume fractions, which is dependent on component thickness; component thickness remained constant in all cases. Choosing the number of layers involved a tradeoff or balance of priorities: for a given cavity and component thickness, increasing the number of layers leads to a higher v_f and components with higher stiffness, but also to preforms that are more difficult to impregnate with resin since the preforms are increasingly less porous and permeable.

Preform manufacturing operations up to placement into the mould are described in more details in Section 3.1.1. PMC component manufacturing is described in further details in Section 3.1.2. Also, PMC components of two different geometries, each requiring a unique mould were manufactured during this thesis: flat plates and IRPs. Both com-

ponents require preforms manufactured similarly, except for with the IRP requiring two base preforms stitched together to create a single, more complex preform. The additional preform and component manufacturing steps for the IRP are described in Sections 3.1.2.3 and 3.1.2.2 respectively.

3.1.1 Preform Manufacturing

Individual preforms were built by stacking set numbers of layers of parallel carbon fibre yarns and stitching them together. The preforms were then compacted, if necessary, to increase v_f through a decrease in thickness ans better packing of the yarns, and cut to match the outline of the mould cavity. Smaller preforms may lead to racetracking upon resin injection. Larger preforms may result in the mould not properly closing, increasing the thickness and therefore decreasing the fibre volume fraction and increasing the risks of fibre buckling and resin escaping between mould. Figure 3.1 shows basic preform layup where stacked layers of individual yarns provide preform thickness.



Figure 3.1: Preform manufacturing - layup

To determine the required number of layers, carbon fibre density and yarn spacing

were used in calculating the surface density of a single unidirectional layer, ρ_s:

$$\rho_s = \frac{\rho_f \cdot A_y}{s_y} \tag{3.1}$$

where A_y is the cross-sectional area of the carbon fibre yarn and s_y the yarn spacing. Once the surface density was determined, the number of layers N_l could be determined from the following:

$$N_l = \frac{\mathsf{v}_{f,t} \cdot t \cdot \rho_f}{\rho_s} \tag{3.2}$$

where $\mathsf{v}_{f,t}$ is the target fibre volume fraction and t is the thickness of the mould cavity. The actual number of layers N_a was taken as the next even integer above N_l to ensure preform symmetry about the neutral axis. The resulting fibre volume fraction was:

$$\mathsf{v}_{f,c} = \frac{\rho_s \cdot N_a}{t \cdot \rho_f} \tag{3.3}$$

where $\mathsf{v}_{f,c}$ is the calculated fibre volume fraction based on the actual number of layers. A list of preform lay-up parameters for the six flat plates manufactured as part of this thesis work is shown in Table 3.1. Similarly, Table 3.2 shows the preform lay-up parameters for the three IRPs manufactured as part of this thesis work, for each IRP, two preforms made using the same parameters were required and assembled.

Table 3.1: Laminating sequences and fibre volume fractions, flat plates

Plate	N_a	$\mathsf{v}_{f,c}$	Laminating Sequence
1	18	52%	$[[0°/90°]_4/0°]_S$
2	18	52%	$[[0°/90°]_4/0°]_S$
3	18	52%	$[[0°/90°]_4/0°]_S$
4	22	63.5%	$[[0°/90°]_5/0°]_S$
5	22	63.5%	$[[0°/90°]_5/0°]_S$
6	22	63.5%	$[[0°/90°]_5/0°]_S$

Table 3.2: Laminating sequences and fibre volume fractions, IRPs

IRP	N_a	$v_{f,c}$	Laminating Sequence
1	18	52%	$[[+45°/-45°]_4/+45°]_S$
2	18	52%	$[[0°/90°]_4/0°]_S$
3	18	52%	$[[+45°/-45°]_4/+45°]_S$

The following sections describe the apparatus used for laying up, stitching and cutting carbon fibre yarns towards creating stitched NCF near net shape preforms from which PMC components were made.

3.1.1.1 Layup

The layup apparatus is comprised of a pinboard, clamping frame and fibre press. To ensure that yarns were placed and remained properly spaced at 4 mm apart, they were laid onto the pinboard as shown in Figure 3.2 on the following page. The pinboard was made of a 13 mm thick acrylic sheet with 0.6 mm diameter needles set in at every 4 mm and extending out approximately 19 mm. Pins were linearly arranged in both horizontal directions spaced by 10 pins for each row as shown in Figure 3.3.

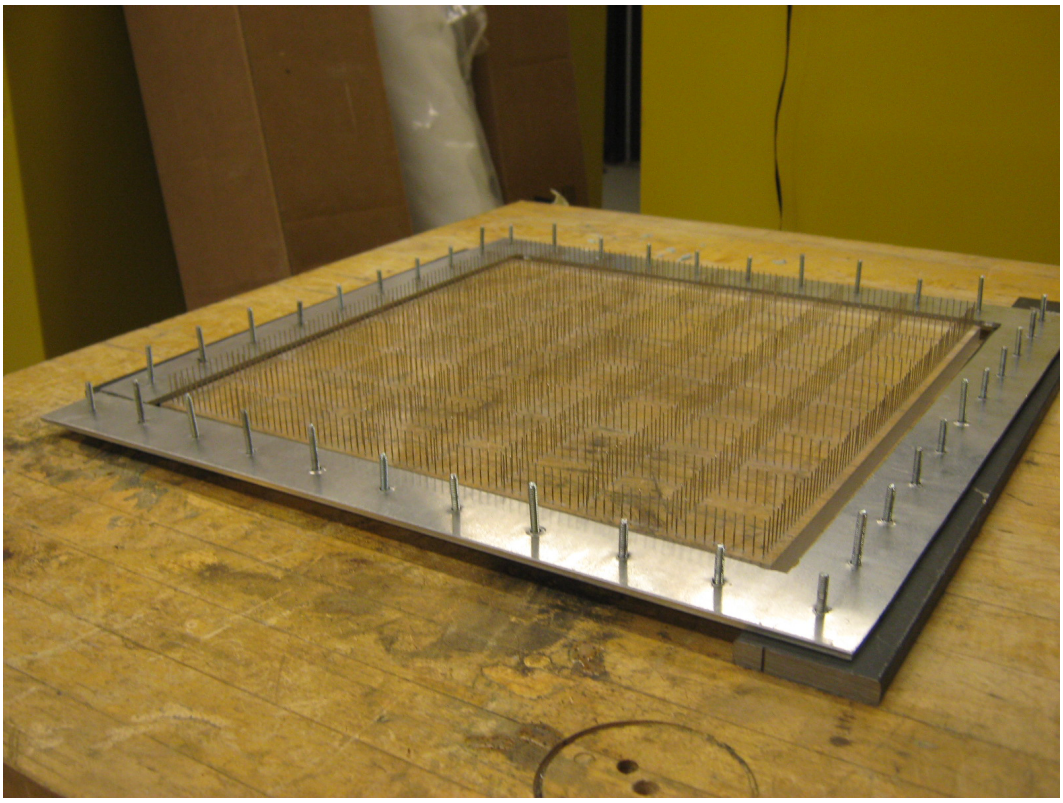


Figure 3.2: 300 mm x 300 mm Pinboard

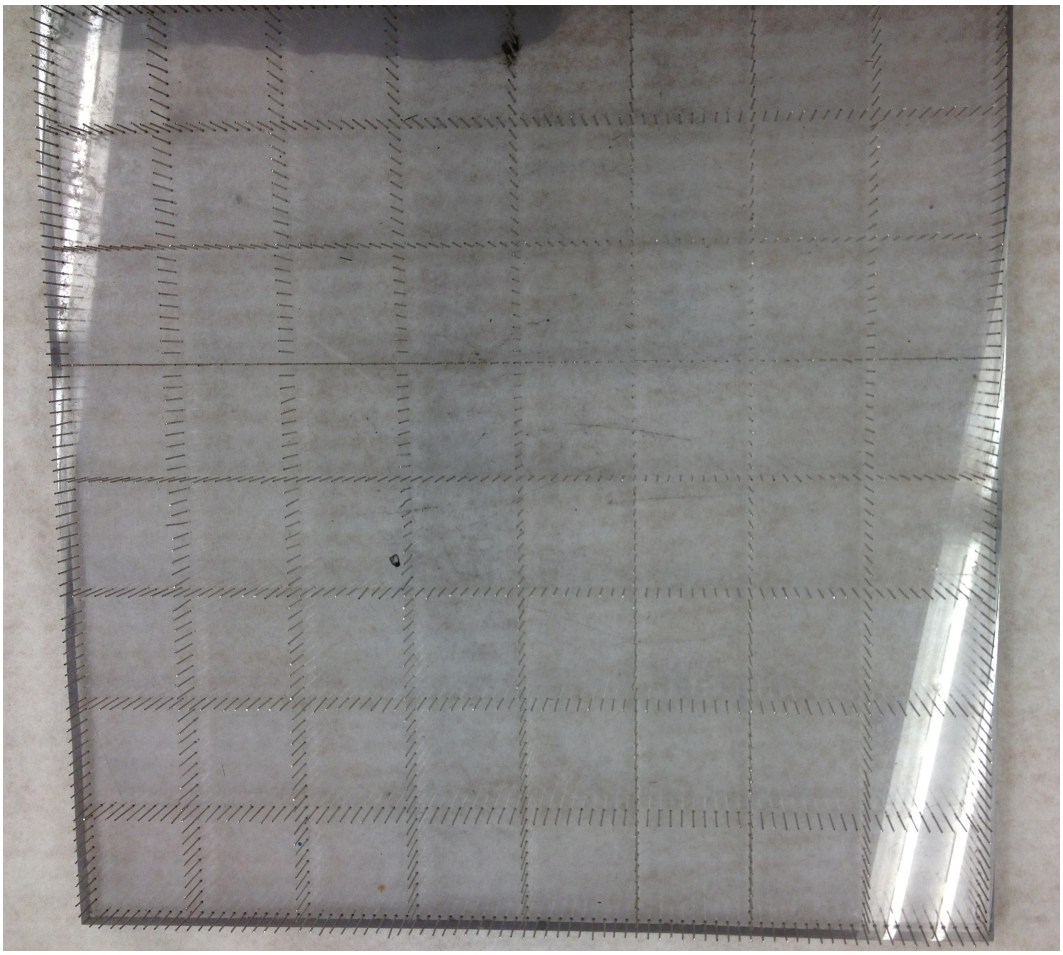


Figure 3.3: Pin arrangement on 300 mm x 300 mm Pinboard

The clamping frame ensured that yarns remained at the desired positions and spacing, reducing in-plane and out-of-plane distortion after removal from the pinboard. It was made of two 3 mm thick aluminium plates with a 330 mm x 330 mm square opening in their centre and held together with 36 #6 flat head machine screws and nuts, Figure 3.4. The fibre press was used for improving flatness of individual yarns and the general surface for the next layer, Figures 3.4 and 3.5. The fibre press was made of a 300 mm x 300 mm x 13 mm thick acrylic sheet with 35 mm x 35 mm x 13 mm thick square blocks glued so that the blocks fit within the open spaces between pin lines on the pinboard.

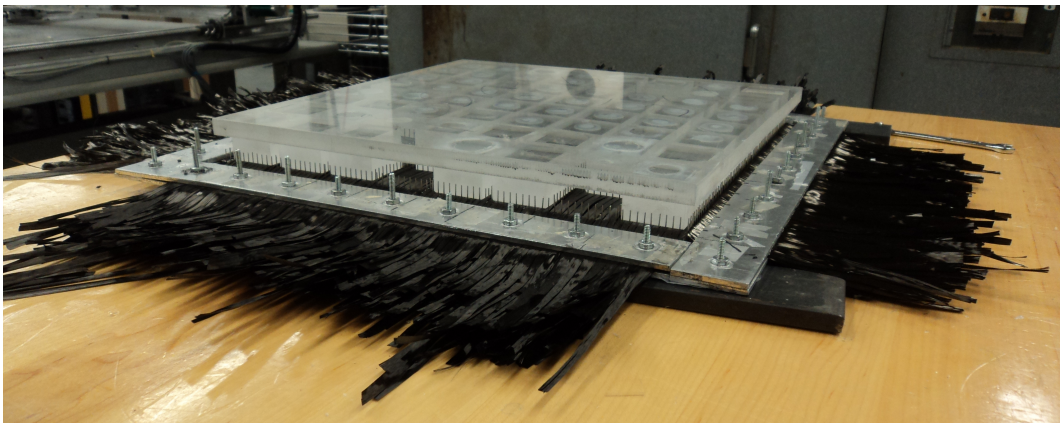


Figure 3.4: Clamping frame for 300 mm x 300 mm preform

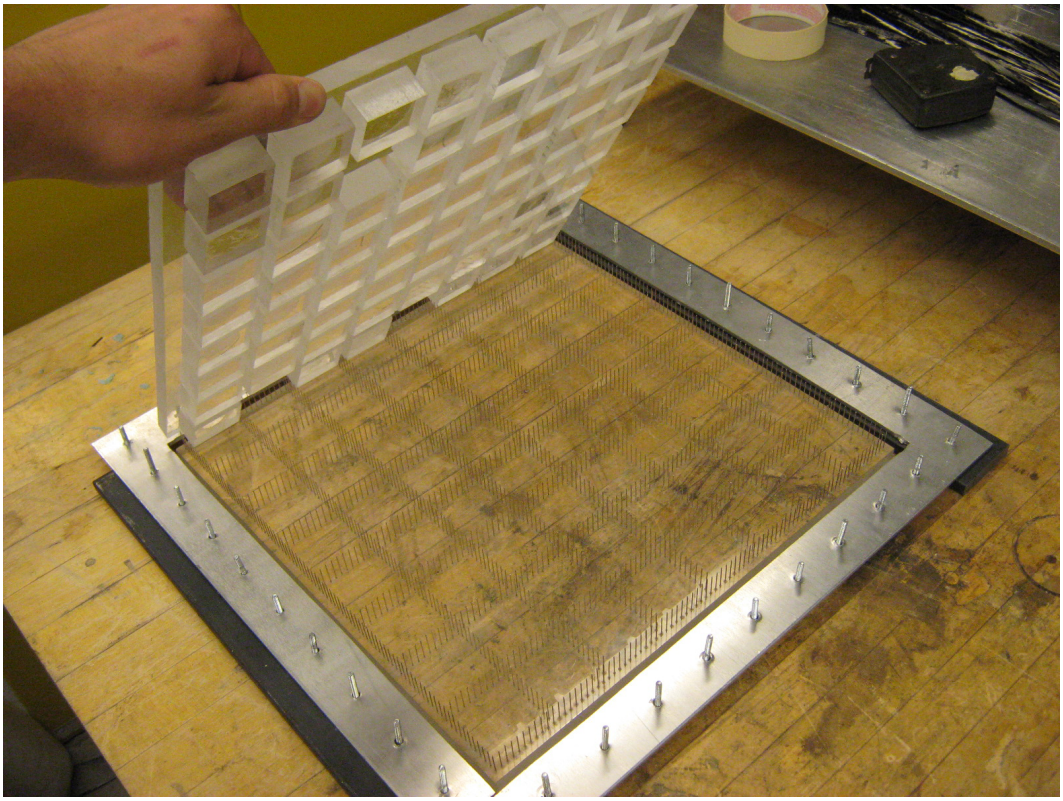


Figure 3.5: Fibre press

The carbon fibre yarn used in making the preforms was Tenax®-J HTS40 E13 12K, 800 Tex. The yarn contains 12 000 carbon fibres, has an equivalent cross-section of 0.462 mm^2 and a linear density of 0.8 $\frac{g}{m}$[4]. The yarn comes on a spool and is cut to length, typically 50 to 55 cm long so that a segment extends 2.5 to 5.0 cm beyond the outer edges of the clamping frame. Manufacturing of a preform began with fibre lay-up, the

physical placement of yarns onto the pinboard, Figure 3.6.

In this thesis, [0°/90°] cross-ply composites with straight yarns were made exclusively, therefore a subsequent layer was laid with yarns oriented at 90° from those of the previous layer, Figure 3.6, with the exception of the two central layers which were laid parallel to maintain symmetry. Between each layer, the fibre press was placed on top of the yarns to flatten and improve the surface for placement of the subsequent layer. The fibre press was placed on the stacked yarns when layup was completed to reduce out-of-plane motion while securing the clamping frame with fasteners. The unstitched preform was then removed from the pinboard with minimal handling prior to stitching.

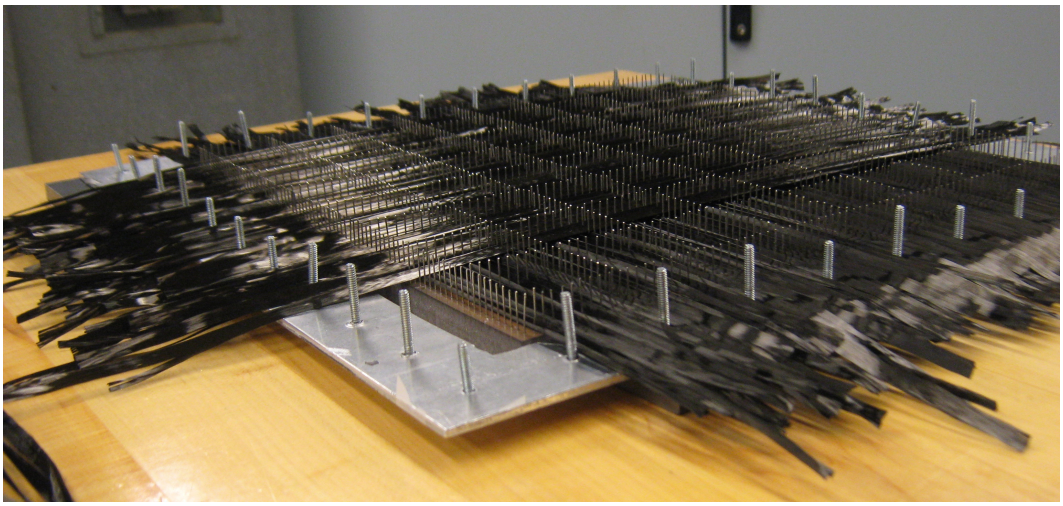


Figure 3.6: Fibre lay-up

3.1.1.2 Stitching

After yarn lay-up, a preform must be stitched so as to maintain yarn placement during preform handling and cutting. Preforms were stitched using commercial grade 100% polyester thread with a lock stitch. All preforms were stitched in one direction, parallel to other stitch lines and at 90° from the direction of the outer yarns. With this preform technology, in theory, stitch lines must be placed parallel to inner yarns and perpendicular to outer yarns so that it is possible to drape to double curvature. The flat plates and the first integral reinforced panel were stitched using 33 Tex thread, whilst the final two integral reinforced panels were stitched using a 16 Tex thread as an attempt to reduce resin racetracking along stitches and resin rich zones. Yarn movement during stitching

was avoided by securing the preform within the clamping frame.

Stitching was completed using a modified Brother LX-3125 sewing machine set with the same thread on top from a spool as on the bottom in the bobbin, Figure 3.7. The first modification made to the sewing machine was to extend the stitching head further away from the motor of the sewing machine, hence enabling stitching of larger preforms. The lengthening of the stitching arm was undertaken prior to this work but the machine was not ready for stitching at the onset of this thesis work. Timing changes were needed as well as proper coupling of the extended rotating arm. Also, as the only stitching type required was a lock stitch, the stitch type selector knob was removed.

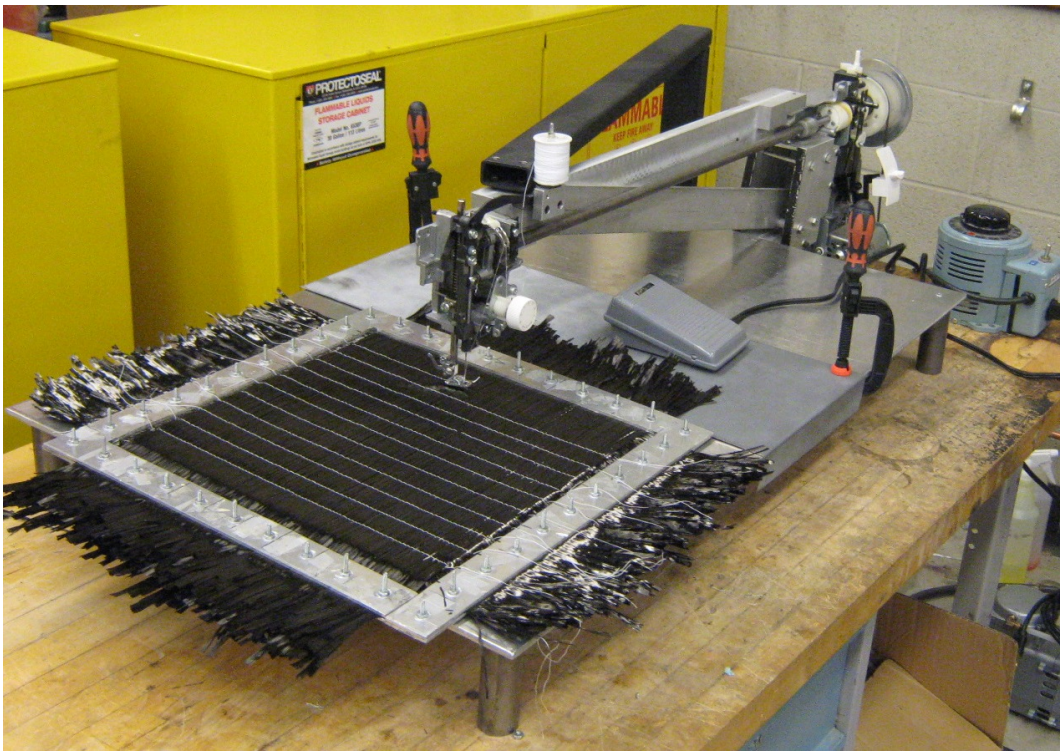


Figure 3.7: Modified Brother LX-3125 sewing machine

The feed dog which normally pulls material through the stitching head and controls stitch length was removed; with the feed dog in place the teeth would pull the yarns apart and fray them, leaving a poor surface on the bottom of the preform. With the feed dog removed the preform was no longer pulled by the machine through the stitching head, hence it needed to be pushed manually through to complete each stitch line.

In light of this, and in view of the relative accuracy sought in preform construction,

it was necessary to modify the sewing machine further so that only one stitch loop would be completed at a time, to allow the preform to be moved manually past the stitching head in the interim. A cam and limit switch were used to cut power to the motor once one revolution of the cam was completed. Figure 3.8 shows how the change in radius on the hand wheel allows the switch lever to move and stop the motor after each revolution. Setting the amount of time for which the limit switch disables the motor, controlled by the ratio of the circumferences of the smaller diameter to that of the larger diameter of the hand wheel, was a trial and error process. The inertia of rotating components of the sewing machine sometimes kept the shaft rotating past the point when the limit switch was off, and so it kept stitching continuously. To ensure that the machine would stop after one revolution every time, the ratio of the smaller radius to the larger radius of the hand wheel was increased and the voltage sent to the motor was reduced to slow the rotation and allow enough time for the machine to stop. After the necessary modifications described, reliable operation of the sewing machine was achieved.

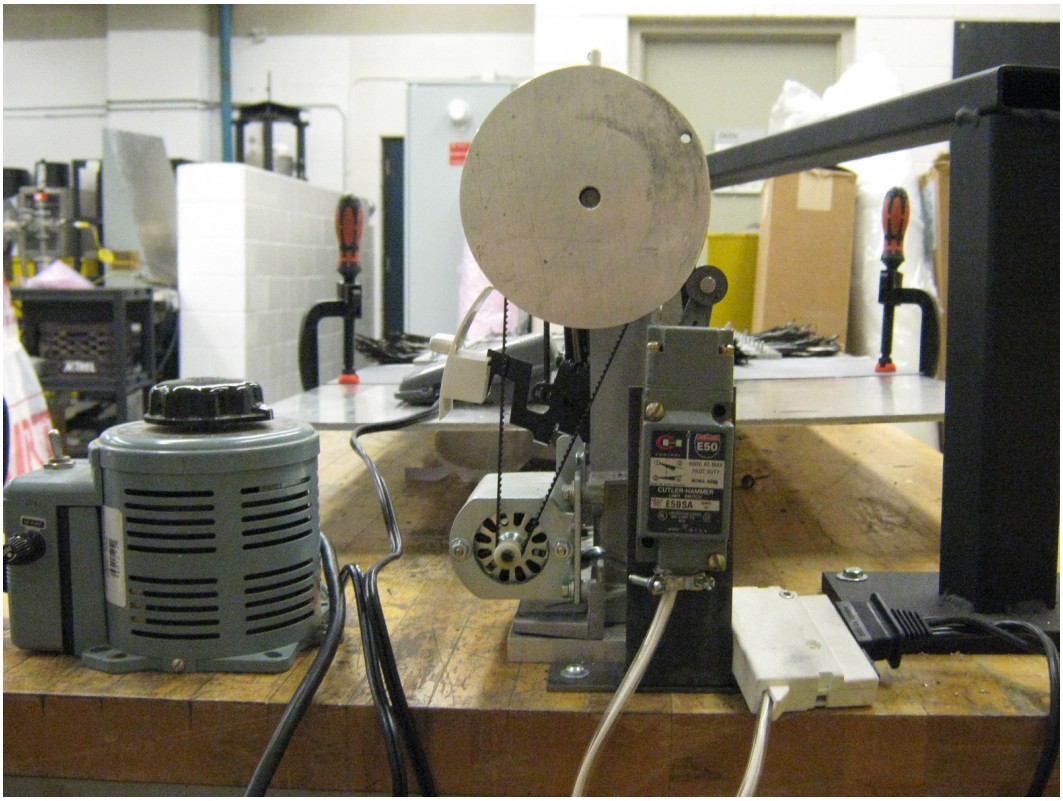


Figure 3.8: Cam and limit switch modification

Stitch lines were placed approximately 38 mm apart for prefoms made with [0º/90º] yarn orientations and 25 mm apart for preforms made with [+45º/-45º] yarn orientations. The stitch lines were closer for the [+45º/-45º] preforms since stitches near the corners must hold very short lengths of fibres. The first stitch line was placed at the centre of the preform and parallel lines were added moving out towards the edges to distribute any out-of-plane distortion towards those edges, which will eventually be cut off. To ensure straight stitch lines at 90° to outer yarns, a guide was made from clamping sheet metal bent at 90° to its length. The clamping frame was slid up against the guide and the pushed through the stitching head to maintain straightness and moved laterally after each stitch line in preparation for the following stitch line. There was approximately one stitch point every 4.7 mm; however, since the preform was pushed manually there was a significant variation in stitch length. For example, some stitches were as short as 3 mm or as long as 6.5 mm. A magnified view of typical stitches in a stitched NCF carbon fibre preform appears in Figure 3.9

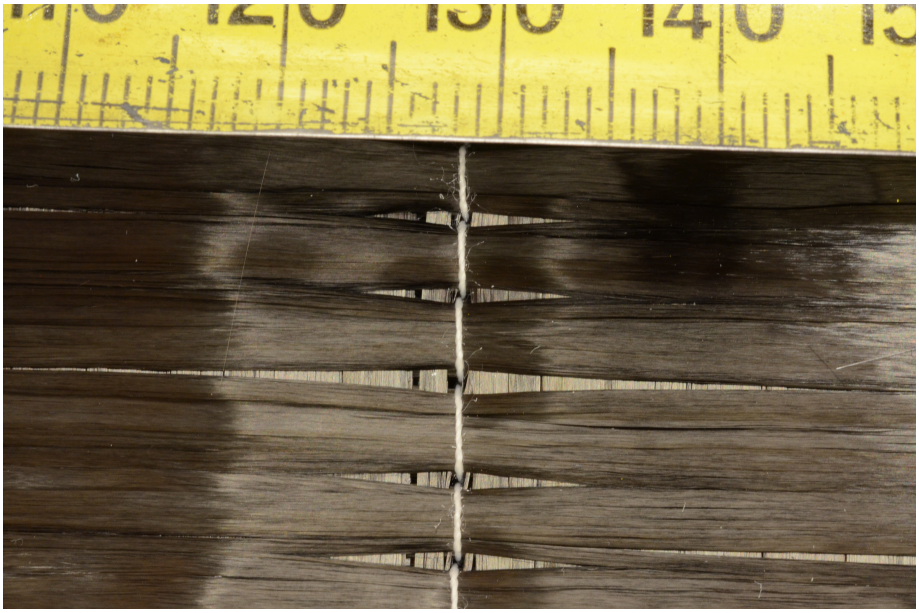


Figure 3.9: Stitches in NCF carbon fibre preform - 9.5x magnification

Excess carbon fibre yarns were trimmed after stitching for easy handling. With the clamping frame removed a preform, as shown in Figure 3.10, could be gently handled with fibre orientation remaining mostly intact.

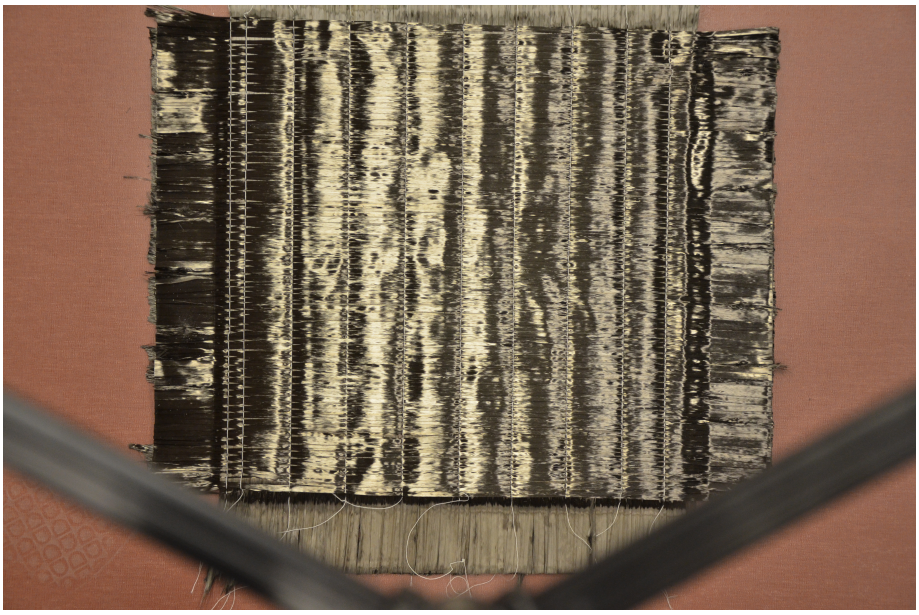


Figure 3.10: Fully stitched NCF carbon fibre preform

3.1.1.3 Preform Compaction

Compaction of preforms for plates 4, 5 and 6, Table 47 featuring 22 layers of carbon fibre yarns was necessary to reduce the thickness of these preforms to slightly greater than 4 mm, the mould cavity thickness. The preforms made of 18 yarn layers were already near the required thickness of 4 mm. Repeatedly compacting the preform also reorganizes the fibre network [65] and allows for a higher fibre volume fraction PMC. The apparatus used for performing compaction consisted in two 25 mm thick aluminium platens, mounted on an Instron 4482 universal testing frame equipped with a 100kN load cell, Figure 3.11. A threaded collar was used for tightening the upper platen against the Instron holder, and limit rotation and ensure platen parallelism. It is imperative that the platens be parallel one to another for effective compaction. Parallelism was ensured by lowering the upper platen until it was near touching the lower one and, using feeler gauges, measuring the gap between the two platens at the corners. Shims of thicknesses 0.025 mm, 0.076 mm or 0.127 mm were placed under the lower platens, at locations where the largest differences were found. Distances at the corners were measured again and further adjustments were made as required, until all four corners were within 0.025 mm of each other.

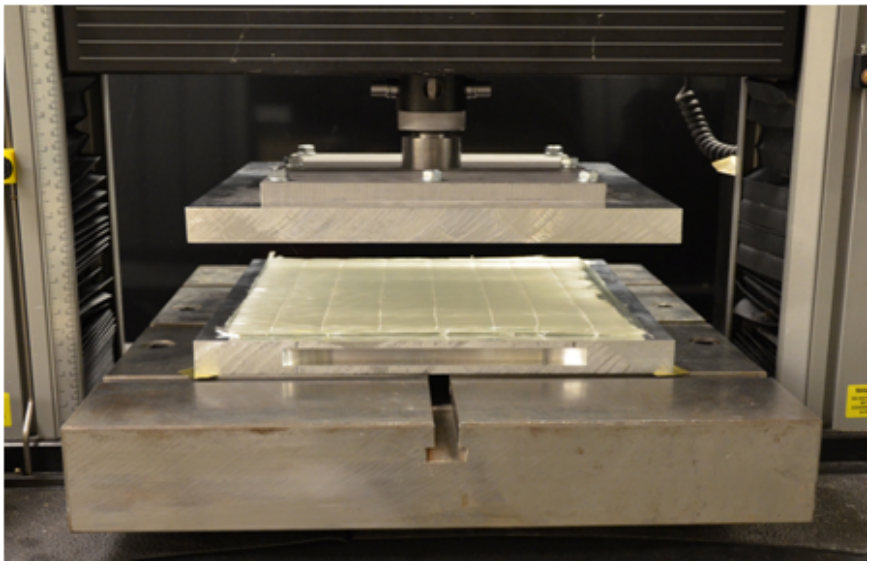


Figure 3.11: Aluminium compaction platens

With the platens in place, the top platen was raised so that the preform could be inserted between the platens. The upper plate was then lowered at a rate of $0.5\frac{\text{mm}}{\text{min}}$ with a force limit set at 50 kN corresponding to a pressure of approximately 50 MPa, based on preform dimensions of 320 mm x 320 mm.

$$P_p = \frac{F_p}{A_p} = \frac{50 \cdot 10^3 \text{N}}{320\,\text{mm} \cdot 320\,\text{mm}} = 48.8\,\text{MPa} \tag{3.4}$$

where P_p is the preform compaction pressure, F_p is the preform compaction force and A_p is the projected area of the compacted preform. Upon reaching the force limit, the top platen remained stationary for ten seconds and then was returned to its original position. This cycle was completed 30 times for each preform, since the change in thickness between successive cycles was negligible beyond 30 cycles. This lead to a typical reduction in thickness from 5.7 mm down to 4.15 mm as measured by calipers around the preform and averaged. Figure 3.12 shows visible change in the aspect of the preform due to compaction.

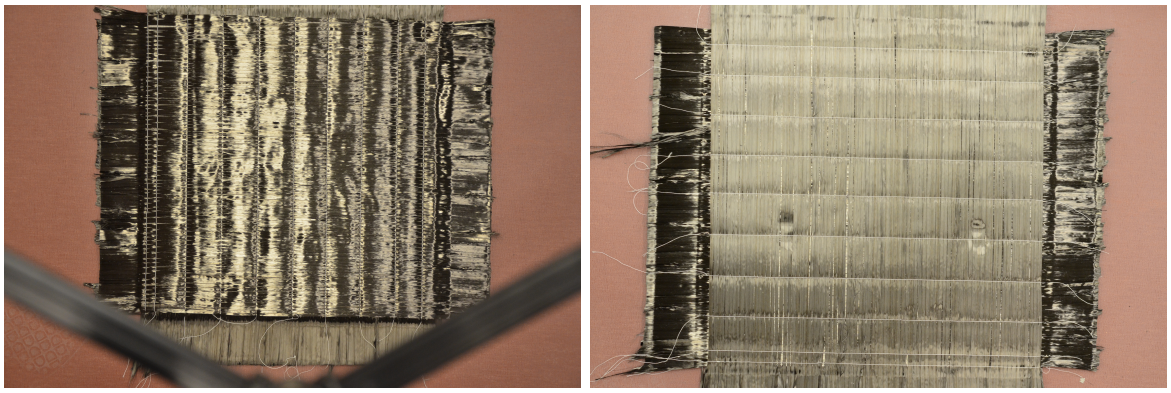


Figure 3.12: Preform before (left) and after (right) compaction cycling

3.1.1.4 Preform Cutting

Following stitching, and compaction if necessary, the preform was cut so that it may fit properly inside the mould cavity. The required net shape of the preforms was a 305 mm square for flat plates and 203 mm squares for each integral reinforced panel preform. The untrimmed preform was placed on a cutting mat attached to a slightly oversized wooden board, and a 3 mm thick steel plate that matched the required preform size was placed on the preform at the required location and orientation. The assembly was secured tightly using nine c-clamps.

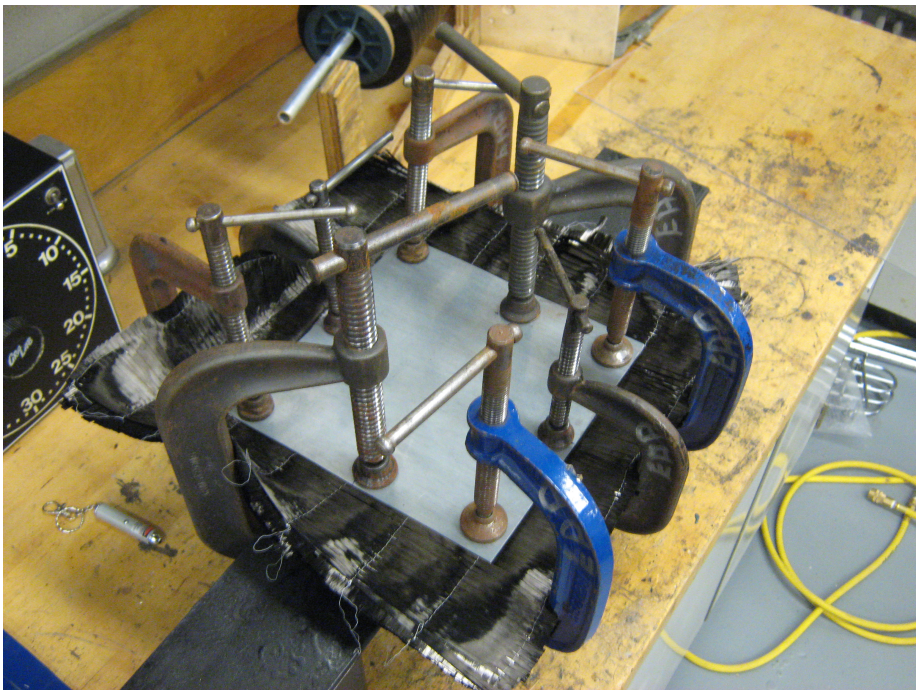


Figure 3.13: Stitched NCF carbon fibre preform cutting setup

Preforms were trimmed using the guide plate and a utility knife in sliding cutting motions and downward shearing cutting motions around the entire guide plate. After careful removal of the excess carbon fibre yarns and confirmation of a smooth clean cut around the entire preform, C-clamps were released and the steel plate and preform were removed from the cutting mat. The guide plate and preform were then weighed together on a Taylor 3865BL digital scale with 1g precision to keep the cut preform intact with minimal handling. The weight of the plate was subtracted to record the weight of the carbon fibre and stitch present in the final preform. IRP preforms require stitching two preforms together using mould apparatus in place and is discussed further in Section 3.1.2.3.

3.1.2 PMC Manufacturing

In a typical PMC manufacturing operation, the finished near net shape NCF preform was placed into the female mould cavity, and then covered by the male mould and sealed with o-rings . Epoxy resin was injected at a constant flow rate using a hydraulic ram pressed by an Instron 4482, universal testing frame. With the cavity full, the imposed flow was

stopped and all inlets and outlets were sealed off. Then the mould was placed inside a Carbolite Inc. PF120 digitally controlled oven to complete the cure cycle, as detailed in Section 3.1.2.6. The cured PMC component was demoulded and finishing operations such as trimming and sanding inlet and outlet locations were completed to produce the finished PMC component. The following sections discuss mould design, preparation and usage of both moulds used to manufacture PMC components towards this thesis work.

3.1.2.1 Flat Plate Mould

The mould used for making flat plates, Figure 3.16, was made from two 406 mm x 406 mm x 25 mm (16" x 16" x 1") thick 6061 T6 aluminium plates. A centred, square 305 mm x 4 mm (12" x 0.16") deep recess was milled to form the mould cavity. A $\frac{1}{8}$" nominal, square o-ring groove was machined 13 mm ($\frac{1}{2}$") outside of the cavity to seal the female mould, housing a 3.2 mm ($\frac{1}{8}$") diameter EPDM rubber o-ring. The following CAD drawings are in inches.

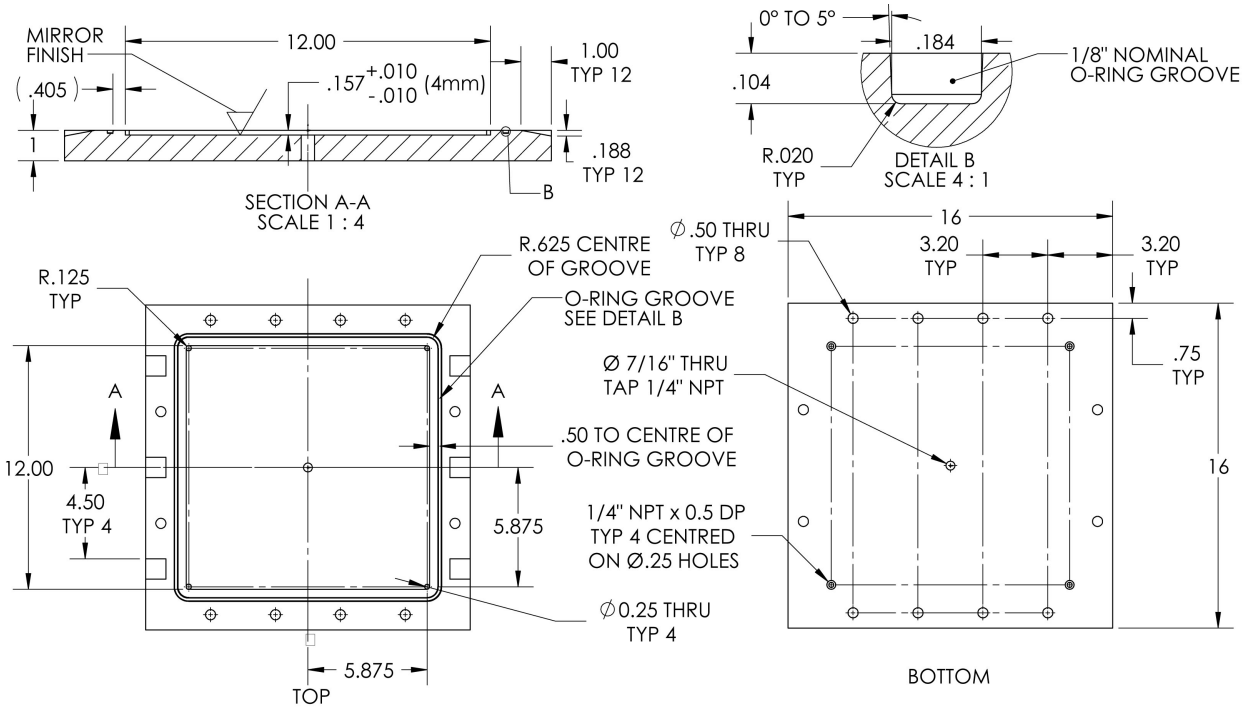


Figure 3.14: CAD drawing of female flat mould

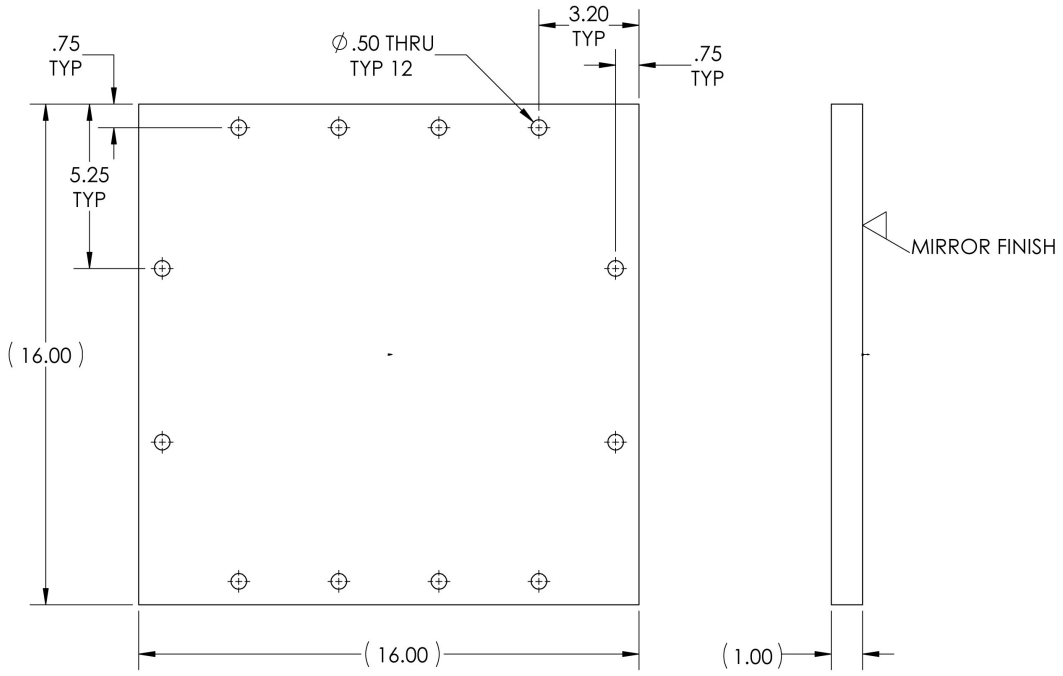


Figure 3.15: CAD drawing of flat mould cover

Cavity surfaces were sanded and polished to a mirror finish. The cover of the flat mould required only sanding and polishing as the cavity in the female mould had sufficient depth to house the preform. Twelve 13 mm ($\frac{1}{2}$") diameter holes, 19 mm ($\frac{3}{4}$") in from the perimeter, four on two opposite sides and two on the other sides were drilled to allow assembly of the mould using Ø13 mm ($\frac{1}{2}$") grade 5 bolts, washers and nuts. A $\frac{1}{4}$" NPT resin inlet port with an 11 mm ($\frac{7}{16}$") through hole was drilled from the face opposite the cavity in the female mould. Four $\frac{1}{4}$" NPT ports with 6.35 mm ($\frac{1}{4}$") through holes were drilled on the face opposite the cavity located at the corners of the cavity for resin outlets/vents. Notched wedges were machined on the cavity side of the female mould for aiding in the separation of the mould pieces.

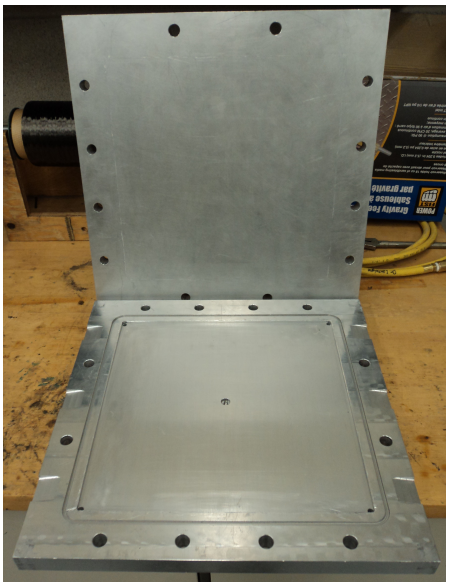


Figure 3.16: Flat plate mould components

3.1.2.2 Integral Reinforced Panel Mould

The mould for the integral reinforced panel (IRP), Figure 3.17, consisted of 4 parts shown in Figure 3.18. The geometry was devised such that it would replicate a flat panel reinforced by an integral spar section. The thickness of the IRP is 4 mm for both the main panel and the curved reinforcing section; hence it is 8 mm where the preforms were stitched together. CAD drawings for mould pieces follow in Figures 3.19 to 3.22. CAD drawings to follow are in inches.

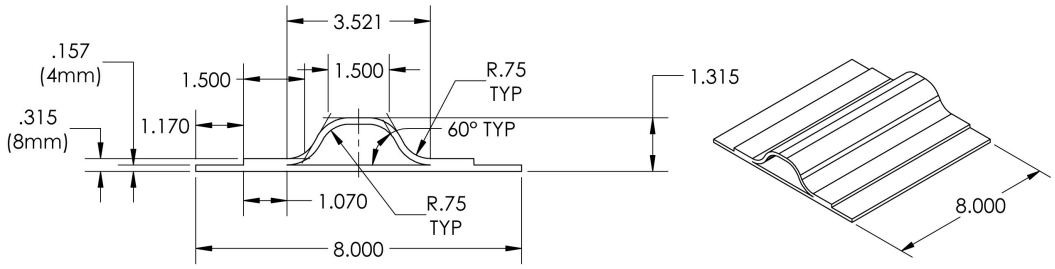


Figure 3.17: CAD drawing of integral reinforced panel

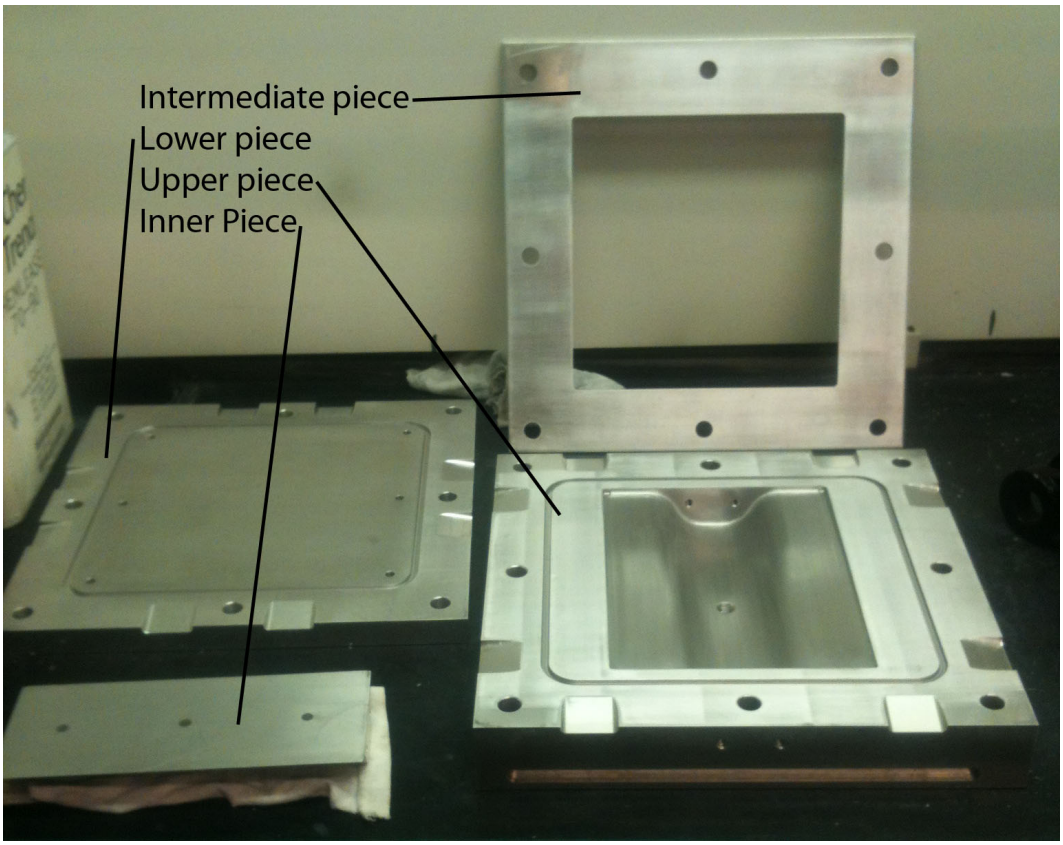


Figure 3.18: IRP mould pieces

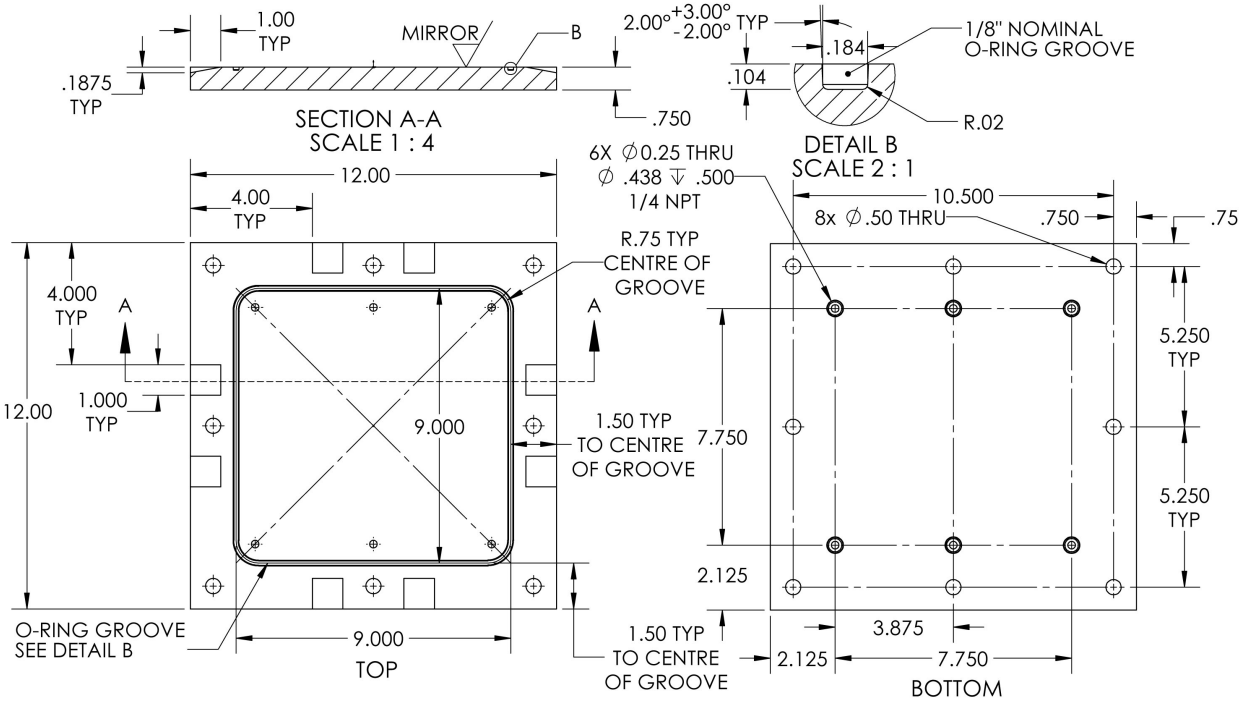


Figure 3.19: CAD drawing of IRP lower mould piece

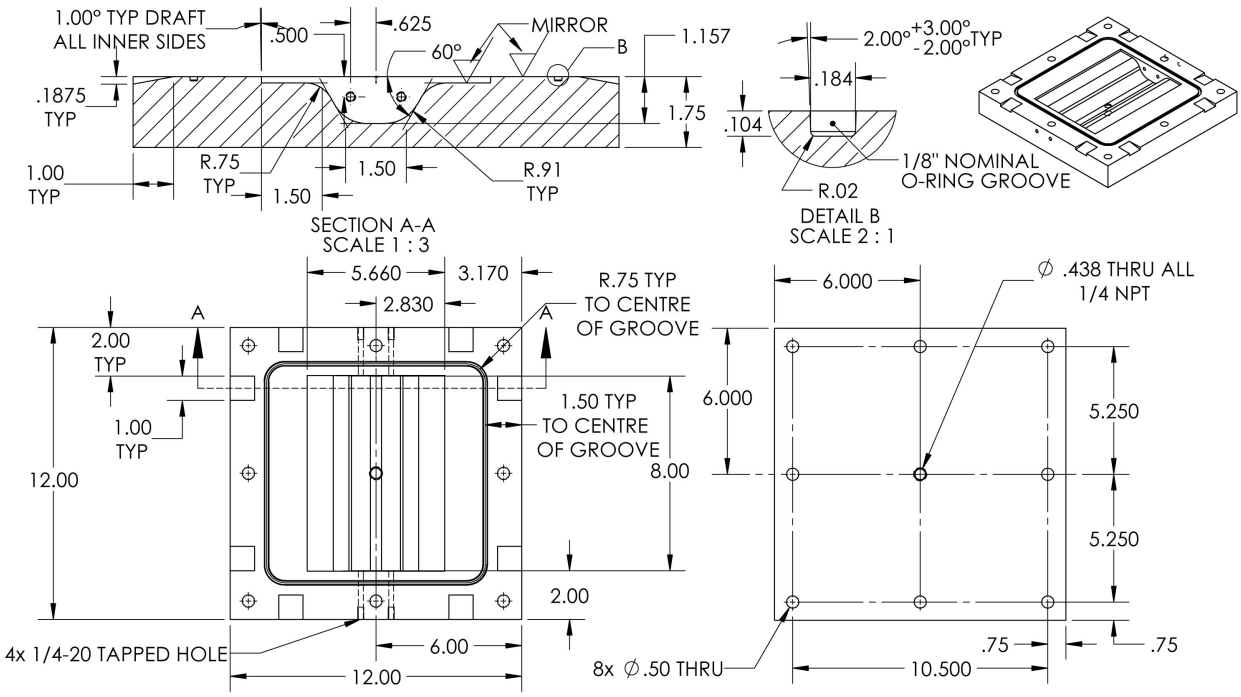


Figure 3.20: CAD drawing of IRP upper mould piece

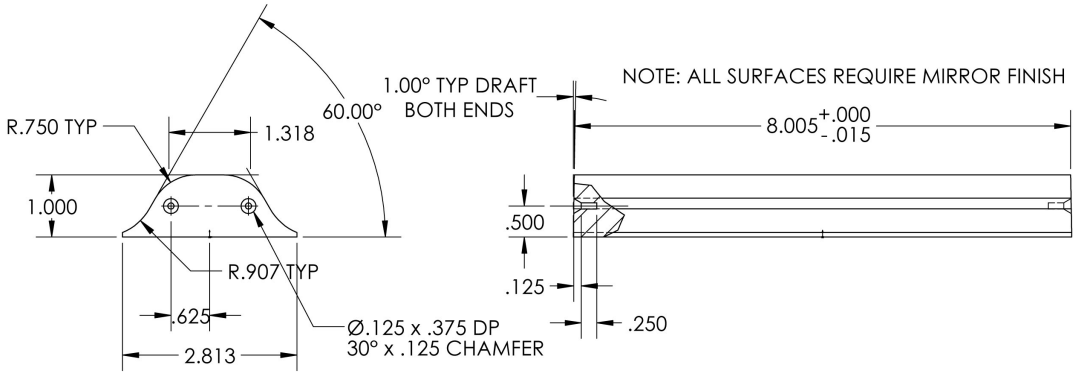


Figure 3.21: CAD drawing of IRP inner mould piece

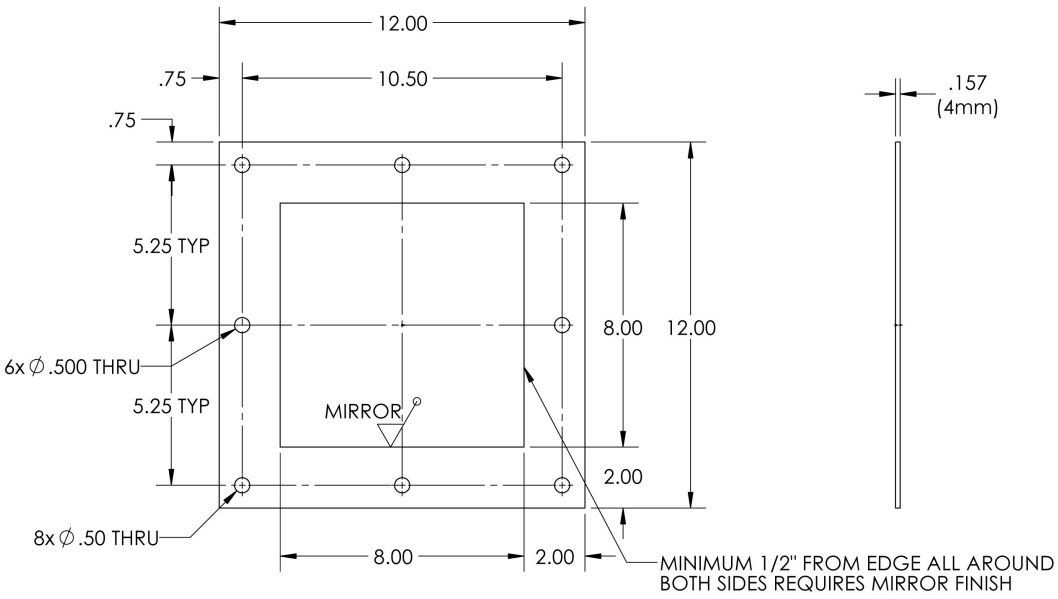


Figure 3.22: CAD drawing of IRP intermediate mould piece

The lower piece was made out of a 305 mm x 305 mm x 19 mm (12" x 12" x $\frac{3}{4}$") 6061 T6 aluminium block provides the flat bottom component surface. Six $\frac{1}{4}$" NPT ports drilled with a $\frac{1}{4}$" through hole make up the outlets/vents on the side opposite the cavity.

The intermediate piece is made from a 305 mm x 305 mm x 4 mm (12" x 12" x 0.160") 6061 T6 aluminium sheet with a 8" square opening removed from the centre. The piece lies flat on top of the bottom piece and creates the 4 mm cavity thickness required for the flat part of the preform.

The inner piece was was contour milled from a 254 mm x 95 mm x 32 mm (10" x $3\frac{3}{4}$" x $1\frac{1}{4}$") 6061 T6 aluminium bar and feature minimum 19 mm ($\frac{3}{4}$") bending radii for the preform on inner surface of the spar. The ends feature a slight 1° draft angle to facilitate demoulding.

The upper piece was made from a 305 mm x 305 mm x 44.5 mm (12" x 12" x $1\frac{3}{4}$") 6061 T6 aluminium block and the inner contour was designed to create a component with a thickness of 4 mm along its local normal, and given the shape of the inner piece. A $\frac{1}{4}$" NPT port was drilled through the centre of the side opposite the inner contoured cavity for the resin inlet. The internal edges of the upper piece feature radii that compact the preform, locally increasing v_f to reduce racetracking along the edges. The internal

side edges that meet the ends of the inner mould match the 1° draft angle to create a tight fit.

To ensure the inner piece doesn't float within the upper piece, 4 holes were drilled and tapped in the ends of the upper piece and matching relief holes were machined in the inner piece. Four Ø$\frac{1}{4}$" - 20 UNC x 2$\frac{1}{4}$" long bolts were machined to a point to fit into the relief holes in the inner piece. All mould cavity surfaces were sanded and polished to a mirror finish. The lower and upper pieces had nominal $\frac{1}{8}$" o-ring grooves milled 12.7 mm ($\frac{1}{2}$") outside the mould surfaces to house a 3.2 mm ($\frac{1}{8}$") diameter EPDM o-ring and seal the mould. The lower, intermediate and upper pieces feature eight matching 13 mm ($\frac{1}{2}$") diameter holes around the outer edges to clamp the mould pieces together using Ø13 mm ($\frac{1}{2}$") grade 5 bolts, washers and nuts.

3.1.2.3 Integral Reinforced Panel Preform Manufacturing

Preform preparation for integral reinforced panels required two of the preforms described above, cut into 302 mm squares. One preform was laid flat inside the intermediate mould piece to maintain shape and keep outer fibres from falling during handling. The inner mould piece was centred on top of the preform and the other preform placed on top of it, Figure 3.23.

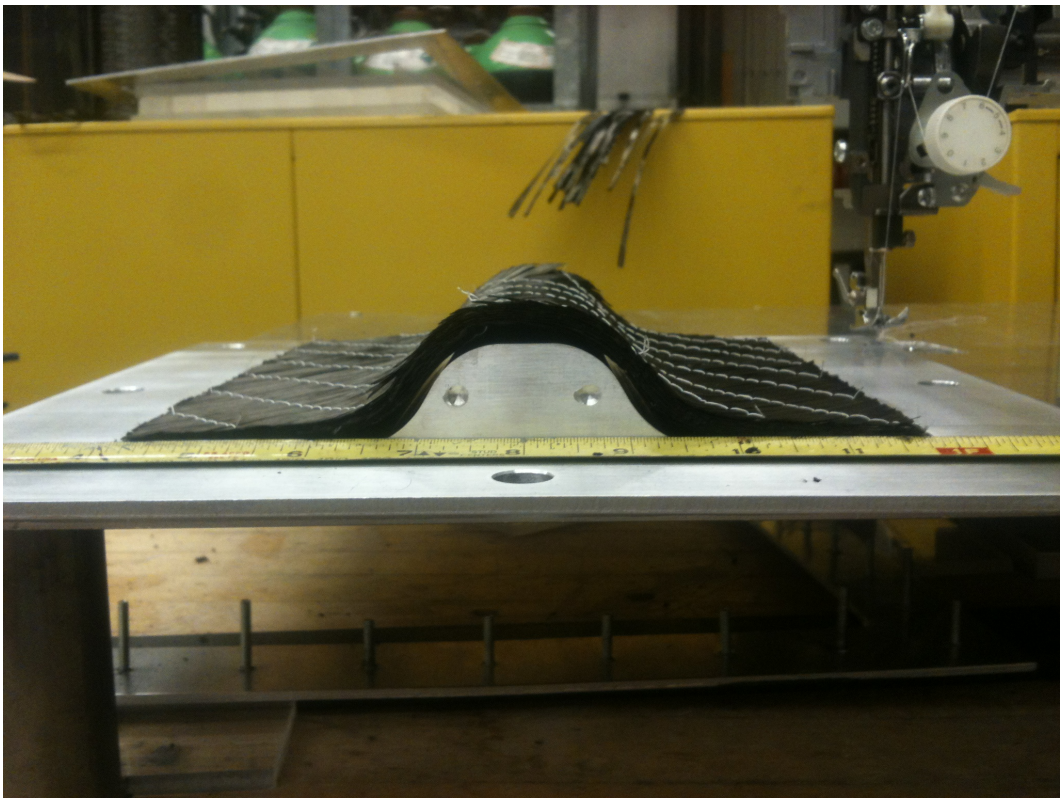


Figure 3.23: IRP pre-stitching preform placement

The two preforms were joined together parallel to the long edge of the inner mould piece at 35 mm from the outer edge of the bottom preform, Figure 3.24. Another parallel stitch line was made 12 mm towards the inner piece. Two more lines were stitched on the other side of the inner piece, at the same distance from the edge of the bottom preform. By sliding a thin cutting mat between both preforms, the upper preform was cut $26mm$ from the other edges on both sides to align with the cavity in the upper piece of the IRP mould. The preform was stitched with the inner mould piece already in place between the preforms as inserting it after stitching would prove very difficult and introduce fibre distortions.

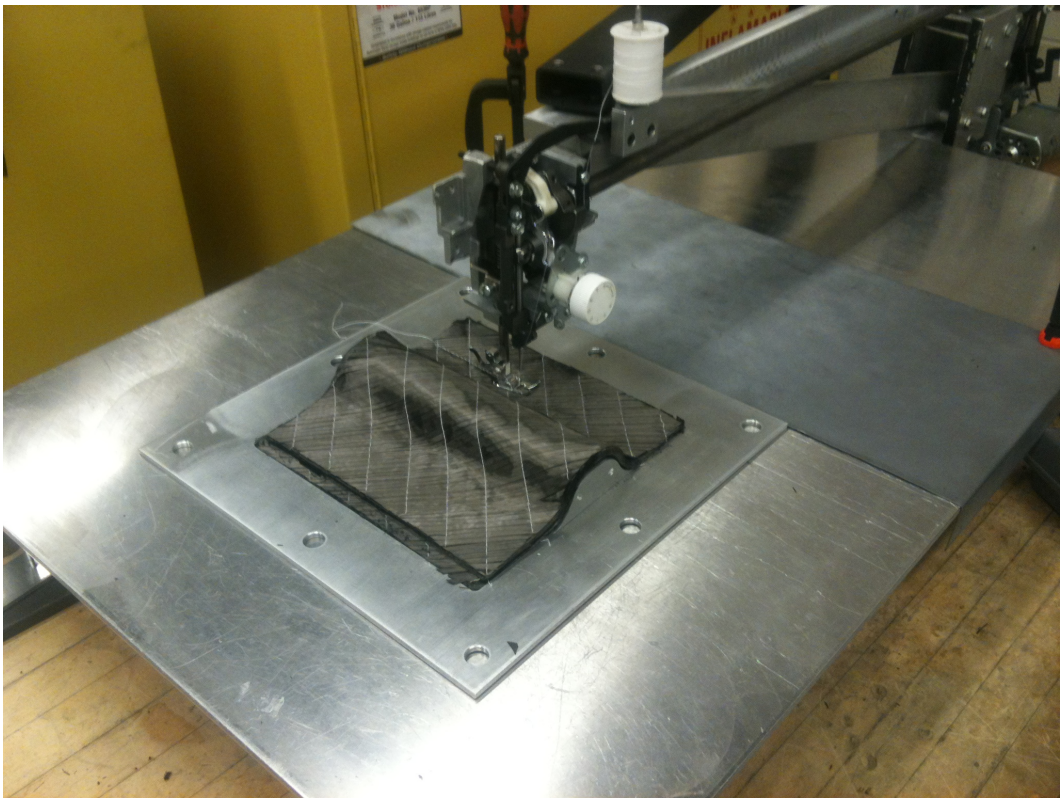


Figure 3.24: IRP preform stitching

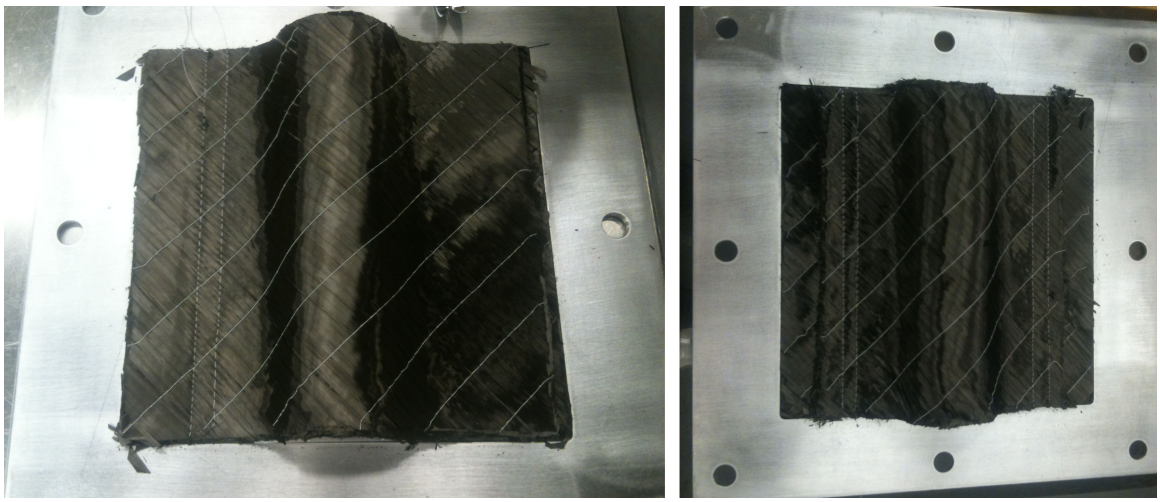


Figure 3.25: IRP preform before (left) and after (right) edge cutting

3.1.2.4 Mould Preparation

The mould cavity surfaces require treatment with mould release compound to allow de-moulding. A chemical treatment, Chem Trend® CHEMLEASE 70-90, was used to treat

both moulds, Figure 3.26. Mould cleaner must be used beforehand to remove any wax, oil or leftover resin from previous uses before the chemical mould release can be applied. Chem Trend® CHEMLEASE Mold Cleaner was used according to manufacturer's specifications under a fume hood to avoid inhalation of vapours. The chemical mould release was then applied in separate coats according to manufacturer's specifications, also under the fume hood. A minimum of five coats was applied with at least 10 minutes between coats. A full cure of 30 minutes was required after the final coat.

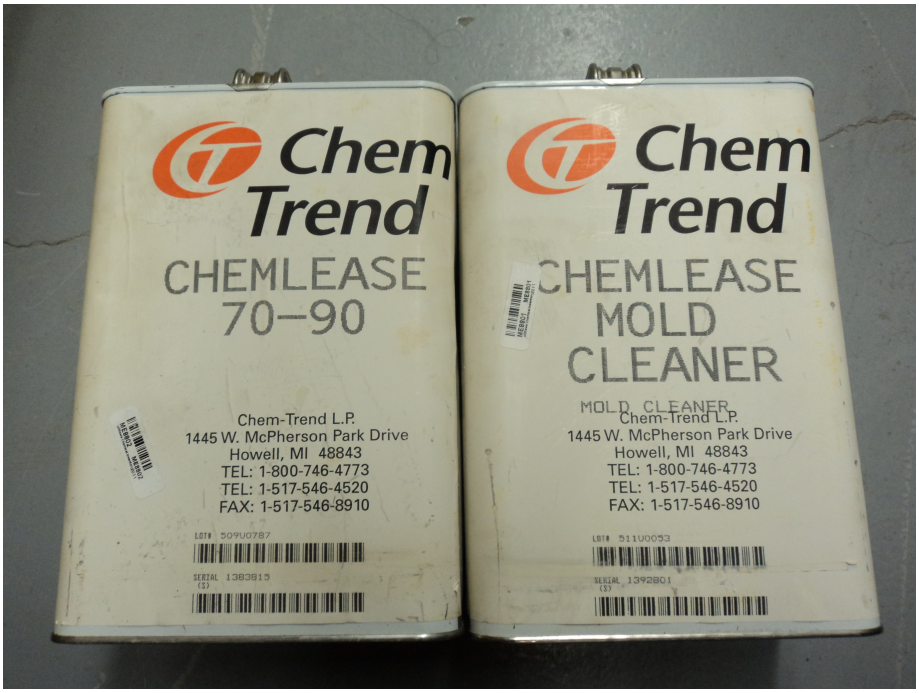


Figure 3.26: Chem Trend® CHEMLEASE 70-90 and accompanying mould cleaner

The preform must be inserted carefully into the mold cavity to avoid losing or disturbing the yarns. Nominal $\frac{1}{8}$" EPDM o-ring cord stock was cut to length to fit the surrounding o-ring grooves in the moulds. The ends of the o-ring were glued together using Loctite® quick set 404 super glue and placed inside the o-ring grooves. A flat plate mould with a preform inserted and o-ring in place is shown in Figure 3.27. The preform had to be fully set in the cavity without any excess yarns overlapping the cavity edges to ensure that the mould would close tightly and seal. The upper mould was then placed over the cavity and $\emptyset\frac{1}{2}" - 12UNC$ bolts, nuts and washers were fastened tightly to close the mould.

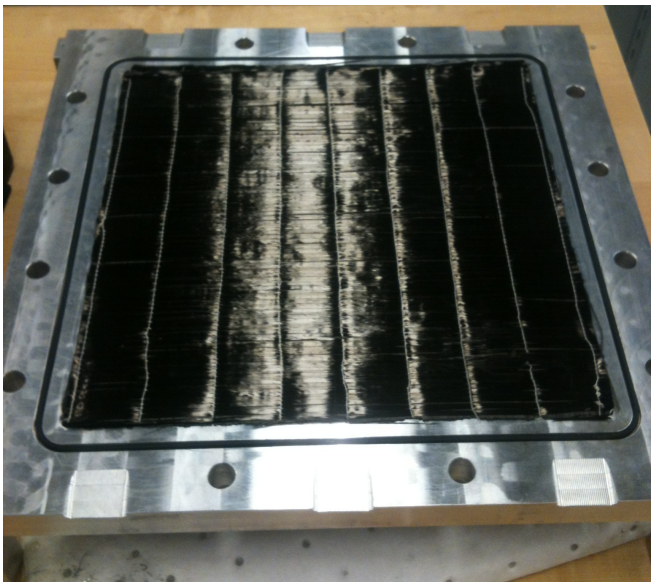


Figure 3.27: Flat plate female mould piece with preform and o-ring

The IRP mould was assembled in a similar procedure except that the preform was stitched inside the intermediate piece as described above and contained the inner piece. The preform was inserted upside down into cavity in the upper piece with the o-ring in the groove within the upper piece. Given the tight fit between the inner piece and the top piece, the preform had to be gently tapped into place with a soft mallet.

The four $\emptyset\frac{1}{4}" - 20$ UNC bolts with the pointed machined ends were then threaded through the upper piece and into the relief holes in the inner piece to position and hold the inner piece in place. With the o-ring in place, the lower piece was placed over the inserted preform onto the intermediate piece to match the bolt holes with the six outlet ports aligned such that the outlets ports are located on the sides where the preform is 4 mm thick.

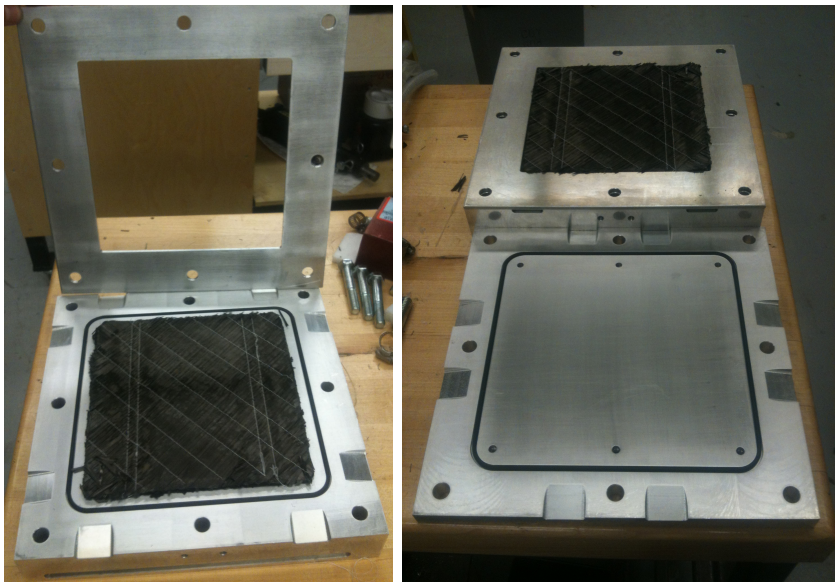


Figure 3.28: IRP mould assembly

3.1.2.5 Resin Injection Apparatus

The resin used for making PMC components was a two component Tri-tex® L-1911 Marine System clear laminating epoxy. This epoxy was selected since it has a low working viscosity of 200-300 cps and a long working time of approximately an hour; cure requires an eight hour cycle at 80°C. Neat L-1911 epoxy has a tensile strength of around 70 MPa and tensile modulus around 3 GPa [5].



Figure 3.29: Tri-tex L-1911 resin used for injections

The injection apparatus, Figure 3.30, used a hydraulic cylinder to inject resin through a system of tubes and into the PMC mould at a constant flow rate as shown schematically in Figure 3.31. The main components of the injection system are the hydraulic cylinder, the vacuum pump, the resin trap, three-way wye and ball valves, tubing and fittings.

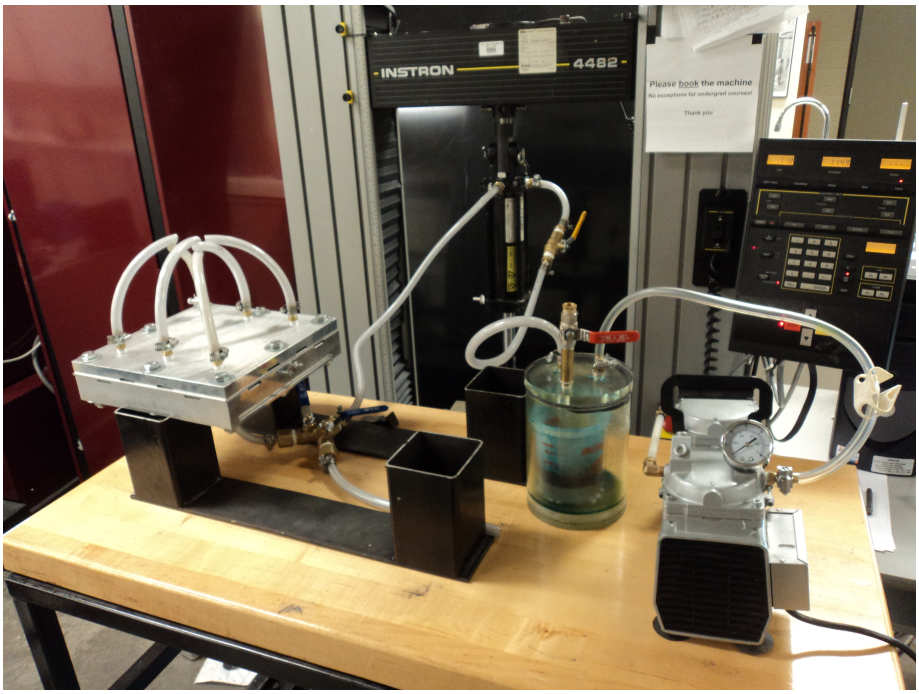


Figure 3.30: Experimental resin injection apparatus

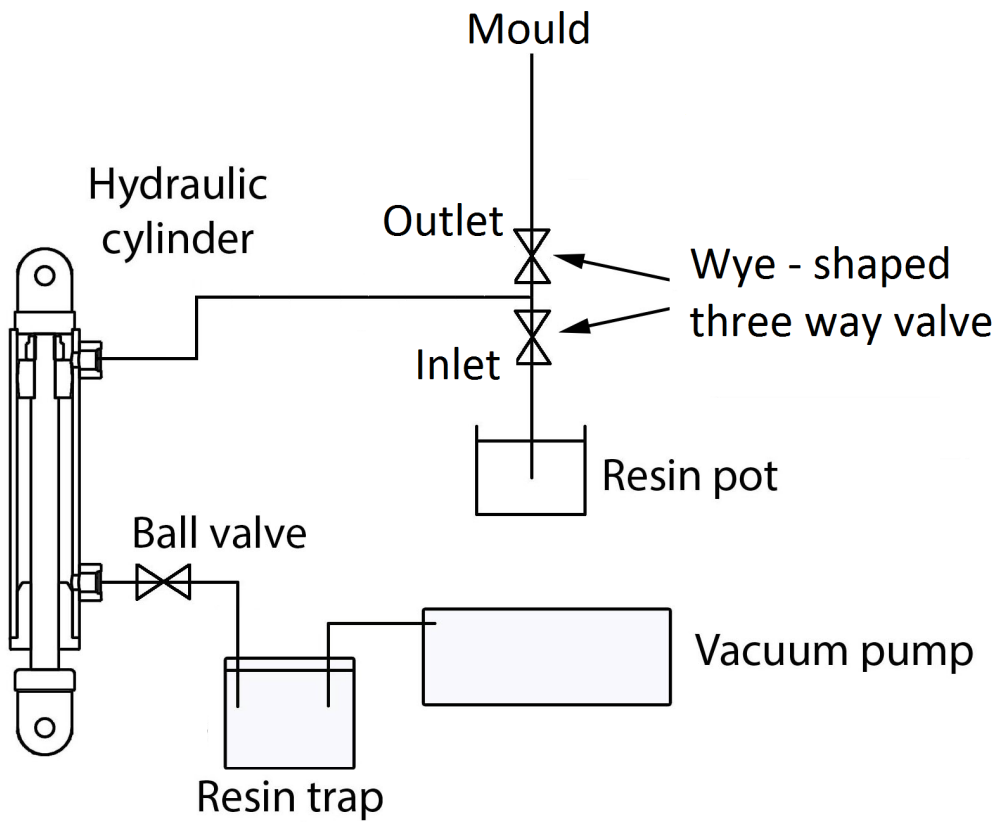


Figure 3.31: Diagram of resin injection apparatus

A GAST Manufacturing DAA-V715A-EB vacuum pump with a $\frac{1}{4}$ hp motor capable of drawing a vacuum of 0.97 atm was connected to a resin trap through vacuum rated tubing. The resin trap was a sealed acrylic cylinder containing a 750 ml removable reservoir and three ports, an inlet, outlet and a safety valve. The outlet was connected to the vacuum rated tube from the vacuum pump with a brass $\frac{1}{4}$" MNPT (male National Pipe Thread) to 9.5 mm ($\frac{3}{8}$") barbed fitting secured with a hose clamp. Barbed fittings throughout the system were secured to tubing using hose clamps. The safety port was a ball valve that may be opened to allow atmospheric air into the system as a safety feature. The inlet was connected to high pressure PVC tubing through a brass $\frac{1}{4}$" MNPT to 9.5 mm ($\frac{3}{8}$") barbed fitting and secured with a hose clamp. The polyester braid reinforced tubing had an internal diameter of 9.5 mm and outer diameter of 15.9 mm and rated for pressures up to 1.9 MPa at 21°C. The high pressure tubing was used throughout the injection apparatus and mould outlets.

The other end of the PVC tubing was connected to a $\frac{1}{2}$" brass ball valve through a brass $\frac{1}{2}$" MNPT to 9.5 mm ($\frac{3}{8}$") barbed fitting. The connections on both ends of the brass ball valve were $\frac{1}{2}$" FNPT (female National Pipe Thread) ports and the valve was rated for maximum pressure up to 4.1 MPa at 38°C. As with fittings assembled throughout the system, $\frac{1}{2}$" wide commercial grade PTFE thread sealant was wrapped 4-5 revolutions around male threads to ensure a proper seal. Another brass $\frac{1}{2}$" MNPT to 9.5 mm ($\frac{3}{8}$") barbed fitting was used to connect the ball valve to the hydraulic cylinder through PVC tubing to another brass $\frac{1}{2}$" MNPT to 9.5 mm ($\frac{3}{8}$") barbed fitting.

A Kinecor AGU cylinder with a Ø76.2 mm (3") bore and 203.2 mm (8") stroke was used for imparting flow to the resin. The three ports on the hydraulic cylinder were $\frac{1}{2}$" FNPT fittings; one was located on the rod end of the cylinder, and the others on the opposite end. Only the two ports were connected as the other was not needed and left open. The remaining port was attached to a length of PVC tubing with a $\frac{1}{2}$" MNPT to 9.5 mm ($\frac{3}{8}$") barbed fitting. The cylinder was set into a 4482 Instron universal testing frame with the end of the cylinder with two ports attached to a 100kN load cell and the other end attached to the bottom frame. Small aluminium blocks were placed between the cylinder pin adaptors and the cylinder, circles in red in Figure 3.32 , to prevent rotation of the cylinder during infusion

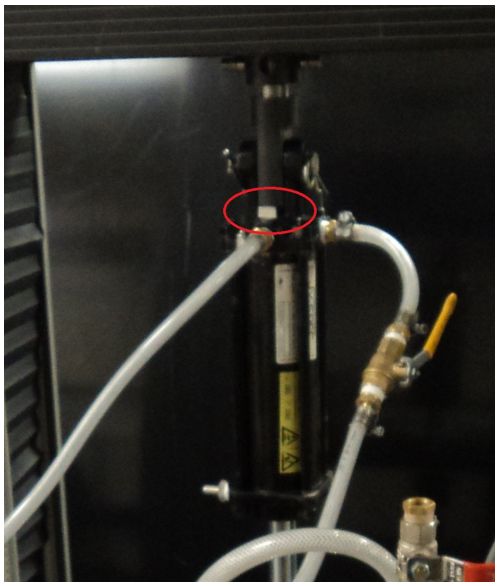


Figure 3.32: Aluminium blocks used for stopping cylinder rotation

PVC tubing leaving the cylinder was attached to the open port of a brass three-way wye valve through a brass $\frac{1}{4}$" MNPT to 9.5 mm ($\frac{3}{8}$") barbed fitting and a brass $\frac{1}{4}$" FNPT to 1" MNPT bushing. The open port of the valve had a 1" FNPT port, hence the need for the bushing. The valve had a maximum pressure rating of 4.14 MPa at 93°C. The two other ports on the valve were $\frac{3}{4}$" MNPT and were both connected to $\frac{3}{4}$" FNPT to $\frac{3}{8}$" barbed fittings and PVC tubing. These exit ports were could opened and closed independently. One length of tubing was submerged into the resin pot and was considered the inlet port, whereas the other length of tubing was connected to the mould through a $\frac{1}{4}$" MNPT to $\frac{3}{8}$" barbed fitting and was considered the outlet port.

The outlet ports of the moulds were all lengths of PVC tubing connected with $\frac{1}{4}$" MNPT to $\frac{3}{8}$" barbed fittings and remained opened to ambient air. All of the valves, fittings, tubing and sealant tape were sourced from McMaster-Carr and the hydraulic cylinder sourced from Wajax Ottawa.

3.1.2.6 Resin Injection Procedure

With the apparatus set up as shown in Figure 3.30, and the cylinder extended 1150 mm from its fully retracted position to create a reservoir for the resin, the PC used to control the Instron testing frame was accessed. Using Bluehill 2 software, a testing method was created to control the flow rate of the resin. The software controlled the crosshead speed of the testing frame as well as distance and load limit restrictions. The method used a compressive test method with a vertical displacement limit of 1100 mm and load limit of 7 kN. The vertical displacent was limited to 1100 mm to ensure that the cylinder would not retract fully with continued displacement. The 7 kN maximum load corresponds to a maximum theoretical pressure of 1.53 MPa, which is a conservative estimate since it assumes that the cylinder is frictionless. The imposed flow rate q is a function of the Instron testing frame crosshead speed s_c and of the cylinder geometry:

$$q = s_c \cdot A_{cyl} \tag{3.5}$$

where A_{cyl} is the internal cross-sectional area of the cylinder. To determine the crosshead speed required, Equation 3.5 was rearranged to find:

$$s_c = \frac{q}{A_{cyl}} = \frac{q}{\frac{\pi}{4} \cdot D_{cyl}^2} \tag{3.6}$$

where D_{cyl} is the diameter of the cylinder. A flow rate of 0.1 $\frac{\text{cc}}{\text{s}}$ commonly chosen for injections in this thesis work, required a crosshead speed of 1.32 $\frac{\text{mm}}{\text{min}}$ based on the cylinder inner diameter of 76.2 mm. The injection method was set to record force and displacement of the crosshead in 10 times per second until the injection ended, based on software load or distance limits or else by manually stopping the machine. Load and displacement values were balanced to zero prior to each injection.

A partial vacuum was initially drawn in the system with the inlet and outlet of the three way wye valve closed and the ball valve open. To ensure that no leakage was present, the vacuum pump was left to run for over ten minutes and then stopped. If the pressure gauge on the vacuum pump showed a pressure decrease over the following few hours, the system was checked and reassembled until the system held an appropriate vacuum.

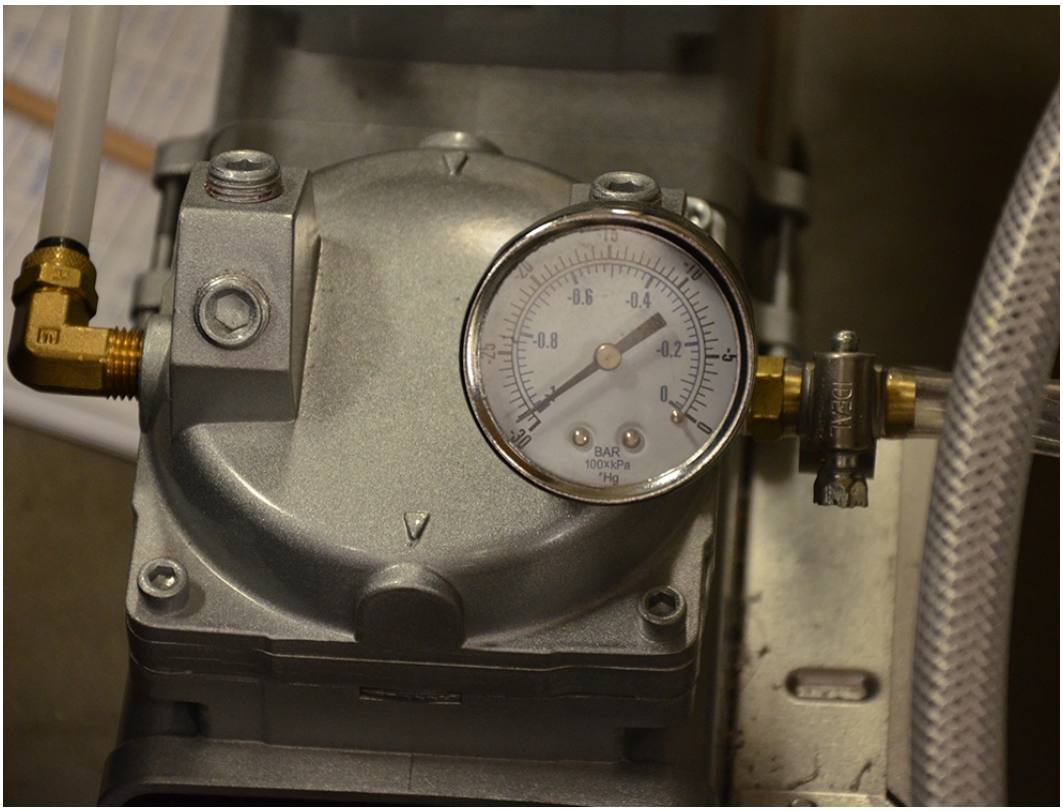


Figure 3.33: Vacuum pump gauge readout at steady state

Resin was mixed in a mould released stainless steel container according to the resin's manufacturer specifications at a ratio of 100 parts resin to 34 parts hardener by weight. On average the total amount of resin mixed was between 1000 g and 1200 g of epoxy. The resin was mixed using an electric drill and paint mixer fitting for a minimum of three minutes until the epoxy mixture looked homogenous. The time at which the resin was mixed was recorded to monitor the resin working time.

With vacuum drawn in the system, the resin inlet tube was submerged in the resin pot, Figure 3.34. The resin inlet side of the three-way valve was opened sufficiently enough to allow resin to flow into the system. Once the resin flow front was beyond the three-way valve, the valve was closed for four to five minutes to allow any air that entered through the open end of the tube to be drawn out. The same inlet valve was opened again to allow resin to fill the cylinder and tubing. When the resin flow continued beyond the ball valve on the vacuum side of the cylinder, the three-way inlet valve and the ball valve were both closed.

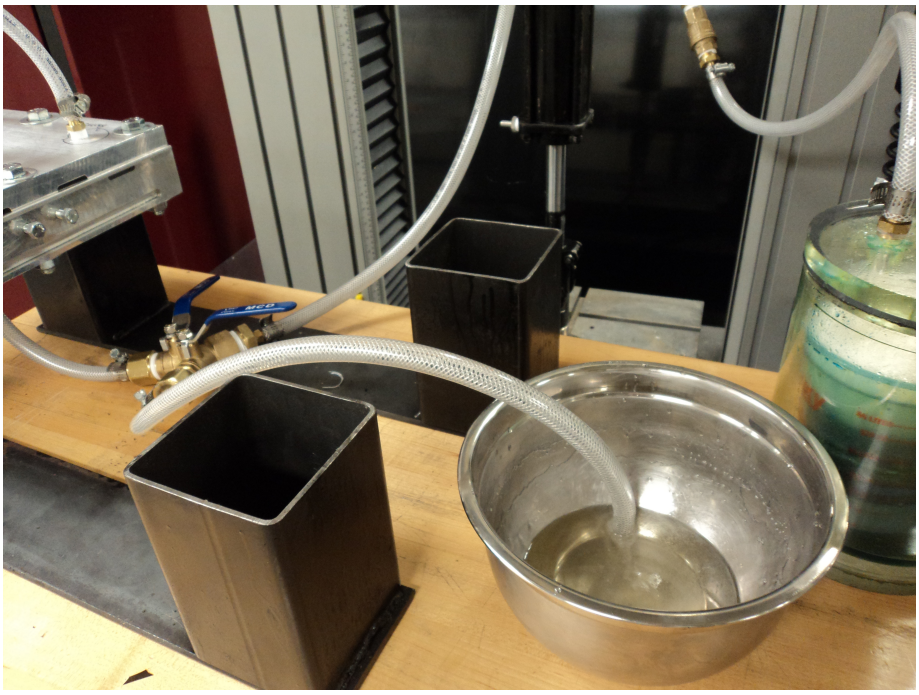


Figure 3.34: Stainless steel resin pot and injection apparatus

The Instron testing frame was initiated and the outlet valve on the three way wye valve was opened simultaneously. The cylinder began to retract and pump epoxy into the mould at the imposed flow rate, Figure 3.35.

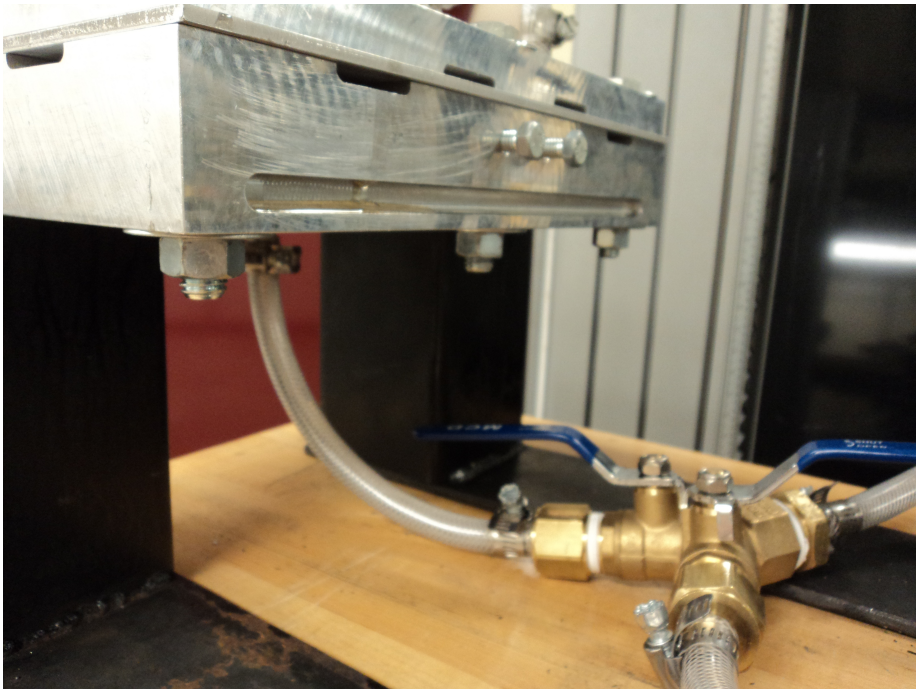


Figure 3.35: Mould inlet tube from three way wye valve

Each outlet port was closed successively after resin flowed 10 to 15 cm beyond the brass associated fitting, until there was a lone open outlet port where the resin was permitted run out until the end of the injection. After the injection was complete the software program was stopped, the outlet valve on the three way wye valve was shut and tubing at the mould inlet was also pinched shut using a c-clamp. With the mould outlets and inlets pinched off, the inlet tube between the wye outlet valve and mould inlet was separated from the injection apparatus. The mould was placed inside an 80 ^{o}C preheated oven for the specified cure time of eight hours.



Figure 3.36: Sealed moulds during oven cure cycle

Resin remaining inside the cylinder was carefully purged by retracting the cylinder to it's initial position using the Instron testing frame while the three way wye outlet valve was closed and the three way wye inlet valve was open to the resin pot. It was important to purge any large volume of uncured resin left within the cylinder to avoid heat-related problems from the exothermic cure reaction.

The bolts holding the mould together were removed and the mould opened after the component had cured and the mould had cooled. The components were demoulded using plastic wedges to avoid any damage to the component or polished mould surface. A hydraulic ram with a Ø19 mm aluminum extension rod was used to remove the inner

mould from the IRP after injection, Figure 3.37. Excess resin from the inlet, outlets and around the edges of the components were trimmed using a utility knife to their final desired shape.



Figure 3.37: Removal of inner mould piece using hydraulic ram, IRP3

3.2 Mechanical Testing

The flat PMC plates were subjected to an array of mechanical tests aimed at documenting their structural behaviour, and to build a first baseline of mechanical properties for plates built from preforms made at the University of Ottawa. The tests conducted in

the context of this thesis were: 1) long span four-point bending tests for determining flexural properties, 2) short span three-point bending tests for determining interlaminar properties and more specifically short beam interlaminar shear strength, and 3) drop-weight impact tests for determining impact resistance.

Details for each test are presented in separate sections. Each test required that specimens of specific dimensions be cut from the same plates so as to quantify the properties as well as their variability between specimen within a single component. Each 320 mm square plate was cut so as to obtain six long span four-point bending specimens, six short span three-point bending specimens, one impact sample and two specimens for optical microscopy characterization. Three of the long span and short span specimens were cut at 90^{o} to the other three to enable testing along both principal directions. Also, the plates were cut such that some specimens were taken near the resin inlet, others near the plate edges, and others yet were taken between these locations to examine any possible effects related to mould filling or general sample location. The cutting pattern shown in Figure 3.38 was used in obtaining all specimens required for mechanical testing of the flat PMC plates. All specimens were cut using a 16" Walker - Turner 3311 vertical band saw with a 13 mm ($\frac{1}{2}$"), 14 tpi fine toothed blade at approximately 2000 surface feet per minute. Sample edges were sanded to smooth out any rough edges resulting from cutting. Visual inspection of the sanded edges showed that the specimens were not damaged by the cutting operation.

The specimen naming convention was chosen as Ax_By, where A represents specimen type: P for flat plate or IRP for integral reinforced panel; and B represents the test for which said sample was used: LSB for long span four-point bending, SSB for short span three-point bending, IMP for impact testing and MIC for optical microscopy. For example, P2_SSB3 represents the third short span three-point bending sample from the 2nd flat plate.

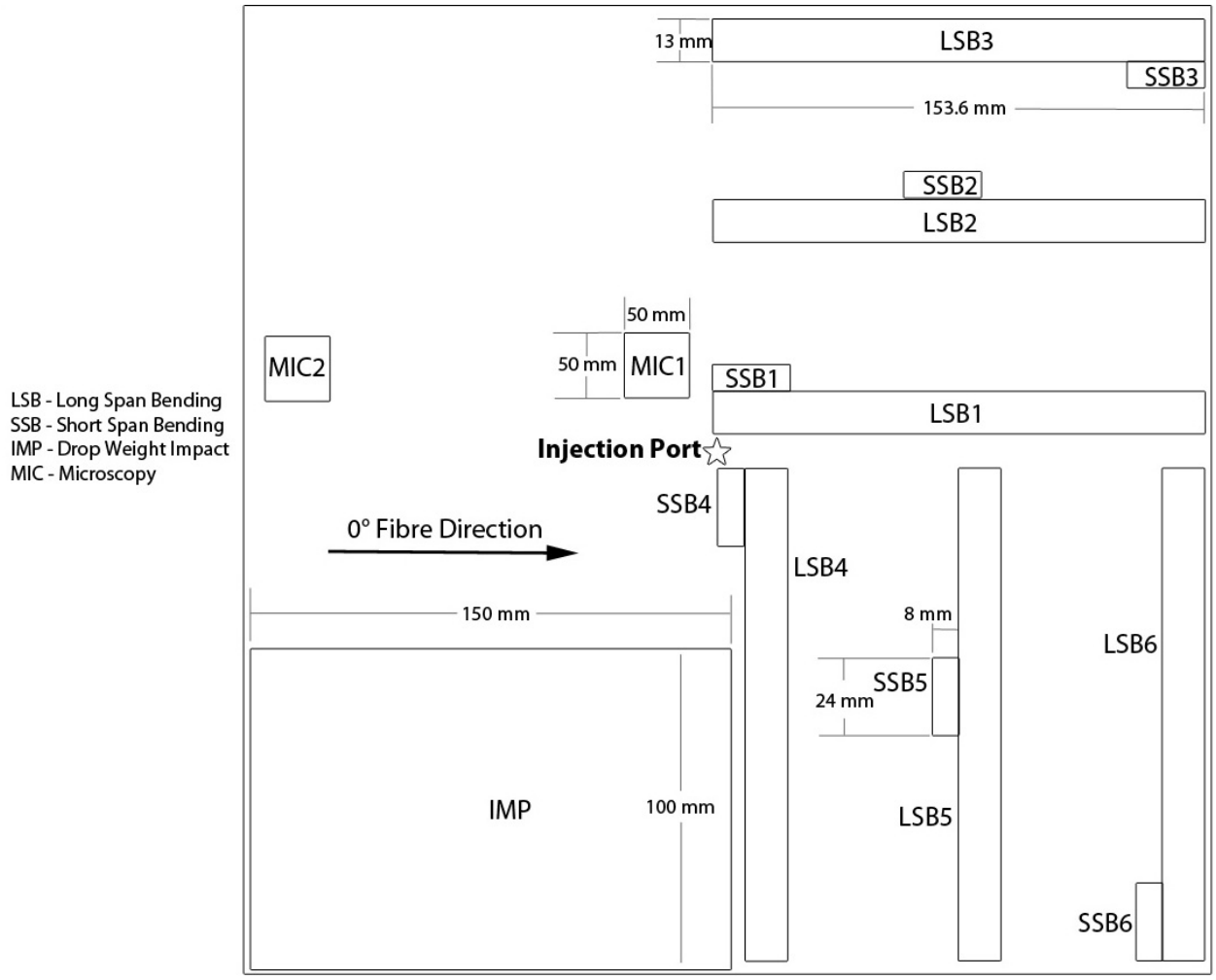


Figure 3.38: 320 mm square plate cutting plan

3.2.1 Long Span Four-Point Bending Tests

Testing for flexural properties was completed using a long span four-point bending test apparatus mounted on a Instron 4482 universal testing frame controlled by a PC running Bluehill 2 software. Testing configuration appears in Figure 3.39.

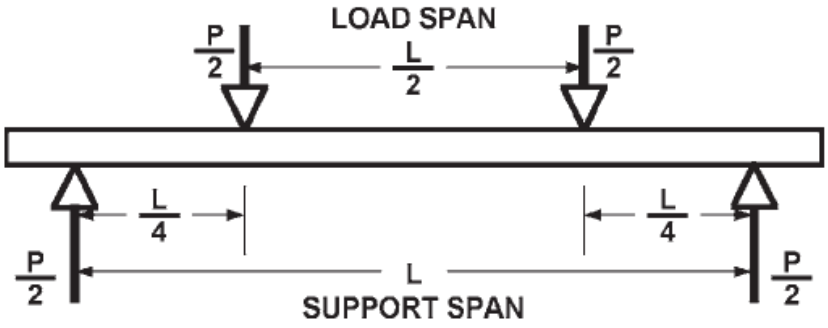


Figure 3.39: Four-point bending test setup [66]

Four-point bending was chosen since it applies a constant bending moment between the central loading noses, as opposed to a maximum moment under the loading nose in three-point bending. Specimen dimensions and test methods consistent with ASTM standard test method D7264/D7264M-07 Flexural Properties of Polymer Matrix Composite Materials[66] were followed. A span to thickness ratio of 32:1 based on the ASTM standard translated to target support span and load span of 128 mm and 64 mm respectively. Also based on the ASTM standard, specimen of nominal size with dimensions 156.3 mm x 13 mm x 4 mm were tested, with three specimens cut along the reference 0^o direction and three cut along the 90^o direction from each of all six plates. Actual specimen width and thickness were measured at three locations using a digital micrometer accurate to 0.001 mm, and averages were recorded. Sample length was also measured using digital callipers accurate to 0.01 mm. Actual support and load spans were measured to the nearest 0.01 mm and recorded. Support and loading noses all featured 3 mm radii. The crosshead of the Instron frame was lowered at 1 $\frac{\text{mm}}{\text{min}}$ until specimen failure. In four-point bending, displacement values recorded by the Bluehill software do not correspond to midspan deflection; instead they represent the displacement of the loading noses. Therefore, an Instron 2663 Advanced Non-contacting Video Extensometer (AVE) with a 200 mm field of view was used, Figure 3.40. The AVE tracks the relative motion of white markers at an accuracy of 0.5% of the reading[67] or approximately 0.05 mm and records the motion as a strain based on the initial distance between the markers, or AVE gauge length. A stationary 2 mm diameter white marker was positioned on a

separate standing device approximately 10 mm directly above the midspan of the test specimen where another 2 mm white marker was placed, Figure 3.41. Gauge length was measured using the calibrated AVE.

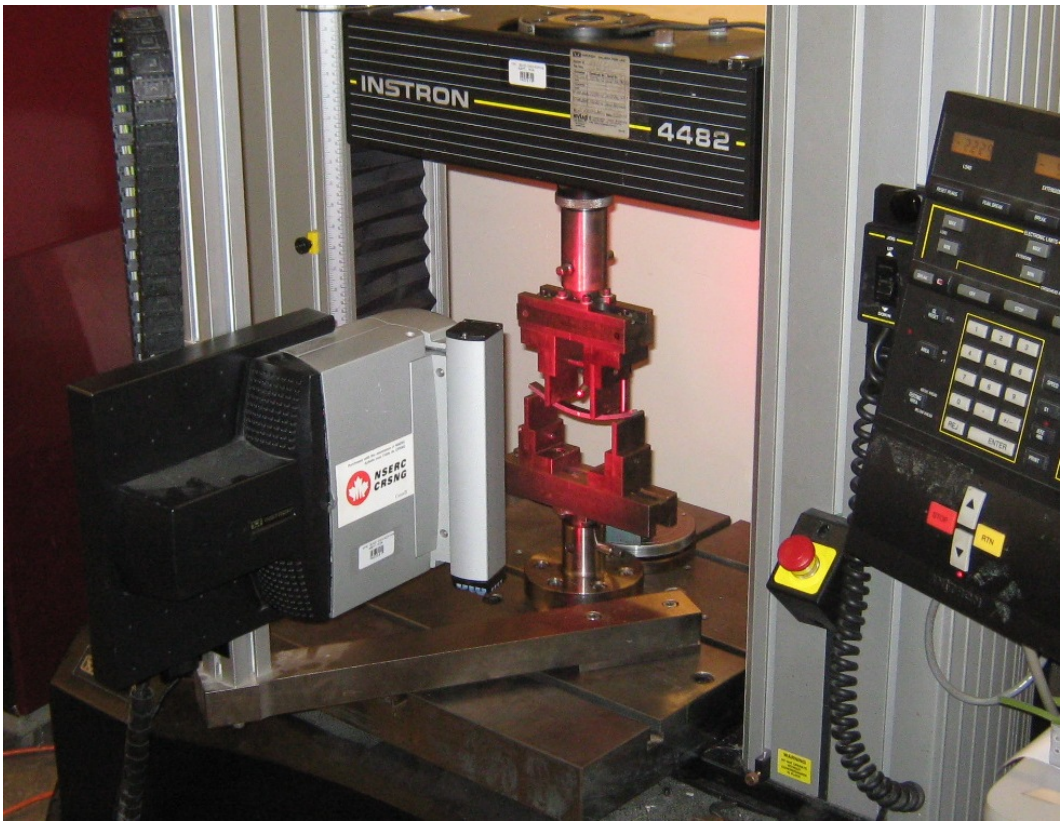


Figure 3.40: Advanced video extensometer set-up

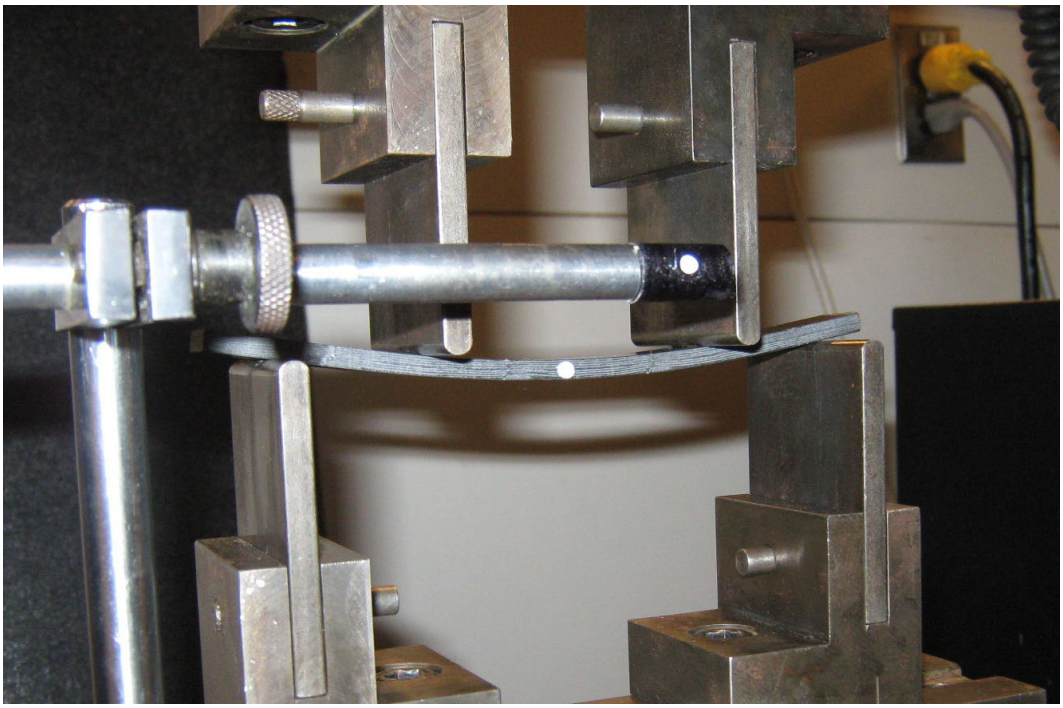


Figure 3.41: Four-point flexural test apparatus

Load, displacement of loading noses, AVE strain output and time were recorded by the Bluehill software every 0.1 s. Failure was considered to have occurred when a 20% decrease in load was recorded between two consecutive data points, or when significant damage was visible on the specimen.

Specimens were inserted normal to and centred on the support noses. Loading noses were lowered until contact with the upper surface of the specimen was detected using the force readout. Load and displacement were reset to zero and the test was launched via software. Failure modes and other visual and audio observations were recorded manually along with corresponding elapsed time.

The load, AVE strain and AVE gauge length data was used in generating load-deflection curves for each specimen. The midpoint deflection δ_m was calculated using Equation 3.7,

$$\delta_m = \epsilon_{AVE} \cdot l_{ga} \tag{3.7}$$

where ϵ_{AVE} is the AVE strain and l_{ga} the AVE gauge length. The load-deflection curve from specimen P1_LSB1 is shown in Figure 3.42.

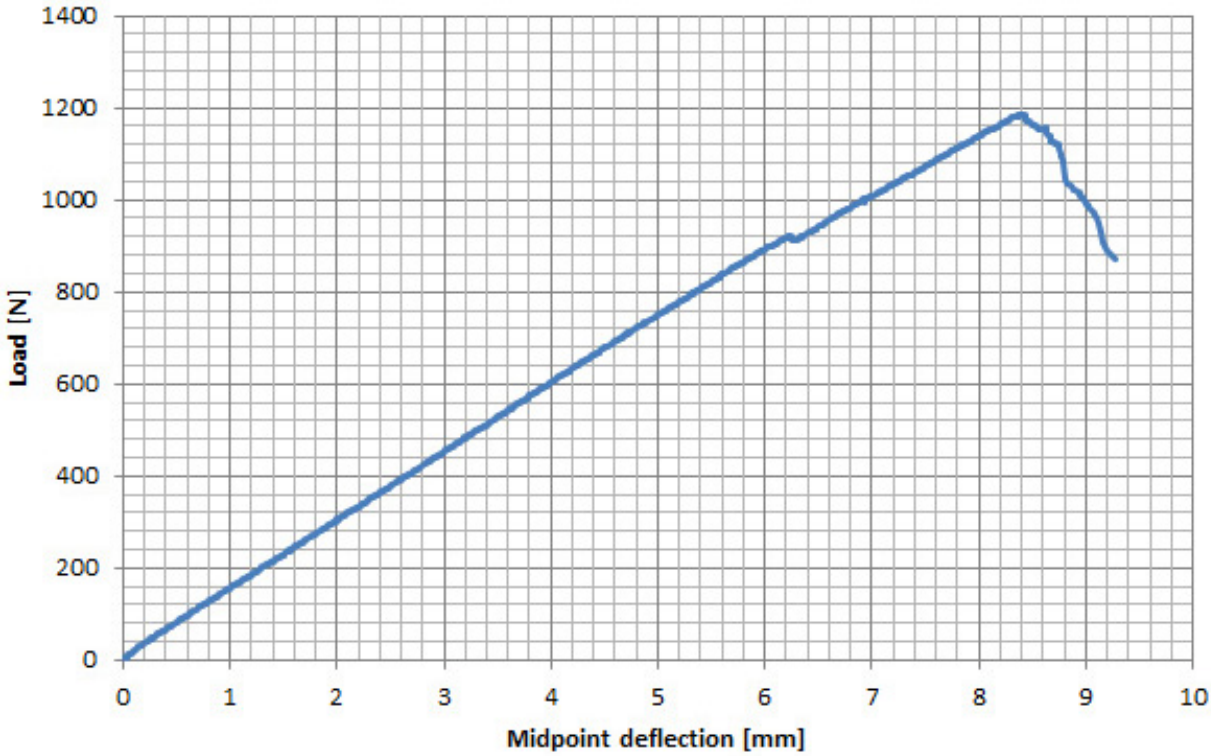


Figure 3.42: Load-deflection curve from long span four-point bending test of specimen P1_LSB1

The outer flexural stress σ_F ,which is the normal stress at the outer surfaces within the load span region, was calculated from any point on the load-deflection curve using Equation 3.8[66]:

$$\sigma_F = \frac{3FL_{ls}}{4b_{ls}t^2} \tag{3.8}$$

where F is the applied force from the loading noses, L_{ls} is the support span, b_{ls} is the width of the specimen and t is the thickness of the specimen.

Flexural strain at the outer surface ϵ_F occurs at mid-span and can be calculated using Equation 3.9 [66]:

$$\epsilon_F = \frac{4.36 \cdot \delta_m \cdot t}{L_{ls}^2} \tag{3.9}$$

Stress-strain curves were generated from the outer flexural stress and flexural strain obtained from all data points throughout the test. The stress-strain curve from specimen P1_LSB1 is shown in Figure 3.43.

The flexural strength of the specimen is equal to the maximum stress corresponding

to the peak force during the test, shown by the green circle in Figure 3.43. However, it is also important to note that prior to experiencing the maximum load, slight damage was imparted on the specimen corresponding to the step in the curve shown by the red circle in Figure 3.43; and this latter stress level is referred to as the first failure stress of the specimen. Results from long span four-point bending tests are discussed in Section 4.2.1.

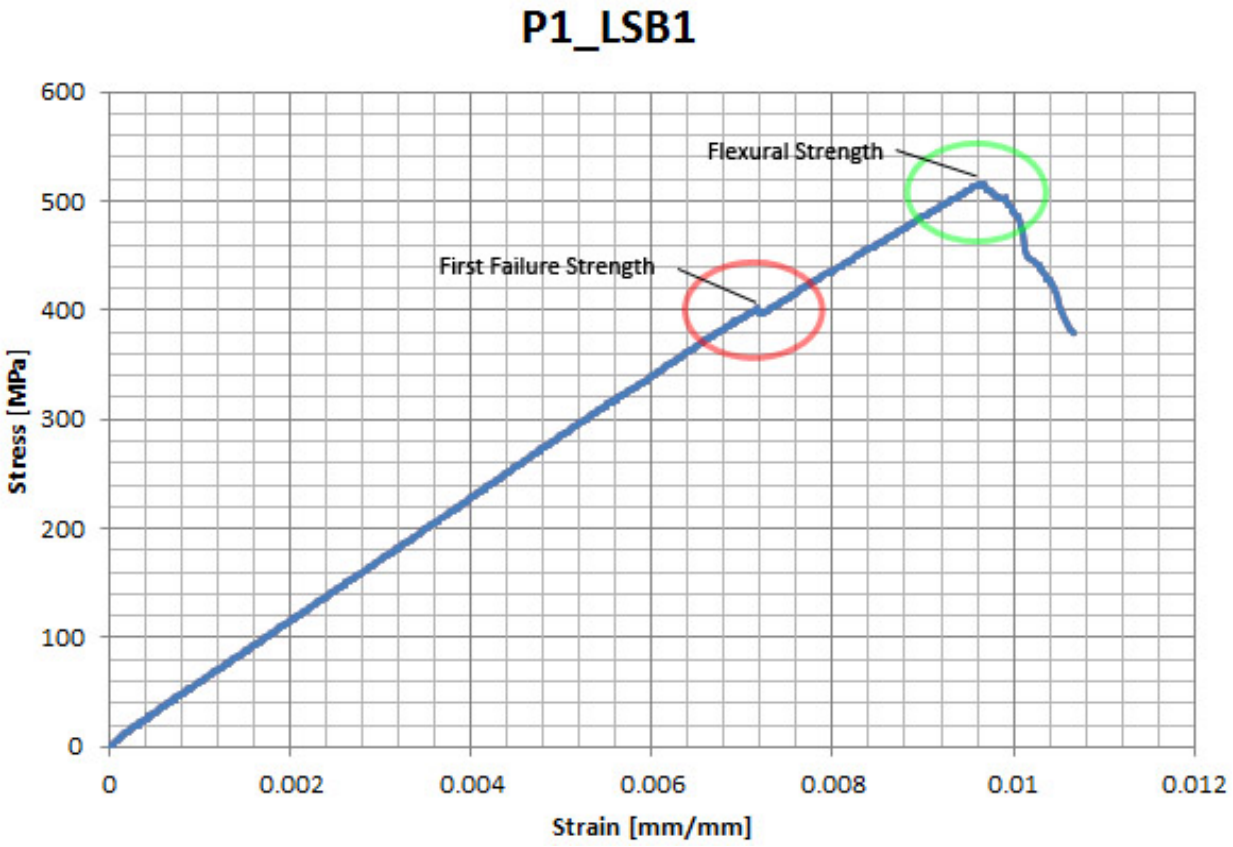


Figure 3.43: Stress-strain curve from long span four-point bending test of specimen P1_LSB1

For calculating flexural strength S_F and first failure strength S_{Ff} of the specimens, Equation 3.8 becomes:

$$S_F = \frac{3 \cdot F_{max} \cdot L_{ls}}{4 \cdot b_{ls} \cdot t^2} \tag{3.10}$$

and

$$S_{Ff} = \frac{3 \cdot F_f \cdot L_{ls}}{4 \cdot b_{ls} \cdot t^2} \tag{3.11}$$

where F_{max} is the peak force and F_f is the force recorded when first failure occurs. Values

for specimen P1_LSB1:

$$\begin{aligned} S_F &= \frac{3 \cdot F_{max} \cdot L_{ls}}{4 \cdot b_{ls} \cdot t^2} & S_{Ff} &= \frac{3 \cdot F_f \cdot L_{ls}}{4 \cdot b_{ls} \cdot t^2} \\ S_F &= \frac{3 \cdot 1186.6\,\mathrm{N} \cdot 127.6\,\mathrm{mm}}{4 \cdot 11.93\,\mathrm{mm} \cdot (4.29\,\mathrm{mm})^2} & S_{Ff} &= \frac{3 \cdot 923.5\,\mathrm{N} \cdot 127.6\,\mathrm{mm}}{4 \cdot 11.93\,\mathrm{mm} \cdot (4.29\,\mathrm{mm})^2} \\ S_F &= 516.3\,\mathrm{MPa} & S_{Ff} &= 401.8\,\mathrm{MPa} \end{aligned} \tag{3.12}$$

The flexural modulus of elasticity, E_F was calculated using Equation 3.13 over the ASTM standard recommended strain range of 0.002, spanning from 0.001 to 0.003[66].

$$E_F = \frac{\Delta\sigma_F}{\Delta\epsilon_F} \tag{3.13}$$

For specimen P1_LSB1, the flexural modulus of elasticity was calculated as follows:

$$E_F = \frac{\Delta\sigma_F}{\Delta\epsilon_F} = \frac{\sigma_{F_{0.003}} - \sigma_{F_{0.001}}}{\Delta\epsilon_F} = \frac{171.7\,\mathrm{MPa} - 59.6\,\mathrm{MPa}}{0.003\,\frac{\mathrm{mm}}{\mathrm{mm}} - 0.001\,\frac{\mathrm{mm}}{\mathrm{mm}}} = 56.1\,\mathrm{MPa} \tag{3.14}$$

Post-test visual analyses were completed in order to classify failure of specimens. Failure mode, failure area and failure location were recorded towards classification. Failure mode refers to how the specimen failed, namely in tension, compression, buckling, interlaminar shear or through a combination of different modes. Failure area refers to where the failure occurred within the sample with respect to the testing apparatus, namely at the loading noses, between the loading noses, at support noses or between loading and support noses. Failure location refers to where specimen failure occurred with respect to the specimen; top, bottom, left, right, middle or various locations. Failure identification codes were used as shown in Table 3.3

Table 3.3: Flexural test specimen failure identification codes [66]

First Character		Second Character		Third Character	
Failure Mode	Code	Failure Area	Code	Failure Location	Code
Tension	T	At loading nose	A	Top	T
Compression	C	Between loading noses	B	Bottom	B
Buckling	B	At Support nose	S	Left	L
Interlaminar shear	S	Between load and support nose	L	Right	R
Multi-mode	M(XYZ)			Middle	M
				Various	V(XYZ)

For example, failure identification code for specimen P1_LSB1 was M(TC)-B-V(TB) based on visual observation relating to Figure 3.44.

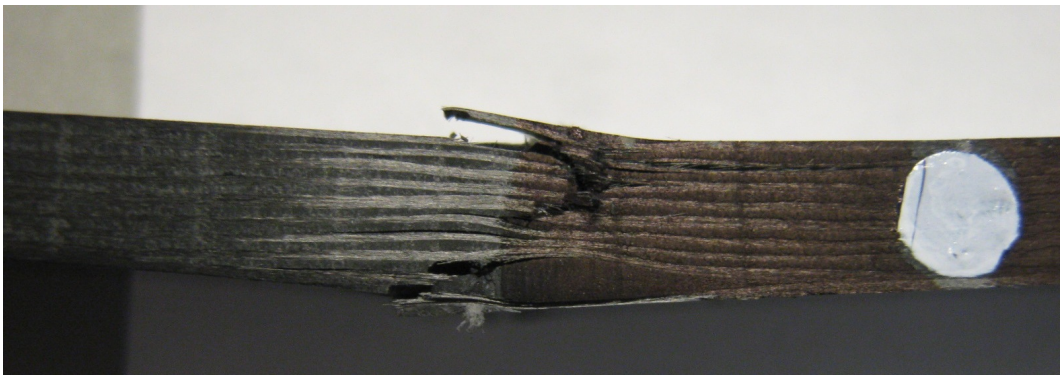


Figure 3.44: Specimen P1_LSB1 post-test image

3.2.2 Short Span Three-Point Bending Tests

Short span three-point bending tests were conducted towards describing short beam properties of the PMC flat plates indicative of their response to interlaminar in plane shear. Using ASTM standard test method D2344/2344M - 00 Short Beam Strength of Polymer Matrix Composite Materials and Their Laminates [68] as a guide, test specimens were placed in a three-point bending apparatus mounted on an Instron 4482 testing frame controlled by a PC running Bluehill 2 software. Figure 3.45 shows the testing configuration.

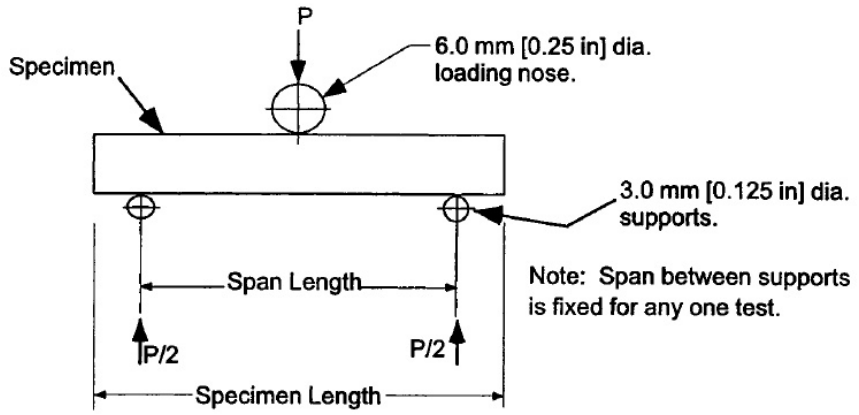


Figure 3.45: Short span three-point bending test setup [68]

The suggested specimen length-to-thickness and width-to-thickness ratios were 6 and 2 respectively based on the ASTM standard. Therefore, with a nominal plate thickness of 4 mm, the specimen dimensions were set to 24 mm x 8 mm x 4 mm, with three specimens cut along the reference 0^{o} direction and three cut along the 90^{o} direction, from each of the six plates. Actual specimen length, width and thickness were measured at three locations using a digital micrometer accurate to 0.001 mm, and averages were recorded. The recommended support span to measured average specimen thickness ratio of 4:1 set the support span at 17.2 mm. Actual support span was measured to the nearest 0.01 mm and recorded. The loading nose featured a 3 mm radius whereas support noses featured 1.5mm radii. Crosshead speed was set to 1 $\frac{\text{mm}}{\text{min}}$ and the test was stopped after any of the following situations: a load drop-off of 30% was detected, specimen fractured into two pieces or the crosshead travel exceeded the specimen nominal thickness of 4 mm.

Specimens were inserted such that their longitudinal axis was perpendicular to the support and loading noses with the centre of the specimen equidistant to the support noses. Load and displacement displays were set to zero and the test was initiated through software. Load and crosshead displacement data were recorded every 0.1s throughout the test, observations of initial cracking or acoustic emission were also noted.

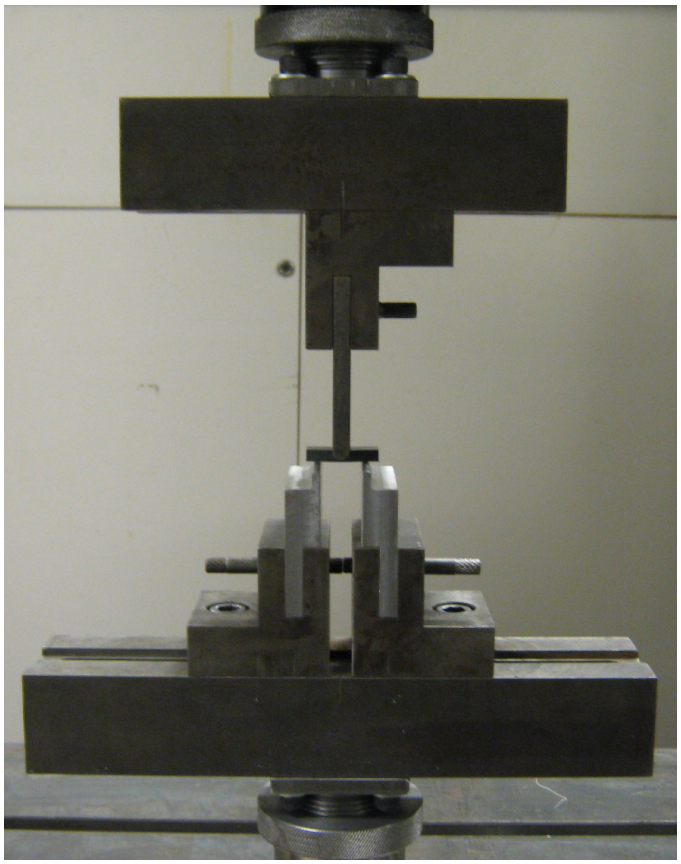


Figure 3.46: Short span three-point bending test apparatus

Load-displacement curves were generated from the data obtained from each test; an example is shown in Figure 3.47 for specimen P1_SSB1.

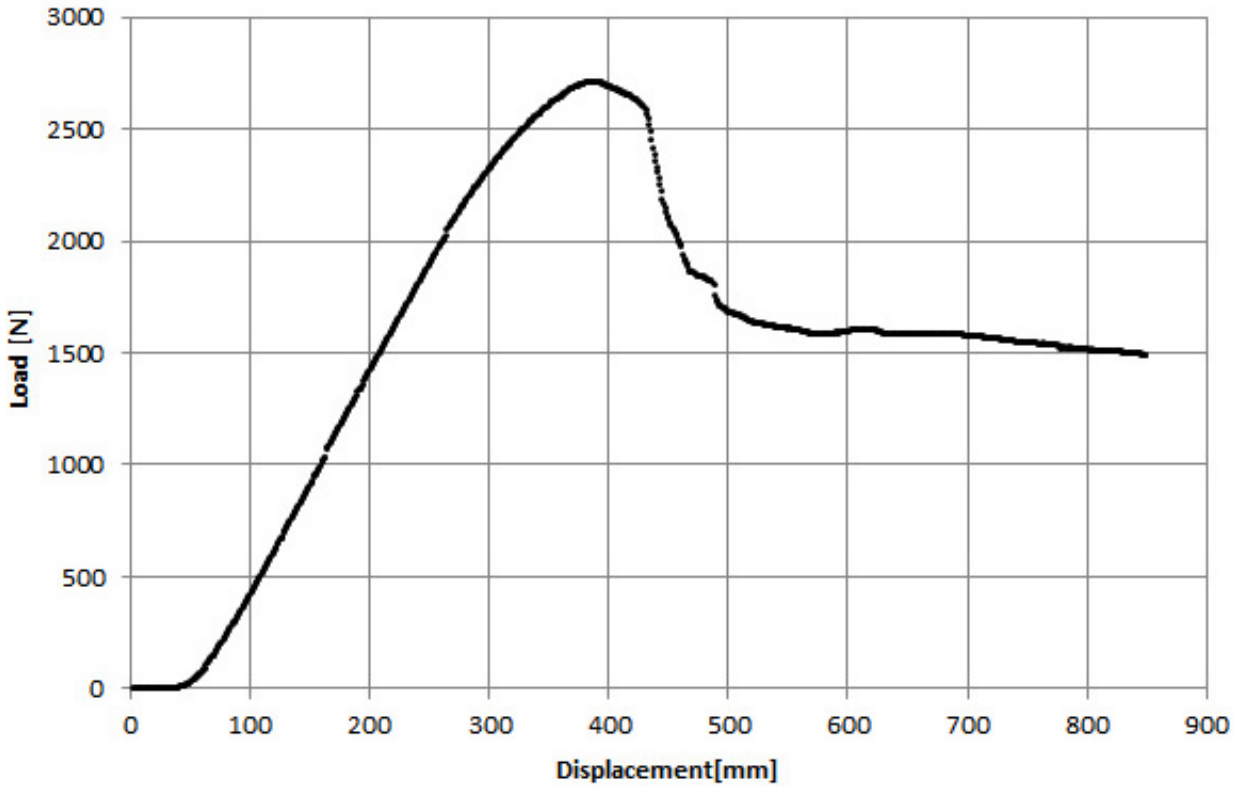


Figure 3.47: Load-displacement curve from short span three-point bending test of specimen P1_SSB1

Short beam shear strength S_{SB} was calculated using Equation 3.15[68]:

$$S_{SB} = 0.75 \cdot \frac{F_{max}}{b_{ss} \cdot t} \tag{3.15}$$

where b_{ss} is the width of the specimen. For example, the short beam shear strength of specimen P1_SSB1 was calculated as follows:

$$S_{SB} = 0.75 \cdot \frac{F_{max}}{b_{ss} \cdot t} = 0.75 \cdot \frac{2714.1\,\mathrm{N}}{8.74\,\mathrm{mm} \cdot 4.37\,\mathrm{mm}} = 53.3\,\mathrm{MPa} \tag{3.16}$$

Possible specimen failure modes were interlaminar shear, compressive/tensile flexure or inelastic deformation as outlined in Figure 3.48. Inelastic deformation refers to failure in which the beam experiences uneven deformation on either side of the support noses and the beam takes an out-of-plane wavy shape.

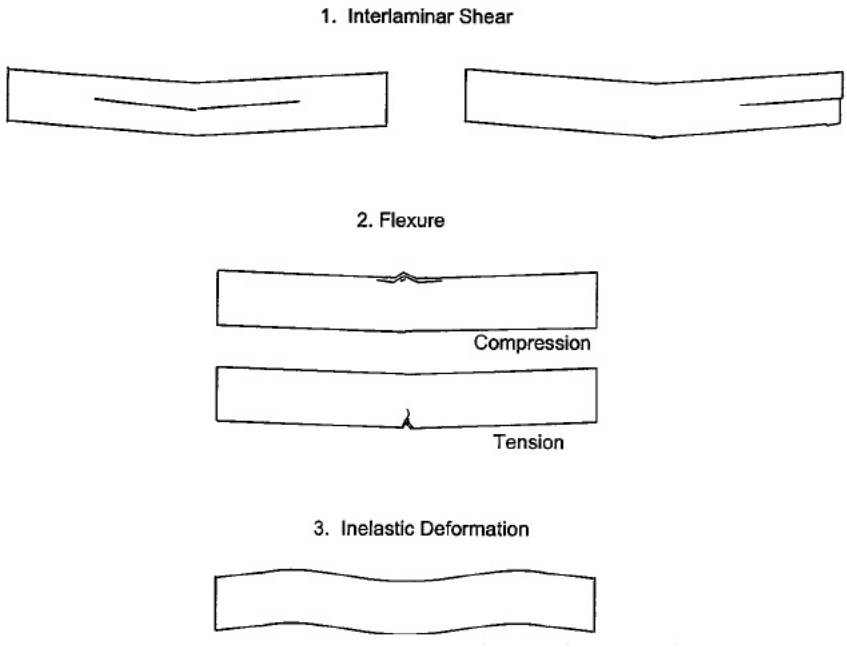


Figure 3.48: Possible short span three-point bending test failure modes[69]

Specimen P1_SSB1 failed in a combination of interlaminar shear and inelastic deformation as shown in Figure 3.49. Interlaminar shear failure can be seen within the red circle whilst the inelastic deformation describes the bent shape on the right side of the loading nose. Short span three-point bending test results will be presented and discussed further in Section 4.2.2.

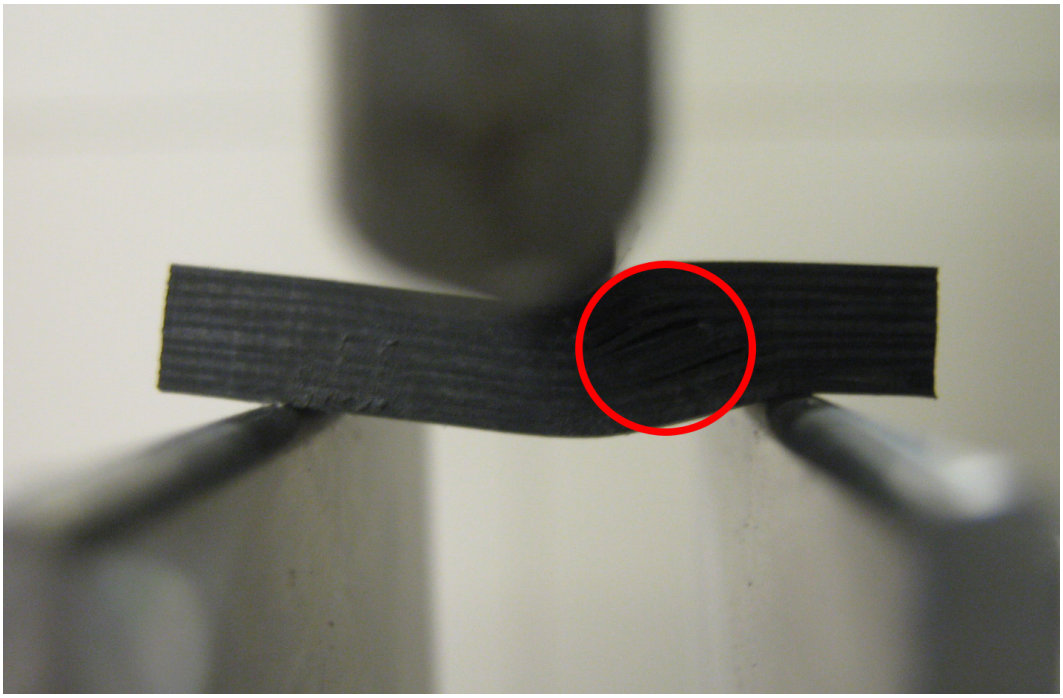


Figure 3.49: Specimen P1_SSB1 post test image

3.2.3 Drop Weight Impact Tests

Drop weight impact testing was conducted to describe the impact damage resistance of the PMC flat plates. ASTM standard test method D7136/D7136M – 07 Measuring the Damage Resistance of a Fiber-Reinforced Polymer Matrix Composite to a Drop-Weight Impact Event [69] was used as guide for specimen testing. Drop-weight impact tests were completed using an Instron 8200 series drop weight impact testing tower equipped with a 22.2 kN (5.0 Kip) capacity Dynatup 8496-1 instrumented strain gauge tup, or load cell, and Impulse data acquisition system. The impact testing tower was located at the NRC in Ottawa, Ontario and operated by NRC staff Richard Desnoyers. Damage was imparted through out-of-plane, concentrated impact from a hemispherical impactor. The drop tower assembly apparatus is shown in Figure 3.50.



Figure 3.50: Instron 8200 series drop weight impact testing tower, NRC Ottawa

The drop head, Figure 3.51 consists of the crosshead, extension bar, tup and impactor. The crosshead was mounted onto vertical tracks to control the drop path. The top end of an extension bar was attached to the bottom of the crosshead and the bottom end connecting to the tup. The impactor was attached to the bottom of the tup and had a smooth 16 mm (0.625”) steel hemispherical striker tip. The total drop head mass, including the crosshead, extension bar, tup and impactor tip was 6.14 kg.

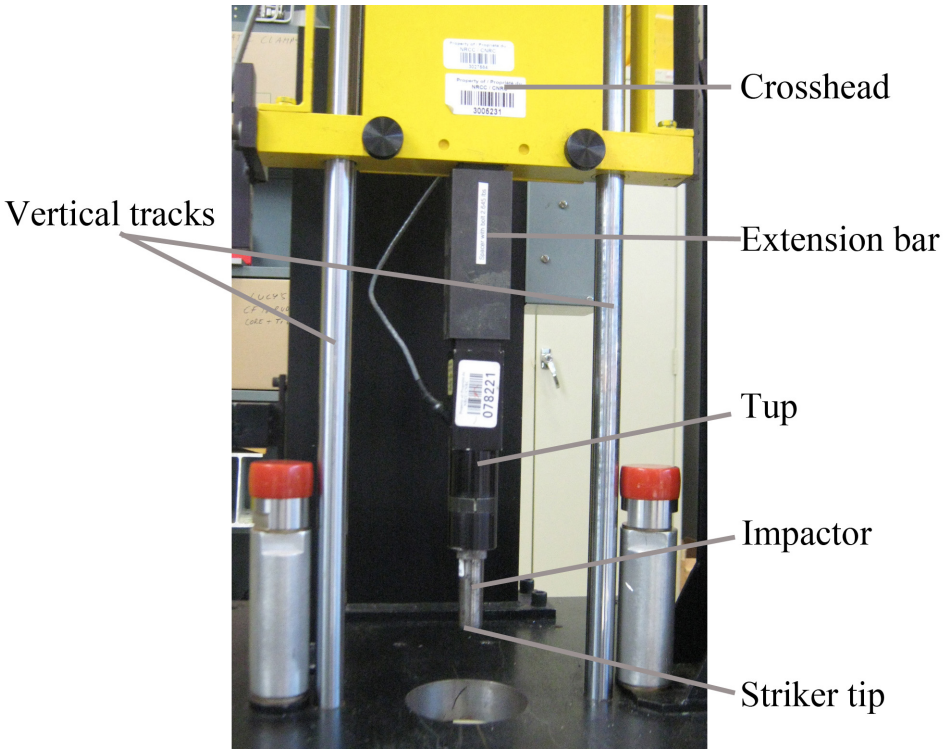


Figure 3.51: Drop head assembly

Test specimens were cut to a nominal size of 150 mm x 100 mm as recommended by the ASTM standard; PMC plates were moulded at a nominal thickness of 4 mm. Actual thicknesses were measured in four locations throughout each specimen using a digital micrometer accurate to 0.001 mm and averages were recorded. Actual lengths and widths were each measured in three locations along each specimen using digital callipers accurate to 0.01 mm and averages were recorded.

Specimens were placed within a 25.4 mm (1") thick support fixture featuring a 125 mm x 75 mm cut-out, shown in Figure 3.52. The specimens were located centrally over the cut-out using guiding pins and held in place with four rubber tipped clamps. The support fixture was mounted securely onto the base of the tower.

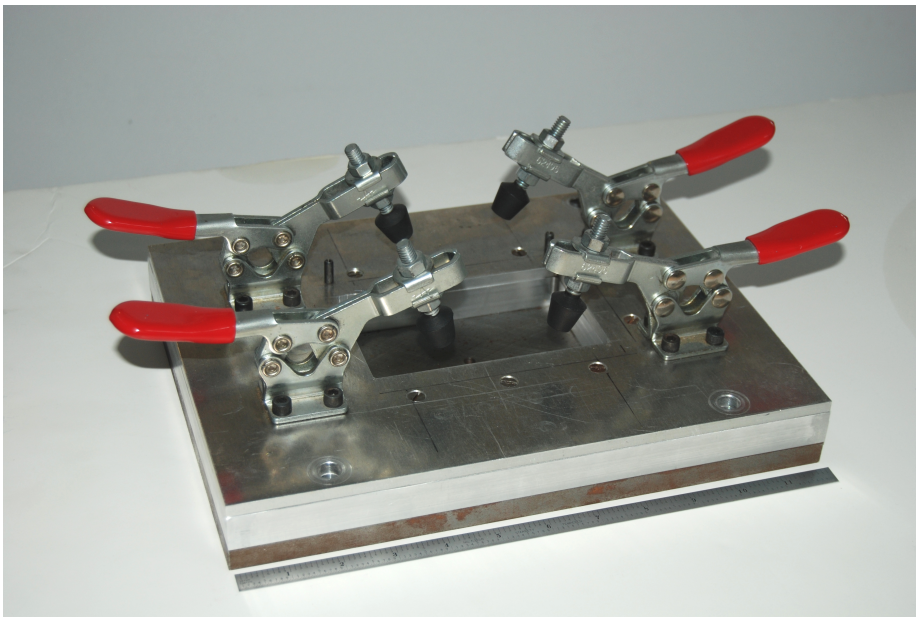


Figure 3.52: Support fixture with clamps

The height from which the impactor was released, called the drop height H was determined from the specified impact energy level E. The specified impact energy level was calculated from the specified ratio of impact energy to specimen thickness C_E using Equation 3.17[69]:

$$E = C_E \cdot t \tag{3.17}$$

From the guidelines set by the ASTM standard, a specified ratio of impact energy to specimen thickness of 6.5 $\frac{J}{mm}$ was used. Therefore the drop height was calculated using Equation3.18:

$$H = \frac{E}{m_{dh} \cdot g} \tag{3.18}$$

where m_{dh} is the mass of the drop head and g is the acceleration due to gravity. The drop height was calculated from the nominal specimen thickness of 4mm using Equations 3.17 and 3.18:

$$E = C_E \cdot t = 6.5 \,\frac{\mathrm{J}}{\mathrm{mm}} \cdot 4 \,\mathrm{mm} = 26 \,\mathrm{J} \tag{3.19}$$

$$H = \frac{E}{m_{dh} \cdot g} = \frac{26 \,\mathrm{J}}{6.14 \,\mathrm{kg} \cdot 9.81 \,\frac{\mathrm{m}}{\mathrm{s}^2}} = 0.43 \,\mathrm{m} \tag{3.20}$$

The drophead was set with the bottom of the impactor tip 0.43 m from the upper

surface of the test specimen. The drop tower was equipped with a catch mechanism to stop any additional contact of the drophead with the specimen after initial impact. This mechanism ensured that the damage imparted on the specimens was exclusive to the initial impact.

The load cell tup and data acquisition system recorded load versus time data every 0.003 ms as well as the instantaneous velocity at the moment of impact. The software used load versus time data along with the instantaneous velocity at the moment of impact to calculate other values such as tup velocity, impact energy and specimen total deflection, which is the deflection at which the load curve returns to zero. Load versus time data for specimen P1_IMP1 is shown in Figure 3.53.

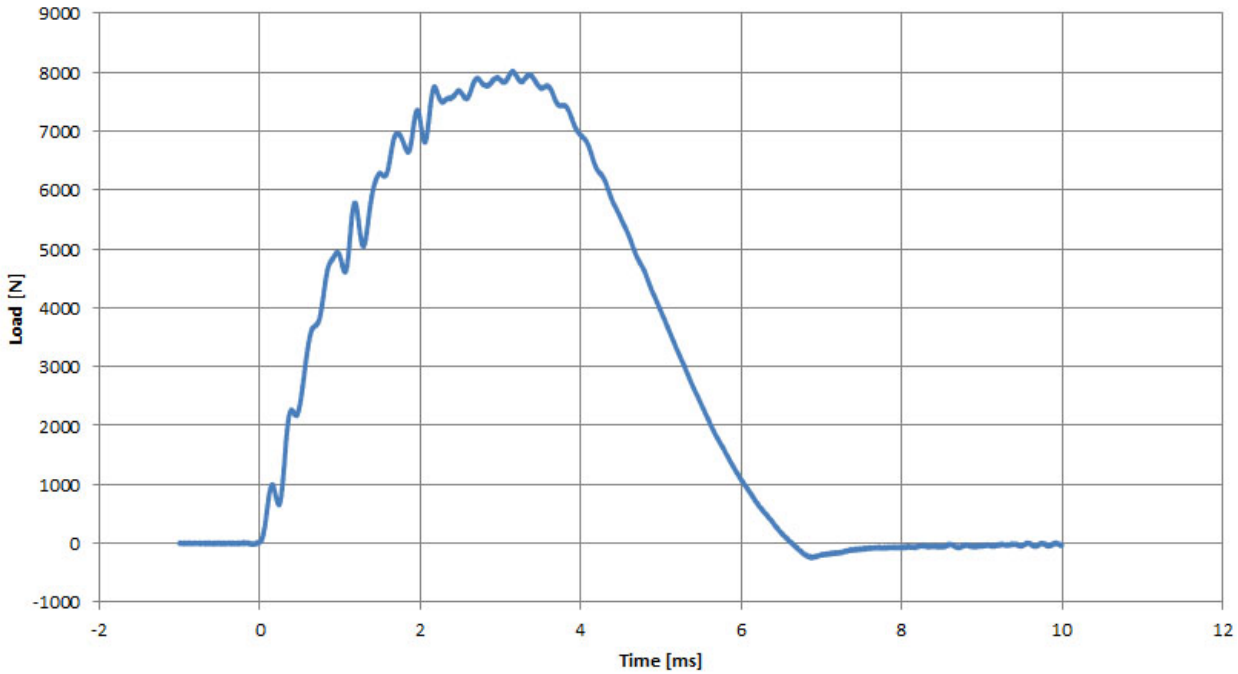


Figure 3.53: Load versus time curve from drop weight impact of specimen P1_IMP1

After the impact event, each specimen was removed from the apparatus and damage was assessed by recording the depth of the dent created by the impactor tip. The dent depth, h_{dent} was measured using a 6.35 mm (1/4") spherical stainless steel ball, two 25.4 mm (1") parallel bars, a Mitutoyo depth micrometer with a 0.0254 mm (0.001") resolution and two other parallel bars whose height was not relevant. The other parallel bars were placed on a flat level surface to raise the specimen above any deformation that

extended through the lower surface of the specimen. The ball was placed into the dent and allowed to settle into its deepest area, and the 25.4 mm parallel bars were placed on the surface undisturbed by the impact and parallel to one another. The depth micrometer was then placed across the bars over the ball and the distance from the upper surfaces of the bars to the top of the ball was measured as shown in Figure 3.54.



Figure 3.54: Dent depth measurement apparatus

To determine the dent depth, the diameter of the ball (6.35 mm) was added and the height of the parallel bars (25.4 mm) was subtracted as shown in Figure 3.55. This method ensured that the deepest measurement of the dent was recorded.

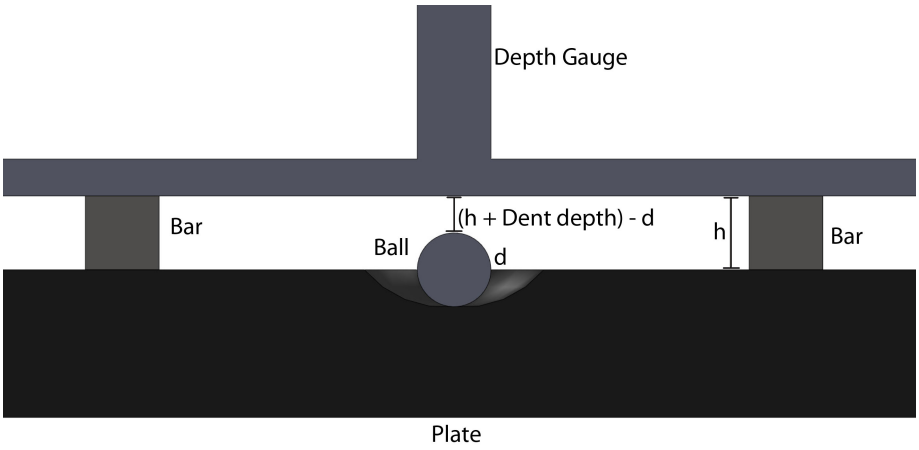


Figure 3.55: Dent depth measurement diagram

Further to the above, the specimen was inspected visually to define and record external damage modes. Possible damage modes experienced were dents/depressions, splits/cracks, delamination, fibre breakage or combinations of modes as shown in Figure 3.56.

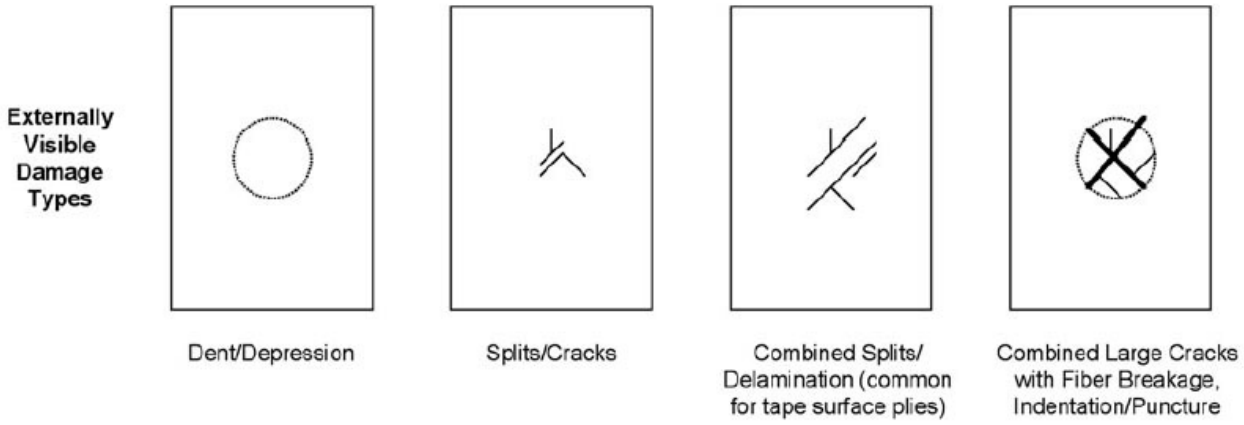


Figure 3.56: Common external damage modes from out-of-plane drop weight impact testing [69]

For example, damage modes experienced by specimen P1_IMP1 were denting with combined splits and delamination based on visual observation, as seen in Figures 3.57 and 3.58. Results from drop weight impact testing are reported and discussed in Section 4.2.3.

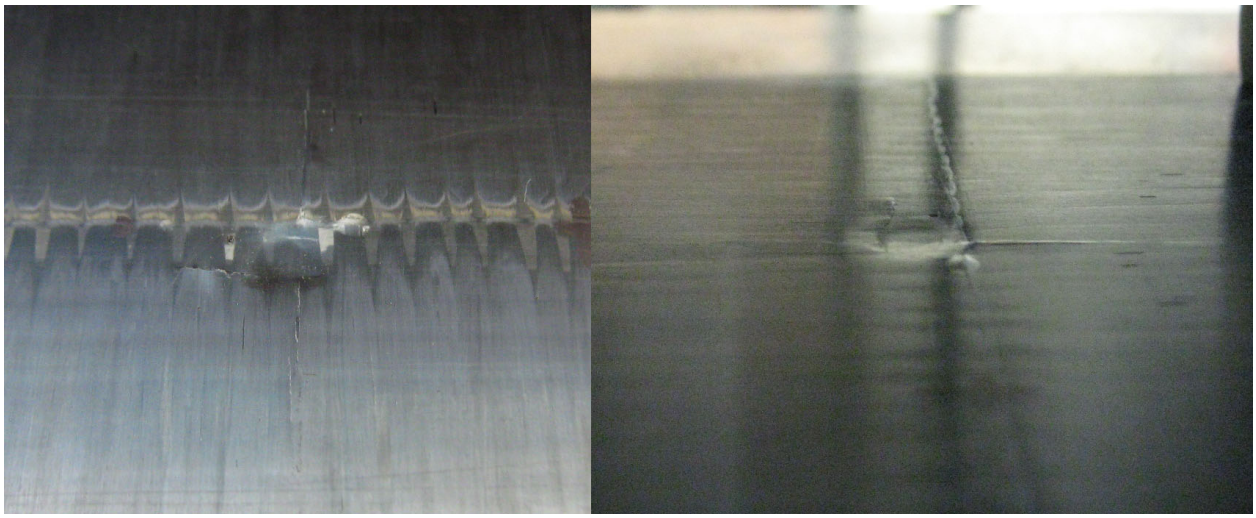


Figure 3.57: Top surface images of P1_IMP1 impact damage

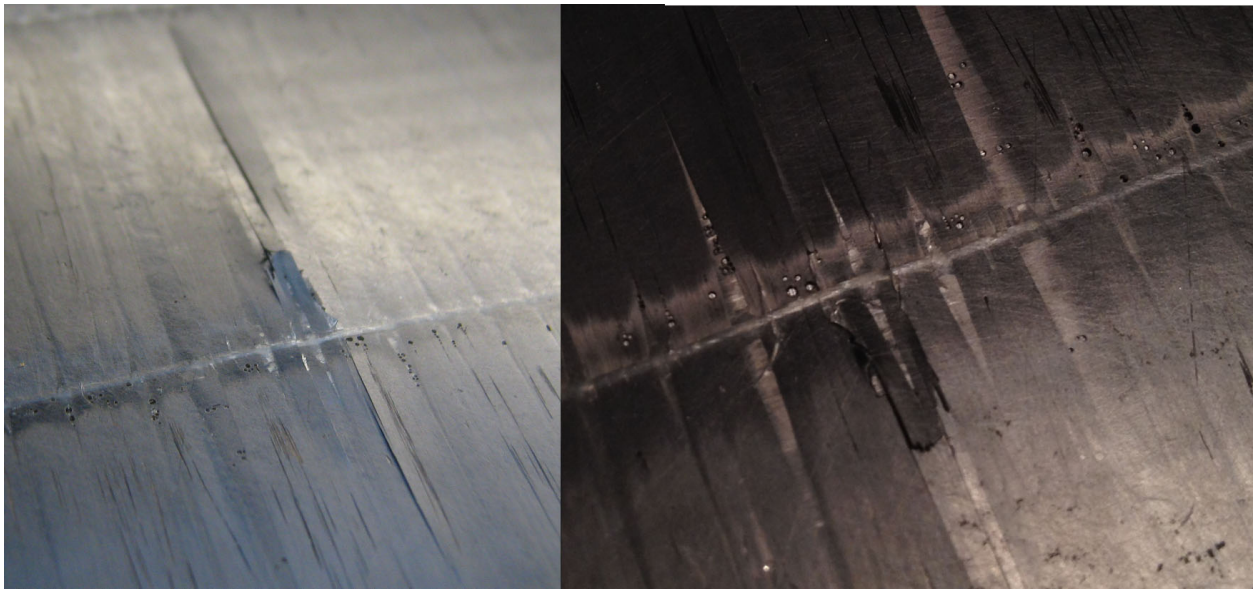


Figure 3.58: Bottom surface images of P1_IMP1 impact damage

3.2.4 Long Span Four-Point Bending Tests of Integral Reinforced Panel

To test the flexural and debonding properties of the IRPs, four-point bending tests were performed using an Instron 4482 testing frame controlled by a PC running Bluehill 2 software. The IRPs as moulded were first cut into 25.4 mm (1") strips using a vertical band saw. Specimens were cut from the IRPs as shown in Figure 3.59 where cut lines are

denoted by dashed lines. Each specimen's nominal footprint was 203.2 (8") x 25.4 mm (1") with varying thickness. The two centre specimens were kept aside for optical microscopy analysis and then the remaining samples were numbered one through 6 beginning at one end. The width and thickness of each numbered specimen was measured using a digital micrometer accurate to 0.001 mm at four locations and averages were recorded.

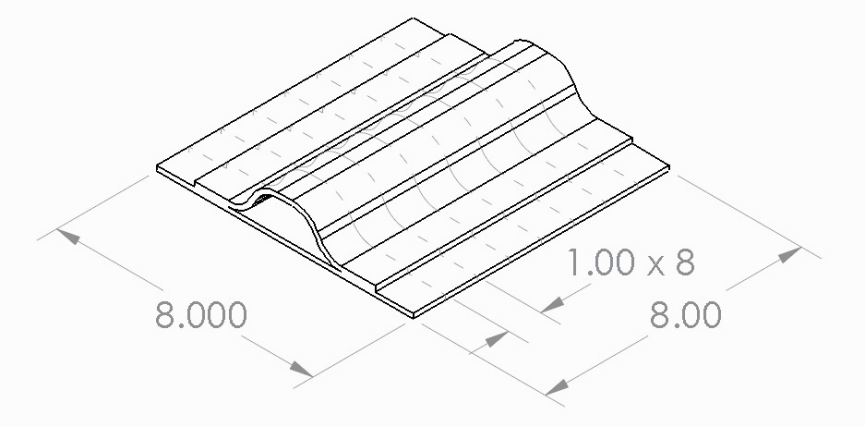


Figure 3.59: Cutting Pattern of Integral Reinforced Panel (dimensions in inches)

Testing parameters and apparatus used were similar to those used for long span four-point bending tests, Section 3.2.1. The testing procedure was consistent with ASTM standard test method D7264/D7264M-07 Flexural Properties of Polymer Matrix Composite Materials [66] whereas the specimen geometry, load and support spans used differed from the standard. The support span was set to 191 mm and the load span to 165 mm as recommended by Bombardier Aerospace project documentation, as shown in Figure 3.60. The documentation cannot be cited or included on grounds of confidentiality.

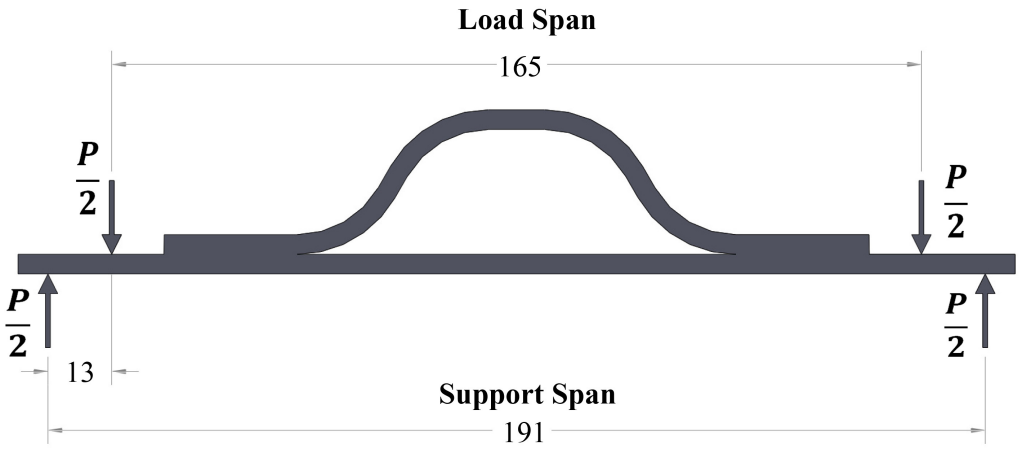


Figure 3.60: IRP four-point bending test setup (dimensions in mm)

As with the previous four-point bending apparatus, an Instron 2663 AVE was required to monitor and record midspan deflection. The AVE field of view, settings and sample testing procedure were identical to the previously described setup while the 2 mm white tracking marker was placed on the lower, flat section of the IRP. A stationary marker was mounted approximately 10 mm above on an external stand. The actual gauge length was recorded using the AVE and the change in distance between the markers was recorded as a strain throughout the test. Load, displacement of loading noses, AVE strain and time were recorded by the Bluehill software every 0.1 s. Failure was considered to have occurred when a 20% decrease in load was recorded between consecutive data points or when there was significant damage visible on the specimen. Specimens were inserted normal to and centred on the support noses. Loading noses were lowered until contact with the upper surface of the specimen was detected using the force readout. Load and displacement were reset to zero and the test was launched via software. Failure modes and other visual and audio observations were recorded manually along with corresponding elapsed time. An example of the testing apparatus in use is shown in Figure 3.61.

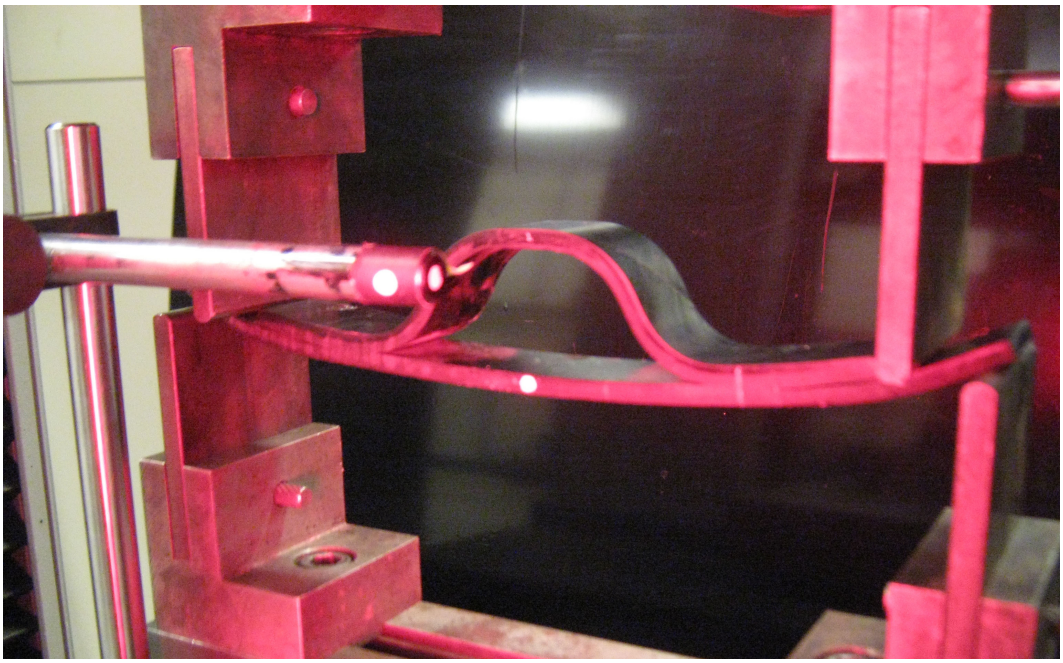


Figure 3.61: Four-point flexural testing apparatus for IRP samples

Data from testing the IRP panel was aimed at determining debonding strength between the flat plate and reinforcing section of the specimen as discussed in Section 4.3.1. Possible failure modes for the IRP were similar to those discussed in Section 3.2.1 with additional failure locations near the thickness transitions from 4 mm to 8 mm. For example, specimen IRP1_LSB6 failed in interlaminar shear initiated at the inner corner where the upper and lower sections of the IRP join as shown in Figure 3.62.

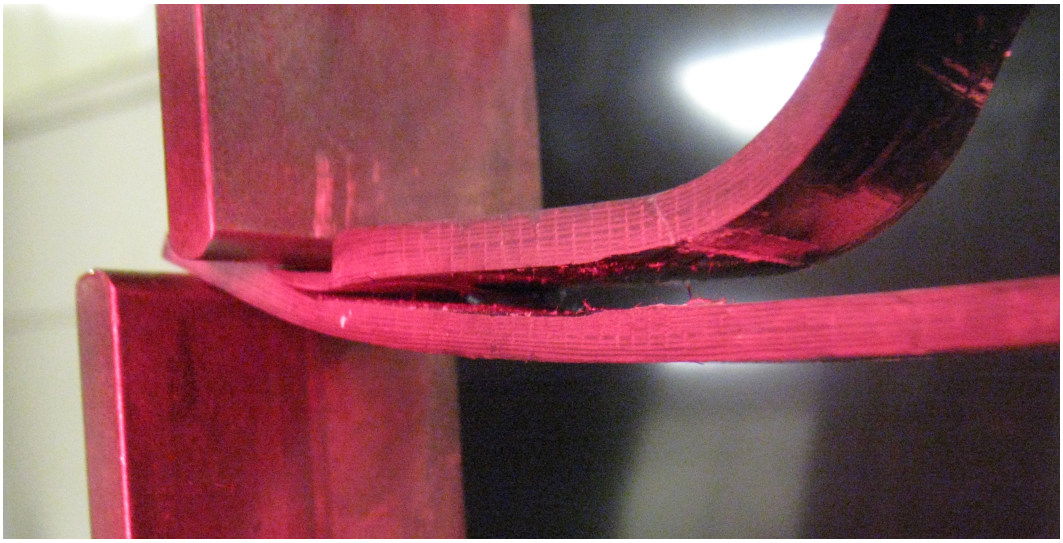


Figure 3.62: Specimen IRP1_LSB6 during test

3.2.5 Optical Microscopy Imaging and Analysis

Optical microscopy was performed on samples cut from PMC flat plates and IRPs to observe internal structure, identify any internal defects and calculate porosity. From the flat plates, two microscopy samples measuring approximately 1 cm x 1 cm were taken from each of two locations, near the inlet and near the outlet. The 2 samples taken from each location were cut at 90^{o} from each other to ensure observation along both principal axes of the plates. From the IRPs, 1 cm x 1 cm samples were cut from the specimen in the zone where the flat and reinforcing sections meet. Here again, two samples were taken from each location and cut at 90^{o} from each other enabling viewing along both principal axes of the IRPs.

The samples were initially cut from the plates using a vertical band saw, followed by trimming using a 200 mm diameter wet diamond blade mounted on a Struers Secotom-10 2200 rpm precision saw [70] to reduce surface roughness and generate a flat cross-section surface. Each sample was mounted into a thermosetting resin with the desired viewing surface oriented at the bottom edge of the cylindrical mount. Fluorescent yellow die was added to the mounting resin to enhance the visibility of voids within samples. The resin was allowed to cure for a minimum of 24 hours before polishing.

Mounted samples were placed into a Struers Tegrapol-31 automatic polishing machine to grind and polish the sample. The polishing machine used rotating magnetic polishing discs while rotating samples in the opposite rotational direction. The samples were polished using a six-step process with rinsing and cleaning applied prior to each step, until a surface roughness of approximately 3 μm was reached.

Micrographs were generated and analyzed using a Clemex PE & Lite 3 megapixel camera mounted on an Olympus XJP-3A optical microscope, Figure 3.63, and accompanying Clemex software package. Micrographs with magnifications of 50x and 400x were generated for this thesis; examples appear in Figure 3.64. Length measurements precalibrated within the software allowed for determining lamina thickness, void sizes and stitching effects.



Figure 3.63: Clemex PE & Lite camera on optical microscope with sample

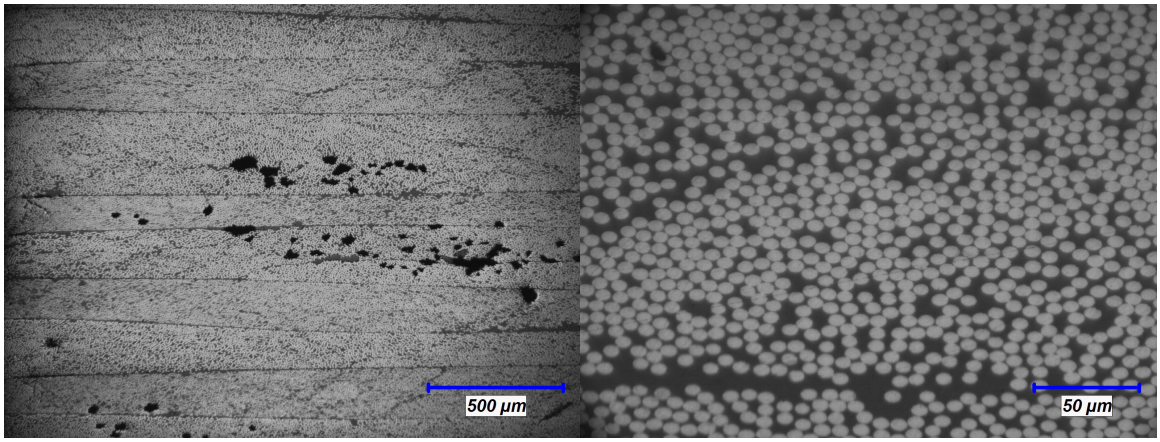


Figure 3.64: Sample micrographs of IRP1 50x (left) and 400x (right)

Porosity was calculated used a subroutine within the Clemex Vision Lite software written by Simon Baril-Gosselin, PhD student at the University of Ottawa. Using an area of micrographs at 400x targeted for analysis, contrast levels were filtered to distinguish dark voids appearing between lighter fibres and resin. The contrast threshold was set

such that only void areas would be highlighted within the image. The ratio of the area of voids to the total image area was calculated as the porosity. Porosity values were taken for a minimum of 50 locations to proved more accurate values. However, as only two small locations from the PMC plates were analyzed and values obtained are based on the selected threshold, conclusions drawn are not necessarily applicable to the complete PMC plates.

Using a method similar to that used for calculating porosity, fibre volume fractions of the samples were also calculated. Contrast filters were set so as to select exclusively the lighter fibre areas. Figure 3.65 shows an example of an area selected for analysis, where the lighter circular areas are fibres. Approximately 15 locations were analyzed to improve accuracy of fibre volume fraction values.

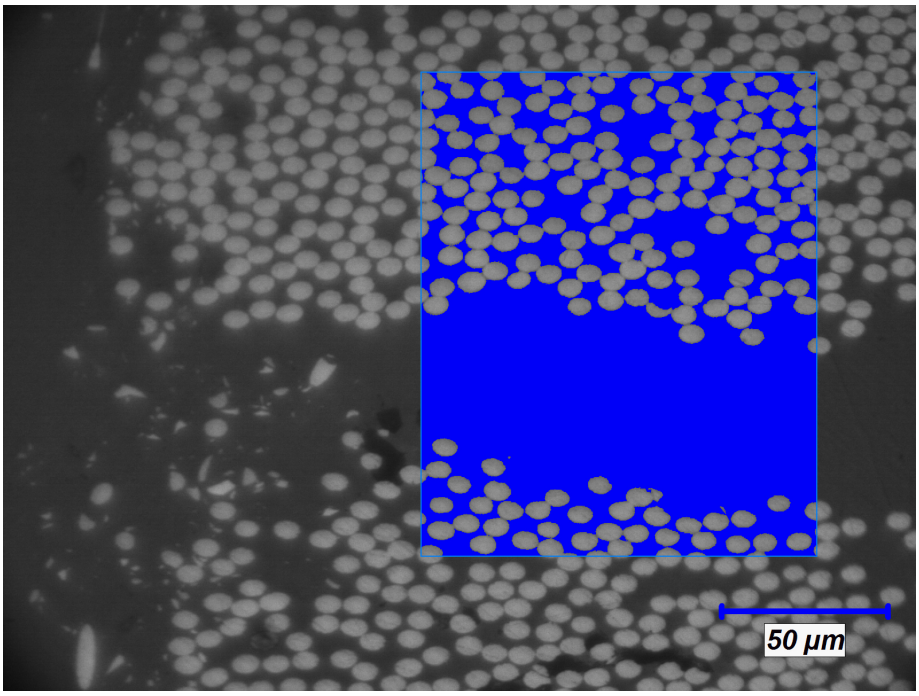


Figure 3.65: Area selected for microscopic fibre volume fraction analysis at 400x magnification, IRP3

Chapter 4

Results and Analysis

4.1 Quality Description and Analysis of PMC Components

Two different components were manufactured towards mechanical testing for this thesis work. Square 305 mm (12") flat plates and square 204 mm (8") plates featuring an integral reinforcement were manufactured using RTM. A major goal upon preform manufacturing and resin injection was to maintain good control over most parameters such as yarn spacing and alignment, stitch density, spacing and tension, and resin flow. However, as much of the preform assembly and stitching operations were done manually, inherent variation between components was present throughout the manufacturing process. Resin flow rates were altered from component to component initially, aiming at achieving balance between resin gel times and complete preform wetting. Basic injection data is presented in Table 4.1, where the maximum pressure was based on load data from the Instron 4482 testing frame. The maximum pressure values are conservative approximations as they ignore any friction within the hydraulic cylinder. Sample resin pressure profiles upon injection of a flat plate and an IRP are shown in Figure 4.1. Other parameters in finished components, such as void content and zones featuring dry fibres, were present. Void content was measured using optical microscope images aiming at quantifying the overall quality of the resin injection process, whereas dry fibre sections

could be removed from finished components and did not represent a significant presence in testing specimens.

Table 4.1: Resin Injection Information

PMC component	$v_{f,c}$	Resin Flow Rate $[\frac{cc}{s}]$	Injection time [min]	Maximum Pressure (Approximate) [MPa (psi)]
P1	52 %	0.2	42	1.31* (190)
P2	52 %	0.1	63	1.31* (190)
P3	52 %	0.1	70	1.31* (190)
P4	63.5 %	0.05	106	0.97 (140)
P5	63.5 %	0.1	55	1.07 (155)
P6	63.5 %	0.1	58	0.78 (114)
IRP1	52 %	0.15	65	1.3 (189)
IRP2	52 %	0.15	71	1.7* (250)
IRP3	52 %	0.15	51	1.7* (250)

*Pressure reached testing frame limit set by user

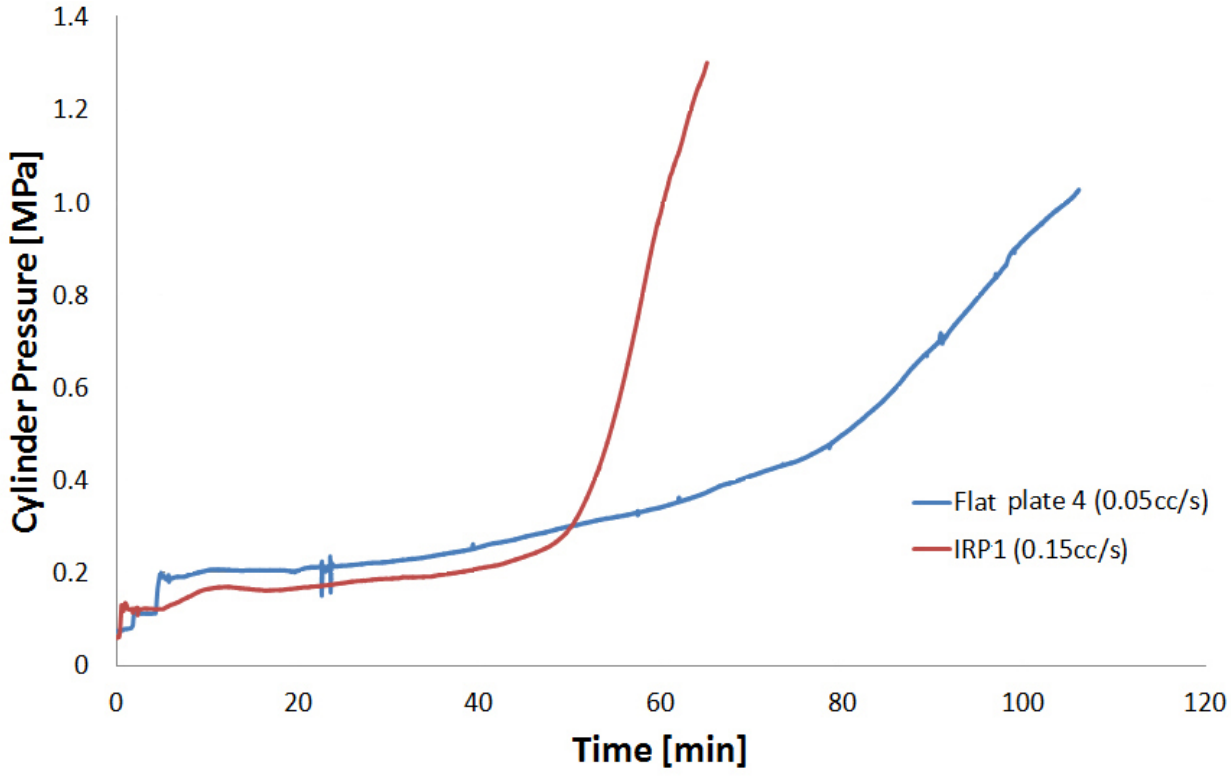


Figure 4.1: Injection pressure profiles from PMC component manufacture

The only variable that was altered between different cross-ply flat plates was their

fibre volume fraction. This was done by increasing the number of layers used in making plates within the same mould cavity. Three flat plates with a targetv_f of 52 % and three additional plates with a target v_f of 63.5 % were manufactured. Three IRPs were manufactured in total; one with cross-ply lamina orientation and two with $\pm 45^o$ angle ply orientation, all with a target fibre volume fraction of 52 %. Visual observation of component quality along with optical microscopy analysis are presented in Sections 4.1.1 and 4.1.2. Long span four-point bending test results appear in Section 4.2.1, short span three-point bending test results appear in Section 4.2.2, drop weight impact test results appear in Section 4.2.3, and long span four-point bending test results for IRPs appear in Section 4.3.1.

4.1.1 Flat Plates

Flat plates were inspected visually for possible defects such as fibre misalignment, dry spots and voids resulting from trapped air and/or volatiles. Most defects were localized on the outer edges of the components and so they could be excluded from testing specimens. Also, the extent of defects increased slightly with an increasing v_f due to the increased mass of fibres leading to additional resistance to resin flow between stitch lines.

Fibre misalignment thought to be caused by fibre washing during injection was more prominent near the resin inlet and plate edges perpendicular to the fibres, Figure 4.2. However, fibre washing did not affect yarns through the thickness of the plate as there was no fibre misalignment on the bottom-side of plates, Figure 4.3. Plate 4 shown in the figures featured the most extensive fibre misalignment observed in all flat plates.

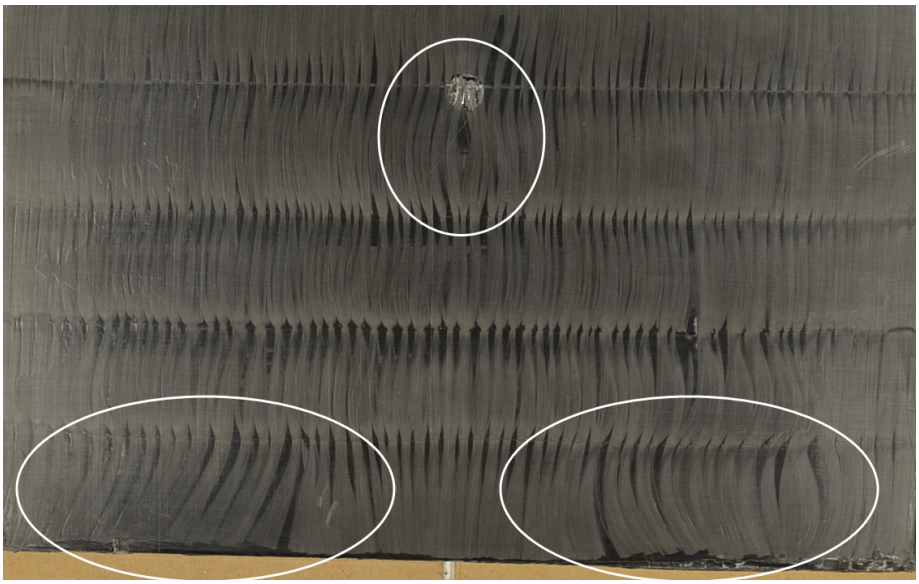


Figure 4.2: Fibre washing from resin flow, plate 4

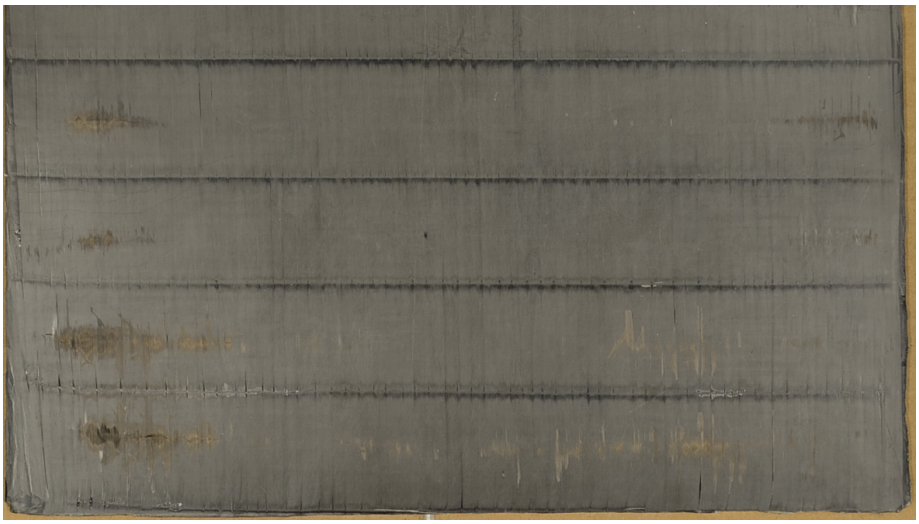


Figure 4.3: Bottom-side of resin inlet, plate 4

Dry spots present on the bottom-side of the flat plates, Figure 4.4, were common as both the inlets and outlets were featured on the female part of the mould, causing minimal pressure gradient through the thickness. Dry spots occurred between stitch lines which acted as channels for resin, therefore starving areas without stitches from resin. The presence of dry spots increased with increasing v_f, therefore plates 4 to 6 featured more, larger dry fibre zones.



Figure 4.4: Dry sports from resin starved areas, plate 6

Voids caused by air trapped on the surface were noticeably present in plates 1 and 3, Figure 4.5. Voids were generally in close proximity to stitch lines and towards the outer edges of plates, Figure 4.6.

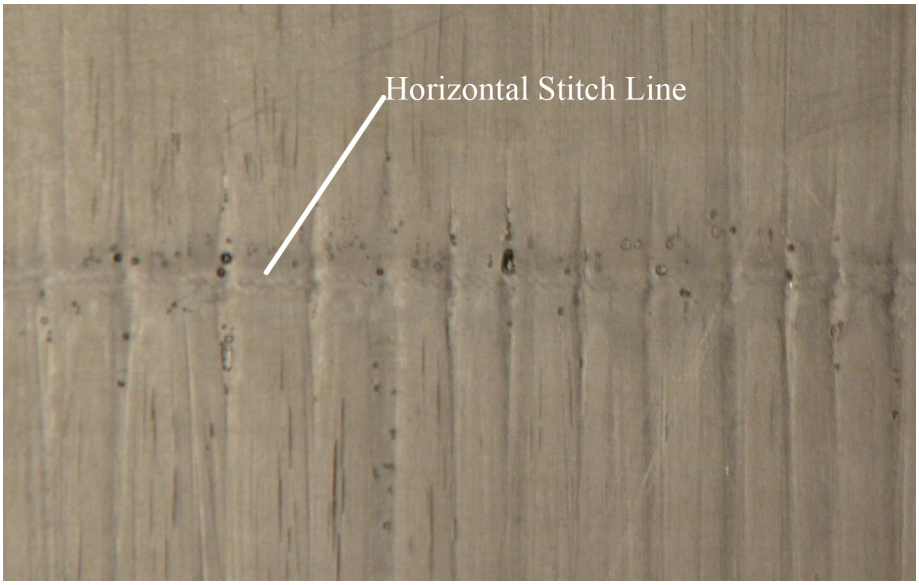


Figure 4.5: Voids caused as a results of trapped air, plate 3



Figure 4.6: Voids near outer edge, plate 1

Inter-plate and intra-plate thickness variability was caused by mould cavity bending during infusion, loose fibres interfering with tight gaps between the mould halves, and springback of preforms after compaction. Desired cavity thickness was nominally 4 mm, however measured thickness varied from 4.10 mm to 5.24 mm. Average flat plate thicknesses obtained from measurements done on test specimens are contained in Table 4.2. Thickness variations are indicative of local fibre volume fraction variations within a plate, therefore increasing the difficulty in determining overall fibre volume fraction for the plates. However, an adjusted fibre volume fraction was calculated from the average measured thicknesses and a constant known fibre volume content, and is also shown in Table 4.2. As expected, the adjusted fibre volume fractions are significantly lower than the target values from the nominal 4 mm thickness. Flat plates 1-3 showed lower average thickness and variance than plates 4-6, likely from increased bending as a result of higher injection pressures along with increased fibre content within the mould cavity in the latter case.

Table 4.2: Measured thicknesses and adjusted fibre volume fraction of flat plates

Plate	Thickness [mm]		Adjusted Fibre Volume Fraction [%]
	Average	Standard Deviation	
P1	4.28	±0.074	48.6
P2	4.17	±0.046	49.9
P3	4.33	±0.063	48.0
P1-3	4.29	±0.093	48.8 ±0.094
P4	4.94	±0.23	51.4
P5	4.62	±0.19	55.0
P6	4.28	±0.090	59.4
P4-6	4.62	±0.32	55.3 ±0.40

Micrographs taken from flat plate samples allowed for viewing defects that are present within the cross-section. These defects mainly include voids caused by trapped air and stitching effects which lead to local out of plane yarn waviness and resin rich zones. Voids varied in size throughout the samples, however they did not cross reinforcing layer boundaries. An example of voids seen within flat plate 2 is shown in Figure 4.7.

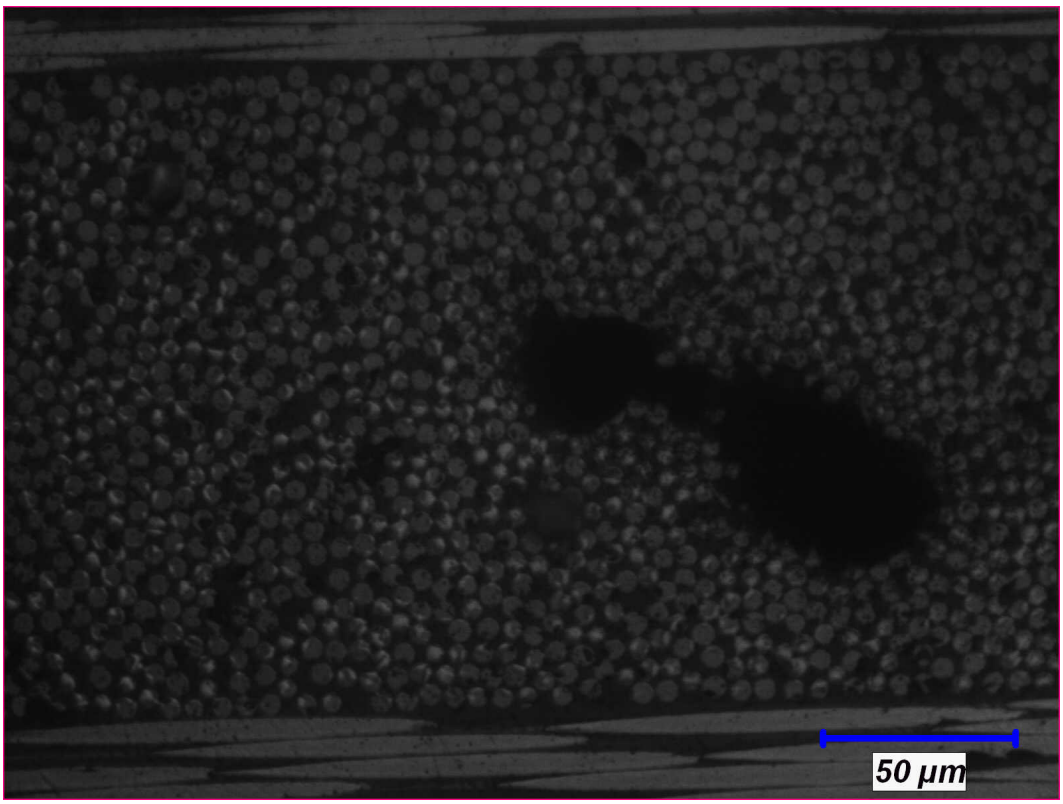


Figure 4.7: Void contained within single reinforcing layer at 400x magnification, plate 2

Stitching alters the reinforcing fibre network by locally compacting yarns within the stitch-loop. Stitch tension tends to induce out of plane yarn waviness, as shown in Figure 4.8. Out of plane yarn waviness reduces in plane tensile and compressive properties of a component as the ratio of properly aligned fibres decreases, however it has been shown that out of plane waviness can cause a shear strengthening effect [71]. Also, channels are created when the stitching needle passes through the preform leaving a region void of yarns. These channels allow for resin flow, however, resin-rich zones remain within the component. Figure 4.9 shows an example of resin rich zones in close proximity to a stitch-loop.

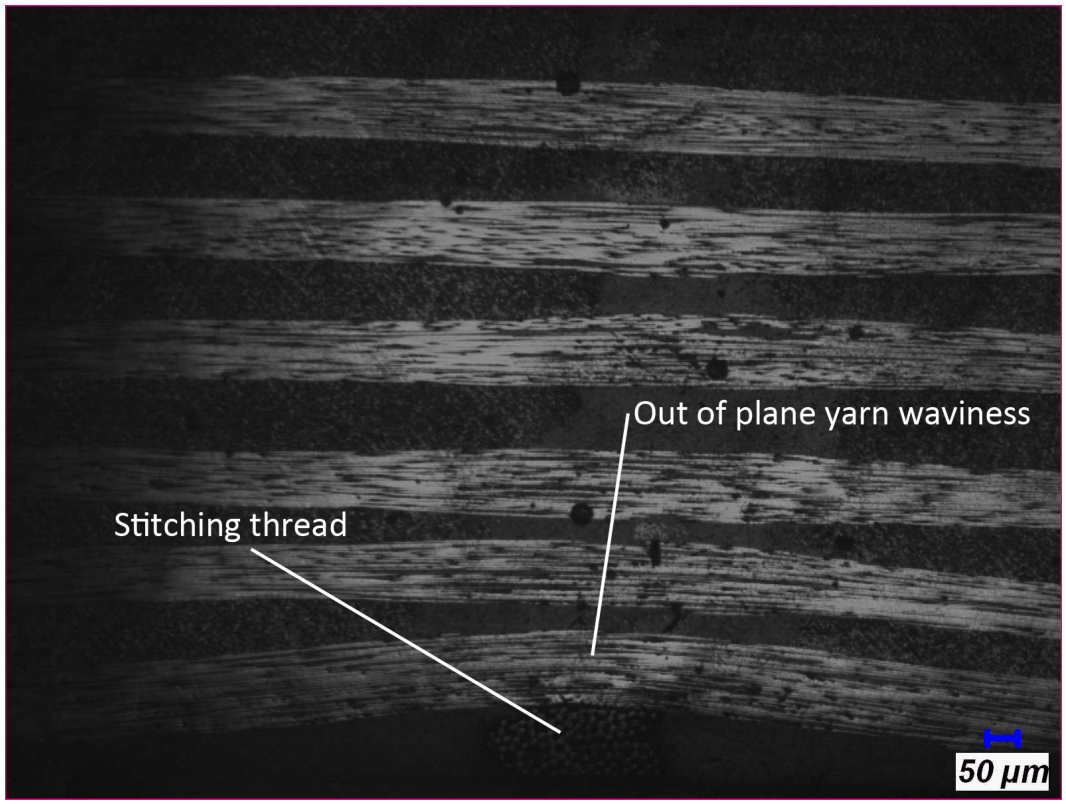


Figure 4.8: Stitch induced out of plane yarn waviness at 50x magnification, plate 3

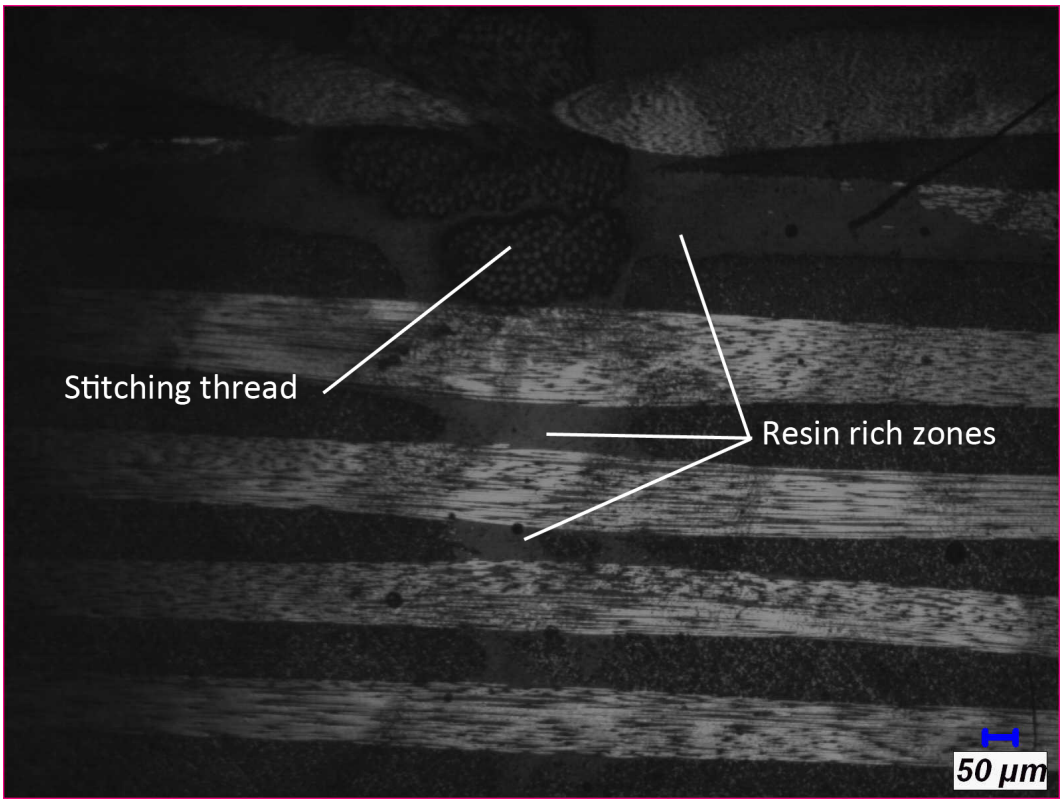


Figure 4.9: Resin rich zone caused by stitch-loop at 50x magnification, plate 3

4.1.2 Integral Reinforced Panels

IRP manufacturing presented issues similar to those seen with the flat plates such as fibre misalignment, dry spots and voids caused by trapped air. However, the geometry of IRPs induced other issues including inner mould shearing and resin-rich zones located specifically where the mould cavity changes thickness. Fibre misalignment was more prominent on the surface where resin was injected, most notably in the vicinity of the inlet, Figure 4.10. On the other hand, fibres on the surface opposite to the inlet and within the flat plate section remained properly aligned, Figure 4.11. Fibre misalignment within IRPs was likely caused by resin flow pushing fibres along their transverse direction causing the fibres to bow.

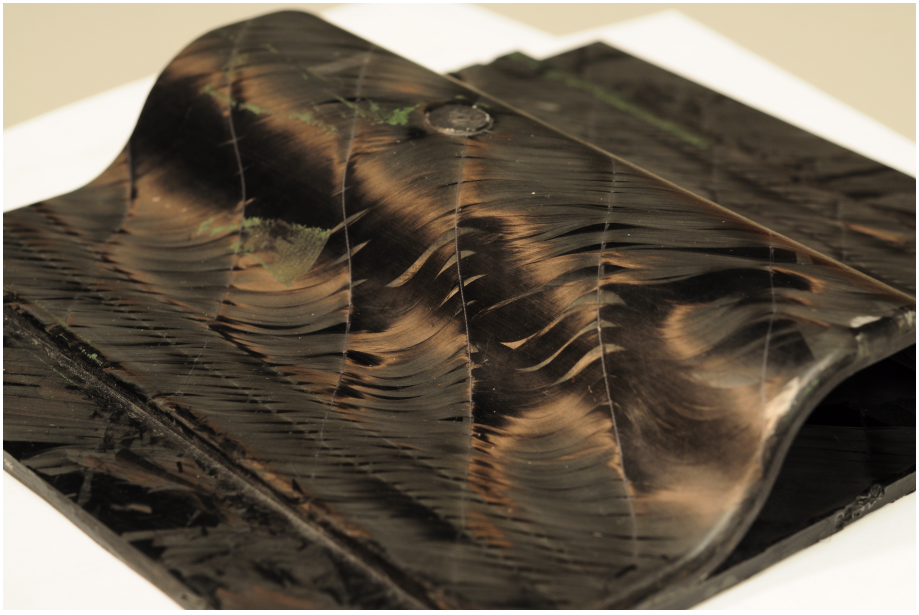


Figure 4.10: Fibre misalignment, top surface IRP 1

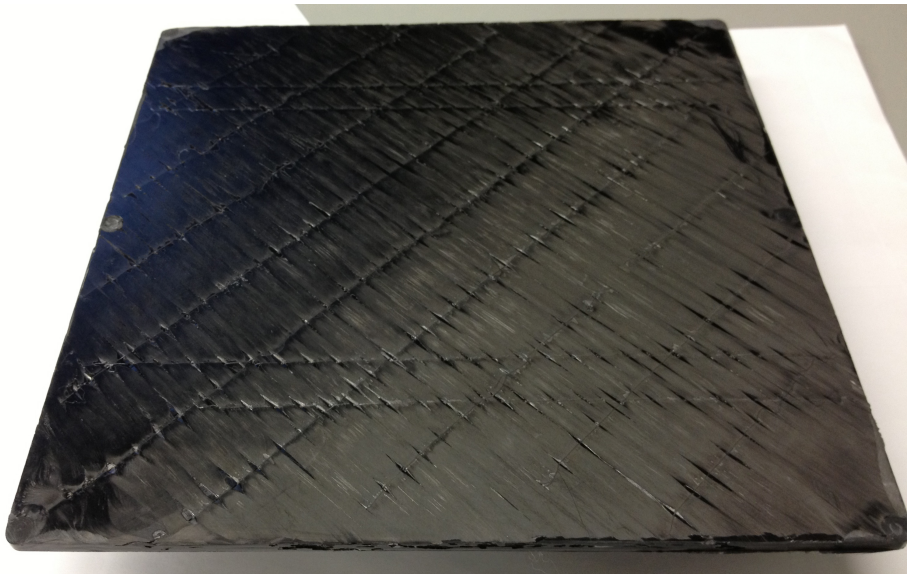


Figure 4.11: Bottom surface, IRP 1

The amount of dry spots due to incomplete resin impregnation, Figure 4.12 was similar to that found in flat plates. However, the occurrence of voids due to trapped air increased on the bottom surfaces of IRPs, Figure 4.13. The increased presence of voids was likely caused by the location of resin outlets with respect to the resin inlet. Since the outlets were near the outer edges of the bottom surface and the inlet was placed

at the centre of the top surface, resin flow followed the path of least resistance towards the outlets without fully wetting the preform and forcing out the air within the mould cavity. Also, as with flat plates, voids from trapped air were in very close proximity to stitch lines.

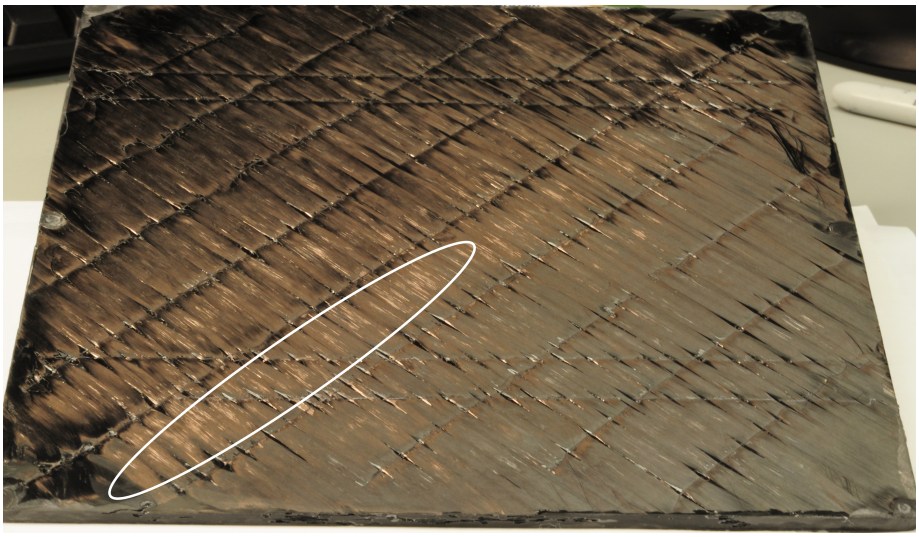


Figure 4.12: Dry spots from incomplete resin impregnation, IRP 3 bottom

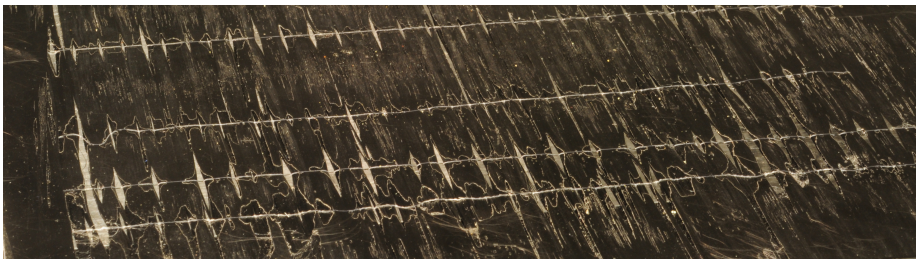


Figure 4.13: Voids from trapped air, IRP 2 bottom

Defects exclusive to the IRPs consisted in inner mould shearing and resin-rich zones near the cavity thickness change. Inner mould shearing was present only in IRP 1 as the inner mould was initially machined with sharp knife edges where the flat plate and reinforcing sections were joined. Figure 4.14 shows the iteration of mould geometry from IRP 1 to IRPs 2 and 3. While demoulding, the thin knife edges sheared leaving traces of aluminum inside the IRP, Figure 4.15.

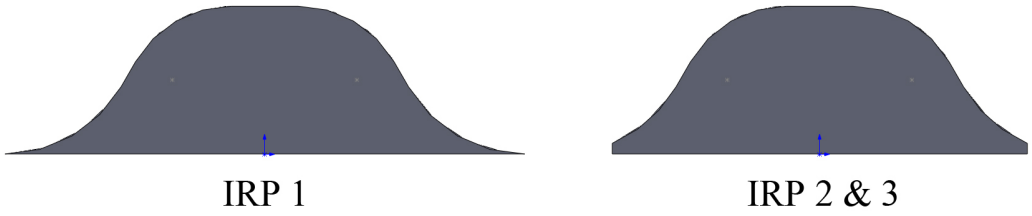


Figure 4.14: End view of the inner mould pieces used for IRP 1 (left) compared to IRPs 2 and 3 (right)

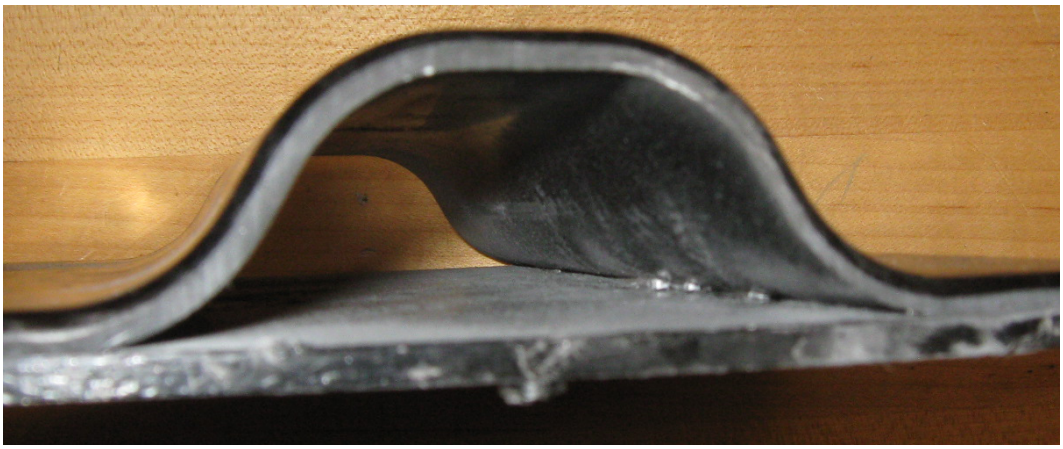


Figure 4.15: Inner mould shearing, IRP 1

The resin rich zones that occurred where thickness changed from nominal 4 mm to 8 mm, Figure 4.16, were caused indirectly by fibre washing during injection and by preform handling. As the flow of resin caused fibres to bend, their projected length along their original path shortened and the area of the mould cavity near their ends was essentially free of fibres. This defect was only present in IRP 2 where the preform featured a crossply laminating sequence.

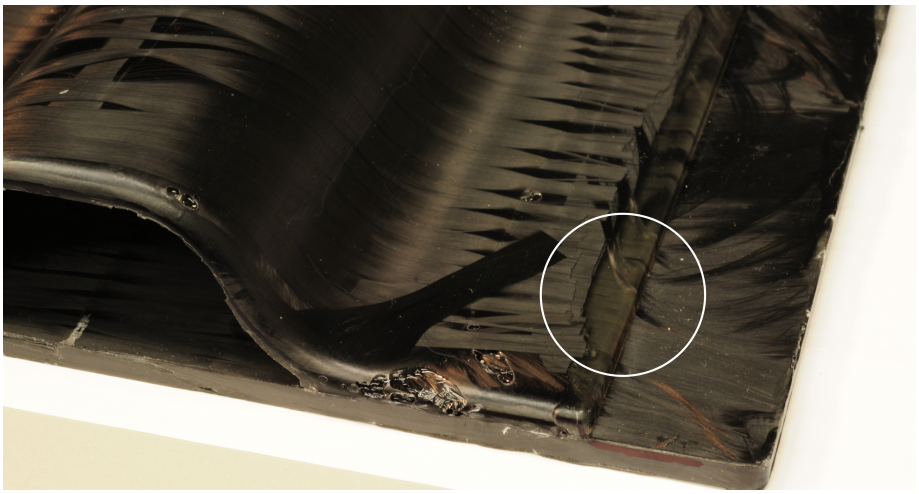


Figure 4.16: Resin rich zone, IRP 2

IRP thickness was measured to determine its variation between different IRPs and among specimens obtained from each single IRP. The resistance of preforms to compaction tends to hinder mould closure leading to thicknesses greater than the nominal cavity thicknesses of 4 mm and 8 mm. It was observed that inter-IRP thickness variation was larger than intra-IRP thickness variation, which was expected as IRP moulds feature parts that are thicker and therefore stiffer, therefore minimizing mould bending and cavity thickness changes. Table 4.3 shows average thicknesses and standard deviations for individual specimens measured in locations where nominal cavity thicknesses were 4 mm 8 mm. Table 4.4 shows average thicknesses of each IRP based on specimen measurements. The average thickness of all IRPs together showed a 6 % increase over nominal thickness, which would have to be considered if this method was used for manufacturing components within tight tolerances over thickness.

Table 4.3: Measured thicknesses of individual IRP specimens

Specimen	Thickness (4 mm nom.) [mm]		Thickness (8 mm nom.) [mm]	
	Average	Standard Deviation	Average	Standard Deviation
IRP1_LSB1	4.14	±0.078	8.07	±0.084
IRP1_LSB2	4.18	±0.10	8.11	±0.098
IRP1_LSB4	4.22	±0.12	8.15	±0.12
IRP1_LSB6	4.20	±0.096	8.12	±0.071
IRP2_LSB1	4.34	±0.083	8.32	±0.13
IRP2_LSB3	4.40	±0.11	8.40	±0.10
IRP2_LSB4	4.34	±0.10	8.47	±0.084
IRP2_LSB5	4.43	±0.10	8.46	±0.12
IRP3_LSB1	4.06	±0.068	7.96	±0.0077
IRP3_LSB2	4.08	±0.063	7.99	±0.0071
IRP3_LSB3	4.09	±0.067	7.99	±0.0014

Table 4.4: Average overall thicknesses of IRPs

IRP	Thickness (4 mm nom.) [mm]		Thickness (8 mm nom.) [mm]	
	Average	Standard Deviation	Average	Standard Deviation
1	4.18	±0.036	8.11	±0.032
2	4.40	±0.043	8.41	±0.070
3	4.08	±0.014	7.98	±0.015
ALL	4.24	±0.14	8.19	±0.19

Micrographs were generated, aiming at measuring thicknesses of reinforcement layers and stitches, as well as analyzing porosity and local fibre volume fraction. Layer thickness measurements ranged from 126 µm to 239 µm. The micrograph in Figure 4.17 is an example where layers were selected randomly for measurements, with the largest layer in the centre corresponded to a double layer about the plane of symmetry. Measurement locations may not have lead to perfectly reproducible values as they may have been close to stitches or near other features that may have resulted in locally compacted layers.

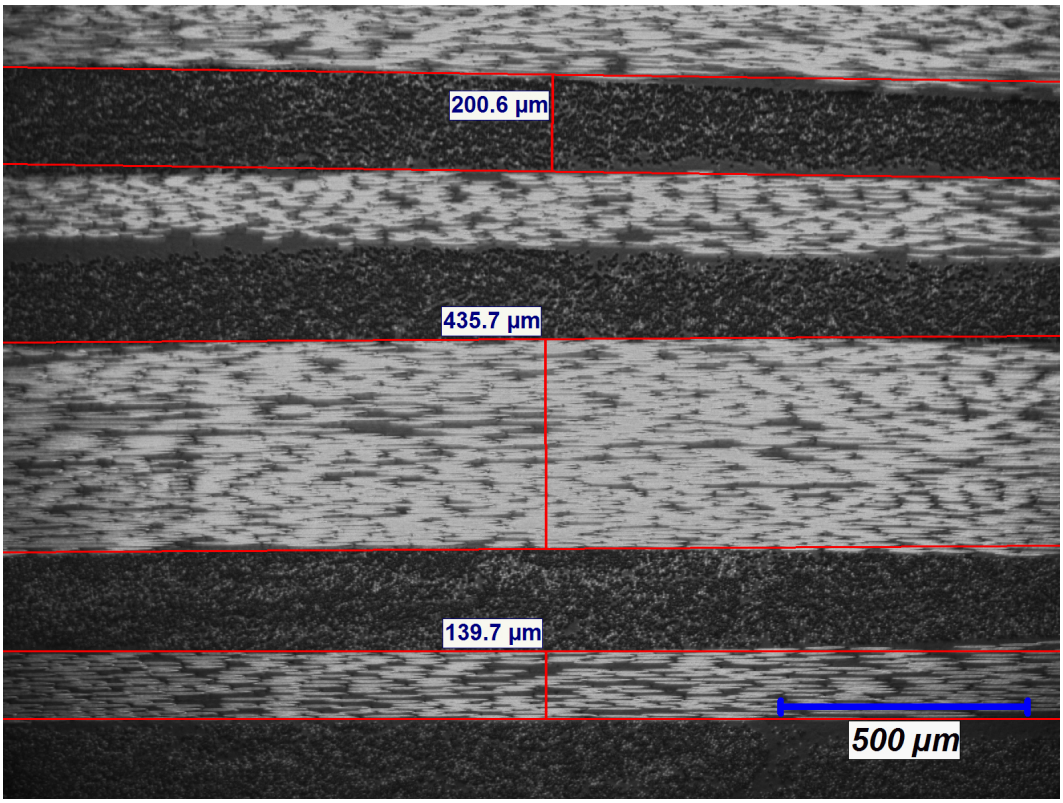


Figure 4.17: Micrograph showing layer thickness measurements at 50x magnification, IRP 2

Stitches also caused fibre distortions, local resin-rich zones and zones of high local fibre volume fraction. The stitch shown in Figure 4.18 measured approximately 330 µm wide and affected the distribution of fibres in different layers.

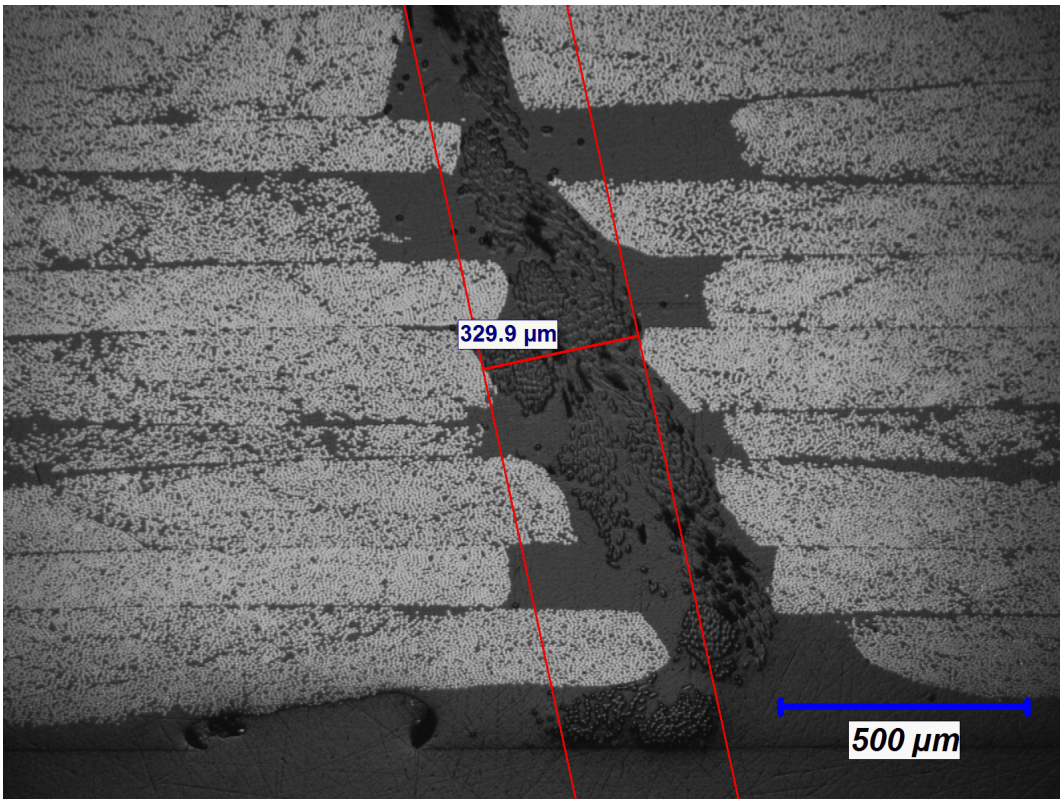


Figure 4.18: Through-thickness stitch at 50x magnification, IRP 2

IRP micrographs taken at locations where curvatures were present showed some interlaminar fibre gaps, Figure 4.19. Interlaminar gaps were noticed throughout other samples, however none were as large as those seen within the areas of curvature. Gaps at the widest sections measure approximately 37 µm.

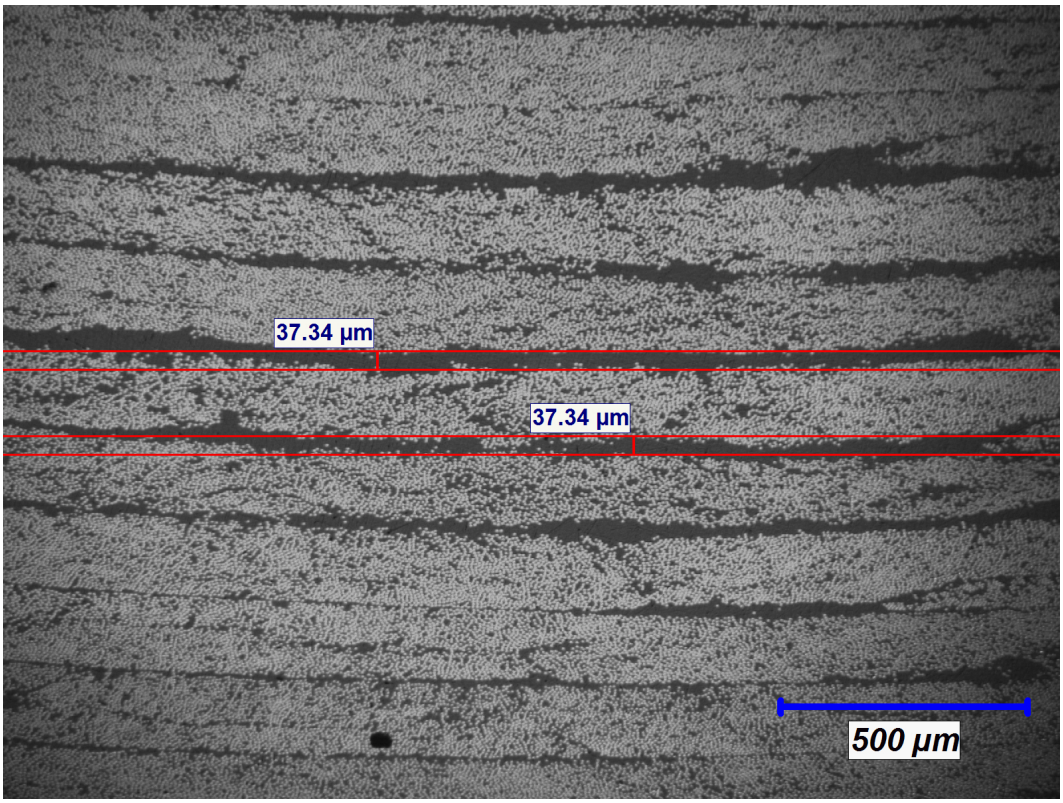


Figure 4.19: Interlaminar gaps of curved section at 50x magnification, IRP 1

Another important region to observe using optical microscopy was the inner corner where the reinforcing and flat sections meet. As discussed in Section 4.1.2, IRP 1 was injected with the inner mould featuring shape knife-edges that were machined to a thicker, blunter edge for IRPs 2 and 3. A knife-edge crack with a tip opening of approximately 68 µm was created during demoulding of IRP 1, which can be seen in Figure 4.20.

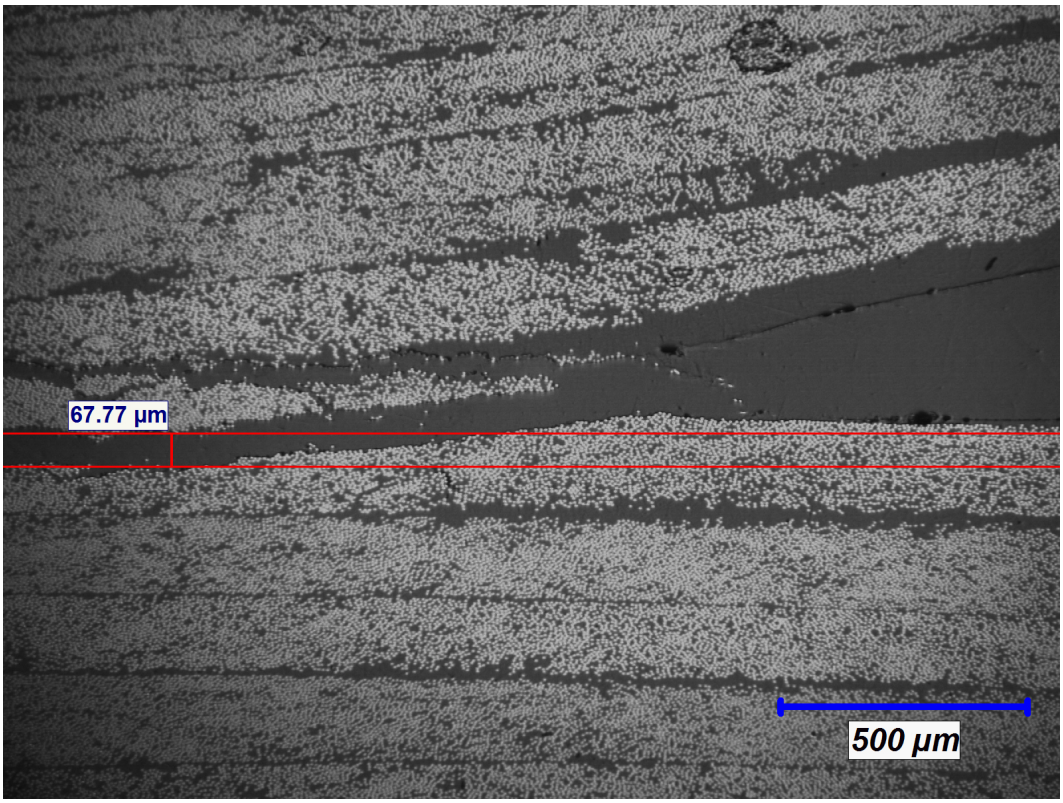


Figure 4.20: Knife-edge crack opening at 50x magnification, IRP 1

Internal voids of varying sizes and shapes were observed in many samples, from small spherical voids to voids with large aspect ratios, Figure 4.21. Overall average occurrences of voids, called porosity, were calculated using the Clemex software and are tabulated in Table 4.5. Sample porosity ranged from 0.22 % to 4.4 % which is within the required practical range for aircraft and cars of 2.5 % to 5 % [72]. However, it is important to note that as the samples taken represent only a small portion of overall components, the reported porosity values are strictly informative.

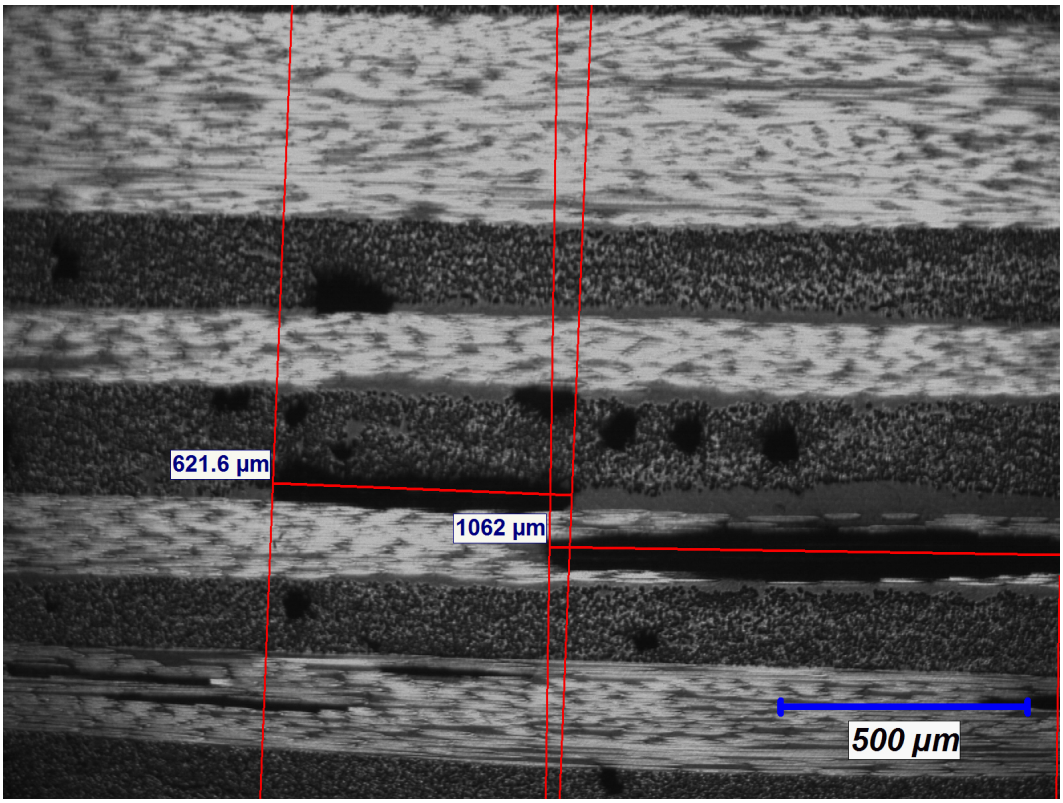


Figure 4.21: Voids of various shapes and sizes at 50x magnification, IRP 2

Table 4.5: Porosity of IRP samples

Sample	Porosity [%]	
	Average	Standard Deviation
IRP1_MIC1	0.22	±0.44
IRP1_MIC2	1.0	±2.5
IRP2_MIC1	1.5	±3.2
IRP2_MIC2	4.4	±6.4
IRP3_MIC1	0.76	±1.8
IRP3_MIC2	1.8	±3.8

Local fibre volume fractions of IRPs were calculated using a method similar to the one used for calculating porosity. Average local fibre volume fractions calculated for IRPs 1 and 3 are shown in Table 4.6; these average values obtained are very close to those that would have been obtained in an ideal case, as determined by calculation.

Table 4.6: Fibre volume fractions of IRPs

IRP	Fibre volume fraction [%]	
	Average	Standard Deviation
1	52.1	±12.4
3	51.3	±12.4

4.2 Mechanical Testing of Flat Plates

4.2.1 Long Span Four-Point Bending

Long span flexural testing of flat plates was separated into four groups of tests, with specimens in each set having similar fibre volume fractions and loading directions. Specimen sets 1 and 2 corresponded to plates 1 through 3 while specimen sets 3 and 4 corresponded to plates 4 through 6. Also, specimen sets 1 and 3 were loaded in such a way that the maximum normal strain was imposed along the 0^o direction of the PMC plate, while specimen sets 2 and 4 were loaded in such a way that the maximum normal strain was imposed along the 90^o direction of the PMC plate. Mechanical properties obtained showed reasonable levels of consistency between specimens as well as between plates. Averages and standard deviations were calculated for each mechanical property recorded from the tests to quantify consistency.

The theoretical overall laminate stiffness matrices for the PMC plates were calculated using Equation 2.35 based on a uniform thickness of 4 mm. For a composite plate with a laminating sequence identical to plates 1, 2 and 3 with units as GPa · mm for the A matrix and GPa · mm^3 for the D matrix terms,

$$\left[\begin{array}{c|c} A & B \\ \hline B & D \end{array}\right] = \left[\begin{array}{ccc|ccc} 290 & 8.12 & 0 & 0 & 0 & 0 \\ 8.12 & 237 & 0 & 0 & 0 & 0 \\ 0 & 0 & 14.1 & 0 & 0 & 0 \\ \hline 0 & 0 & 0 & 403 & 10.8 & 0 \\ 0 & 0 & 0 & 10.8 & 298 & 0 \\ 0 & 0 & 0 & 0 & 0 & 18.7 \end{array}\right] \tag{4.1}$$

where

$$\left[D^{-1}\right] = \begin{bmatrix} 2.48 \cdot 10^{-3} & 8.98 \cdot 10^{-5} & 0 \\ 8.98 \cdot 10^{-5} & 3.35 \cdot 10^{-3} & 0 \\ 0 & 0 & 5.34 \cdot 10^{-2} \end{bmatrix} (\mathrm{GPa} \cdot \mathrm{mm}^3)^{-1} \tag{4.2}$$

therefore the effective theoretical flexural moduli for plates 1, 2 and 3, could be calculated from the $[D^{-1}]$ matrix and Equations 2.46 and 2.47. With the x-axis of the matrix corresponding to the 0º direction of the composite and the y-axis of the matrix corresponding to the 90º direction of the composite, therefore $\bar{E}_1$ is the theoretical flexural modulus for comparison with specimen set 1 and $\bar{E}_2$ is the theoretical flexural modulus for comparison with specimen set 2,

$$\bar{E}_1 = \frac{12}{h^3} \cdot \frac{1}{d_{xx}} = \frac{12}{(4\,\mathrm{mm})^3} \cdot \frac{1}{0.00248\,(\mathrm{GPa} \cdot \mathrm{mm}^3)^{-1}} = 75.5\,\mathrm{GPa} \tag{4.3}$$

$$\bar{E}_2 = \frac{12}{h^3} \cdot \frac{1}{d_{yy}} = \frac{12}{(4\,\mathrm{mm})^3} \cdot \frac{1}{0.00335\,(\mathrm{GPa} \cdot \mathrm{mm}^3)^{-1}} = 55.9\,\mathrm{GPa} \tag{4.4}$$

Similarly, the theoretical flexural moduli for plates 4, 5 and 6 for a nominal thickness of 4 mm were calculated, where $\bar{E}_3$ is the theoretical flexural modulus of specimen set 3 and $\bar{E}_4$ is the theoretical flexural modulus of specimen set 4,

$$\bar{E}_3 = 90.3\,\mathrm{GPa} \tag{4.5}$$

$$\bar{E}_4 = 70.8\,\mathrm{GPa} \tag{4.6}$$

The theoretical values are considered ideal values, whereas test specimens featured imperfections and may not return these theoretical values.

The main observations made through flexural testing were that specimen location within the plate had an impact on results and the transverse stitch lines caused premature failure. With plates 1 to 3, specimens cut nearest to the inlet returned lower flexural strengths and moduli due to fibre misalignment and increased plate thickness near the inlet. Since the thickness increased the calculated stress was lower, reducing both the flexural strength and modulus. However, in plates 4 to 6 specimens furthest from the inlet featured lower strengths resulting from poor impregnation of the preform near the

outer edges of the plate.

Specimen sets 1 and 3, which featured transverse stitch lines, failed almost exclusively near these stitch lines. Stitch line tension pulled the carbon fibres closer to the midplane creating resin rich areas above and below the stitch which was weaker than surrounding areas. Buckling, compressive and tensile cracks initiated at these locations, either causing failure or leading to interlaminar cracks which caused failure. After initial cracking, significant residual strength remained with only one specimen experiencing complete sudden fracture and all others failing progressively.

Table 4.7 presents average flexural moduli for each specimen set compared with theoretical values. However, it is important to note that theoretical values were calculated from laminate stiffness matrices based on the measured average thicknesses of each specimen set rather than the nominal thickness of 4 mm as was calculated above in Equations 4.3 to 4.6. This was done since there is a very high sensitivity to flexural properties from variation in thickness.

As the target fibre volume fraction increased, the ratio of experimental modulus to theoretical modulus decreased significantly. This was likely from the increased presence of defects within plates 4-6 from the extra fibre content.

Table 4.7: Experimental flexural moduli compared with theoretical flexural moduli

Specimen Set	Average Thickness [mm]	Flexural Modulus [GPa]		Ratio of Experimental to Theoretical [%]
		Ave. Experimental	Theoretical	
1	4.28	58.1	71.1	81.7
2	4.22	42.3	53.0	79.8
3	4.57	57.3	79.5	72.1
4	4.64	43.2	59.4	72.7

Load-deflection curves for all long span four-point bending specimens are shown in Appendix A.

4.2.1.1 Specimen Set 1: $v_{f,c}$ = 52%, Tested Along 0º Reference Direction

Specimen set 1 tested flat plates 1, 2 and 3 with laminating sequence $[[0°/90°]_4/0°]_S$. The specimens were cut such that their length was parallel to the fibre direction of the

outer layers. All specimens featured stitch lines running across the width, spaced by approximately 25 mm.

In the elastic region specimens behaved as expected providing reasonable flexural moduli between 54.4 GPa and 64.3 GPa and flexural strengths between 516 MPa and 668 MPa. Table 4.8 presents flexural properties and failure codes from Table 3.3, while Table 4.9 contains statistical data for specimen set 1. Flexural moduli for the specimen set averaged 58.1 GPa with a standard deviation of ±3.38 GPa, and flexural strength averaged 575 MPa with a standard deviation of ±45.7 MPa. The average experimental flexural modulus reached only 81.7 % of the calculated theoretical flexural modulus.

Table 4.8: Flexural properties and failure codes for specimen set 1

Specimen	Width [mm]	Thickness [mm]	Flexural Strength [MPa]	Flexural Modulus [GPa]	Failure Code
P1_LSB1	11.93	4.29	516	56.1	M(TC)-B-V(TB)
P1_LSB2	13.27	4.32	527	57.0	M(TC)-B-V(TB)
P1_LSB3	12.27	4.34	539		M(TC)-L-V(TBLR)
P2_LSB1	11.76	4.17	574	61.6	M(CB)-B-T
P2_LSB2	12.84	4.14	596	59.5	M(CB)-B-T
P2_LSB3	12.85	4.10	668	64.3	M(CB)-B-T
P3_LSB1	12.00	4.39	581	56.0	M(CB)-B-T
P3_LSB2	13.38	4.41	598	54.4	M(CB)-B-T
P3_LSB3	12.93	4.33	571	56.2	M(CB)-B-T

Table 4.9: Statistical values from specimen set 1 flexural properties

Plate	Flexural Strength [MPa]		Flexural Modulus [GPa]	
	Average	Standard Deviation	Average	Standard Deviation
P1	528	±11.6	56.6	±0.636
P2	613	±49.2	61.8	±2.39
P3	583	±13.8	55.5	±0.997
All	575	±45.7	58.1	±3.38

Specimens behaved linearly within the elastic region. However, soon after the onset of initial cracking detected by acoustic emission from fibre breakage, behaviour became less

predictable. In six of the nine specimens, buckling failure from compression of the upper surface was observed, Figure 4.22. Also, failure locations were always in close proximity to stitch lines where resin-rich zones were present, Figure 4.23. Eight of the nine samples failed between the loading noses under maximum bending moment, with one outlier with failure occurring between loading and support noses.

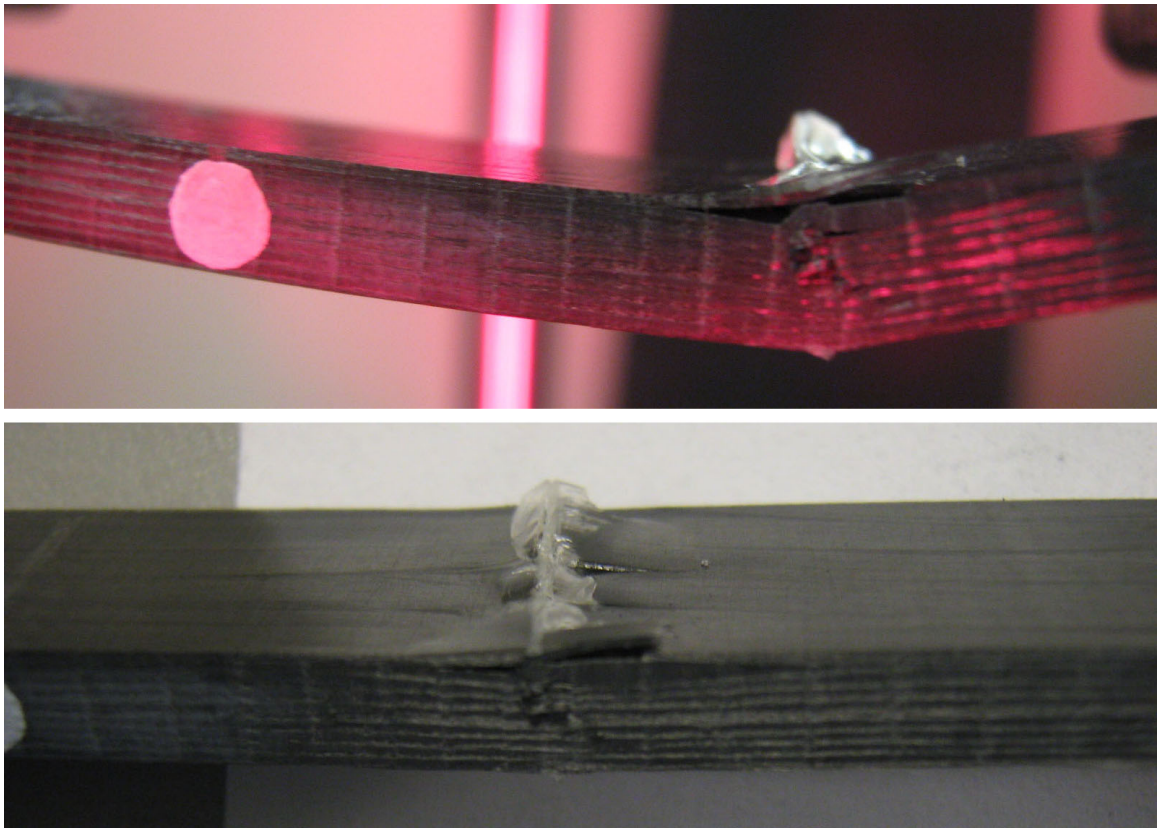


Figure 4.22: Compression-buckling failure on top surface during test (top) and after test (bottom), P2_LSB1

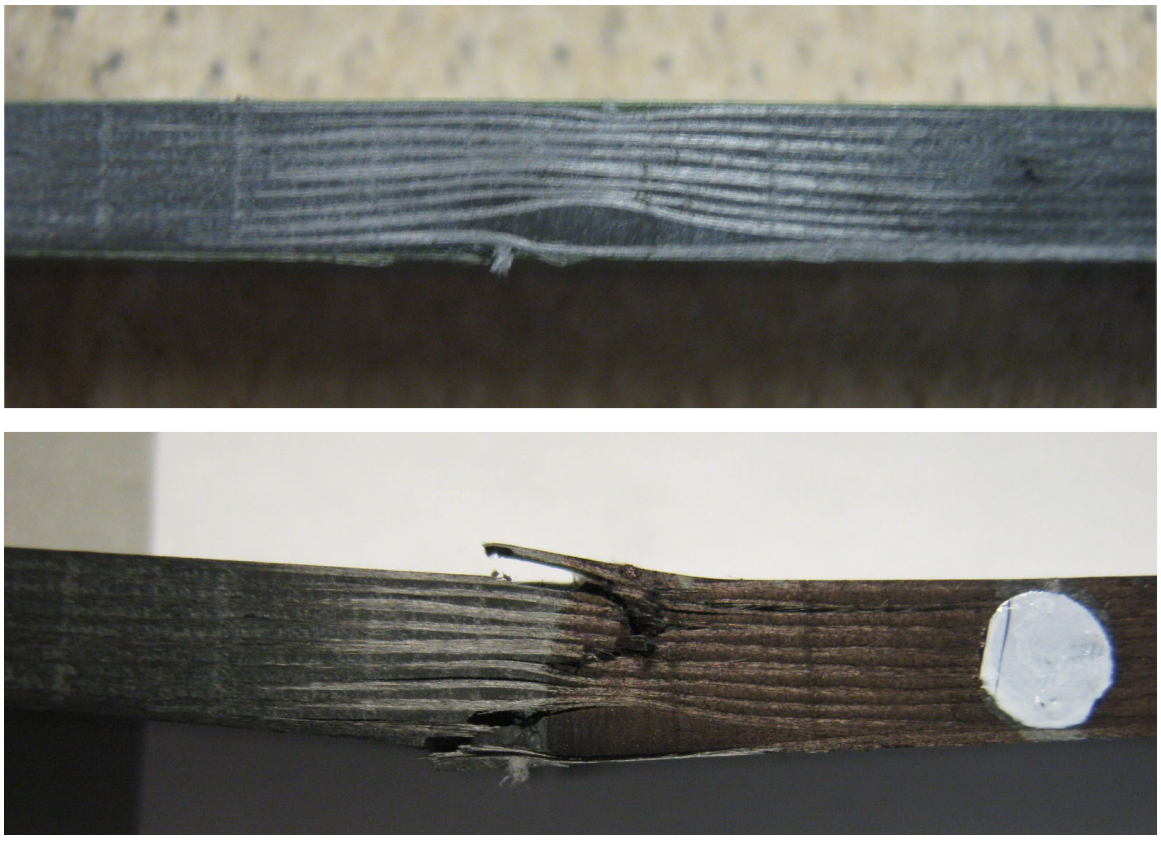


Figure 4.23: Resin-rich zone caused by stitch before test (top) and after test (bottom), P1_LSB1

4.2.1.2 Specimen Set 2: $v_{f,c}$ = 52%, Tested Along 90º Reference Direction

Specimen set 2 tested flat plates 1, 2 and 3 with the same $[[0°/90°]_4/0°]_S$ laminating sequence as specimen set 1. However, specimens were cut in a direction prependicular to that of specimens in set 1 such that the specimen length corresponded to the transverse fibre direction of the outer layers. Contrary to specimen set 1, specimen set 2 included specimens without any stitch-line present while others within the set featured a stitch line running along the length of the specimen. Table 4.10 presents flexural properties, failure codes from Table 3.3 and stitch information, while Table 4.11 contains statistical data for specimen set 2 for each plate and separated based on stitch-line presence or absence.

Flexural moduli of specimens ranged from 36.5 GPa to 49.4 GPa with an average of 42.3 GPa and a standard deviation of ±4.72 GPa. The average flexural modulus of

specimen set 2 reached 79.8 % of the theoretical value, which is very similar to the equivalent observation made for specimen set 1. In two of the three plates, the specimen nearest the inlet exhibited a lower flexural modulus. Contrary to flexural strength, the testing direction had an effect on the flexural modulus, as expected. The average flexural moduli of 42.3 GPa was 27.2 % lower than that of specimen set 1. The presence of a longitudinal stitch had little to no effect on the flexural modulus.

Flexural strengths of specimens ranged from 493 MPa to 642 MPa with an average of 573 MPa and standard deviation of ±47.5 MPa. It was observed that specimens taken nearest to the resin inlet exhibited lower flexural strengths than those taken further away. The average flexural strength of specimen set 2 was nearly equal to that of specimen set 1. The likely cause of this was the premature failure of specimens in set 1 from resin rich zones resulting from transverse stitch lines. Conversely, the presence of a stitch line had no observable effect on the flexural strengths of the specimens from set 2.

Table 4.10: Flexural properties and failure codes for specimen set 2

Specimen	Width [mm]	Thickness [mm]	Flexural Strength [MPa]	Flexural Modulus [GPa]	Failure Code	Longitudinal Stitch present?
P1_LSB4	11.84	4.27	528	41.7	M(TC)-A-V(BT)	No
P1_LSB5	12.36	4.25	611	49.4	M(BS)-B-T	Yes
P1_LSB6	12.50	4.13	543	44.6	M(BS)-B-T	No
P2_LSB4	13.13	4.23	576	41.6	T-A-B	Yes
P2_LSB5	12.36	4.19	642	40.3	T-A-B	Yes
P2_LSB6	12.79	4.15	615	40.3	M(CS)-A-T	No
P3_LSB4	12.54	4.27	493	36.5	M(TS)-A-B	Yes
P3_LSB5	13.55	4.30	553	42.7	M(CS)-A-T	Yes
P3_LSB6	11.69	4.21	594	44.1	C-A-T	No

Table 4.11: Statistical values from specimen set 2 flexural properties

Plate	Flexural Strength [MPa]		Flexural Modulus [GPa]	
	Average	Standard Deviation	Average	Standard Deviation
P1	561	±43.9	45.2	±3.94
P2	611	±33.1	40.7	±0.763
P3	547	±50.8	41.1	±4.05
All	573	±47.5	42.3	±3.58
No Stitch	570	±41.0	42.7	±2.06
Stitch	575	±56.9	42.1	±4.72

Failure was much more variable with set 2 compared to set 1. Of the nine specimens, initial failure from tension occurred in four specimens, Figure 4.24; it occured in compression in three specimens, Figure 4.25, and buckling in two specimens. Where multiple modes were present, only the initial failure mode was considered as interlaminar shear occurred commonly but only after initial through-thickness cracks from tension and compression had appeared. Of the five samples where interlaminar shear appeared as a secondary failure mode, three contained longitudinal stitches and two did not. However, in the specimens without stitch lines, the interlaminar cracks propagated much further than those with, Figure 4.26 shows a possible increase in interlaminar toughness from the addition of a stitch line.

Also, failure locations were more variable within specimen set 2. Tension and compression failures were located underneath loading noses, whereas buckling and shear failures were located between the loading noses.

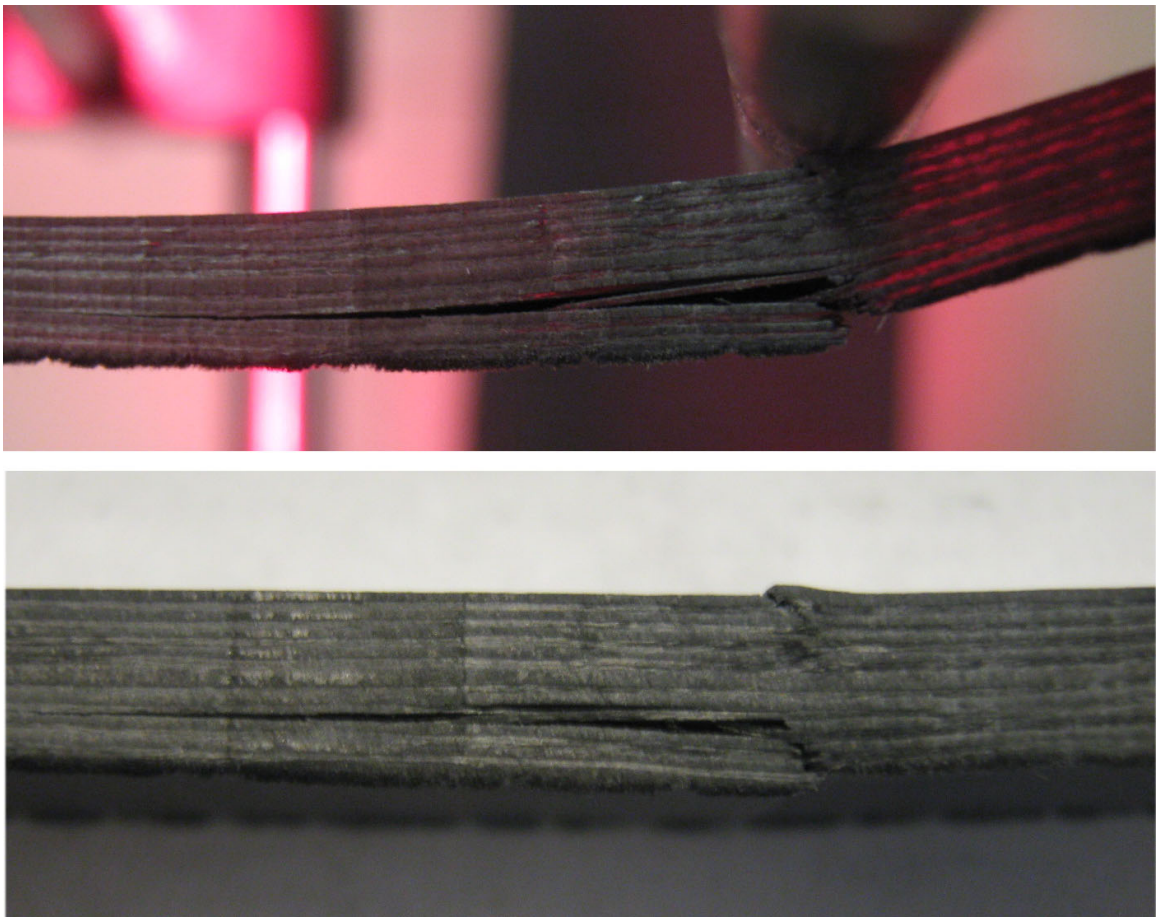


Figure 4.24: Initial tension failure of bottom surface followed by interlaminar shear during test (top) and after test (bottom), P3_LSB4

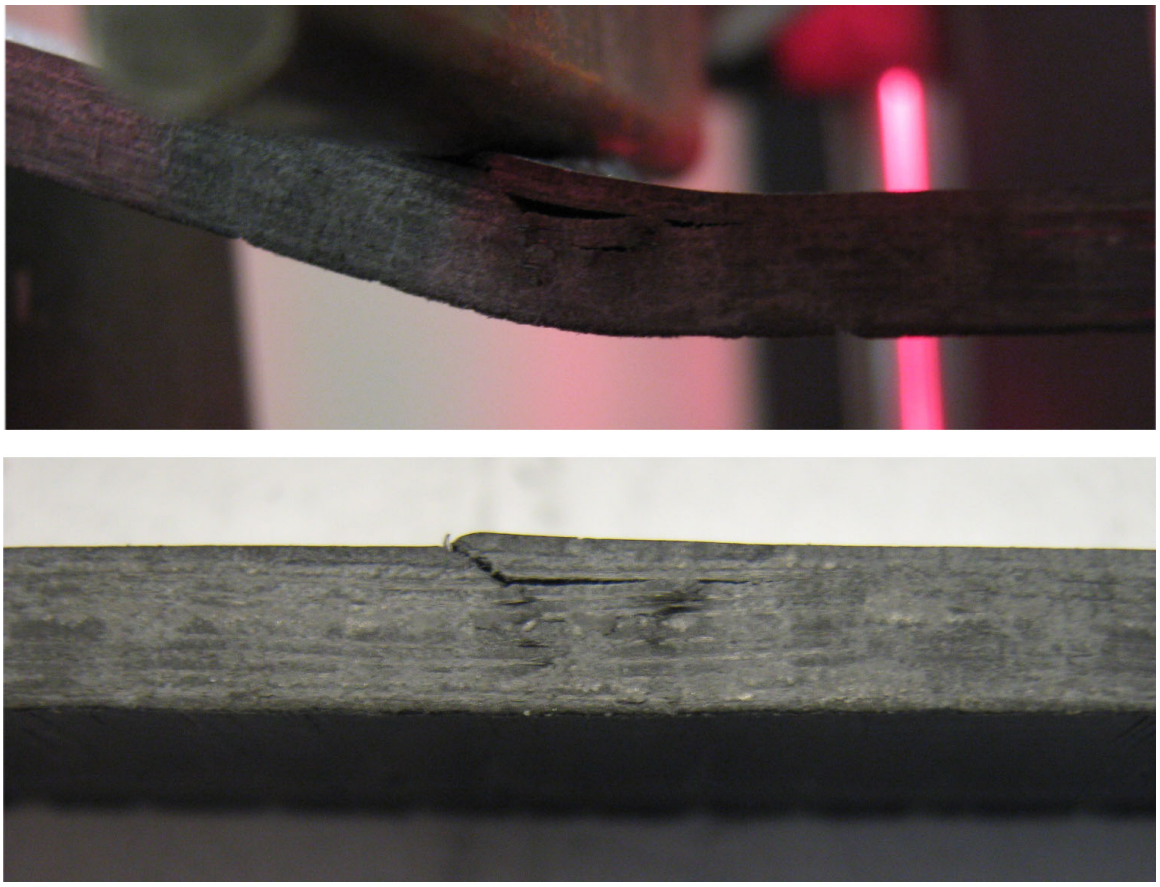


Figure 4.25: Initial compression failure of top surface followed by interlaminar shear during test (top) and after test (bottom), P3_LSB5

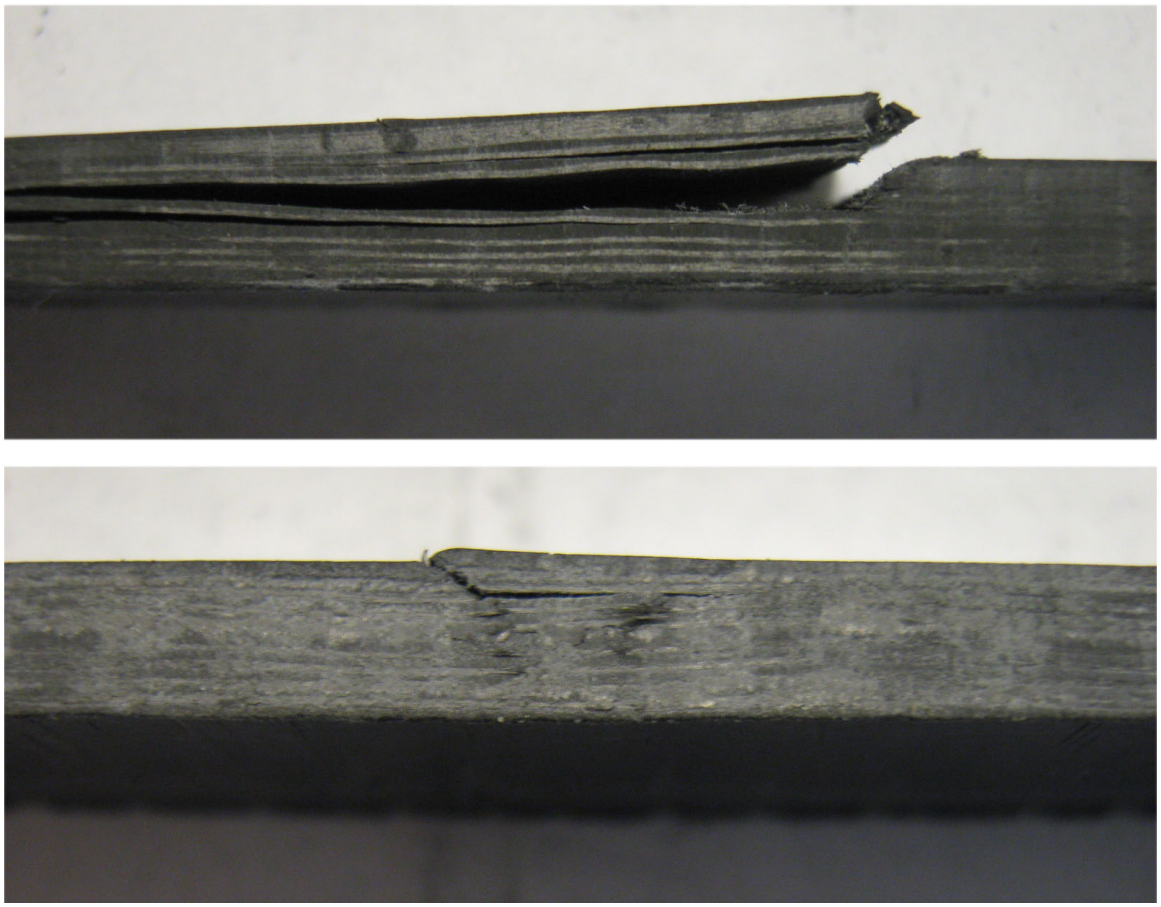


Figure 4.26: Interlaminar shear cracks without stitch line (top), P2_LSB6 and with stitch line (bottom), P3_LSB5

Tensile flexural failures were also observed in samples P2_LSB4 and P2_LSB5. Tensile cracks initiated on the bottom surface and propagated through the thickness leading to complete vertical separation, Figure 4.27.

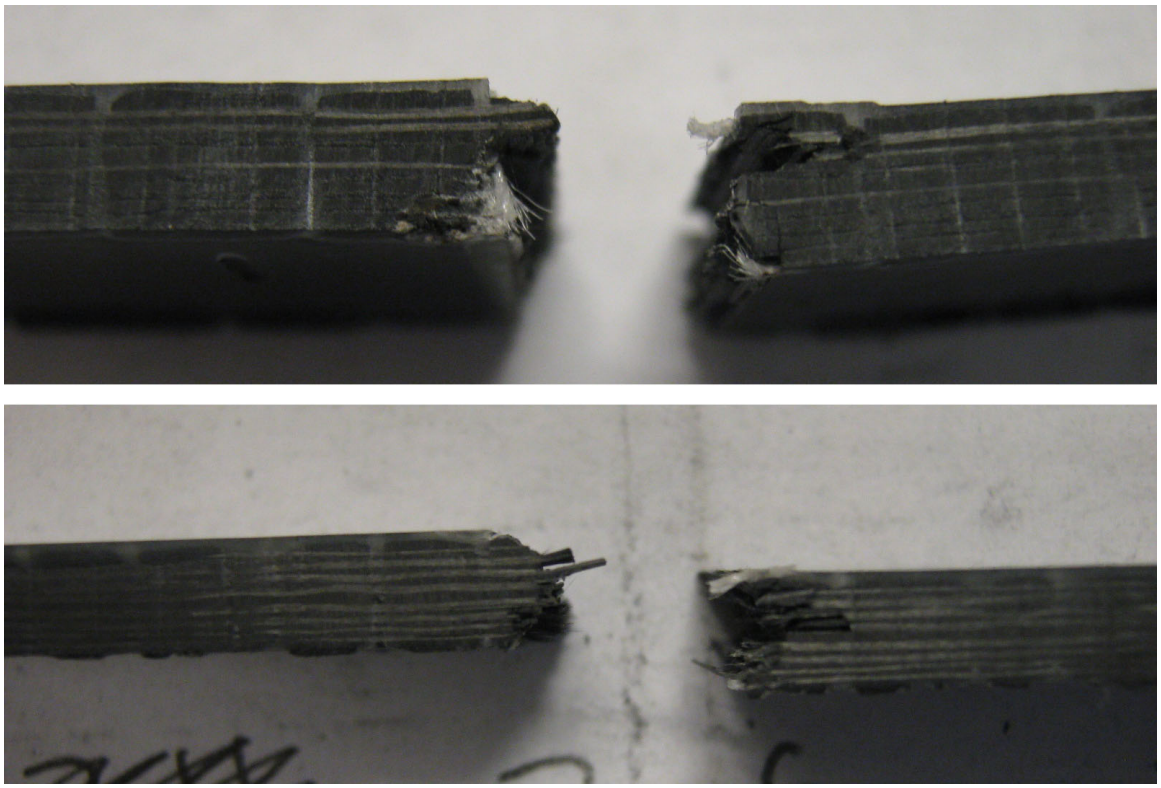


Figure 4.27: Tensile flexural failure causing complete separation, P2_LSB4 (top) and P2_LSB5 (bottom)

4.2.1.3 Specimen Set 3: $v_{f,c}$ = 63.5%, Tested Along 0º Reference Direction

Specimen set 3 tested flat plates 4, 5 and 6 with laminating sequence $[[0°/90°]_5/0°]_S$. The specimens were cut such that their length was parallel to the fibre direction of the outer layers. All specimens featured stitch lines running across the width, spaced approximately 25 mm. Since specimen set 3 features higher fibre volume fractions, flexural moduli and strengths were expected to increase compared to specimen set 1. However, the increase in fibre volume fraction led to an increase in defects in plates caused from problematic resin impregnation. Therefore, dry spots were more common in specimen set 3 leading to unpredictable test results. Table 4.12 presents flexural properties and failure codes from Table 3.3 while Table 4.13 contains statistical data for each plate in specimen set 3.

Flexural moduli ranged from 41.4 GPa to 67.8 GPa with an average of 57.3 GPa and a standard deviation of ±8.99 GPa. The average flexural modulus of specimen set 3 reached 72.1 % of the theoretical value and was slightly lower than that of specimen set

1. This was not expected from the increase in fibre volume fraction, but plates 4 and 5 featured increased dry areas. However, the average flexural modulus of specimens from plate 6 was significantly greater at 66.4 GPa than those of plates 4 and 5 at 53.4 GPa and 52.0 GPa respectively. This likely resulted from a combination of a more complete injection with thorough wetting, and tighter mould closure leading to better compaction and thickness tolerance. Although average flexural moduli were very similar between specimen sets 1 and 3, the values for specimen set 3 were more variable. This was caused from the inconsistent resin infusion quality of plates 4, 5 and 6 which featured a higher fibre volume fraction.

Flexural strengths ranged from 212 MPa to 798 MPa with an average of 613 MPa and standard deviation of ±210 MPa. However, seven of the nine specimens achieved a maximum stress level greater than 583 MPa and within ±27 % of the average, whereas the two specimens which failed prematurely were outside ±48 % of the average. The average flexural strength of 613 MPa for specimen set 3 was 6.6 % higher than the equivalent value for specimen set 1. However, the results were much more variable within set 3 with a standard deviation of ±210 MPa compared with ±45.7 within set 1. If the outliers, specimens P5_LSB2 and P5_LSB3 were removed from the set, the average flexural strength becomes 711 MPa and standard deviation of ±81.1 MPa. These values are much closer to the expected values for specimen set 3 and are more representative of the specimen set. Specimens furthest from the inlet failed at a significantly lower stress level compared to those closer to the centre of the plate. The variation caused by distance from the centre of the plates was likely due to an increased occurrence of dry spots near the outlets as discussed in Section 4.1.1.

Table 4.12: Flexural properties and failure codes for specimen set 3

Specimen	Width [mm]	Thickness [mm]	Flexural Strength [MPa]	Flexural Modulus [GPa]	Failure Code
P4_LSB1	13.00	5.10	616	47.5	M(CS)-B-V(TLR)
P4_LSB2	13.13	4.87	726	51.6	M(BTS)-AB-TBL
P4_LSB3	12.31	4.51	583	61.0	M(CS)-L-MR
P5_LSB1	12.34	4.76	747	57.9	M(BS)-B-T
P5_LSB2	12.18	4.64	326	56.8	M(SB)-B-V(MT)
P5_LSB3	11.61	4.29	212	41.4	S-B-M
P6_LSB1	13.19	4.34	798	65.0	M(BS)-B-V(TM)
P6_LSB2	13.51	4.29	794	67.8	M(BS)-B-V(TM)
P6_LSB3	13.08	4.20	714	66.4	S-B-M

Table 4.13: Statistical values from specimen set 3 flexural properties

Plate	Flexural Strength [MPa]		Flexural Modulus [GPa]	
	Average	Standard Deviation	Average	Standard Deviation
P4	641	±75.0	53.4	±6.92
P5	428	±282	52.0	±9.21
P6	769	±47.5	66.4	±1.37
All	613	±210	57.3	±8.99

All specimens within specimen set 3 failed by interlaminar shear or a combination including shear. This may suggest that the span-to-thickness ratio may have been too small as axial stresses did not control failure. However, in seven of the nine specimens interlaminar shear cracks were preceded by buckling, compressive or tensile cracks either near stitch lines or at a loading nose. Figure 4.28 shows an interlaminar crack preceded by buckling near a stitch-line.

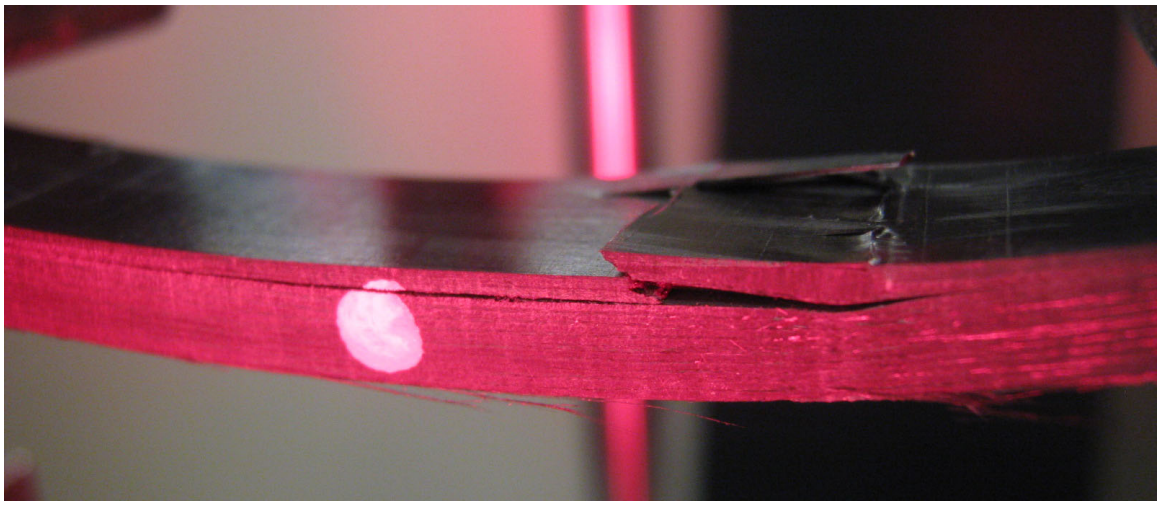


Figure 4.28: Combined failure mode: buckling followed by interlaminar shear, P5_LSB1

Two specimens, both taken furthest from the inlet, failed solely by interlaminar shear, P5_LSB3 and P6_LSB3. P5_LSB3 failed prematurely from interlaminar shear cracking from the centre to the left end, Figure 4.29, whereas specimen P6_LSB3 failed at a much higher stress state with multiple layers failing underneath both loading noses, Figure 4.30. Specimen P5_LSB3 featured a significant amount of dry fibres within the thickness which led to premature failure, whereas specimen P6_LSB3 showed good impregnation along with minimal out-of-plane fibre distortion. The decreased out-of-plane fibre distortion may not have created a resin rich zone sufficiently large to cause premature failure at the stitch line, as with other samples.

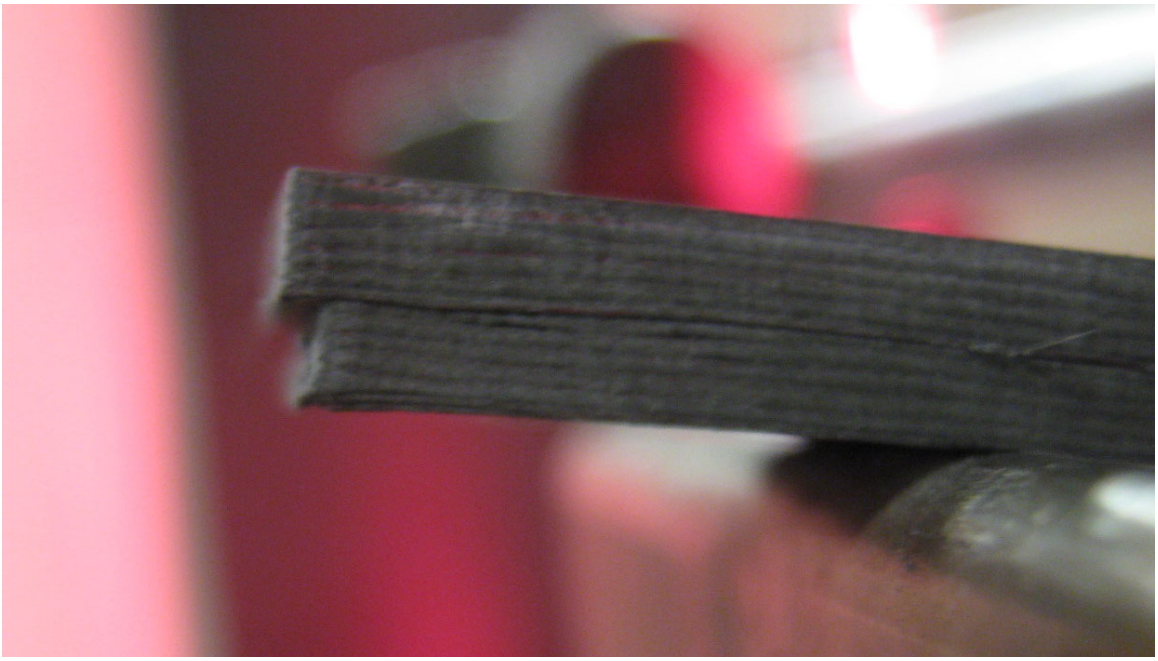


Figure 4.29: Premature interlaminar shear failure, P5_LSB3

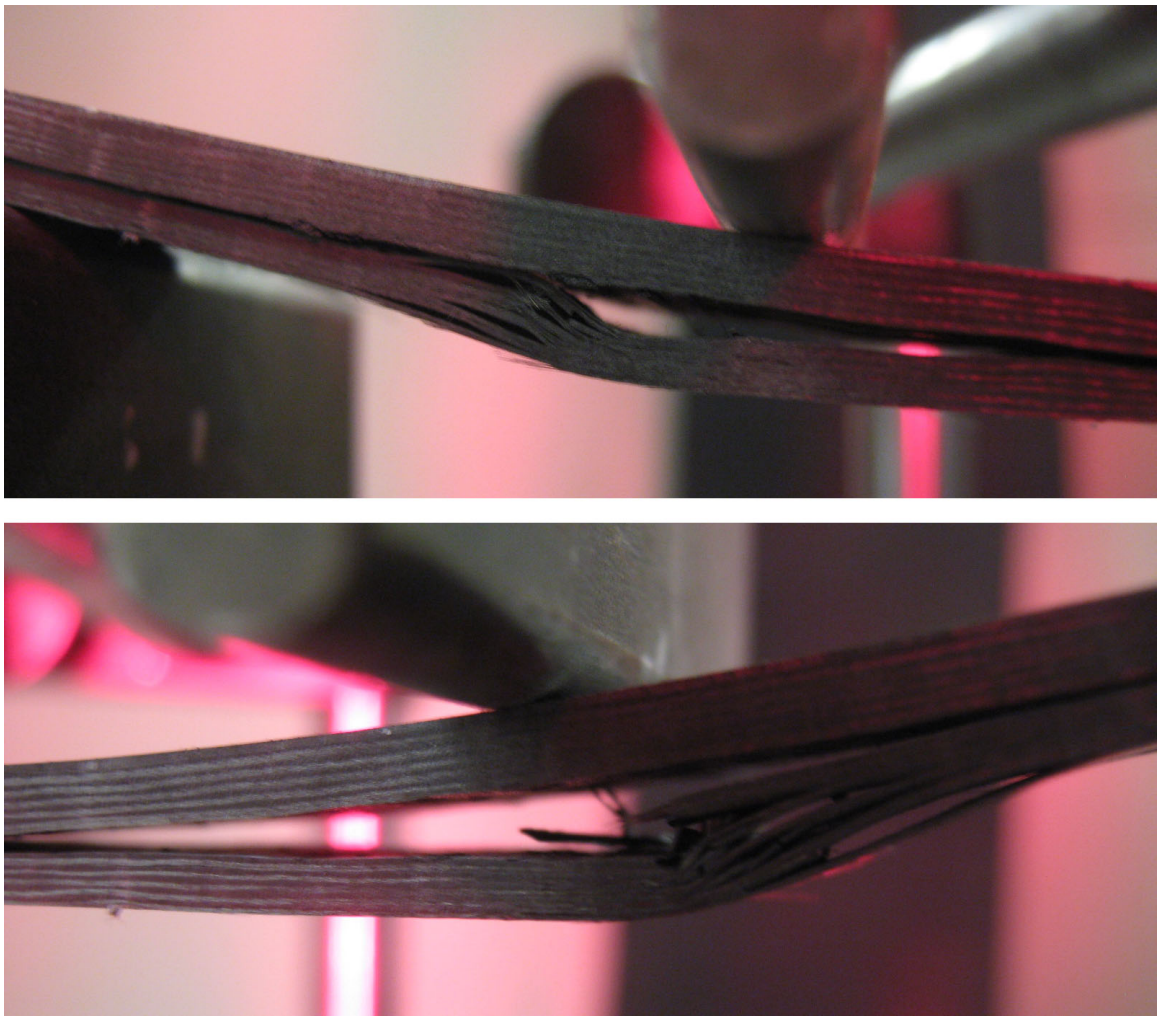


Figure 4.30: Interlaminar shear failure of multiple layers under left (top) and right (bottom) loading noses, P6_LSB6

However, stitch lines may not only contribute to crack initiation, as it was observed while testing specimens P5_LSB2 and P5_LSB3 that shear crack propagation was halted at a stitch line, Figure 4.31. This interlaminar shear toughening effect was not seen in other specimens; however, as this occurred with non-structural stitching proper structural stitching may potentially lead to a significant improvement.

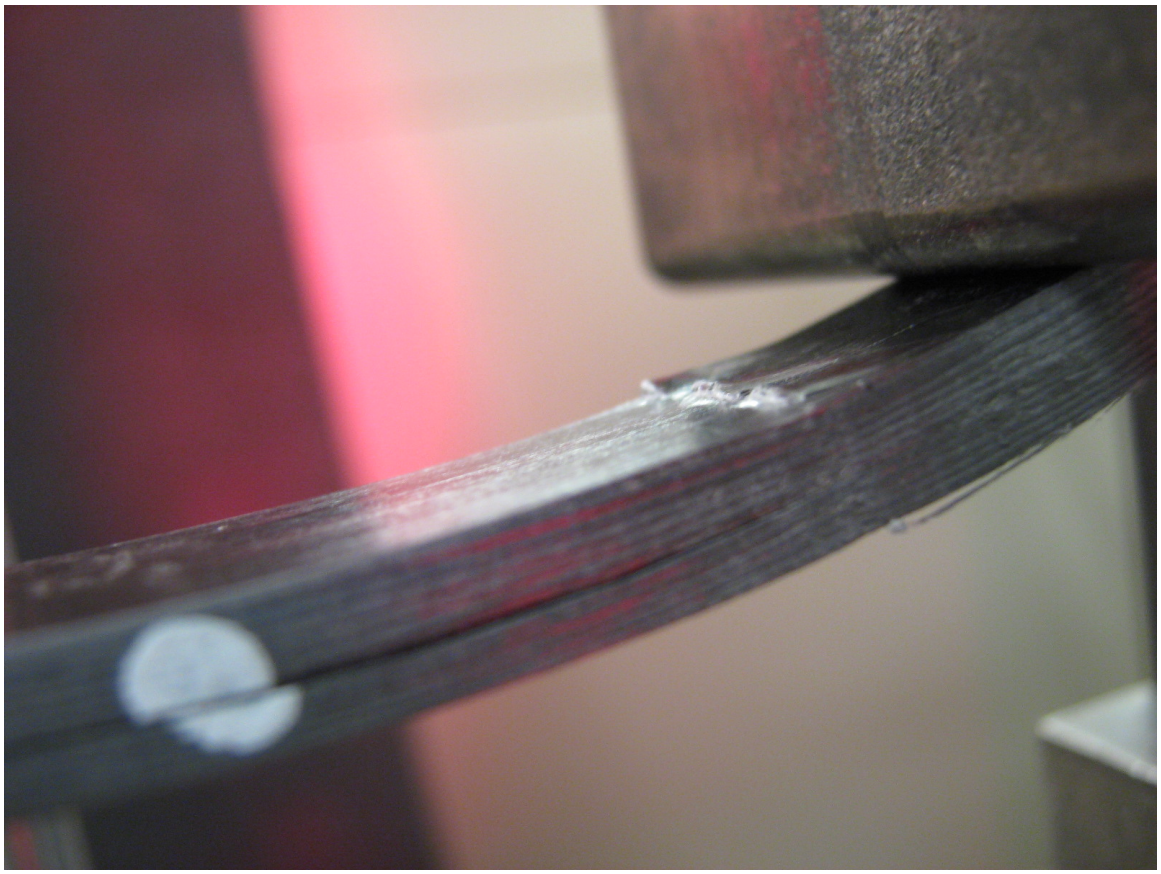


Figure 4.31: Interlaminar shear crack propagation halted at stitch-line, P5_LSB2

4.2.1.4 Specimen Set 4: $v_{f,c}$ = 63.5%, Tested Along 90º Reference Direction

Specimen set 4 tested flat plates 4, 5 and 6 with same $[[0°/90°]_5/0°]_S$ laminating sequence as specimen set 3. However, specimens were cut in a direction perpendicular to that of specimens in set 3 such that specimen length corresponded to the transverse fibre direction of the outer layers. Table 4.12 presents flexural properties, and failure codes from Table 3.3 while Table 4.13 contains statistical data for specimen set 4. Specimens were cut in a direction similar to those in specimen set 2; however, none included longitudinal stitch lines.

Specimens reached flexural strengths from 255 MPa to 751 MPa with an average value of 592 MPa and standard deviation of ±190 MPa. The average flexural strength of specimen set 4 was 3.3 % higher than the equivalent value for specimen set 2. However, the maximum flexural strength observed within specimen set 4 was 17 % greater than the

maximum flexural strength within specimen set 2. Specimens P4_LSB6 and P5_LSB6, which were cut furthest from the inlet, experienced a severe reduction in flexural strength compared to the other specimens within the same plate. This reduction was a result of decreased resin saturation as flow progressed to the outer edges of the mould, Figure 4.32.

Flexural moduli ranged from 31.9 GPa to 59.4 GPa with an average of 43.2 GPa, standard deviation of ±9.18 GPa and reached only 72.7 % of the theoretical flexural modulus. Large variations in thickness led to large variations in flexural moduli between plates 4 and 6 with average thicknesses of 4.94 mm and 4.28 mm respectively.

Table 4.14: Flexural properties and failure codes for specimen set 4

Specimen	Width [mm]	Thickness [mm]	Flexural Strength [MPa]	Flexural Modulus [GPa]	Failure Code
P4_LSB4	12.05	5.13	723	36.0	S-B-M
P4_LSB5	13.16	5.10	578	31.9	M(CS)-B-V(TR)
P4_LSB6	11.44	4.86	255	37.6	M(BS)-B-V(TR)
P5_LSB4	13.08	4.79	751	44.1	M(CS)-B-V(TM)
P5_LSB5	12.67	4.67	747	35.4	M(BS)-B-V(TM)
P5_LSB6	11.98	4.34	291	42.0	S-B-M
P6_LSB4	12.35	4.36	628	48.1	S-B-M
P6_LSB5	12.68	4.31	721	53.9	M(BS)-LB-V(TM)
P6_LSB6	13.15	4.15	631	59.4	S-B-M

Table 4.15: Statistical values from specimen set 4 flexural properties

Plate	Flexural Strength [MPa]		Flexural Modulus [GPa]	
	Average	Standard Deviation	Average	Standard Deviation
P4	519	±240	35.2	±2.95
P5	596	±265	40.5	±4.56
P6	660	±52.7	53.8	±5.67
All	592	±190	43.2	±9.18

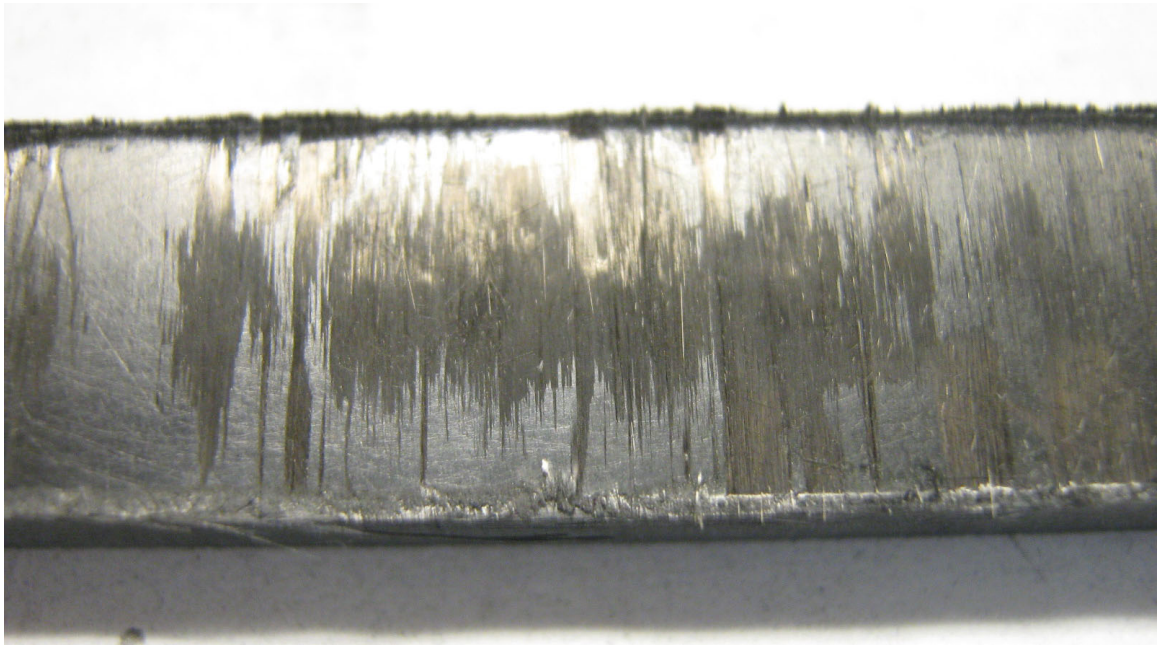


Figure 4.32: Dry spots from poor resin saturation, P4_LSB6

All specimens within set 4 failed with some degree of interlaminar shear. As with specimen set 3, span-to-thickness ratios changed throughout testing as specimen thickness increased. Early failure, as observed within specimen P4_LSB6, initiated as a crack caused by buckling of the top surface near a dry fibre region followed by propagation through the thickness, which led to crack propagation between plies and eventually interlaminar shear failure, Figure 4.33.

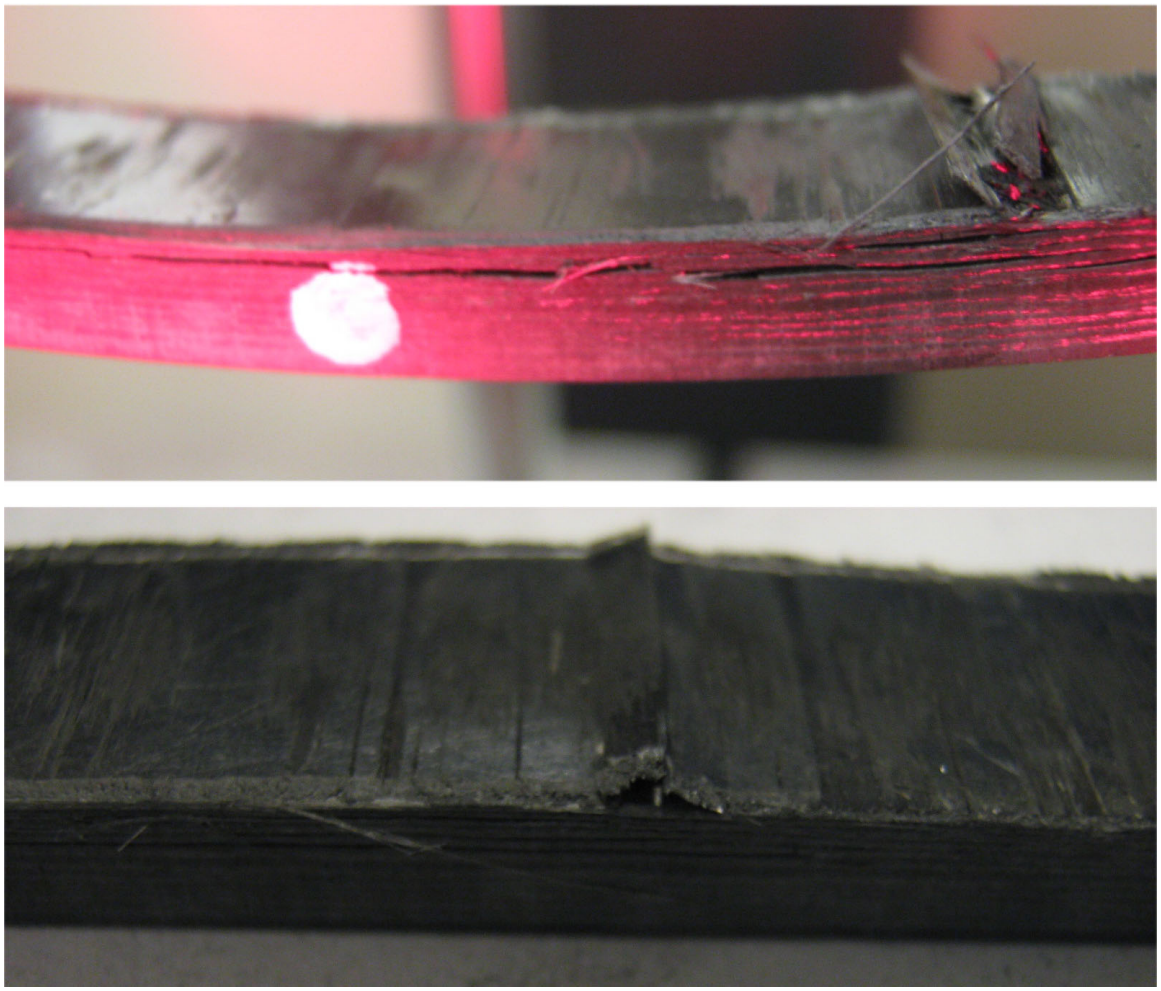


Figure 4.33: Buckling near dry fibre region during test (top) and after test (bottom), P4_LSB6

Buckling near the loading nose occurred in specimen P6_LSB5, Figure 4.34. The crack initiated through the thickness, then changed directions and propagated along the specimen length leading to interlaminar shear failure. This type of failure was undesired since the specimen failed prematurely from localized contact stresses caused by the loading nose.

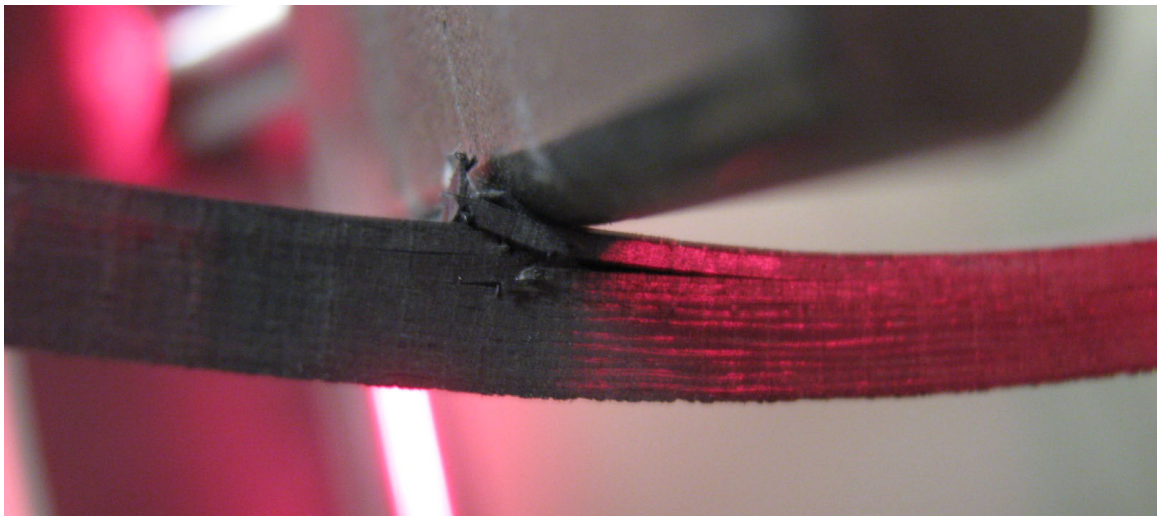


Figure 4.34: Buckling near left loading nose, P6_LSB5

4.2.2 Short Span Three-Point Bending

Short span three-point bending tests were conducted on specimens to quantify short beam shear strength as an indicator of interlaminar shear strength. Similar to long span four-point bending, four specimen sets were tested to determine load resistance as a function of loading direction and fibre volume fraction. Characteristics of the specimen sets defined for long span four-point testing were the same as those of specimens used for short span three-point testing; dimensions differed as highlighted below. Short beam shear strength and failure modes were recorded for statistical analysis. Interlaminar shear failure and inelastic deformation failure modes, as described in Section 3.2.2, are labelled as ILS and ID respectively in following tables. Average short beam shear strengths for specimen sets appeear in Table 4.16. The short beam shear strength seemed to have little dependance on fibre volume fraction, which was in agreement with trends reported by Lavengood [73].

Table 4.16: Short beam testing results

Specimen Set	$v_{f,c}$	Short Beam Shear Strength [MPa]	
		Average	Standard Deviation
5	52 %	51.9	±2.81
6	52 %	42.3	±4.64
7	63.5 %	47.2	±9.81
8	63.5 %	45.3	±6.80

Approximate experimental values from literature are shown in Table 4.17 for comparison with above results. Short beam shear strengths from this work are on average 22 % lower than values reported by Ghiorse for a cross-ply Hercules AS4/3501-6 prepreg and 38 % lower than values reported by Beier et al. from stitched layers of 0°/90° NCF[48, 74]. Results obtained from components tested during this work showed that improvements are required in order to achieve results comparable to typical materials currently used in the aerospace industry.

Table 4.17: Short beam shear strength values obtained from literature

Material Description	Laminating Sequence	Short Beam Shear Strength [MPa]
Hercules AS4/3501-6 prepreg [74] (nominal thickness = 2.08 mm)	$[0^o/90^o]_{4s}$	~ 60
Biaxial layers of stitched NCF (Tenax HTS 12 K fibre with Hexcel HEXFLOW RTM6 resin;v_f =53 - 55%; nominal thickness = 2.0) [48]	$[0^o/90^o]_{4s}$	~ 70

Load-deflection curves for all short span three-point bending specimens are shown in Appendix B.

4.2.2.1 Specimen Set 5: $v_{f,c}$ = 52%, Tested Along 0º Reference Direction

Specimen set 5 tested flat plates 1, 2 and 3 with laminating sequence $[[0°/90°]_4/0°]_S$. Specimens were cut such that specimen length was parallel to the fibre direction in the outer layers. Table 4.18 contains short span properties and failure codes for specimen set 5 and Table 4.19 contains statistical data. Short beam shear strengths for specimen set

5 ranged from 46.2 MPa to 55.0 MPa and averaged 51.9 MPa with a standard deviation of ±2.81 MPa. Plate locations where the specimens were cut from had no clear effect on the short beam shear strength. Also, average short beam shear strengths had a low standard deviation which shows consistency between plates.

Table 4.18: Short span properties and failure modes of specimen set 5

Specimen	Width [mm]	Thickness [mm]	Short Beam Shear Strength [MPa]	Failure Mode
P1_SSB1	8.74	4.37	53.4	ID & ILS
P1_SSB2	8.68	4.34	53.7	ID & ILS
P1_SSB3	8.62	4.31	51.6	ID & ILS
P2_SSB1	8.62	4.20	46.2	ID & ILS
P2_SSB2	8.17	4.14	53.0	ID & ILS
P2_SSB3	8.51	4.10	54.6	ID & ILS
P3_SSB1	8.57	4.41	49.7	ID & ILS
P3_SSB2	8.70	4.41	55.0	ID & ILS
P3_SSB3	8.99	4.35	50.3	ID & ILS

Table 4.19: Statistical values from specimen set 5 short span properties

Plate	Short Beam Shear Strength [MPa]	
	Average	Standard Deviation
P1	52.9	±1.10
P2	53.6	±4.43
P3	51.7	±2.93
All	51.9	±2.81

The dominant failure mode was a combination of inelastic deformation and interlaminar shear. Initially, specimens deformed in an out-of-plane wavy shape typical of inelastic deformation followed by interlaminar cracks, Figure 4.35.

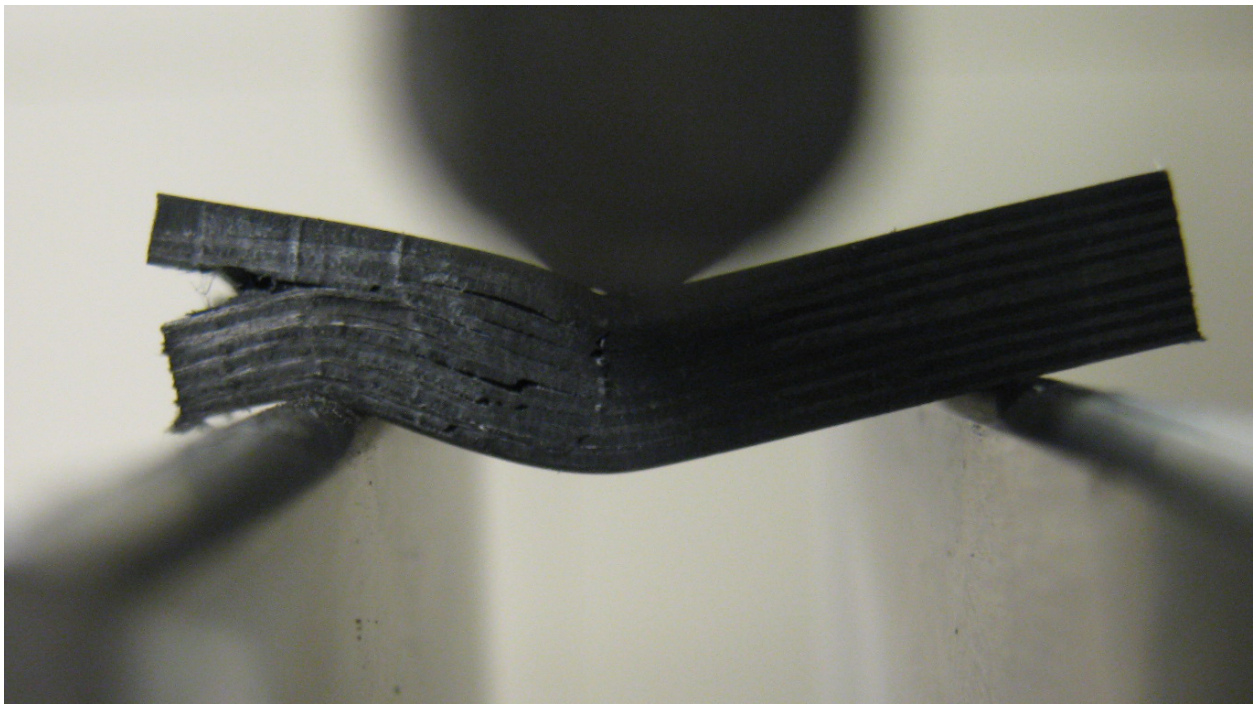


Figure 4.35: Inelastic deformation with combined interlaminar cracks, P2_SSB2

This failure mode was very common throughout testing, and the likely cause of inelastic deformation within this thesis work was displacement of the loading nose. The loading nose occasionally shifted to the left or right during tests, with no obvious preference. The movement of the loading nose generated a horizontal force causing failure on the side of the specimen toward which the loading nose shifted.

Failure planes observed were at approximately $\pm 45^{o}$ within 90^{o} layers, Figure 4.36 which is common with shear failures since the principal stresses occur at $\pm 45^{o}$.

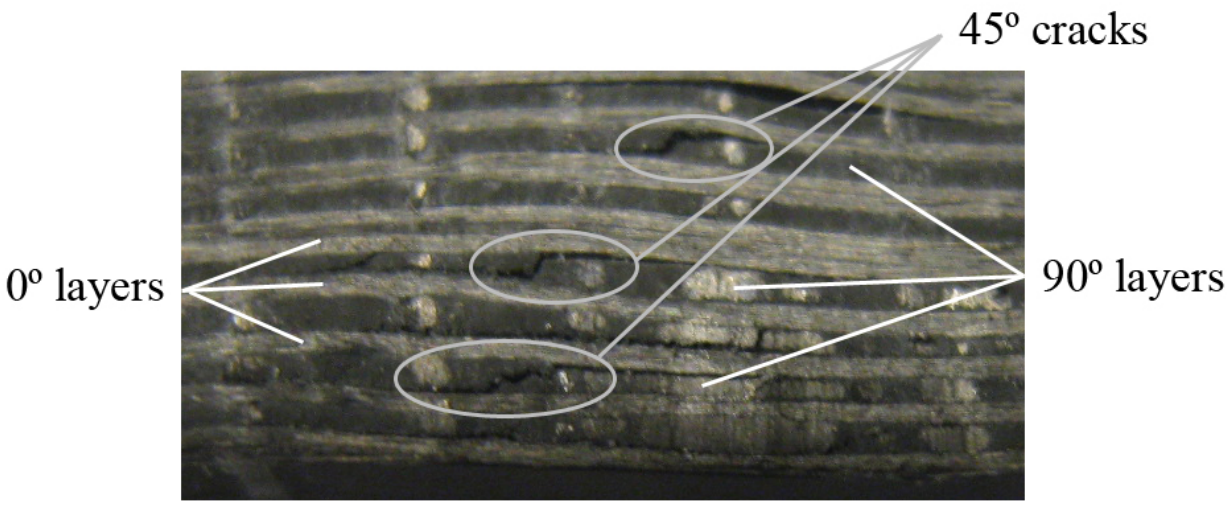


Figure 4.36: Failure of 90º layers at ±45º angle, P2_SSB3

4.2.2.2 Specimen Set 6: $v_{f,c}$ = 52%, Tested Along 90º Reference Direction

Specimen set 6 tested flat plates 1, 2 and 3 with laminating sequence $[[0°/90°]_4/0°]_S$. Specimens were cut in a direction opposite to that of specimens in set 5, such that the length of the specimens correspond to the direction transverse to fibres in the outer layers. Table 4.20 contains short span properties and failure codes for specimen set 6, and Table 4.21 contains statistical data. Short beam shear strengths of specimen set 6 ranged from 36.9 MPa to 50.7 MPa and averaged 42.3 MPa with a standard deviation of ±4.64 MPa. Plates 2 and 3 showed significantly higher short beam shear strengths nearest to the inlet, whereas plate 1 showed no location dependence.

Specimen set 6 showed an 18.5 % decrease in short beam shear strength when compared with specimen set 5, as expected since there is a greater number of transverse fibre layers. Also, as the specimens were cut from the rotated plate, the midplane layers were two stacked 90º layers as opposed to 0º layers in specimen set 5. As discussed above, cracks occured within 90º layers which, combined with the increased number of 90º layers, leads to lower short beam shear strength.

Table 4.20: Short span properties and failure modes of specimen set 6

Specimen	Width [mm]	Thickness [mm]	Short Beam Shear Strength [MPa]	Failure Mode
P1_SSB4	8.65	4.35	36.9	ID & ILS
P1_SSB5	8.62	4.26	43.6	ID & ILS
P1_SSB6	8.69	4.16	36.9	ILS & Tensile
P2_SSB4	8.76	4.24	47.4	ID & ILS
P2_SSB5	8.60	4.20	42.0	ID & ILS
P2_SSB6	8.52	4.15	42.7	ID & ILS
P3_SSB4	8.60	4.34	50.7	ID & ILS
P3_SSB5	8.85	4.29	41.6	ID & ILS
P3_SSB6	8.87	4.29	38.6	ILS & Tensile

Table 4.21: Statistical values from specimen set 6 short span properties

Plate	Short Beam Shear Strength [MPa]	
	Average	Standard Deviation
P1	39.1	±3.86
P2	44.0	±2.97
P3	43.7	±6.30
All	42.3	±4.64

Failure modes observed with specimen set 6 were similar to those in specimen set 5; however two specimens failed from a combination of tensile and interlaminar shear, P1_SSB6, Figure 4.37 and P3_SSB6.

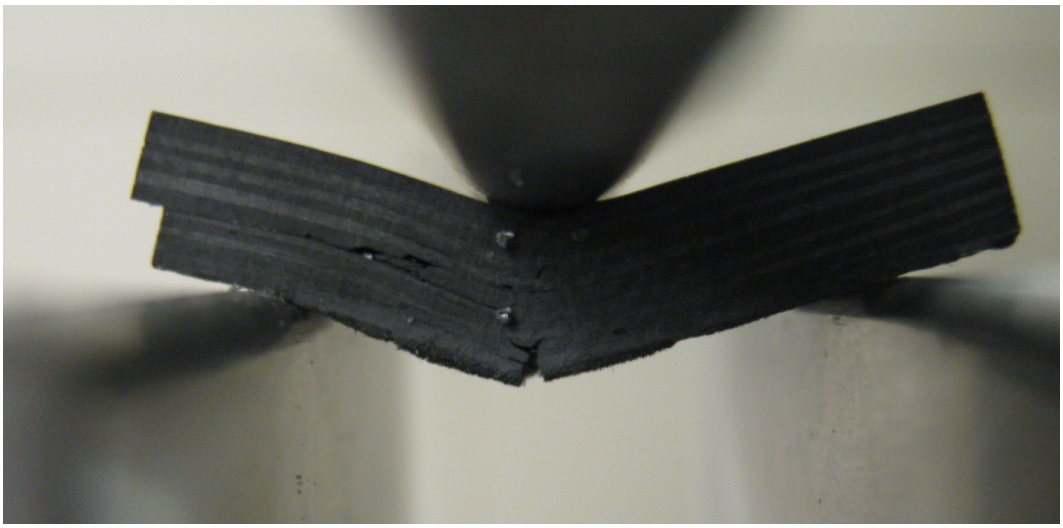


Figure 4.37: Combined tensile and interlaminar shear short beam failure, P1_SSB6

Failure along ±45º planes was also common within specimen set 6. However, there were fewer 0º fibre layers to inhibit crack growth. Figure 4.38 shows larger ±45º cracks within the double 90º layers at the midplane.

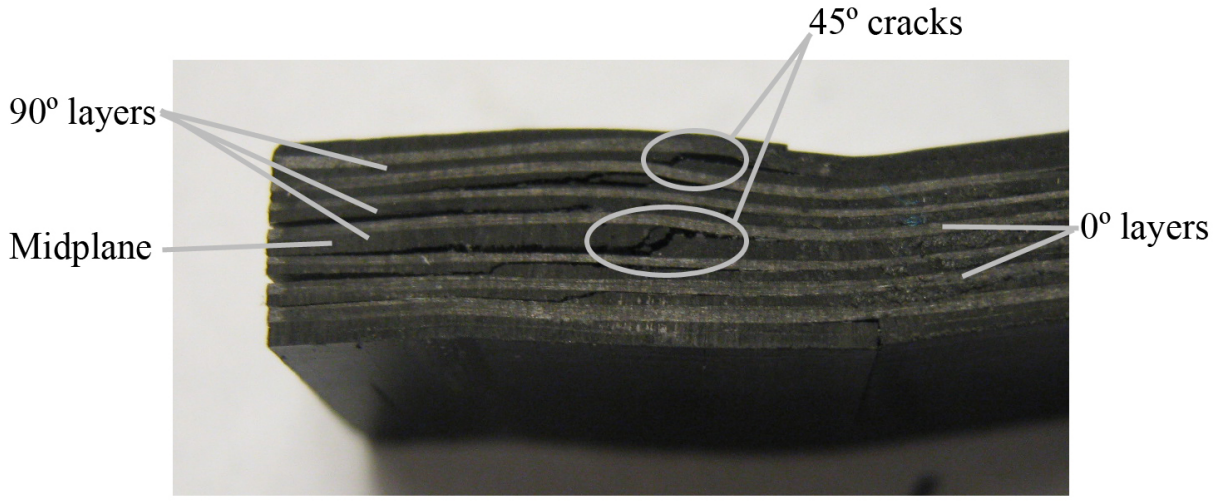


Figure 4.38: ±45º cracks within 90º layers, P2_SSB6

4.2.2.3 Specimen Set 7: $v_{f,c}$ = 63.5%, Tested Along 0º Reference Direction

Specimen set 7 tested flat plates 4, 5 and 6 with laminating sequence $[[0°/90°]_5/0°]_S$. Specimens were were cut such that specimen length was parallel to the fibre direction in

the outer layers. Table 4.22 contains short span properties and failure codes for specimen set 7, and Table 4.23 contains statistical data. Short beam shear strength ranged from 28.9 MPa to 56.7 MPa with an average of 47.2 MPa and a standard deviation of ±9.81 MPa. Plates 4 and 6 showed a significant decrease in short beam shear strength with an increase in distance from the inlet, whereas plate 5 showed little to no change. The average short beam shear strength featured a decrease of 9.06 % compared to specimen set 5 which shows reasonable consistency between plates, considering that the average was skewed by two specimens that failed prematurely.

Table 4.22: Short span properties and failure modes of specimen set 7

Specimen	Width [mm]	Thickness [mm]	Short Beam Shear Strength [MPa]	Failure Mode
P4_SSB1	8.80	5.12	50.9	ID & ILS
P4_SSB2	8.42	4.81	49.9	ID & ILS
P4_SSB3	9.00	4.55	28.9	ILS
P5_SSB1	8.48	4.86	52.2	ID, ILS & Compression
P5_SSB2	8.59	4.61	54.3	ID & ILS
P5_SSB3	8.65	4.45	56.7	ID & ILS
P6_SSB1	8.86	4.39	52.2	ID & ILS
P6_SSB2	8.77	4.28	47.9	ID & ILS
P6_SSB3	8.85	4.19	32.3	ID & ILS

Table 4.23: Statistical values from specimen set 7 short span properties

Plate	Short Beam Shear Strength [MPa]	
	Average	Standard Deviation
P4	43.2	±12.4
P5	54.4	±2.26
P6	44.1	±10.46
All	47.2	±9.81

Failures similar to those previously observed were seen within specimen set 7. However, instead of a tensile failure one samples experienced compressive failure. Specimen

P5_SSB1 suffered compressive cracks underneath the loading nose, Figure 4.39.

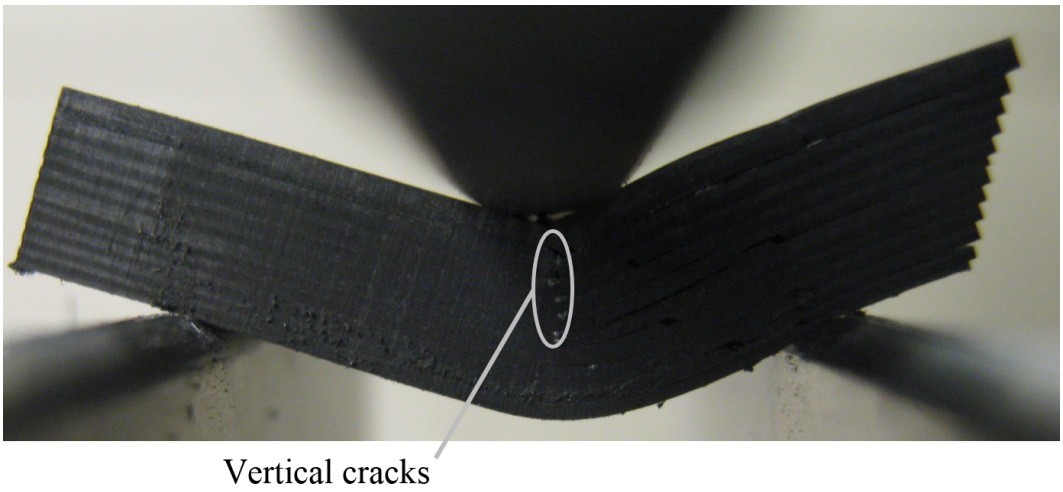


Figure 4.39: Compressive cracks underneath loading nose and ILS failure towards right end, P5_SSB1

4.2.2.4 Specimen Set 8: $v_{f,c} = 63.5\%$, Tested Along 90º Reference Direction

Specimen set 8 tested flat plates 4, 5 and 6 with same laminating sequence as specimen set 7, $[[0°/90°]_5/0°]_S$. However, specimens were cut opposite to those in set 7 such that the length of the specimens corresponds to the direction transverse to the fibres in the outer layers. Table 4.24 contains short span properties and failure codes for specimen set 8 and Table 4.13 contains statistical data. Short beam shear strength ranged from 30.8 MPa to 51.2 MPa with an average of 45.3 MPa and standard deviation of ±6.80 MPa. Two of the three plates experienced lower short beam shear strengths for specimens taken further away from the inlet. However, plates 4 and 5 within specimen set 8 had decreasing short beam shear strengths based on distance from the inlet, whereas within specimen set 7, plates 4 and 6 had decreasing short beam shear strengths based on distance from the inlet. The average short beam shear strength was 7 % greater than the average short beam shear strength for specimen set 6, which featured a similar orientation with a double thickness 90º midplane layer.

Table 4.24: Short span properties and failure modes of specimen set 8

Specimen	Width [mm]	Thickness [mm]	Short Beam Shear Strength [MPa]	Failure Mode
P4_SSB4	8.76	5.24	47.2	ID
P4_SSB5	8.13	5.14	45.4	ID & ILS
P4_SSB6	9.00	4.89	37.4	ILS & Compression
P5_SSB4	8.48	4.89	47.4	ID & ILS
P5_SSB5	8.92	4.67	48.8	ID & ILS
P5_SSB6	8.76	4.36	30.8	ID & ILS
P6_SSB4	8.92	4.41	49.7	ID & ILS
P6_SSB5	8.64	4.32	50.0	ID
P6_SSB6	8.52	4.16	51.2	ID & ILS

Table 4.25: Statistical values from specimen set 8 short span properties

Plate	Short Beam Shear Strength [MPa]	
	Average	Standard Deviation
P4	43.3	±5.20
P5	42.3	±10.0
P6	50.3	±0.817
All	45.3	±6.80

Here again, failure was consistent with previous specimen sets with inelastic deformation failure preceding other modes.

4.2.3 Drop Weight Impact

Six specimens were subjected to out-of-plane localized impact to monitor absorbed energy, plate deflection and physical damage imparted on the specimens. The tests were performed at a velocity of 2.9 $\frac{\text{m}}{\text{s}}$ and an impact energy level of 25.9 J which exceeded the elastic response level of the material. Figure 4.40 shows load vs. time curves for specimens P1_IMP and P5_IMP. The maximum load for P5_IMP was greater than for P1_IMP. However, the contact time of P1_IMP was longer than for P5_IMP. Initial oscillations

were resonance of the testing equipment, however the oscillations above ~4000N indicate damage, likely intraply cracking or delamination. Load vs. time curves and load vs. deflection curves for all drop-weight impact specimens are shown in Appendix C and Appendix D respectively.

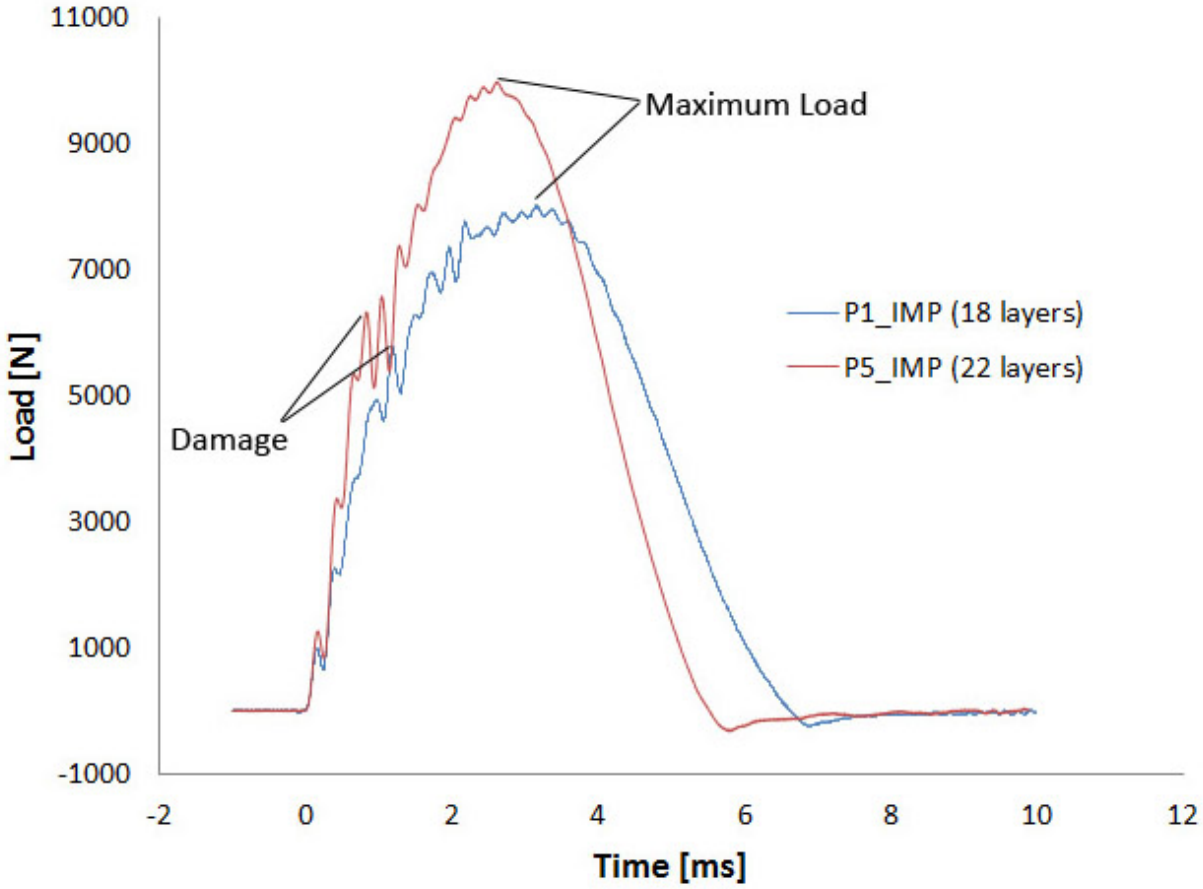


Figure 4.40: Load vs. time curves for impacted specimens P1_IMP and P5_IMP

Load vs. deflection curves show the load-unload impact cycle and allow determining energy levels absorbed by the specimens. Load vs. deflection curves from similar 18 layer specimens P1_IMP and P2_IMP are shown in Figure 4.41. The changes in slopes, of the linear fits, indicate a decrease in stiffness as deflection increases. Deflection accounts for both the elastic plate deformations, and plate indentation characterized by matrix crushing and fibre breakage. Five of the six specimens featured a distinct knee section where the local stiffness changes abruptly, as in the load vs. deflection curve for P2_IMP. However, the load-deflection curve for P3_IMP featured a more gradual stiffness change.

P3_IMP was the only plate impacted directly on a stitch-line with a resin rich zone, which likely altered plate indentation characteristics.

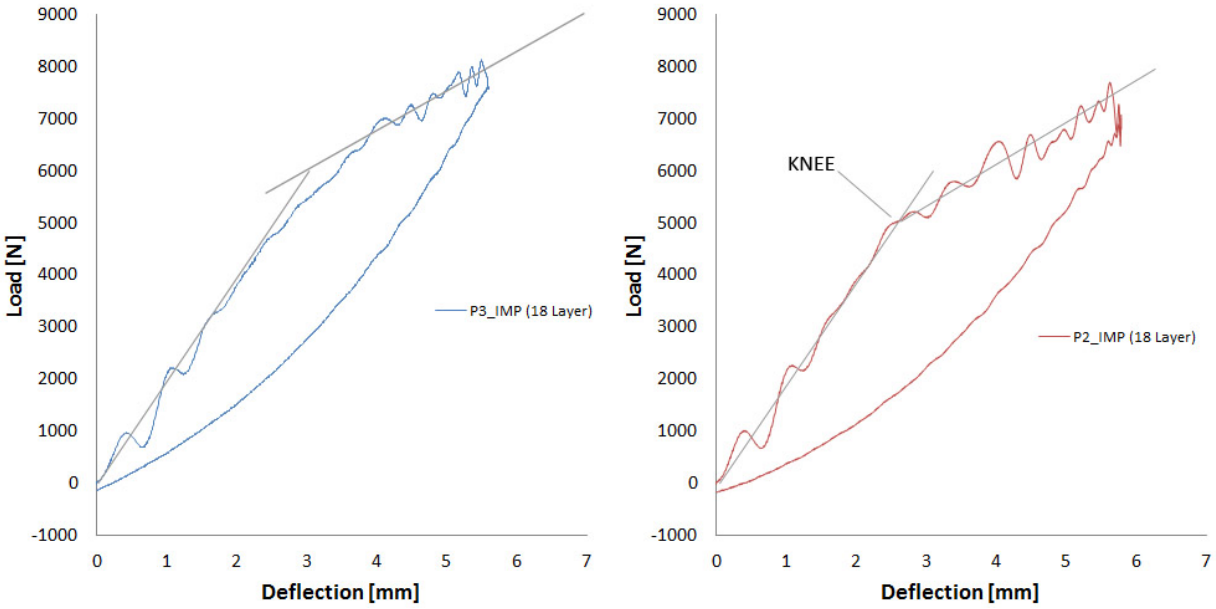


Figure 4.41: Load vs. Deflection curves for specimens P3_IMP (left) and P2_IMP (right)

Drop weight impact testing results are shown in Table 4.26. The maximum load and absorbed energy values have been normalized, dividing by thickness, Table 4.27. Statistical data from the drop weight impact results are presented in Table 4.28.

Maximum load values were greater while total absorbed energy values were lower for specimens from plates 4-6. Therefore plates 4-6 exhibit a stronger impact resistance. Dents were on average 57 % deeper for specimens from plates 1-3 compared to those from plates 4-6, indicating a higher degree of damage within specimens 1-3.

It is difficult to conclude whether the increased impact resistance within plates 4-6 was due to the increased fibre volume fraction, increased thickness, or both. However, noticing that the thickness of specimen P6_IMP is similar to thickness of plates 1-3 whilst achieving greater normalized maximum load values, it is very likely that the plates with a higher fibre volume fraction are more resistant to impact.

Table 4.26: Drop weight impact testing data ($m_{dh} = 6.14$ kg, $H = 0.432$ m)

Plate	Thickness [mm]	Target v_f	Maximum Load [N]	Total Absorbed Energy [J]	Dent Depth [mm]
1	4.19	52 %	8024.0	10.144	0.381
2	4.17	52 %	7701.5	11.743	0.457
3	4.14	52 %	8132.7	9.917	0.279
4	4.53	63.5 %	10089.4	9.727	0.178
5	4.42	63.5 %	9987.1	9.173	0.127
6	4.15	63.5 %	9487.6	10.096	0.178

Table 4.27: Normalized impact data

Plate	Normalized Maximum Load $[\frac{N}{mm}]$	Normalized Total Absorbed Energy $[\frac{J}{mm}]$
1	1914	2.419
2	1850	2.819
3	1964	2.395
4	2230	2.150
5	2260	2.075
6	2286	2.433

Table 4.28: Statistical data from drop weight impact testing

Plates	Thickness		Normalized Maximum Load $[\frac{N}{mm}]$		Normalized Total Absorbed Energy $[\frac{J}{mm}]$		Dent Depth [mm]	
	Average	Std. Dev.	Average	Std. Dev.	Average	Std. Dev.	Average	Std. Dev.
1-3	4.170	±0.026	1909	±57.81	2.545	±0.2381	0.373	±0.0892
4-6	4.365	±0.190	2258	±28.25	2.219	±0.1886	0.161	±0.0293

Similar testing was performed by Winkel and Adams in which AS4/3501-6 prepreg components were tested using drop-weight impact testing at slightly lower initial energy levels than was used for this work. Material descriptions and normalized impact data from Winkel and Adams are shown in Figure 4.42 [64]. The experimental normalized load for

all plates in this work was found to be greater than those from literature. However, since the energy levels were slightly lower within literature, it is difficult to conclude based solely on maximum impact load. Whereas, the normalized absorbed energy from plates in this work was much lower than the absorbed energy found within literature. Therefore, the damage resistance of plates manufactured in this thesis work was superior to those from literature since those from literature absorbed more energy, indicating more damage from a even lower initial energy level.

Table 1. Average plate thicknesses and fibre volumes

Material	Lay-up	Average thickness* (mm)	Average fibre volume** (%)
AS4 graphite			
Cross-ply	$[0/90]_{5s}$	3.00 (0.05)	42.8 (0.02)
Fabric	$[0/90]_{10}$	2.16 (0.02)	49.7 (0.02)

Table 5. Normalized impact force and energy values*

Composite material system	Normalized force, P_m/t (kN mm^{-1})	Normalized maximum energy E_m/t (J mm^{-1})
AS4 graphite/epoxy		
10-ply cross-ply	1.07	2.92
10-ply fabric	1.21	3.94

Figure 4.42: Material description and normalized impact data for AS4/3501-6 prepreg [64]

Visual observation was also important in determining and understanding the impact behaviour of the PMC flat plates. All plates featured a spherical indent from the impactor tip with cracks progressing outwards either along the fibre direction or transverse to the fibres, and additional cracking or splitting on the bottom surface.

Interestingly, surface cracks on the impacted face of the plates were aligned transverse to the fibres, whereas surface cracks on the back side were parallel to the fibres, Figure 4.43. This makes it difficult to conclude which type of damage is present within the plate.

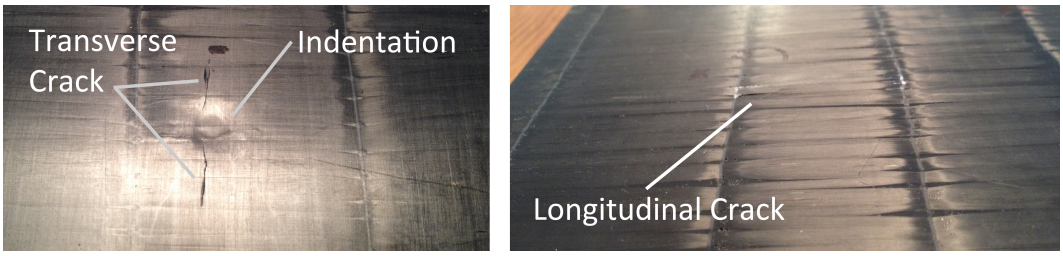


Figure 4.43: Images of impact surface (left) and bottom surface (right), P2_IMP

Also, it was noticed that plates 4-6 which showed better impact resistance based on testing data, featured longer transverse cracks, up to 70 mm long on the impacted surface,

than plates 1-3 with cracks up to 25 mm, Figure 4.44. However, there was significant damage, cracking and splitting, seen on the bottom surfaces of plates 1-3 and very little on the bottom surfaces of plates 4-6, Figure 4.45. Comparisons of crack patterns outlines the difficulty of visually inspecting for impact damage if only one surface is visible. Plates 1-3 featured shorter cracks on the impact surface, indicating less damage, than plates 4-6 , however bottom surfaces of plates 1-3 showed significantly more damage than plates 4-6, which was shown to have greater impact resistance by testing data. Therefore, viewing both sides of components are are important in determining the extent of impact damage.

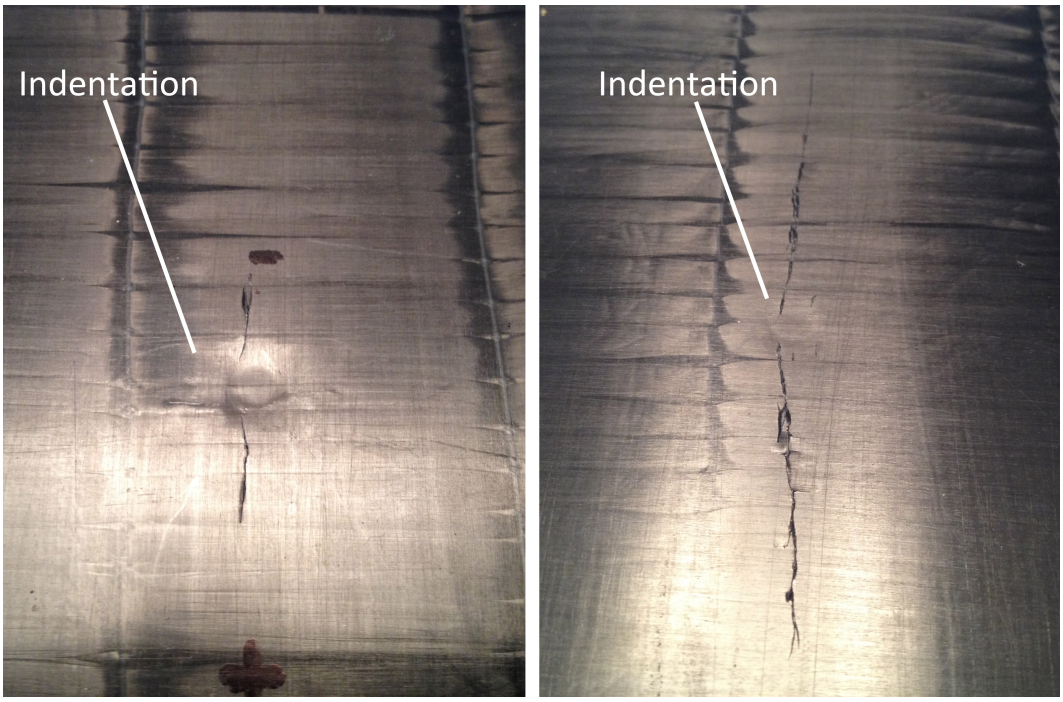


Figure 4.44: Impact surface crack length comparison of P2_IMP (left) and P6_IMP (right)

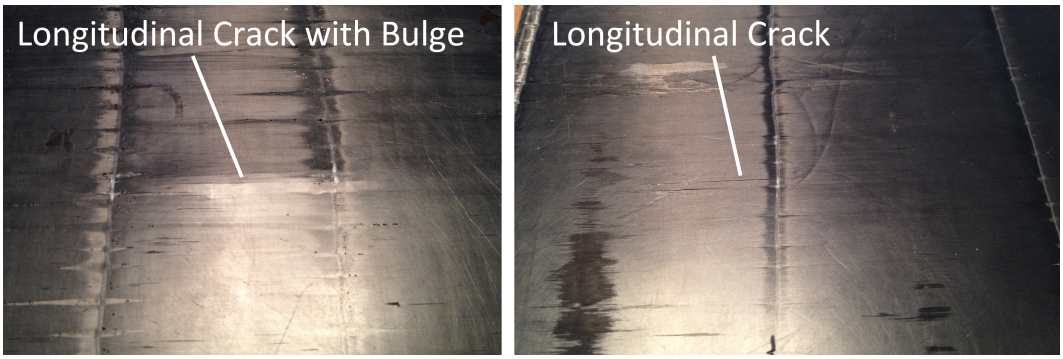


Figure 4.45: Bottom surface crack comparison of P2_IMP (left) and P6_IMP (right)

4.3 Mechanical Testing of Integral Reinforced Panels

4.3.1 Long Span Four-Point Bending

IRP specimens were tested in long span four point bending to determine debonding strength where flat and curved sections were joined, as proposed by A. Atarsia of Bombardier Aerospace. The test setup used for IRPs featured a load span to support span of 165:191, much different from the 64:128 (1:2) recommended by ASTM standard D7264. However, the goal in this case was not examine flexural properties. Table 4.29 presents testing data from long span four-point bending of IRPs while Table 4.30 contains statistical data for each IRP. Load-deflection curves for all long span four-point bending IRP specimens are shown in Appendix E.

Average maximum loads ranged from 3398 N with a standard deviation of ±460.6 N for IRP 1 to 6338 N with a standard deviation of ±663.5 for IRP 2. IRPs 1 and 3, which were made from ±45º angle-ply preforms experienced failure at a much lower maximum load than IRP 2 made from the crossply preforms. It was expected that specimens from IRP 2 would allow a greater maximum load as 56 % of its reinforcement was oriented along the length of the specimens as opposed to IRPs 1 and 3, where all reinforcing fibres were oriented at ±45º from the length of the specimens. Although IRPs 1 and 3 featured the same laminating sequence, IRP 1 failed at a lower average maximum load than IRP

3. This was likely a result of a stress concentration at an inner corner where the flat plate and curved sections join, created by the sharp knife-edge of the inner mould used in making IRP 1, as discussed in Section 4.1.2. In addition to the stress concentration at the inner corner, cracks generated from removal of the inner mould may also have been present in the specimens as shown previously in the micrograph of Figure 4.20.

Table 4.29: Specimen and test data from long span four-point bending of IRPs

Specimen	Width [mm]	Thickness [mm]		Maximum Load [N]
		4 mm nom.	8 mm nom.	
IRP1_LSB1	25.28	4.139	8.071	2991
IRP1_LSB2	25.53	4.181	8.111	3514
IRP1_LSB4	25.87	4.222	8.146	3999
IRP1_LSB6	25.23	4.203	8.124	3088
IRP2_LSB1	26.90	4.343	8.318	6877
IRP2_LSB3	25.41	4.397	8.401	5597
IRP2_LSB4	25.86	4.434	8.471	6540
IRP3_LSB1	25.84	4.063	7.965	4110
IRP3_LSB2	26.25	4.083	7.993	4068
IRP3_LSB3	25.78	4.090	7.989	3904

Table 4.30: Statistical data from long span four-point bending of IRPs

IRP	Laminating Sequence	Maximum Load [N]	
		Average	Std. Dev.
1	$[[+45°/-45°]_4/+45°]_S$	3398	±460.6
2	$[[0°/90°]_4/0°]_S$	6338	±663.5
3	$[[+45°/-45°]_4/+45°]_S$	4027	±108.9

Observations describing failure mechanisms for each IRP specimen appear in Table 4.31. Failure mechanisms were fairly consistent within IRPs, but they varied significantly between IRPs.

Specimens from IRP 1 mostly experienced interlaminar debonding cracks between the curved and flat plates, which propagated towards the thickness transition and led to debonding separation of the sections, Figures 4.46 to 4.48. Failure of specimens from IRP 1 were localized to the junction of curved and flat sections, likely a result of cracks that were present prior to testing.

Specimens from IRP 2 failed primarily from interlaminar shear cracks which formed within multiple layers located between the loading noses and support noses with no observable effect to the central region between both loading noses, Figures 4.49 and 4.50. For IRP 2 specimens, the debonding strength exceeded that of the interlaminar shear strength of the outer flat plate sections which failed in a manner similar to the short span three-point bending specimens.

Specimens from IRP 3 failed with some combination of mechanisms observed in specimens from IRPs 1 and 2; however, without complete debonding as observed within specimens from IRP 1. Failure of specimens from IRP 3 was caused by interlaminar debonding cracks between the curved and flat sections and interlaminar cracks within the flat sections outside of the loading noses, Figure 4.51. Therefore debonding strength and interlaminar shear strength were similar for IRP 3.

Table 4.31: Failure observations for long span four-point testing of IRPs

Specimen	Failure Observations	Figure
IRP1_LSB1	Interlaminar debonding cracks through left and right stitched joints, originating at thickness transitions, debonding of left side.	
IRP1_LSB2	Interlaminar debonding cracks through left and right stitched joints, originating at thickness transitions, debonding of right side.	4.46
IRP1_LSB4	Interlaminar cracks through left and right stitched joints, originating at thickness transitions, complete sudden debonding of curved and flat sections.	4.47
IRP1_LSB6	Interlaminar cracks through left and right stitched joints, originating at inner junction of curved and flat sections and propagating downward through layers, debonding of curved and flat sections on left side along with with shear failure of flat section.	4.48
IRP2_LSB1	Interlaminar shear cracking of right and left side flat sections outside of loading nose.	4.49
IRP2_LSB3	Interlaminar shear cracking of left side flat plate section outside of loading nose.	
IRP2_LSB4	Interlaminar shear cracking of right and left side flat sections outside of loading nose, with 45^{o} through-thickness cracks originating under loading nose towards support nose.	4.50
IRP3_LSB1	Interlaminar debonding cracks through left and right stitched joints originating at thickness transitions and interlaminar cracks flat plate between loading and support noses.	4.51
IRP3_LSB2	Interlaminar debonding cracks through left and right stitched joints originating at thickness transitions and interlaminar cracks flat plate between loading and support noses	
IRP3_LSB3	Interlaminar debonding cracks through left stitched joint originating at thickness transition and interlaminar cracks within flat plate section on left and right sides between loading and support noses	

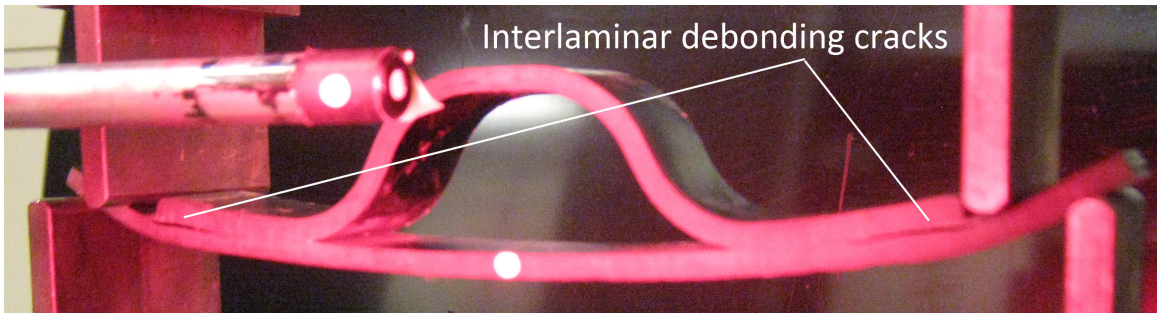


Figure 4.46: Interlaminar debonding cracks originating at thickness transition, IRP1_LSB2



Figure 4.47: Complete separation of curved section from flat section, IRP1_LSB4

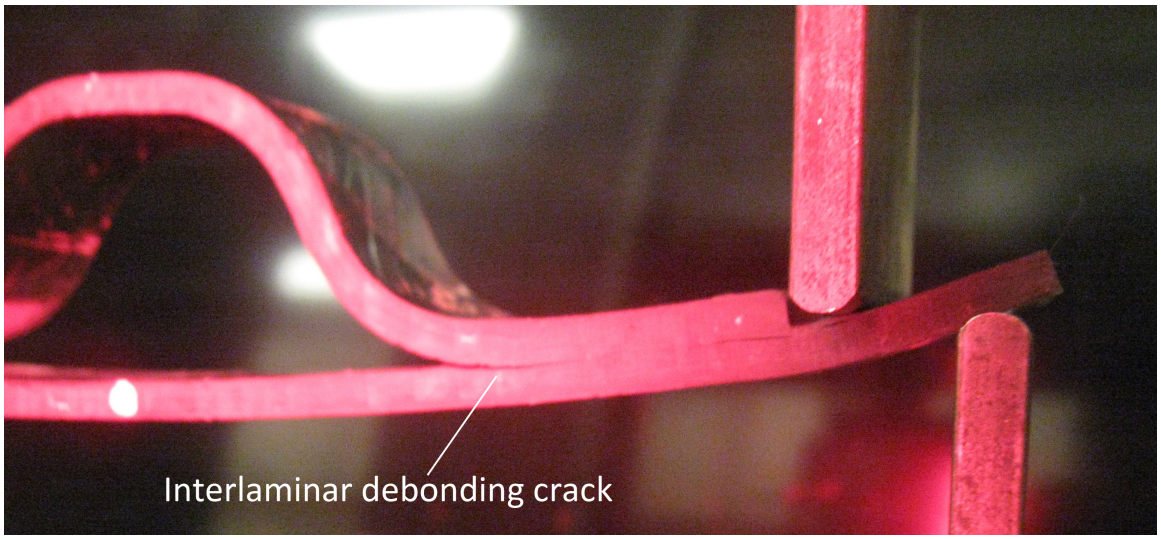


Figure 4.48: Interlaminar debonding cracks originating inside junction of curved and flat sections, IRP1_LSB6

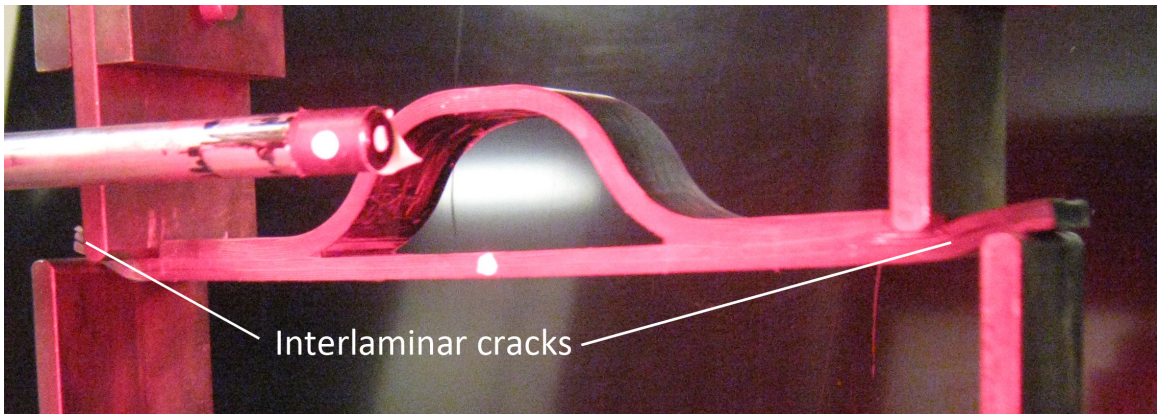


Figure 4.49: Interlaminar cracking of left and right side flat sections outside of loading noses, IRP2_LSB1

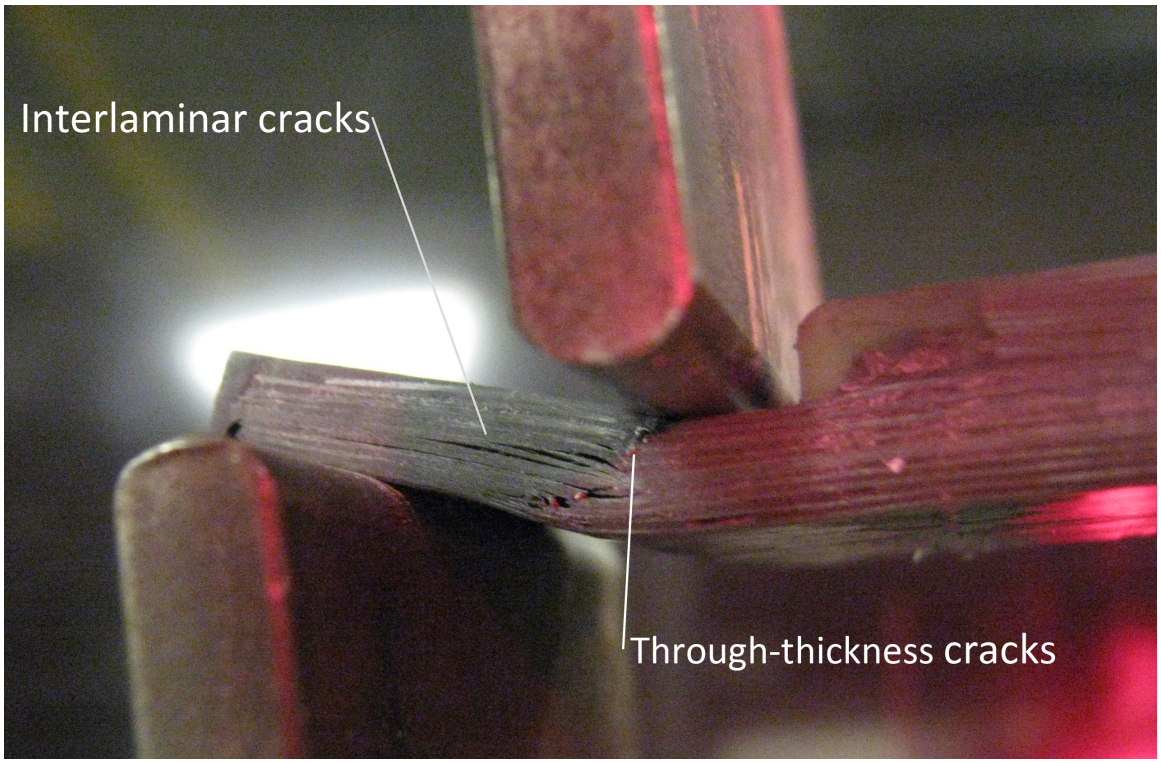


Figure 4.50: Through-thickness and combined interlaminar cracks outside of loading nose, IRP2_LSB4

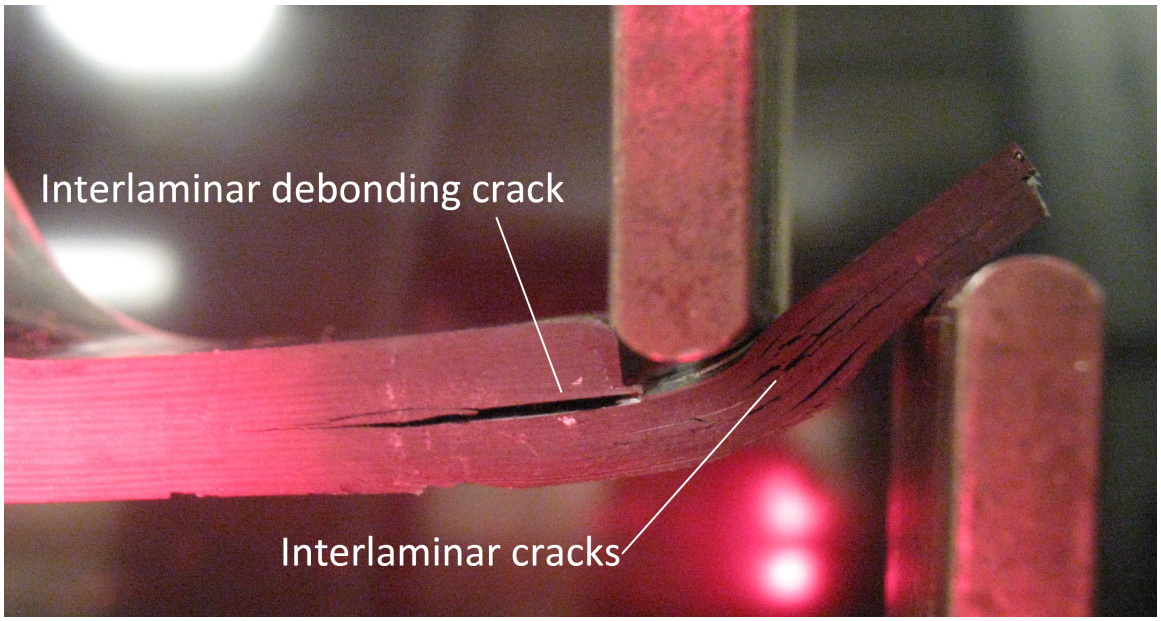


Figure 4.51: Interlaminar debonding crack between flat section and curved section and interlaminar cracks within outer flat section, IRP3_LSB1

Based on the failure mechanisms observed from long span four-point testing of IRPs, it can be concluded that the debonding strength was highly dependant on the laminating sequence. Specimens from IRP 2 with a cross-ply laminating sequence did not feature any damage or cracking within the central region between the loading noses. However, IRPs 1 and 3 featuring angle-ply laminating sequences experienced cracking near the junctions of curved and flat sections along with failure at lower load levels. The other main factor to consider when comparing IRPs 1 and 3 was the change made in the inner mould as discussed in Section 4.1.2, in which the sharp inner edges were machined to a blunt edge. Initially the sharp inner edges created stress concentrations and generated small cracks from demoulding; both were mitigated by blunting the edges of the mould. This lead to better performance of specimens from IRP 3 compared with those from IRP 1 in both maximum load and failure.

Chapter 5

Conclusion and Recommendations

The goal of this thesis was to document and analyze physical quality and mechanical properties of PMC composite components manufactured from stitched multilayer 3D carbon fibre preforms using RTM. The preforms used for the components were made from layers of straight carbon fibre yarns laid into layers and stitched. Flat plates and integral reinforced panels, which consisted of a curved hat shaped section attached to a flat plate. Flat plates featured cross-ply preforms of different fibre volume fractions, and IRPs featured either cross-ply or angle-ply preforms.

Visual observation indicated that resin infusion was reasonably successful as components achieved near complete wetting with few resin starved areas. Resin starved areas generally occurred between adjacent stitch lines and occurred were larger in components with higher fibre volume fractions. Also, fibre misalignment caused by resin flow was observed in components. Fibre misalignment would likely impact mechanical properties, however its effect on mechanical properties were not examined. Internal quality of components was evaluated using optical microscopy of small samples taken from components. Imaging also verified successful resin injection, however minor internal defects were discovered. Porosity, fibre distortions from stitching and interlaminar gaps were observed, however the frequency of these defects was low within the samples used for analysis. Average calculated porosity values were within typically accepted piratical ranges.

Flexural testing of flat plate specimens showed reasonable alignment of flexural moduli with theoretical expectations, however, as fibre volume fraction increased, the sep-

aration between experimental and theoretical values increased. Flexural strength was limited by transverse stitch lines where resin-rich zones from stitch induced fibre crimp caused variations in surface properties, leading to isolated failure at stitch lines. Samples tested without stitch-lines achieved strengths closer to expected. Short beam shear strength values were significantly less than comparable values found in literature and were more dependent on testing orientation than fibre volume fraction. Short beam specimens frequently exhibited unexpected failure modes, therefore making it difficult to conclude that short beam shear strength represented actual interlaminar shear strength. Specimens with higher fibre volume fractions showed improved impact resistance based on reaching higher maximum loads, lower absorbed energies and decreased indentation. Also, energy release indicative of delamination, was less severe than was observed in literature. Debonding resistance of IRP specimens was largely dependent on laminating sequence as cross-ply IRPs allowed much higher loads than angle-ply IRPs. However, debonding failure was observed in angle-ply specimens only, therefore determining debonding resistance of cross-ply specimens was not possible.

Future work is required to study the effects of preforming and injection parameters not explicitly studied within this thesis. Preform manufacturing parameters such as stitch tension, density and material, as stitches were shown to impact flexural strength and fracture toughness. Also, injection parameters such as resin flow rate and placement of resin inlets and outlets should be studied in order to optimize final part quality. Automating the manufacture of preforms is an important step in reducing time spent manufacturing components and would decrease geometric variations between preforms. Thickness variation within components was not insignificant, therefore reinforcing current moulds or using more rigid moulds would improve dimensional accuracy. Also, decreasing resin injection flow rates, in turn decreasing injection pressures may reduce mould deflection during injection improving dimensional accuracy. Thickness variation also affected test results obtained from both four point and three point bending. Span-to-thickness ratios required to induce desired failure modes were not held constant. Therefore, more specific studies relating to each test method by ensuring proper span-thickness-ratios should be performed. Further investigation into damage resulting from drop-weight impact testing

using non-destructive methods should also be explored. Ultrasonic C-scan plots could potentially provide more information regarding delamination behaviour by measuring internal damage.

References

[1] Boeing. Boeing 777 Facts.

[2] Boeing. 787 Dreamliner - Program Fact Sheet.

[3] W. D. Callister Jr. *Materials Science and Engineering*. Wiley, Utah, USA, 6th edition, 2003.

[4] Toho Tenax America. Tenax-J HTS240, 2010.

[5] Tri-Tex. Marine System L-1911 (Temporary) Clear Laminating/Infusion System, 2006.

[6] National Research Council Canada. Liquid Composite Moulding, 2012.

[7] A Mills. Automation of carbon fibre preform manufacture for affordable aerospace applications. *Composites Part A: Applied Science and Manufacturing*, 32:955–962, 2001.

[8] X. Wu, J. Li, and R. a. Shenoi. A New Method to Determine Fiber Transverse Permeability. *Journal of Composite Materials*, 41(6):747–756, May 2006.

[9] Suresh G. Advani. Resin Transfer Molding, 2004.

[10] C Greb, A Schnabel, F Kruse, M Linke, and T Gries. Cost efficient preform production for complex FRP-structures. In *International SAMPE Technical Conference*, 2011.

[11] A Mills. Development of an automated preforming technology for resin infusion processing of aircraft components. *Proceedings of the Institution of Mechanical Engineers, Part G: Journal of Aerospace Engineering*, 220(5):499–505, October 2006.

[12] Patrick Schiebel, Tim Block, and Axel S Herrmann. Prospects and risks of tailored preforms for advanced composite applications. In *Texcomp 9*, pages 1–29, Newark, DE USA, 2008.

[13] T Uozumi, A Kito, and T Yamamoto. CFRP using braided preforms / RTM process for aircraft applications. *Advanced Composite Material*, 14(4):365–383, 2005.

[14] Yong Kok Swee. Fabric types and structures, 2004.

[15] B K Behera and Rajesh Mishra. 3-Dimensional weaving. *Indian Journal of Fibre & Textile Research*, 33(September):274–287, 2008.

[16] L Tong, A P Mouritz, and M K Bannister. *3D Fibre Reinforced Polymer Composites*. Elsevier, 2002.

[17] A.P. Mouritz, M.K. Bannister, P.J. Falzon, and K.H. Leong. Review of applications for advanced three-dimensional fibre textile composites. *Composites Part A: Applied Science and Manufacturing*, 30(12):1445–1461, December 1999.

[18] A.P. Mouritz and B.N. Cox. A mechanistic approach to the properties of stitched laminates. *Composites Part A: Applied Science and Manufacturing*, 31(1):1–27, January 2000.

[19] Isaac M. Daniel and Ori Ishai. *Engineering Mechanics of Composite Materials*. Oxford University Press, Inc., New York, NY, 1st edition, 1994.

[20] J. E. Ashton and J. C. Halpin. Primer on Composite Materials: Analysis, 1969.

[21] J.C. Halpin and J.L. Kardos. The Halpin-Tsai Equations: A Review. *Polymer Engineering and Science*, 16(5), 1976.

[22] Vincent Calard. Formulas and Equations for the Classical Laminate Theory, 2011.

[23] J.N. Reddy. Classical and First Order Theories of Laminated Composite Plates. In *Mechanics of Laminated Composite Plates and Shells Theory and Analysis*, chapter 3, pages 109–156. CRC Press LLC, Boca Raton, FL, USA, 2nd edition, 2004.

[24] Wim Van Paepegem. What Are Composites?, 2009.

[25] David Roylance. Laminated composite plates. Technical report, Massachusetts Institute of Technology, Cambridge, MA, 2000.

[26] P.K. Mallick. *Fiber-Reinforced Composites Materials, Manufacturing and Design*. CRC Press Taylor & Francis Group, Boca Raton FL, USA, 3rd edition, 2007.

[27] L.B. Greszczuk. Theoretical and experimental studies on properties and behavior of filamentary composites. *Proceedings of the 21st Annual Techincal Conference, Society of the Plastics Industry*, 1966.

[28] B. W. Rosen. Mechanics of composite strengthening. In *Fiber Composite Materials*. American Society for Metals, Metals park, OHIO, 1965.

[29] T.a. Collings. Transverse compressive behaviour of unidirectional carbon fibre reinforced plastics. *Composites*, 5(3):108–116, May 1974.

[30] M. Kuwata and P.J. Hogg. Interlaminar toughness of interleaved CFRP using non-woven veils: Part 2. Mode-II testing. *Composites Part A: Applied Science and Manufacturing*, 42(10):1560–1570, October 2011.

[31] M. Kuwata and P.J. Hogg. Interlaminar toughness of interleaved CFRP using non-woven veils: Part 1. Mode-I testing. *Composites Part A: Applied Science and Manufacturing*, 42(10):1551–1559, October 2011.

[32] a.B. de Morais. A new fibre bridging based analysis of the Double Cantilever Beam (DCB) test. *Composites Part A: Applied Science and Manufacturing*, 42(10):1361–1368, October 2011.

[33] Jangkyo Kim, Caroline Baillie, Jareoph Poh, and YW Mai. Fracture toughness of CFRP with modified epoxy resin matrices. *Composites Science and Technology*, 43(1992):283–297, 1992.

[34] John F. Mandell, Douglas S. Cairns, Daniel D. Samborsky, Robert B. Morehead, and Darrin J. Haugen. Prediction of Delamination in Wind Turbine Blade Structural Details. *Journal of Solar Energy Engineering*, 125(4):522, 2003.

[35] A Standard. D5528-01 2001. Standard Test Method for Mode I Interlaminar Fracture Toughness of Unidirectional Fiber-Reinforced Polymer Matrix Composites. *American Society for Testing and Materials*, pages 1–13, 2014.

[36] Ronald Krueger. Computational fracture mechanics for composites. *State of the art and challenges, NAFEMS Nordic . . .*, 2006.

[37] Naveed a. Siddiqui, Ricky S.C. Woo, Jang-Kyo Kim, Christopher C.K. Leung, and Arshad Munir. Mode I interlaminar fracture behavior and mechanical properties of CFRPs with nanoclay-filled epoxy matrix. *Composites Part A: Applied Science and Manufacturing*, 38(2):449–460, February 2007.

[38] Denis D.R. Cartié, Jean-Martin Laffaille, Ivana K. Partridge, and Andreas J. Brunner. Fatigue delamination behaviour of unidirectional carbon fibre/epoxy laminates reinforced by Z-FiberÂ® pinning. *Engineering Fracture Mechanics*, 76(18):2834–2845, December 2009.

[39] Craig a. Steeves and Norman a. Fleck. In-plane properties of composite laminates with through-thickness pin reinforcement. *International Journal of Solids and Structures*, 43(10):3197–3212, May 2006.

[40] Kimberley Dransfield, Caroline Baillie, and Yiu-wing Mai. Improving the Delamination Resistance of CFRP by Stitching - A Review. *Composites Science and Technology*, 50:305–317, 1994.

[41] M.P. Rao, B.V. Sankar, and G. Subhash. Effect of Z-yarns on the stiffness and strength of three-dimensional woven composites. *Composites Part B: Engineering*, 40(6):540–551, September 2009.

[42] N.E. Naik, Sk. N. E Azad, and P Durga Prassad. Stress and Failure Analysis of 3D Angle Interlock Woven Composites. *Journal of Composite Materials*, 36(01):93–123, 2002.

[43] Xuekun Sun and Changjie Sun. Mechanical properties of three-dimensional braided composites. *Composite Structures*, 65(3-4):485–492, September 2004.

[44] Heoung-Jae Chun, Hyung-Woo Kim, and Joon-Hyung Byun. Effects of through-the-thickness stitches on the elastic behavior of multi-axial warp knit fabric composites. *Composite Structures*, 74(4):484–494, August 2006.

[45] K. B. Su. Delamination resistance of stitched thermoplastic matrix composite laminates. *ASTM STP 1044*, pages 279–300, 1989.

[46] a. E. Bogdanovich. *Multi-scale modeling, stress and failure analyses of 3-D woven composites*, volume 41. August 2006.

[47] R. McIlhagger, J.P. Quinn, A.T. McIlhagger, S. Wilson, D. Simpson, and W. Wenger. The influence of binder tow density on the mechanical properties of spatially reinforced composites. Part 1 - Impact resistance. *Composites Part A: Applied Science and Manufacturing*, 38(3):795–801, March 2007.

[48] Uwe Beier, Jan K.W. Sandler, Volker Altstädt, Hermann Spanner, and Christian Weimer. Mechanical performance of carbon fibre-reinforced composites based on stitched and bindered preforms. *Composites Part A: Applied Science and Manufacturing*, 40(11):1756–1763, November 2009.

[49] V. Koissin, A. Ruopp, S.V. Lomov, I. Verpoest, V. Witzel, and K Drechsler. On-surface fibre-free zones and irregularity of piercing pattern in structurally stitched NCF preforms. *Advanced Composites Letters*, 15(3):81–88, 2006.

[50] P. Chang, A.P. Mouritz, and B.N. Cox. Flexural properties of z-pinned laminates. *Composites Part A: Applied Science and Manufacturing*, 38(2):244–251, February 2007.

[51] Aerospace Engineering. Carbon Nanotube Hierarchical Composites for Interlaminar Strengthening, 2012.

[52] Enrique J. Garcia, Brian L. Wardle, and a. John Hart. Joining prepreg composite interfaces with aligned carbon nanotubes. *Composites Part A: Applied Science and Manufacturing*, 39(6):1065–1070, June 2008.

[53] Geon-Woong Lee, Joong Sik Choi, Sang-Soo Lee, Min Park, Junkyung Kim, Chul-Rim Choe, and Soonho Lim. Mechanical properties and failure mechanism of the polymer composite with 3-dimensionally stitched woven fabric. *Macromolecular Research*, 11(2):98–103, April 2003.

[54] Yuqing Wei and Junqian Zhang. Characterization of microstructure in stitched unidirectional composite laminates. *Composites Part A: Applied Science and Manufacturing*, 39(5):815–824, May 2008.

[55] H. Talvensaari, E. Ladstätter, and W. Billinger. Permeability of stitched preform packages. *Composite Structures*, 71(3-4):371–377, December 2005.

[56] Y. Q. Ding, W. Wenger, and R. McIlhagger. Structural characterization and mechanical properties of 3-D woven composites. *Broadening horizons with advanced materials and processes*, pages 1–9, 1993.

[57] P.J. Callus, A.P. Mouritz, M.K. Bannister, and K.H. Leong. Tensile properties and failure mechanisms of 3D woven GRP composites. *Composites Part A: Applied Science and Manufacturing*, 30(11):1277–1287, November 1999.

[58] Ryuta Kamiya, Bryan a Cheeseman, Peter Popper, and Tsu-Wei Chou. Some recent advances in the fabrication and design of three-dimensional textile preforms: a review. *Composites Science and Technology*, 60(1):33–47, January 2000.

[59] Michael Bannister. Challenges for composites into the next millennium - a reinforcement perspective. *Composites Part A: Applied Science and Manufacturing*, 32:901–910, 2001.

[60] G. Williams, R. Trask, and I. Bond. A self-healing carbon fibre reinforced polymer for aerospace applications. *Composites Part A: Applied Science and Manufacturing*, 38(6):1525–1532, June 2007.

[61] G.a. Schoeppner and S. Abrate. Delamination threshold loads for low velocity impact on composite laminates. *Composites Part A: Applied Science and Manufacturing*, 31(9):903–915, September 2000.

[62] S. Ujihashi, K. Sakanoue, T. Adachi, and H. Matsumoto. Experimental measurement of the mechanical properties of fibre-reinforced plastics under impact loading. In *Proceedings of the Institution of Mechanical Engineers, 4th International Conference FRC'90*, pages 157–162, Liverpool, 1990.

[63] Sadayuki Ujihashi. An intelligent method to determine the mechanical properties of composites under impact loading. *Composite Structures*, 23(2):149–163, January 1993.

[64] J.D. Winkel and D.F. Adams. Instrumented drop weight impact testing of cross-ply and fabric composites. *Composites*, 16(4):268–278, October 1985.

[65] Francois Robitaille and Raymond Gauvin. Compaction of Textile Reinforcements for Composites Manufacturing. III: Reorganization of the Fibre Network. *Polymer Composites*, 20(1):48–61, 1999.

[66] ASTM Standard D7264/D7264M-07. Standard Test Method for Flexural Properties of Polymer Matrix Composite Materials, 2007.

[67] Instron. Advanced Video Extensometer AVE 2663-821. Technical report, Illinois Tool Works Inc., 1991.

[68] ASTM Standard D2344. Standard Test Method for Short-Beam Strength of Polymer Matrix Composite Materials, 2006.

[69] ASTM Standard D7136/D7136M-07. Standard Test Method for Measuring the Damage Resistance of a Fiber-Reinforced Polymer Matrix Composite to a Drop-Weight Impact Event, 2007.

[70] Struers. Secotom-10 Instruction Manual, 2010.

[71] R.T. Durai Prabhakaran, Hans Lilholt, Francis Aviles, Tom Logstrup Anderson, and Hans Knudson. Fibre waviness and misalignment measurement of unidirectional glass/lpet commingled composites - effect of mechanical properties. In B Madsen, H Lilholt, Y Kusano, S Faester, and B Ralph, editors, *Proceedings of the 34th Rise International Symposium on Materials Science - Processing of fibre composites*, pages 349–363, 2013.

[72] J Kastner, B Plank, D Salaberger, and J Sekelja. Defect and Porosity Determination of Fibre Reinforced Polymers by X-ray Computed Tomography. *2nd International Symposium on NDT in Aerospace*, pages 1–12, 2010.

[73] R.E. Lavengood and M. J. Michno. Composite Shear Strength - Tube Torsion vs Short Beam Shear, 1973.

[74] S.R. Ghiorse. Effect of Void Content of the Mechanical Properties of Carbon/Epoxy Laminates. *S.A.M.P.E. quarterly*, 24(2):54–59, 1993.

Appendix A

Load-Deflection Curves for Long Span Four-Point Bending of Flat Plates

Specimen Set 1

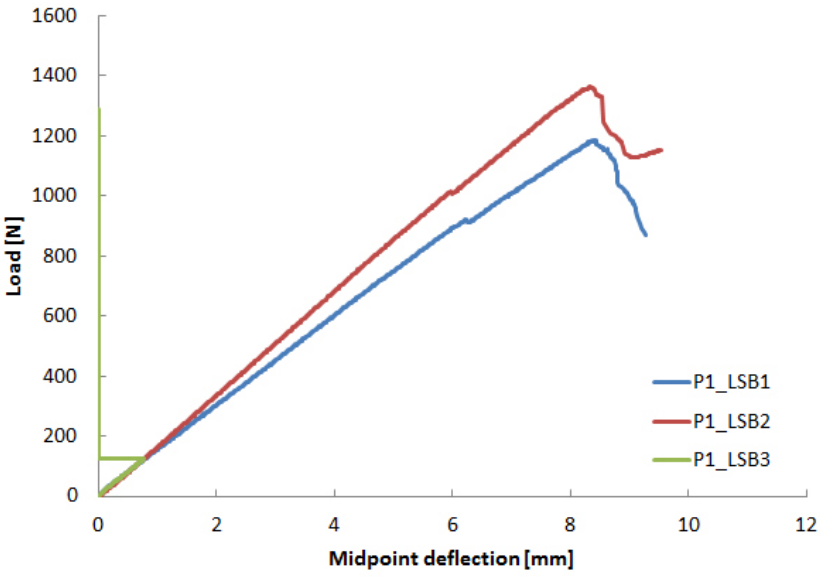


Figure A.1: Load-deflection curves for P1_LSB1, P1_LSB2 and P1_LSB3
*The AVE error occurred while testing specimen P1_LSB3

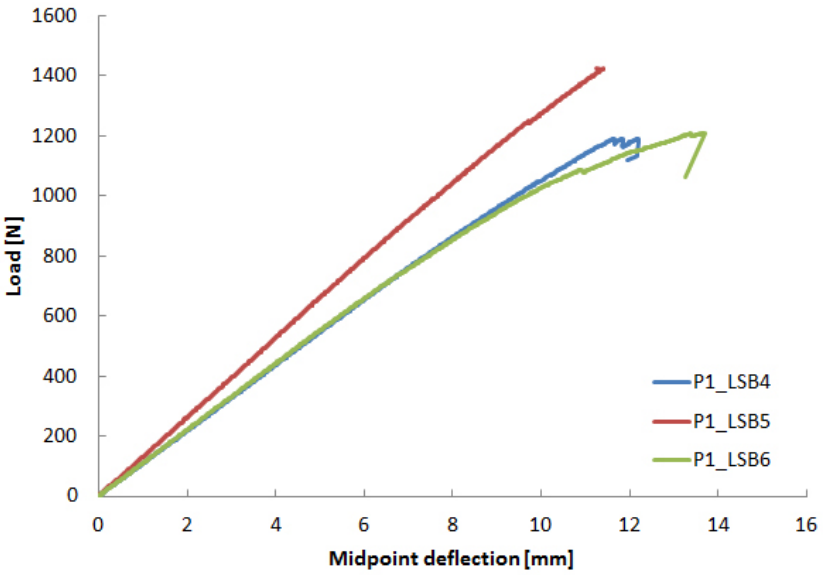


Figure A.2: Load-deflection curves for P2_LSB1, P2_LSB2 and P2_LSB3

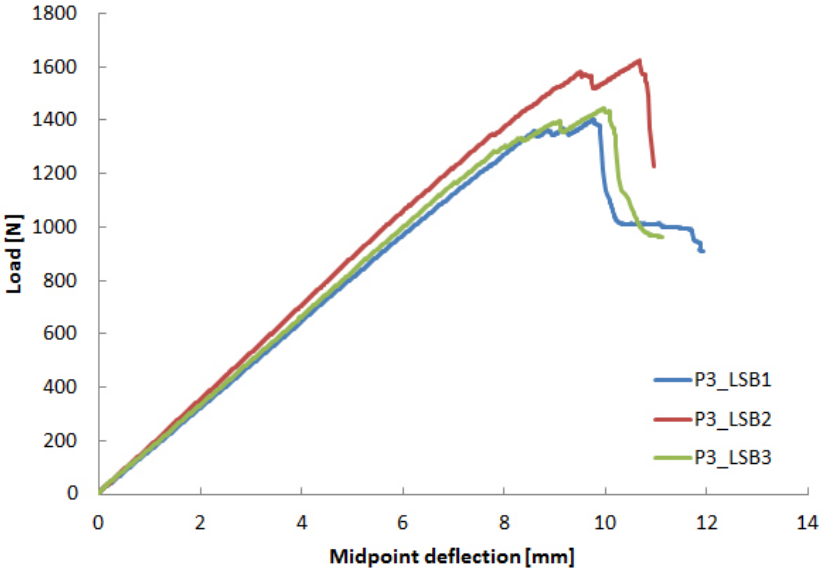


Figure A.3: Load-deflection curves for P3_LSB1, P3_LSB2 and P3_LSB3

Specimen Set 2

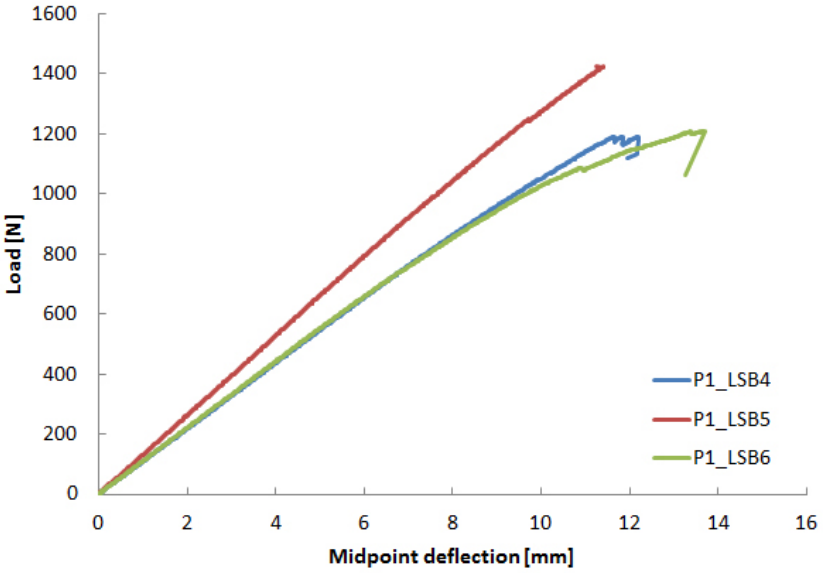


Figure A.4: Load-deflection curves for P1_LSB4, P1_LSB5 and P1_LSB6

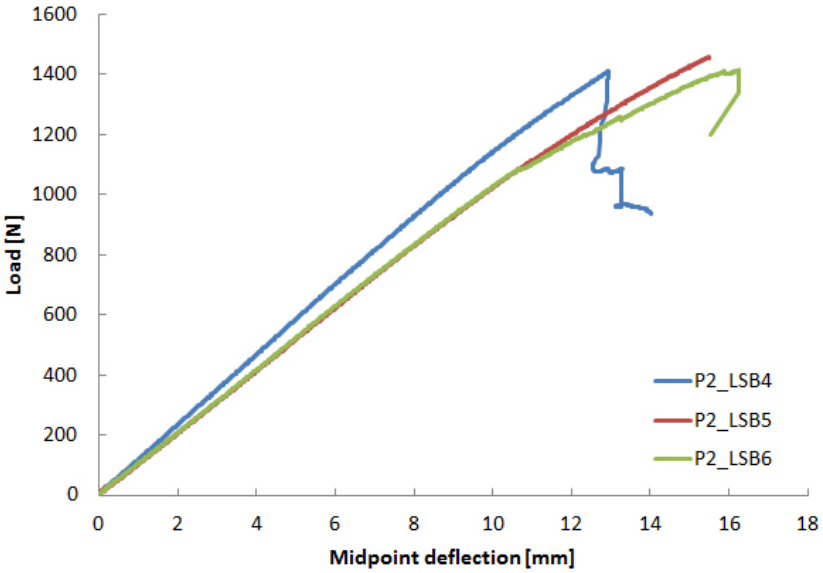


Figure A.5: Load-deflection curves for P2_LSB4, P2_LSB5 and P2_LSB6

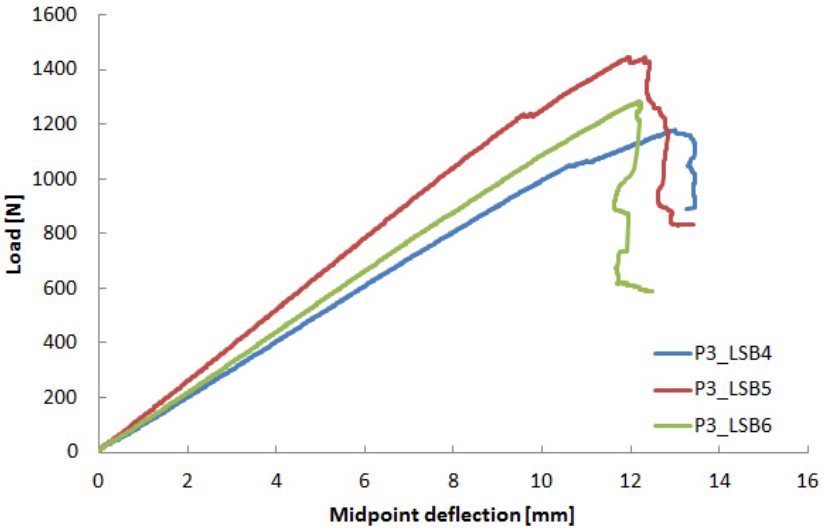


Figure A.6: Load-deflection curves for P3_LSB4, P3_LSB5 and P3_LSB6

Specimen Set 3

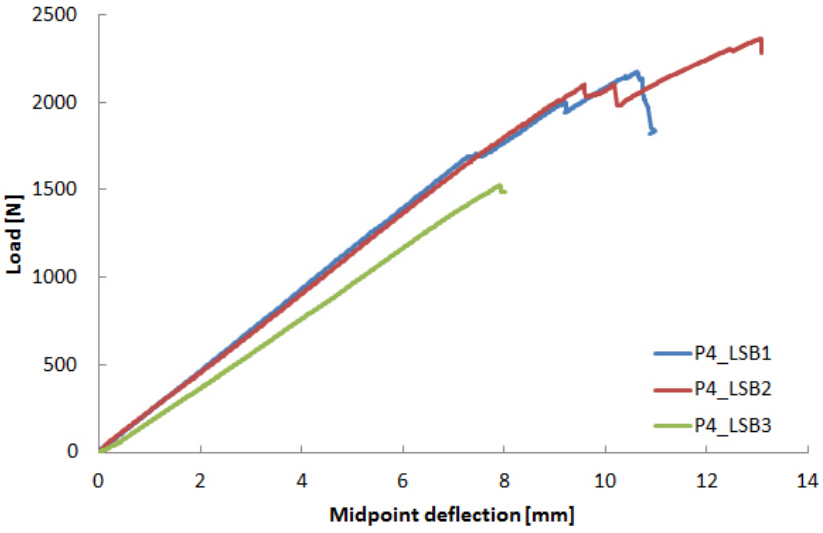


Figure A.7: Load-deflection curves for P4_LSB1, P4_LSB2 and P4_LSB3

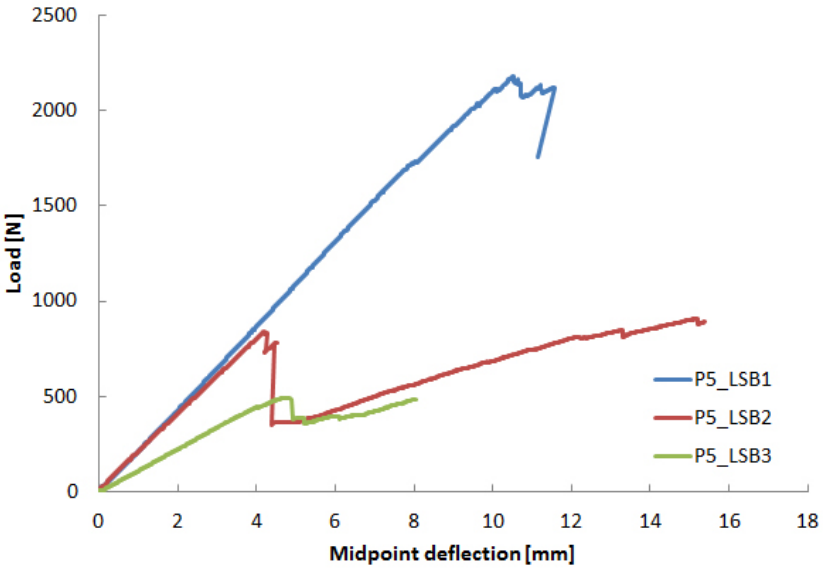


Figure A.8: Load-deflection curves for P5_LSB1, P5_LSB2 and P5_LSB3

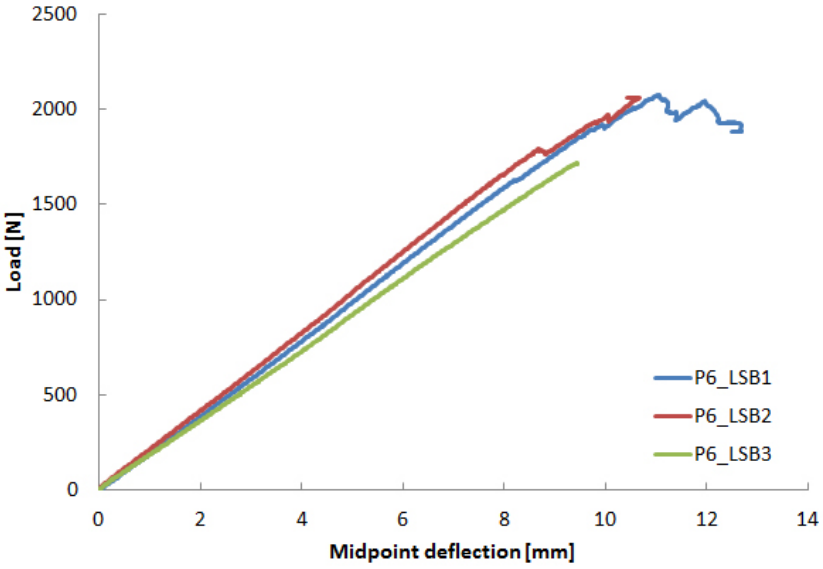


Figure A.9: Load-deflection curves for P6_LSB1, P6_LSB2 and P6_LSB3

Specimen Set 4

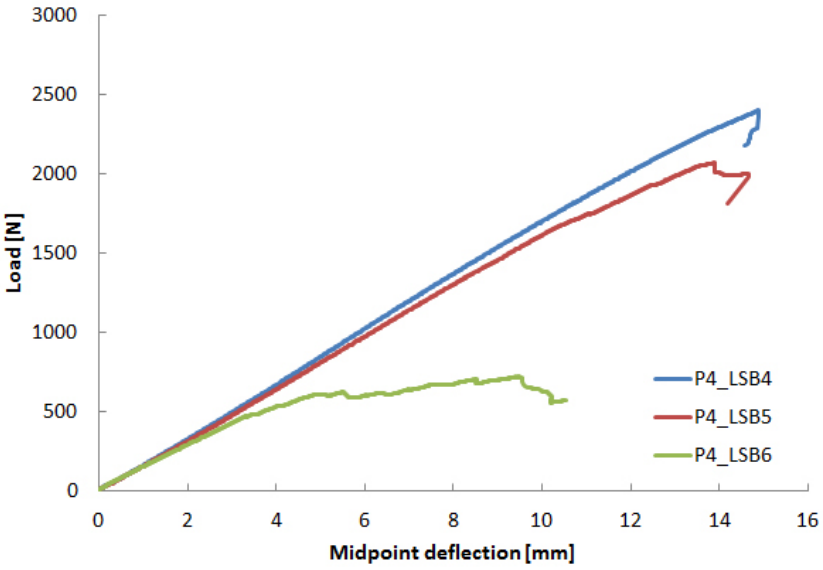


Figure A.10: Load-deflection curves for P4_LSB4, P4_LSB5 and P4_LSB6

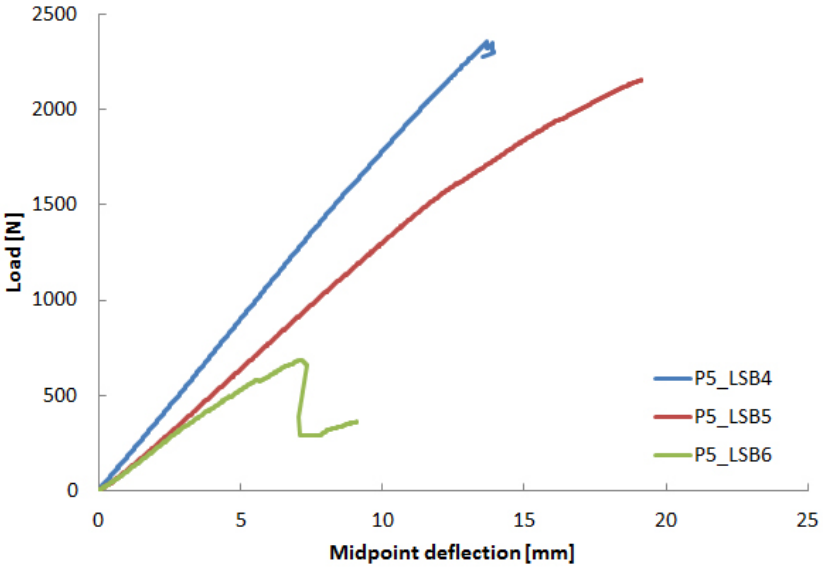


Figure A.11: Load-deflection curves for P5_LSB4, P5_LSB5 and P5_LSB6

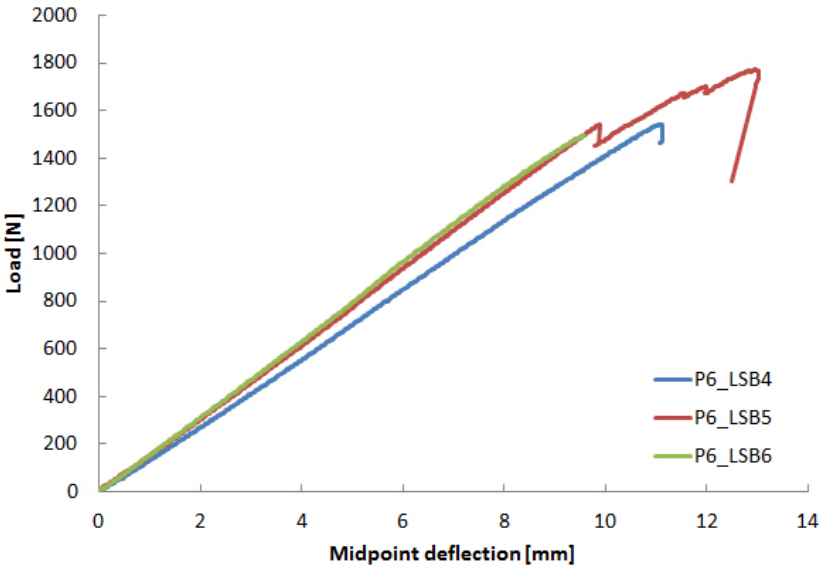


Figure A.12: Load-deflection curves for P6_LSB4, P6_LSB5 and P6_LSB6

Appendix B

Load vs. Deflection Curves for Short Span Three-Point Bending of Flat Plates

Specimen Set 5

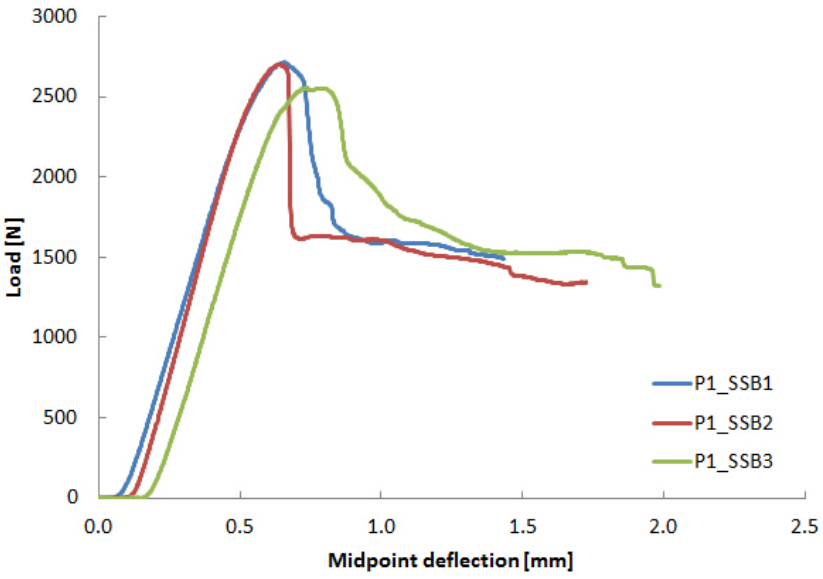


Figure B.1: Load-deflection curves for P1_SSB1, P1_SSB2 and P1_SSB3

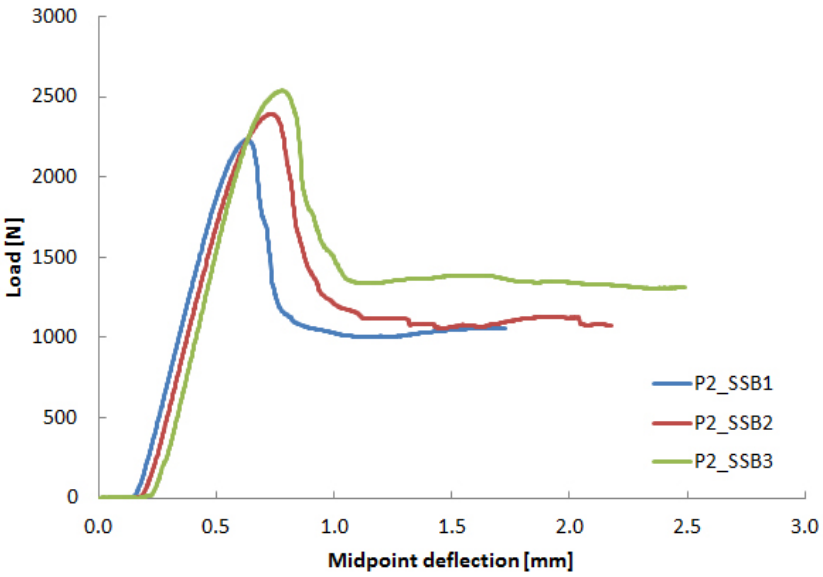


Figure B.2: Load-deflection curves for P2_SSB1, P2_SSB2 and P2_SSB3

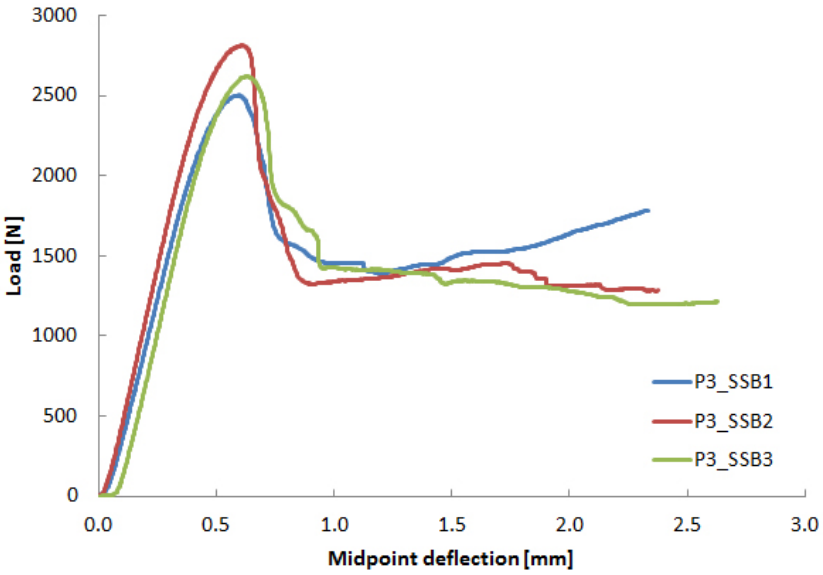


Figure B.3: Load-deflection curves for P3_SSB1, P3_SSB2 and P3_SSB3

Specimen Set 6

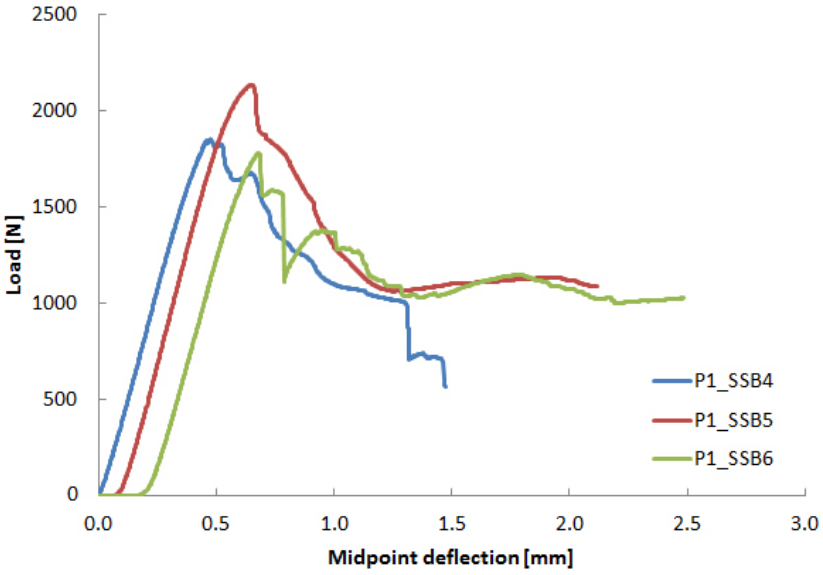


Figure B.4: Load-deflection curves for P1_SSB4, P1_SSB5 and P1_SSB6

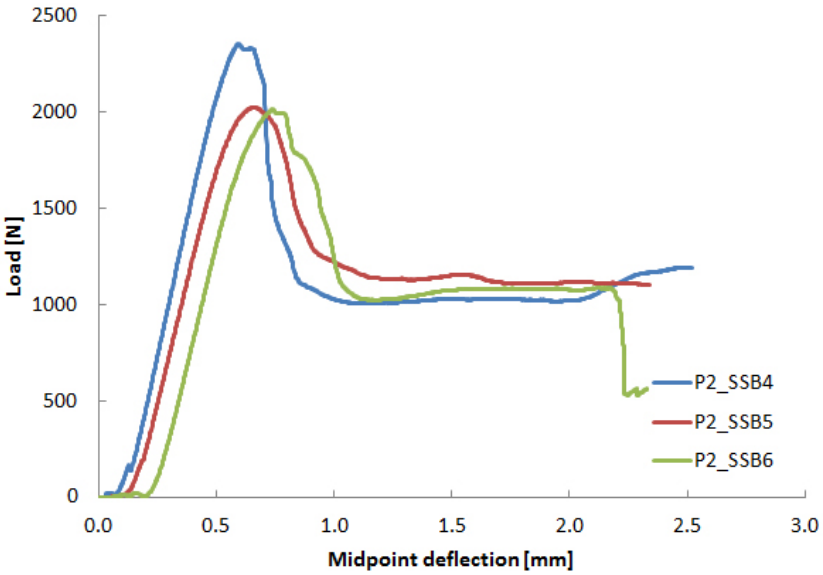


Figure B.5: Load-deflection curves for P2_SSB4, P2_SSB5 and P2_SSB6

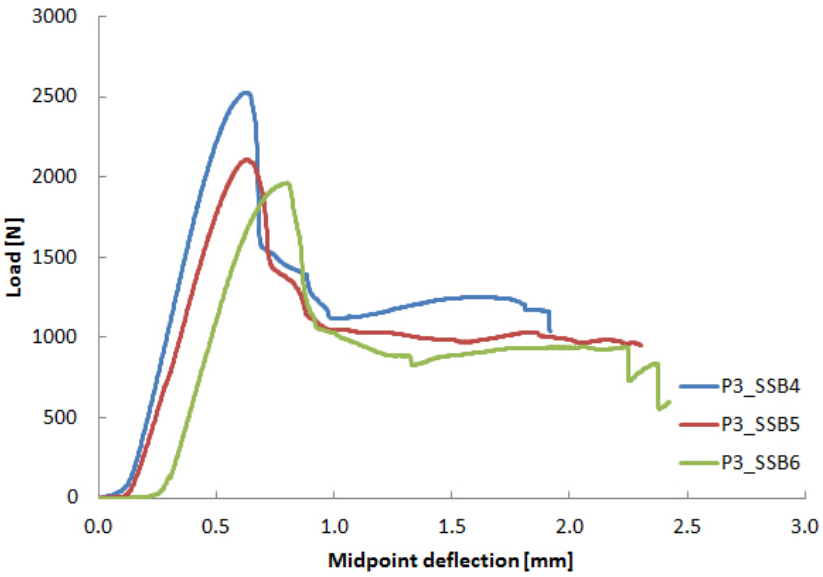


Figure B.6: Load-deflection curves for P3_SSB4, P3_SSB5 and P3_SSB6

Specimen Set 7

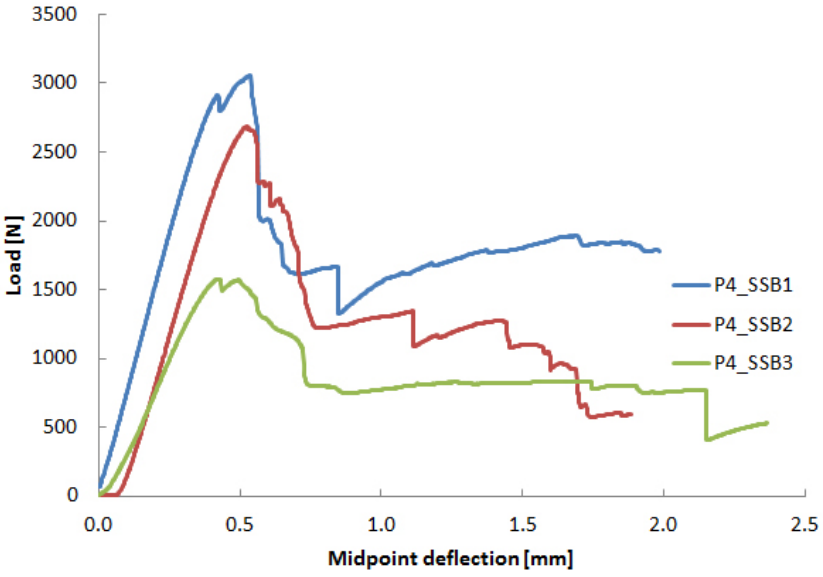


Figure B.7: Load-deflection curves for P4_SSB1, P4_SSB2 and P4_SSB3

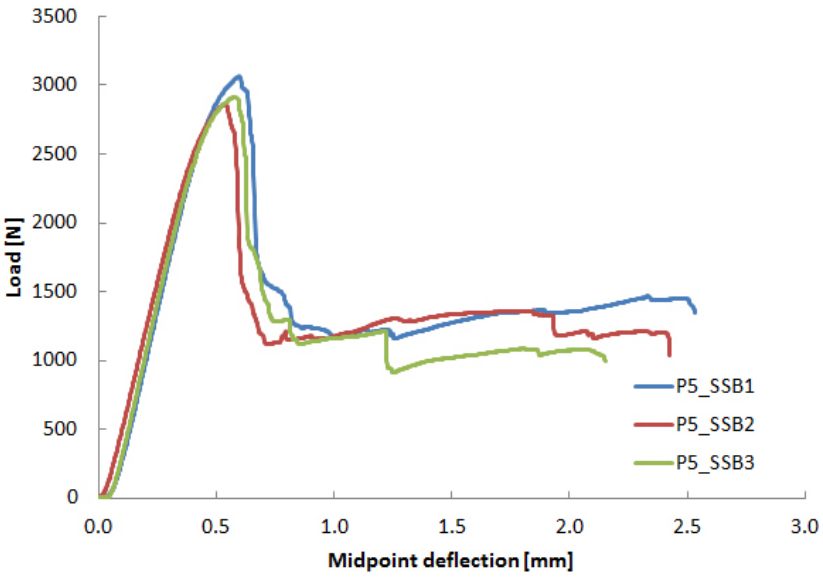


Figure B.8: Load-deflection curves for P5_SSB1, P5_SSB2 and P5_SSB3

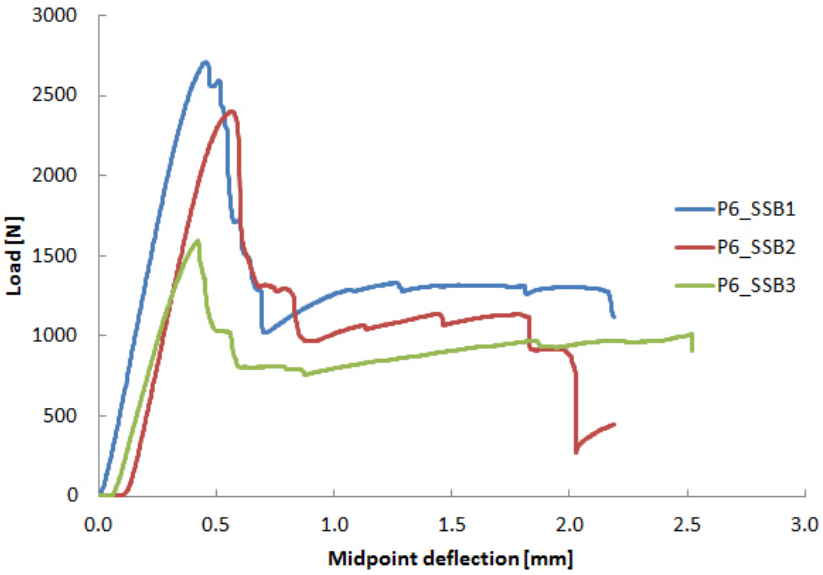


Figure B.9: Load-deflection curves for P6_SSB1, P6_SSB2 and P6_SSB3

Specimen Set 8

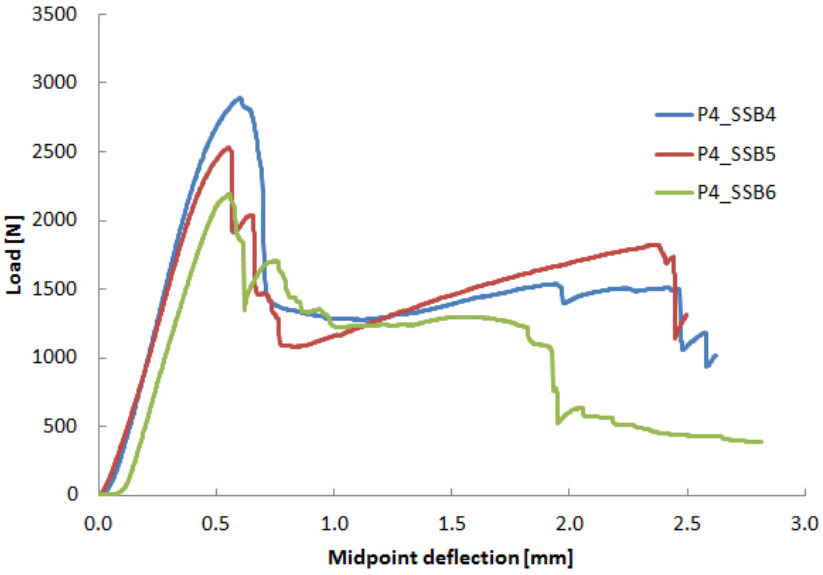


Figure B.10: Load-deflection curves for P4_SSB4, P4_SSB5 and P4_SSB6

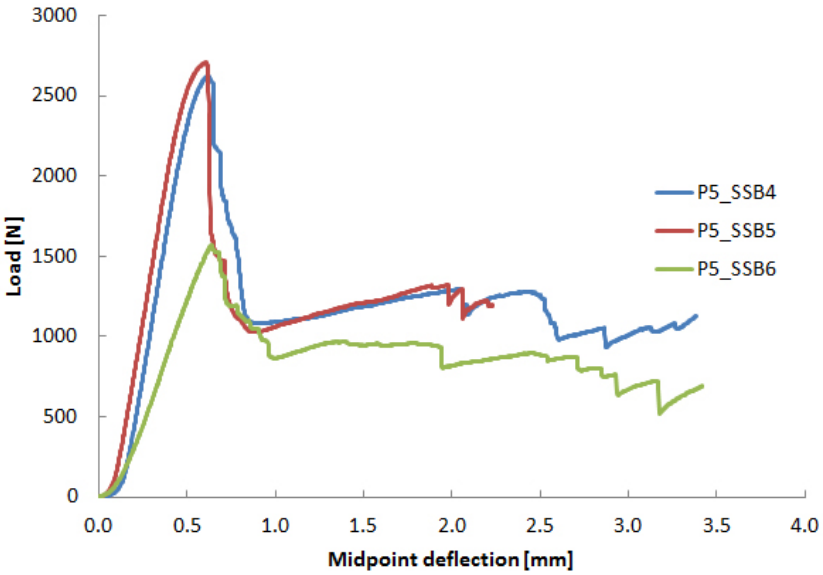


Figure B.11: Load-deflection curves for P5_SSB4, P5_SSB5 and P5_SSB6

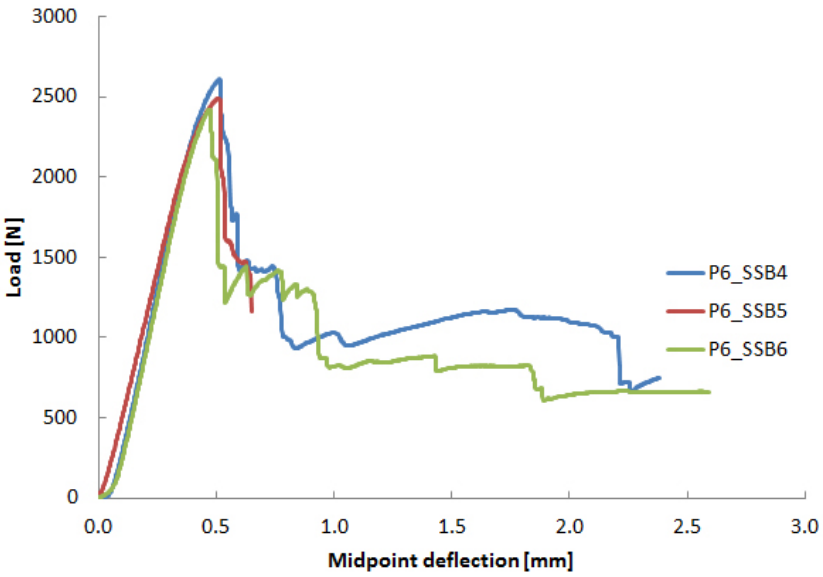


Figure B.12: Load-deflection curves for P6_SSB4, P6_SSB5 and P6_SSB6

Appendix C

Load-Time Curves for Drop-Weight Impact Tests of Flat Plates

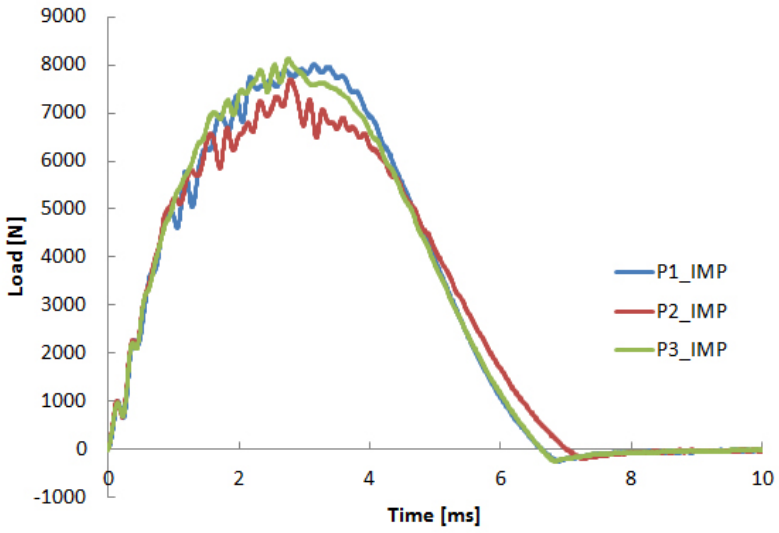


Figure C.1: Load-time curves for P1_IMP, P2_IMP and P3_IMP

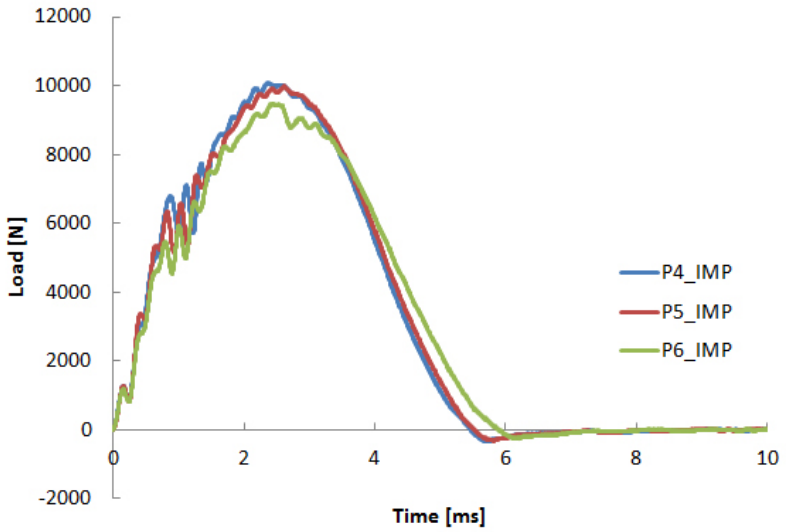


Figure C.2: Load-time curves for P4_IMP, P5_IMP and P6_IMP

Appendix D

Load-Deflection curves for Drop-Weight Impact Tests of Flat Plates

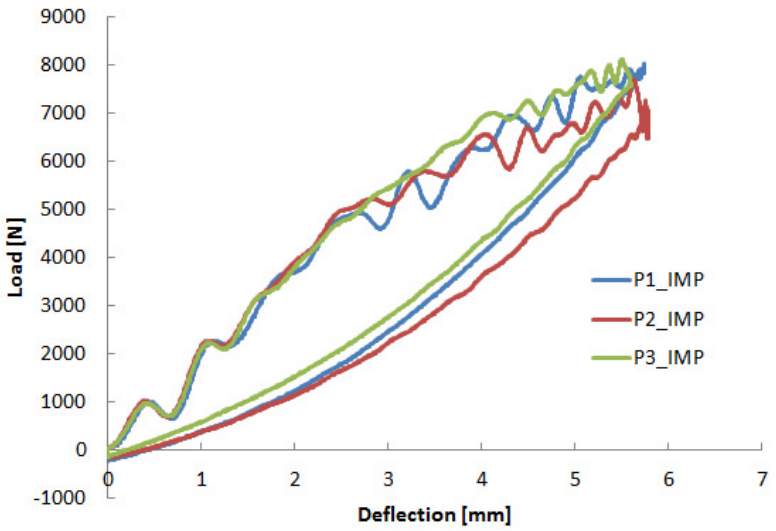


Figure D.1: Load-deflection curves for P1_IMP, P2_IMP and P3_IMP

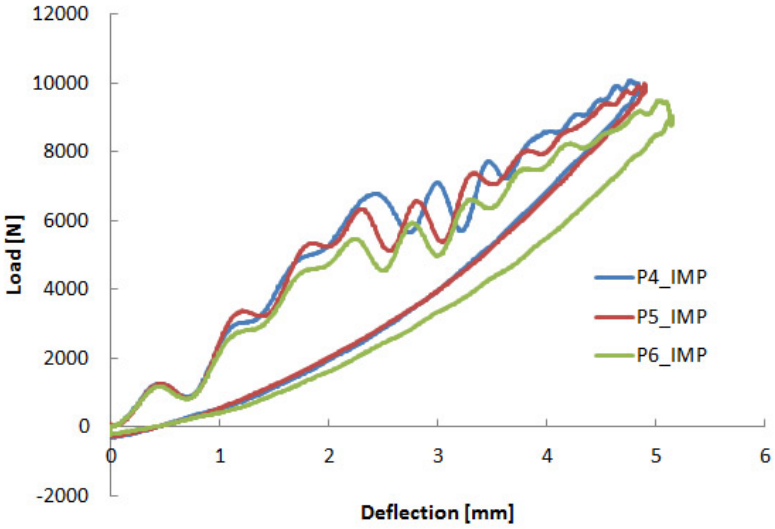


Figure D.2: Load-deflection curves for P4_IMP, P5_IMP and P6_IMP

Appendix E

Load-Deflection Curves for Long Span Four-Point Bending of IRPs

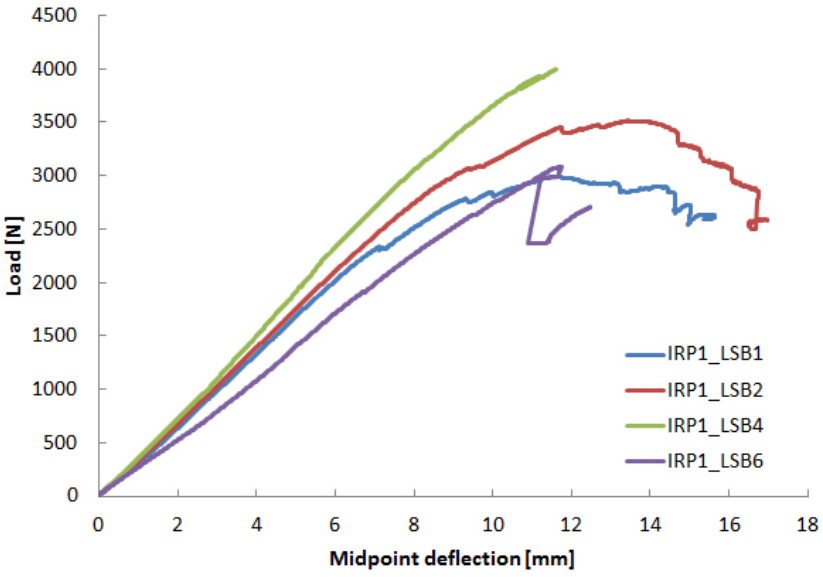


Figure E.1: Load-deflection curves for IRP1_LSB1, IRP1_LSB2, IRP1_LSB4 and IRP1_LSB6

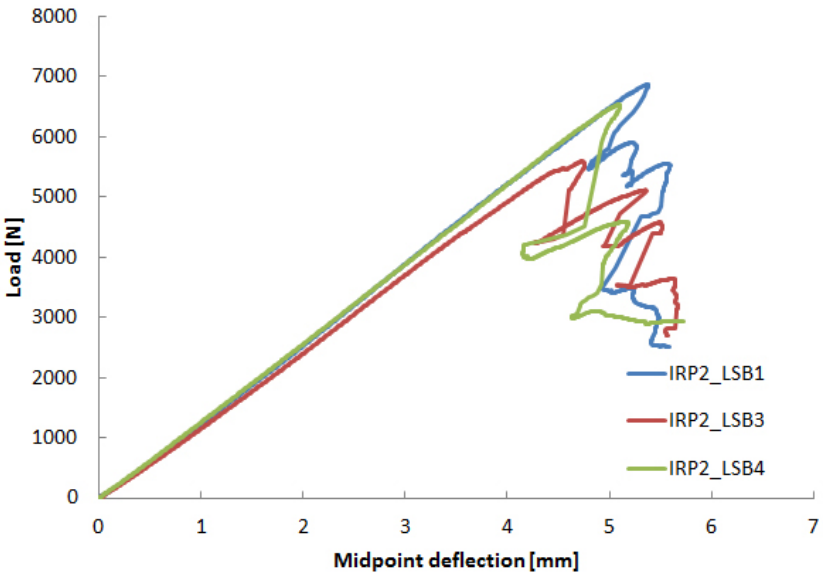


Figure E.2: Load-deflection curves for IRP2_LSB1, IRP2_LSB3 and IRP2_LSB4

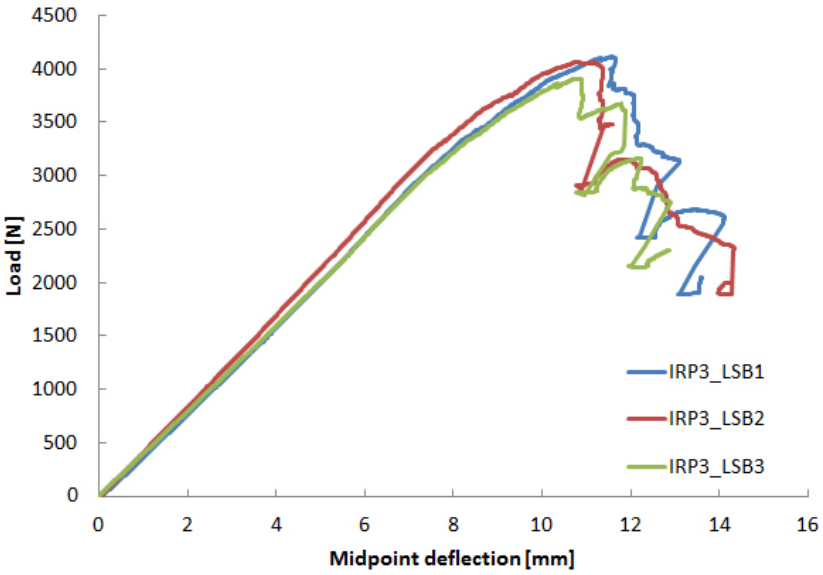


Figure E.3: Load-deflection curves for IRP3_LSB1, IRP3_LSB2 and IRP3_LSB3